

Portland State University

PDXScholar

---

Dissertations and Theses

Dissertations and Theses


---

Fall 11-18-2013

# Investigation of the Structure and Dynamics of Regioisomeric $\text{Eu}^{3+}$ and $\text{Gd}^{3+}$ Chelates of NB- DOTMA: Implications for MRI Contrast Agent Design

Benjamin Charles Webber  
*Portland State University*

Follow this and additional works at: [https://pdxscholar.library.pdx.edu/open\\_access\\_etds](https://pdxscholar.library.pdx.edu/open_access_etds)

 Part of the [Diagnosis Commons](#), [Medicinal Chemistry and Pharmaceutics Commons](#), and the [Radiochemistry Commons](#)

**Let us know how access to this document benefits you.**

---

## Recommended Citation

Webber, Benjamin Charles, "Investigation of the Structure and Dynamics of Regioisomeric  $\text{Eu}^{3+}$  and  $\text{Gd}^{3+}$  Chelates of NB-DOTMA: Implications for MRI Contrast Agent Design" (2013). *Dissertations and Theses*. Paper 1498.

<https://doi.org/10.15760/etd.1497>

This Dissertation is brought to you for free and open access. It has been accepted for inclusion in Dissertations and Theses by an authorized administrator of PDXScholar. Please contact us if we can make this document more accessible: [pdxscholar@pdx.edu](mailto:pdxscholar@pdx.edu).

Investigation of the Structure and Dynamics of Regioisomeric  $\text{Eu}^{3+}$  and  $\text{Gd}^{3+}$  Chelates of

NB-DOTMA: Implications for MRI Contrast Agent Design

by

Benjamin Charles Webber

A dissertation submitted in partial fulfillment of the  
requirements for the degree of

Doctor of Philosophy  
in  
Chemistry

Dissertation Committee:  
Mark Woods, Chair  
Ninian Blackburn  
Andrea Goforth  
Todd Rosenstiel  
Robert Strongin

Portland State University  
2013

© 2013 Benjamin Charles Webber

### *Abstract*

The detection of disease and abnormal pathology by magnetic resonance imaging (MRI) has been aided significantly by the use of gadolinium ( $Gd^{3+}$ )-based contrast agents (CAs) over the past three decades. MRI and MRI CAs play a critical role in diagnosing tumors and diseases of the central nervous system. The agents used clinically have been shown to safely increase MRI contrast despite the toxicity of  $Gd^{3+}$ , owing to the high kinetic and thermodynamic stability of these chelates. However, current CAs enhance contrast at a small fraction of what is theoretically possible. This leads to the necessity of introducing high CA doses in practice in order to afford sufficient contrast. Lanthanide ( $Ln^{3+}$ ) chelates based on 1,4,7,10-tetraazacyclododecane-1,4,7,10-tetraacetate (DOTA) have been shown to be particularly stable and effective. Chelates of DOTA exist in two interconverting coordination geometries which have varying water exchange rates. Researchers have envisioned a way to increase the per-dose efficacy both by control of the  $Gd^{3+}$ -inner-sphere water exchange rate and *via* binding specificity (*i.e.* to tumors). The efficacy gains using these approaches have thus far been modest.

A thorough structural characterization of europium ( $Eu^{3+}$ ) chelates of a DOTA-derivative which cannot undergo conformational exchange was carried out. These studies show that a single enantiomer of the ligand (*S*)-2-(4-nitrobenzyl)-1,4,7,10-tetraazacyclododecane-1,4,7,10-tetra( $\alpha$ -methyl)acetate (NB-DOTMA) can yield chelates which are both diastereoisomeric (previously reported) and regioisomeric (not previously speculated). Molecular mechanics simulations generated from the characterization data indicate that the nitrobenzyl (NB) substituent is oriented in different directions for the two possible

regioisomers. The NB group can be chemically converted to confer macromolecular binding capability, and the orientation of the NB substituent may have a significant impact on the binding and/or relaxation behavior of a prototypical CA.

The nuclear magnetic resonance (NMR) spectra of Eu-NB-DOTMA at various temperatures were compared. Unexpectedly, the chelates showed time-averaged structures which differ with a change in water exchange rate – the faster the rate, the greater the deviation from the expected structure. Consideration of the structures of  $\text{Ln}^{3+}$  chelates without accounting for their dynamic behavior does not yield an accurate value for the time-averaged hydration state. These observations suggest the “optimal” water exchange rate calculated using Solomon-Bloembergen-Morgan (SBM) theory may not lead to the highest-efficacy CAs. Binding and relaxometric studies of macromolecule-targeting derivatives of Gd-NB-DOTMA both by the author and in another lab showed that the coordination isomer with the slower water exchange rate should lead to more effective contrast, in direct opposition to the prevailing view of water exchange in the MRI community. Preliminary data do not indicate that regioisomeric chelates have significantly different relaxivity or macromolecular binding behavior.

The ratios between regioisomeric Ln-NB-DOTMA chelates formed were shown to be dependent on the concentration and pH of the chelation reaction, but conditions were not found which led to the production of a single regioisomer. Attempts to carry out an efficient synthesis of a  $\text{Ln}^{3+}$  chelate with no potential for regioisomerism were unsuccessful.

### *Acknowledgements*

I would like to express my gratitude to:

**Prof. Mark Woods** for working tirelessly to inspire, educate, and provide the resources for his students to become successful scientists. Also, for having the vision behind the research described herein and for constant encouragement.

**Katherine Payne, Julian Haigh, Annah Farashishiko, and Jacqueline Slack** for support, discussion, and assistance of all kinds, willingness to listen to numerous presentations of my research, and generally making the lab a great environment in which to work.

**Prof. Mauro Botta** for providing access to laboratory facilities for the acquisition of relaxometric data, assistance in interpreting the aforementioned data, invaluable insight, and many discussions with Mark concerning NMRD, hydration states, and the design and properties of contrast agents in general.

**Prof. David Peyton, Robert Jensen, and Dr. Andrea DeBarber** for invaluable assistance in acquiring and interpreting spectral data.

**Prof. Kevin Reynolds, Prof. Andrea Goforth, Prof. Dirk Iwata-Reuyl, and various members of their respective groups** for graciously permitting the use of their laboratory facilities and instrumentation.

**My family** for all their support and patience throughout my graduate education.

**Professors Andrea Goforth, Robert Strongin, Ninian Blackburn, and Todd Rosenstiel** for providing their time and critical feedback at various stages of the process of working toward a Ph.D.

**Portland State University, Oregon Health & Sciences University, National Institutes of Health, Oregon Nanoscience and Microtechnology Institute, National Science Foundation and Oregon Opportunity for Biomedical Research** for financial support.

Finally, to many members of the Chemistry Department over the years for their collaborations, camaraderie, and fostering a welcoming, creative environment.

## *Table of Contents*

Abstract	i
Acknowledgements	iii
List of Tables, Figures, Equations and Schema	x
List of Tables	x
List of Figures	xii
List of Equations	xvi
List of Schema	xvii
List of Terms and Abbreviations	xix
CHAPTER 1. Introduction	1
1.1 Magnetic resonance imaging: a safe, effective, versatile mode of medical imaging	1
1.1.1 Comparison of medical imaging techniques	1
1.1.2 History and benefits of MRI	2
1.1.3 Utility and safety considerations of MRI contrast agents	4
1.2 Chemistry of the lanthanides and their DOTA chelates	6
1.2.1 Synthesis of the macrocyclic ligand DOTA	8
1.2.2 Chelation mechanism of Ln[DOTA] <sup>-</sup>	10
1.2.3 Coordination geometry of Ln[DOTA] <sup>-</sup> and conformational exchange	11
1.3 The efficacy of Gd <sup>3+</sup> chelates as CAs	15
1.3.1 Relaxivity of Gd <sup>3+</sup> chelates as a measure of MRI CA efficacy	15
1.3.2 The central role of water (solvent) exchange in Ln <sup>3+</sup> -chelate CAs in generating contrast	16
1.3.3 Inner-sphere relaxivity and its dependence on molecular reorientation, water exchange, and electronic relaxation	19
1.4 Structural characterization of Ln <sup>3+</sup> chelates and MRI CAs	23



1.4.1 Measuring relaxivity of CAs over a range of magnetic field strengths by nuclear magnetic relaxation dispersion (NMRD)	23
1.4.2 Probing structure by taking advantage of lanthanides' electronic properties	27
1.4.3 Structure determination by NMR	29
1.4.4 Determination of $q$ and $\tau_M$	31
1.4.5 Examination of the motion and angle of a coordinated water molecule with respect to the lanthanide	33
1.5 The scope of this work: increasing the efficacy of MRI CAs	36
1.5.1 Strategy for decreasing $\tau_M$ via coordination isomer selection	37
1.5.2 Strategies for increasing relaxivity based on $\tau_R$	39
1.6 References	42
CHAPTER 2. Regioisomerism in conformationally rigid NB-DOTA-type chelates	50
2.1 Utility of conformationally rigid chelates for probing subtle, structurally related differences in solution behavior	50
2.2 Rationalizing the appearance of multiple isomers in a conformationally rigid chelate of single stereochemistry	52
2.3 Structural characterization of regioisomeric chelates by correlational NMR spectroscopy (COSY)	55
2.3.1 Previous studies of two-dimensional NMR spectra of arm- and ring-substituted DOTA-type chelates	55
2.3.2 Structural characterization of isomeric Eu- <i>S</i> -SSSS- <b>2</b> chelates by correlational spectroscopy (COSY)	59
2.3.3 Molecular mechanics simulation of the NB position and orientation based on NOE peaks observed in the COSY spectra	67
2.3.4 Structural characterization of isomeric Eu- <i>S</i> -RRRR- <b>2</b> chelates	69
2.4 Investigation of the chelation mechanism as it relates to regioisomer formation	80
2.4.1 $pK_a$ and conformational changes of the ligand <b>2</b> in solution	80
2.4.2 Modeling the solution conformation and the position of the NB substituent to gain insight into the chelation mechanism.	88

2.4.3 Thermodynamic stability of conformationally rigid SAP and TSAP Ln <sup>3+</sup> chelates	93
2.5 Conclusions and future directions	98
2.6 References	99
CHAPTER 3. Temperature dependence of the paramagnetic shifts of Ln-2 and evidence for time-averaged structural changes as a function of water exchange rate	101
3.1 Unexpected trends in <sup>1</sup> H NMR spectra of Eu-2 chelates at varying temperatures	103
3.2 Changes in Eu <sup>3+</sup> -induced <sup>1</sup> H NMR shifts between closely related structures have a spatial dependence	107
3.2.1 A crystal structure containing a unique type of unit cell provides a basis for structural comparison of $q = 1$ and $q = 0$ chelates	108
3.2.2 Comparison of the structural information given by the LIS with the principal axis of a Ln <sup>3+</sup> chelate and its paramagnetic field	109
3.2.3 Comparison of the temperature dependence of Eu-2 chelates to a chelate with no inner-sphere water exchange	113
3.3 VT data for Yb-2	116
3.4 Examination of the prevailing view of hydration state of MRI CAs in light of new evidence	118
3.4.1 The treatment of $q$ and $r$ as separate, static parameters provides an incomplete description of solution structure and dynamics	119
3.4.2 Variable-temperature NMR data yield a time-averaged coordination geometry and hydration state	122
3.4.3 Reviewing the relaxivity behavior of conformationally rigid SAP and TSAP chelates bound to slowly tumbling species	127
3.5 Further research/future directions	130
3.5.1 Measuring $q/r^6$ by variable-temperature luminescence and X-ray absorbance spectroscopy	130
3.5.2 Assessment of water exchange rate and molecular probe capability of a DOTA-type chelate with phosphonate pendant arms	131
3.6 References	133

CHAPTER 4. Relaxometric studies of regioisomeric Gd-NB-DOTMA chelates	136
4.1 Relaxometric studies of Gd- <b>2</b> chelates	137
4.2 Measurement of $\tau_M$ in Gd- <b>2</b> chelates by variable-temperature $^{17}\text{O}$ NMR shift and $T_2$	143
4.3 Relaxometric properties of regioisomeric, slowly tumbling biphenyl analogues of Gd- <b>2</b>	145
4.4 Conclusions and future directions	155
4.5 References	157
CHAPTER 5. Overcoming regioisomerism: a potential path toward synthetically efficient, conformationally rigid chelates	159
5.1 Motivation for study and summary of synthetic research plan	159
5.2 Attempted synthesis of a 1,4,7,10 tetraaza-crown with no potential for regioisomerism	160
5.2.1 Efforts to synthesize cyclohexylcyclen based on the Richman-Atkins method	160
5.2.2 Efforts based on the Kiefer-Athey method	163
5.2.3 Developments based on the cyclen synthesis published by Weisman <i>et al.</i>	169
5.2.4 Efforts based on a modified nitro-Mannich reaction	182
5.3 Conclusions	186
5.4 References	186
CHAPTER 6. Experimental Section	188
6.1 General Procedures	188
6.1.1 Synthesis, purification, and characterization of Ln- <b>2</b> chelates	188
6.1.2 Organic syntheses	189
6.2 Regioisomeric Ln- <b>2</b> -type chelates	190
6.2.1 Synthesis and characterization	190
6.2.2 Variable concentration and pH conditions for the chelation of $\text{Yb}^{3+}$ with S- <i>RRRR-2</i>	200

6.2.3 Epimerization study of Yb- <i>S</i> -SSS-3	203
6.2.4 Modification of <i>S</i> -SSSS-2 to form a bifunctional chelate	204
6.3 Variable-temperature NMR analysis	209
6.3.1 Synthesis	209
6.4 Synthesis of precursors to a fused-ring macrocycle	212
6.5 Synthesis and kinetic resolution of pendant arms	228
6.5.1 Synthesis	228
6.5.2 Enantiomeric enrichment using enzymatic resolution	229
6.5.3 Kinetic resolution of phosphonyl alcohols with copper catalyst	230
6.6 DOTAM derivatives to be used for CEST	236
6.7 References	245
Complete list of references	246

***LIST OF TABLES, FIGURES, EQUATIONS AND SCHEMA***

***List of Tables***

<b>Table 1.1:</b> Influence of the most important parameters in fitting experimental NMRD data.	26
<b>Table 2.1:</b> Acid dissociation constants of DOTA-type ligands	82
<b>Table 2.2:</b> Thermodynamic stability constants of Ln[DOTA]-type chelates	94
<b>Table 3.1:</b> Calculation of geometric parameters in the crystal structures of YDO3AP(ABn)	112
<b>Table 3.2:</b> Differences in $q$ and $r_{Ln-O}$ dependent on coordination geometry	120
<b>Table 4.1:</b> Relaxometric parameters obtained from the fit of the $^1H$ NMRD profiles	141
<b>Table 4.2:</b> Fitting parameters used in the fitting of the $^{17}O$ relaxation profiles of the complexes	144
<b>Table 4.3:</b> Best-fit parameters of the NMRD profiles of Gd- <i>S</i> -SSSS-6	150
<b>Table 4.4:</b> Fitting parameters for the binding of the two isomers of Gd to poly- $\beta$ -CD	152
<b>Table 4.5:</b> Best-fit parameters of the NMRD profiles (25 °C) of the inclusion complexes of the two isomers of Gd with poly- $\beta$ -CD	154
<b>Table 5.1:</b> Exploration of Scheme 4.13 using <b>21a</b> as a starting point	184
<b>Table 6.1:</b> Gradient for the preparative HPLC purification of $H_4[S-RRRR-7]$	192
<b>Table 6.2:</b> Step-wise solvent gradient used during the RP-HPLC purification of Ln-2	196
<b>Table 6.3:</b> Buffers employed to maintain pH in chelation study of Yb-2	201

**Table 6.4:** Step-wise solvent gradient used during the RP-HPLC purification of crude Gd-S-SSSS-6 207

**Table 6.5:** Step-wise solvent gradient used to resolve corner and side isomers of Gd-S-SSSS-6 208

*List of Figures*

<b>Figure 1.1:</b> Contrast agents approved for clinical use	5
<b>Figure 1.2:</b> Lanthanides on the periodic table	6
<b>Figure 1.3:</b> Chelation mechanism of Ln[DOTA] <sup>-</sup>	11
<b>Figure 1.4:</b> Structure and geometry of Ln[DOTA] <sup>-</sup>	12
<b>Figure 1.5:</b> Structures of the coordination geometries available to Ln[DOTA] <sup>-</sup> chelates	13
<b>Figure 1.6:</b> Conformational equilibria of Ln[DOTA] <sup>-</sup> chelates in solution	14
<b>Figure 1.7:</b> Water exchange of Ln[DOTA]-type chelates	17
<b>Figure 1.8:</b> Inner-sphere paramagnetic relaxivity ( $r_1^{is}$ ) dependence on $\tau_R$ and $\tau_M$	21
<b>Figure 1.9:</b> NMRD profile of a typical Gd <sup>3+</sup> chelate with varying $\tau_R$ values	24
<b>Figure 1.10:</b> NMRD profile of Gd(H <sub>2</sub> O) <sub>9</sub> <sup>3+</sup> in ethylene glycol	25
<b>Figure 1.11:</b> Water proton distances and angles calculated for Gd[DOTA] <sup>-</sup>	35
<b>Figure 1.12:</b> Examples of DOTA derivatives with arm (R) and ring (R') substituents	38
<b>Figure 2.1:</b> Partial <sup>1</sup> H NMR spectra of the two isomers of Yb-S-RRRR-2	53
<b>Figure 2.2:</b> Two possible sites of ring substitution	58
<b>Figure 2.3:</b> Two possible arrangements for the macrocyclic ring in <b>2</b>	58
<b>Figure 2.4:</b> COSY spectrum of the major isomer of Eu-S-SSSS-2	60
<b>Figure 2.5:</b> Transitions between nuclear spin states that may give rise to NMR peaks due to the nuclear Overhauser effect	62

<b>Figure 2.6:</b> COSY spectrum of the minor isomer of Eu- <i>S</i> -SSSS-2	64
<b>Figure 2.7:</b> Newman projection (not to scale) showing distortion of the dihedral angle from ideal gauche conformation	66
<b>Figure 2.8:</b> Molecular models of the proposed regioisomeric structures	68
<b>Figure 2.9:</b> COSY spectrum of the major isomer of Eu- <i>S</i> -RRRR-2	70
<b>Figure 2.10:</b> COSY spectrum of a minor isomer isolated from the synthesis of Eu- <i>S</i> -RRRR-2	72
<b>Figure 2.11:</b> COSY spectrum of a minor isomer from the synthesis of Eu- <i>S</i> -RRRR-2	74
<b>Figure 2.12:</b> COSY spectrum of a minor isomer isolated from the synthesis of Eu- <i>S</i> -RRRR-2	76
<b>Figure 2.13:</b> Molecular models of the proposed diastereoisomeric structures	78
<b>Figure 2.14:</b> The relationship between pH and regioisomeric ratio	85
<b>Figure 2.15:</b> The relationship between <i>S</i> -RRRR-2 concentration and regioisomeric ratio	86
<b>Figure 2.16:</b> Crystal structure of H <sub>4</sub> DOTMA·2HCl·3H <sub>2</sub> O	88
<b>Figure 2.17:</b> Crystal structure of (RRSS)-TCE-DOTA	90
<b>Figure 2.18:</b> Proposed chelation mechanism when Ln <sup>3+</sup> approaches the ligand from the face opposite the NB group	91
<b>Figure 2.19:</b> Mechanism for forming Ln- <i>S</i> -SSSS-2 with nitrobenzyl group on the side	93
<b>Figure 2.20:</b> Reversal and retention of configuration at the α-carbonyl carbon in H <sub>4</sub> TCE-DOTA	94
<b>Figure 2.21:</b> <i>ax</i> <sup>S</sup> region of NMR spectra of Yb- <i>S</i> -SSS-3 from epimerization study	96



<b>Figure 2.22:</b> Ratio of Yb- <i>S-SSS-3</i> TSAP isomers as a function of time	96
<b>Figure 2.23:</b> Acid-induced epimerization mechanism of a Ln-NCCO chelate ring	97
<b>Figure 3.1:</b> Chelates referred to in this chapter	102
<b>Figure 3.2:</b> Variable temperature <sup>1</sup> H NMR spectra of the ‘corner’ (left) and ‘side’ (right) isomers of Eu- <i>S-SSSS-2</i>	104
<b>Figure 3.3:</b> Variable temperature <sup>1</sup> H NMR spectra of Eu- <i>S-RRRR-2</i> and Eu- <i>S-SRRR-2</i>	105
<b>Figure 3.4:</b> Absolute change of chemical shift, 5 – 40 °C, as a function of shift at 25 °C	106
<b>Figure 3.5:</b> A structural comparison of the isomeric <i>q</i> = 1 and <i>q</i> = 0 YDO3AP(ABn) chelates	110
<b>Figure 3.6:</b> Comparison of the temperature dependence of SAP <i>S-SRRR</i> , SAP <i>S-RRRR</i> , and TSAP <i>S-SSSS</i> regioisomeric Eu- <b>2</b> chelates with Eu[DOTP] <sup>5-</sup>	115
<b>Figure 3.7:</b> Shift change as a function of temperature in Yb- <b>2</b> vs. Yb[DOTP] <sup>5-</sup>	117
<b>Figure 3.8:</b> Dissociative exchange of a water molecule from Ln[DOTA] <sup>-</sup>	119
<b>Figure 3.9:</b> A representation of the dissociative inner-sphere water exchange mechanism in Ln[DOTA]-type chelates	122
<b>Figure 3.10:</b> The distance of the inner-sphere water molecule from Ln <sup>3+</sup> as a function of time	123
<b>Figure 3.11:</b> A model for average Ln-OH <sub>2</sub> distance as a function of exchange rate under dissociative exchange conditions	124
<b>Figure 3.12:</b> The NMRD profiles of <i>S-RRR-Gd-6(-1-Me)</i> and <i>S-SSS-Gd-6(-1-Me)</i>	128

<b>Figure 3.13:</b> Design of a DOTP-type chelate with possible SAP geometry and $q = 1$	132
<b>Figure 4.1:</b> NMRD profiles of Gd-2 SAP chelates at 25 °C	139
<b>Figure 4.2:</b> NMRD profiles of Gd-2 TSAP chelates at 25 °C	140
<b>Figure 4.3:</b> Variable temperature $T_2$ and shift $^{17}\text{O}$ data for Gd-2 isomers	143
<b>Figure 4.4:</b> Relaxation properties of Gd- <i>S</i> -SSSS-6 above and below critical micelle concentration(cmc)	148
<b>Figure 4.5:</b> NMRD profiles of <i>S</i> -SSSS-6 corner and side isomers at 0.15 mM and 298 K	149
<b>Figure 4.6:</b> Interaction with poly- $\beta$ -cyclodextrin (20 MHz, 298 K)	152
<b>Figure 4.7:</b> NMRD of the supramolecular adducts (298 K)	153
<b>Figure 5.1:</b> Representative mass spectrum of the reaction of <b>13</b> and <b>14b</b> and proposed structures corresponding to observed $m/z$ peaks	165

*List of Equations*

<b>Equation 1.1:</b> The Boltzmann distribution of spins	3
<b>Equation 1.2:</b> The observed relaxation rate	16
<b>Equation 1.3:</b> The longitudinal relaxivity observed	18
<b>Equation 1.4:</b> The inner-sphere dependence of paramagnetic relaxivity	18
<b>Equation 1.5:</b> The longitudinal relaxation time of a CA-bound water proton	19
<b>Equation 1.6:</b> $\tau_c$ is a correlation time constant associated with interactions at the Larmor frequency	19
<b>Equation 1.7:</b> The contact contribution to NMR shifts of a paramagnetic metal ion	29
<b>Equation 1.8:</b> The dipolar contribution to NMR shifts of a paramagnetic metal ion	29
<b>Equation 3.1:</b> Spatial dependence on the axial dipolar contribution to LIS	110
<b>Equation 3.2:</b> Direct relationship between $q$ and $r_{\text{Ln-O}}$ in solution	121

*List of Schema*

<b>Scheme 1.1:</b> Richman-Atkins synthesis of polyazacrowns	9
<b>Scheme 1.2:</b> Kiefer/Athey route to cyclen	9
<b>Scheme 1.3:</b> Weisman synthesis of cyclen	10
<b>Scheme 1.4:</b> Alkylation of cyclen by nucleophilic substitution to yield DOTA	10
<b>Scheme 2.1:</b> Structures of ligands and chelates referenced in Chapter 2	51
<b>Scheme 2.2:</b> Nucleophilic substitution to alkylate nitrobenzyl cyclen	53
<b>Scheme 2.3:</b> Racemization of a (2-methyl)acetate arm leading to two chelates	54
<b>Scheme 3.1:</b> Preparation of enantiomerically enriched phosphonate esters	133
<b>Scheme 4.1:</b> Conversion of the nitrobenzyl group in <b>2</b> to confer macromolecular binding ability	146
<b>Scheme 5.1:</b> Experimental details of the synthesis from the patent by Desreux and co-workers	161
<b>Scheme 5.2:</b> Attempted adaptation of the Richman-Atkins method to yield <b>8</b>	162
<b>Scheme 5.3:</b> Attempted adaptation of Kiefer-Athey method using <b>14</b>	163
<b>Scheme 5.4:</b> Attempt to prepare <b>8</b> from 1,2-substituted ethylene	167
<b>Scheme 5.5:</b> Formylation of <b>10</b> in attempt to prepare <b>9</b>	168
<b>Scheme 5.6:</b> Approach to tetramine <b>19</b> for use in a Weisman-type synthesis using an activated, <i>N</i> -protected amino acid	170
<b>Scheme 5.7:</b> Alkylation of <b>10</b> using Boc- or Cbz-Gly-OSu ( <b>17a</b> or <b>17b</b> )	171

<b>Scheme 5.8:</b> Hydrogenation of Cbz groups to yield <b>20</b> and subsequent attempts at reduction of the amides	172
<b>Scheme 5.9:</b> Approach to tetramine <b>19</b> for use in a Weisman-type synthesis using an N-protected <b>10</b> ( <b>21</b> ) and an amide alkylating agent	172
<b>Scheme 5.10:</b> Alkylation of N-protected <b>10</b> with a $\beta$ -amide	173
<b>Scheme 5.11:</b> Incomplete alkylation of <b>21a</b> with <b>22</b> and reaction of base with <b>22</b>	174
<b>Scheme 5.12:</b> Replacement of the benzyl protecting group of <b>10</b> with benzil	175
<b>Scheme 5.13:</b> Reduction of the amides in <b>23</b>	179
<b>Scheme 5.14:</b> Removal of benzylic protecting groups in <b>24a</b> <i>via</i> catalytic hydrogenation	180
<b>Scheme 5.15:</b> A possible pathway to <b>8</b> via glyoxal-type cyclization	181
<b>Scheme 5.16:</b> Nitro-Mannich reaction for <i>N</i> -cyclization	182
<b>Scheme 5.17:</b> A possible pathway to <b>11</b> using a modified nitro-Mannich reaction	183

*List of Terms and Abbreviations*

<i>ac</i>	Acetate or an acetate proton
<i>ax</i>	Proton in an axial position
Bn	Benzyl or benzylic
Boc	<i>tert</i> -butoxycarbonyl
CA	Contrast agent (in the context of MRI)
Cbz	Carboxybenzyl
COSY	Correlational Spectroscopy (NMR)
CT	Computed tomography
DMF	<i>N,N</i> -dimethylformamide
DOTA	1,4,7,10-tetraazacyclododecane-1,4,7,10-tetraacetate
DOTAM	1,4,7,10-tetraazacyclododecane-1,4,7,10-tetraacetylamine
DOTMA	1,4,7,10-tetraazacyclododecane-1,4,7,10-tetra( $\alpha$ -methyl)acetate
EPR	Electron paramagnetic resonance
<i>eq</i>	Proton in an equatorial position
ESI-MS	Electrospray ionization mass spectrometry
Et <sub>2</sub> O	Diethyl ether
EXSY	Exchange spectroscopy (NMR technique)
IR	Infrared
Ln	Any lanthanide element or (3+) ion
Me	Methyl
MRI	Magnetic resonance imaging
NB-cyclen	( <i>S</i> )-2-(4-nitrobenzyl)-1,4,7,10-tetraazacyclododecane

NB-DOTMA	( <i>S</i> )-2-(4-nitrobenzyl)-1,4,7,10-tetraazacyclododecane-1,4,7,10-tetra( $\alpha$ -methyl)acetate
NMR	Nuclear magnetic resonance spectroscopy
NMRD	Nuclear magnetic relaxation dispersion
-OSu	<i>N</i> -hydroxysuccinimide ester
-OTf	Trifluoromethanesulfonate
-OTs	<i>p</i> -Toluenesulfonate
R <sub>1</sub>	Longitudinal nuclear spin relaxation rate
r <sub>1</sub>	Longitudinal relaxivity
RF	Radio frequency
R <sub>f</sub>	Retention factor
SAP	Square anti-prismatic geometry
T <sub>1</sub>	Longitudinal nuclear spin relaxation time
T <sub>2</sub>	Transverse nuclear spin relaxation time
THF	Tetrahydrofuran
T <sub>ie</sub>	Electronic relaxation time, where i = 1 (longitudinal) or 2 (transverse)
TLC	Thin-layer chromatography
TSAP	Twisted-square anti-prismatic geometry
TTP	Tri-capped trigonal prismatic geometry
UV-Vis	Ultraviolet-visible spectrum (spectroscopy)
VT	Variable-temperature
$\tau_M$	Inner-sphere water residence time constant
$\tau_R$	Molecular reorientation time constant
ZFS	Zero-field splitting

**CHAPTER 1. INTRODUCTION*****1.1 Magnetic resonance imaging: a safe, effective, versatile mode of medical imaging****1.1.1 Comparison of medical imaging techniques*

Medical imaging encompasses a range of techniques that are minimally invasive and allow rapid and accurate diagnosis of a broad spectrum of diseases, disorders, and other health concerns. The field of medical imaging is experiencing significant growth in imaging power, utility, and the ability to diagnose and even to treat disease.<sup>1</sup> The most commonly employed imaging modalities are X-rays and computed tomography (CT, which uses X-rays), at 62 million scans/yr as of 2007.<sup>2</sup> The other most prevalent types are magnetic resonance imaging (MRI) and ultrasound. X-ray techniques are useful due to their high sensitivities and rapid imaging time. However, X-rays and particularly CT (which involves a higher dose of ionizing radiation) can increase the risk of DNA damage and of developing some forms of cancer.<sup>2-4</sup> Ultrasound, another popular modality, uses sound waves instead of electromagnetic radiation. The risks associated with ultrasound are very low and the technique has excellent temporal resolution, but poor spatial resolution. The use of MRI is very attractive as MRI eliminates the problems associated with radioactive tracers and ionizing radiation. In comparison with other imaging techniques, MRI has superior spatial resolution and greater utility in early detection and diagnosis of restricted blood flow (risk for heart attack, stroke)<sup>5,6</sup> and of tumors.<sup>7-9</sup> MRI excels at distinguishing between body tissues, but scans typically last significantly longer than for the types of imaging above. Because of the complementary nature of these



techniques, a combination of medical imaging analyses is often utilized for optimal diagnosis and treatment.

### *1.1.2 History and Benefits of MRI*

A method for using magnetic resonance to generate images was first devised by Paul Lauterbur in 1973,<sup>10</sup> who along with Peter Mansfield was awarded the Nobel prize in Physiology or Medicine in 2003 for the discovery. Around the same time, magnetic resonance had been tested *in vivo*<sup>11</sup> and was eventually extended to human imaging, pioneered by Damadian, Hinshaw and others.<sup>12-14</sup> These momentous discoveries, in combination with two-dimensional and Fourier-transform techniques developed by Ernst and colleagues,<sup>15</sup> made possible the use of MRI as a versatile and ubiquitous diagnostic for disease and abnormal pathology today.<sup>16,17</sup>

In an MRI exam the subject is placed in a strong (typically 0.5 T or greater), homogeneous magnetic field ( $B_0$ ). For any atomic nucleus in this magnetic field having spin state  $> 0$ , its nuclear magnetic moment will tend to align with or against the direction of the field according to the Boltzmann equation (Equation 1.1). A nuclear magnetic moment can be thought of as a miniature magnet that nutates (spins) about the direction of the  $B_0$  axis.

The Boltzmann population distribution causes a net magnetization aligned parallel to  $B_0$  and is directly proportional to field strength. The population difference is only a few parts per million, however, inherently making MRI a less sensitive technique<sup>18</sup> compared with other imaging modes.

$$\frac{N_{anti}}{N_{||}} = e^{-B_0 h \gamma / kT}$$

**Equation 1.1:** The Boltzmann distribution of spins, where  $N_{anti}$  is the population of nuclear spin momenta aligned against the field,  $N_{||}$  is the population aligned with the field,  $\gamma$  is the magnetogyric ratio of the nucleus in question,  $B_0$  is the magnetic field strength,  $h$  is Planck's constant,  $k$  is Boltzmann's constant, and  $T$  is absolute temperature

In an MRI, a gradient field is applied on top of the  $B_0$  field, which causes spins to resonate at different frequencies dependent upon their spatial location within the gradient field. This relationship between resonance frequency and spatial location is the basis for the construction of a three-dimensional image. The nuclei are then perturbed by a sequence of radio frequency (RF) pulses which induce a magnetic field ( $B_1$ ) perpendicular to the main field. The  $B_1$  field is much weaker than the main magnetic field  $B_0$  (on the order of  $1:10^4$ ). However, the RF pulses are sufficient to transfer the net magnetization into the plane perpendicular to  $B_0$  and manipulate this magnetization so that it can be detected. The RF field induces the nuclear spins to rotate about  $B_0$  coherently (in phase, instead of having their momenta point in random directions in the  $B_1$  plane). The RF field is turned off and two relaxation processes return the population of spins to their equilibrium alignment with  $B_0$ . The net magnetization in the  $B_1$  plane returns to the Boltzmann distribution in the  $B_0$  direction (termed longitudinal relaxation,  $T_1$ ). In a separate process, the spins lose their coherence in the  $B_1$  direction (termed transverse relaxation,  $T_2$ ). The relaxation times of nuclei vary within the body based on local environment and this variation is observed by the detector (which is also an RF coil). The signal is processed such that the density of spins and their relaxation time in

each volume element (typically on the order of  $1 \text{ mm}^3$ ) is assigned a relative brightness, making differences between tissue types apparent in image contrast. MR images are nearly always acquired based on the nuclear magnetic resonance of water protons, the most abundant nuclei *in vivo*.

### 1.1.3 Utility and safety considerations of MRI contrast agents

To compensate for the sensitivity limitations, MRI can be complemented by a minimally invasive injection of an extracellular contrast agent (CA). Data from 2007 showed that 43% of the 27 million MRI scans performed that year in the US employed a contrast agent.<sup>19</sup> CAs are most useful when one cannot easily differentiate adjacent tissue types.<sup>20</sup> Diseases of the central nervous system (CNS) and cancer are major areas where contrast agents have proven useful.<sup>20,21</sup> Paramagnetic atoms or molecules are known to affect nuclear spin relaxation. The introduction of paramagnetic ions to study biological systems, including nucleic acids<sup>22</sup> and proteins<sup>23</sup>, dates back 50 years. Unpaired electrons which take longer to relax in a magnetic field can affect more nuclear spins at a given concentration. The paramagnetic gadolinium ion ( $\text{Gd}^{3+}$ ) has 7 unpaired *f* electrons and a long electronic relaxation time, making  $\text{Gd}^{3+}$  an ideal basis for CAs.  $\text{Gd}^{3+}$ -based contrast agents (Figure 1.1) are widely used in conjunction with MRI and have been shown to confer excellent contrast enhancement in the tissues in which they are distributed.<sup>24</sup>

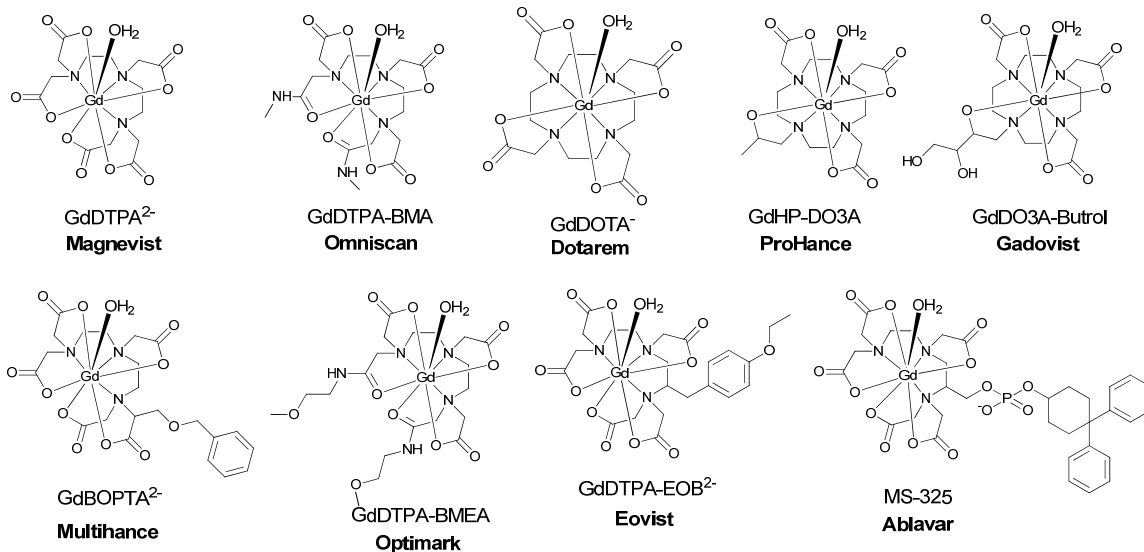


**Figure 1.1:** Contrast agents approved for clinical use, with common and brand names, respectively.

In order to be useful clinically, a contrast agent must be well tolerated in the body: non-toxic, stable, rapidly and fully eliminated, and effective in dosing and formulation which must be carefully administered to compensate for their high osmolality. For *in vivo* use, an organic multidentate ligand is first bound to the Gd<sup>3+</sup> ion generating a highly thermodynamically stable chelate ( $\log K_{GdL} > 20$  for most clinical agents).<sup>25</sup> While thermodynamic stability tends to receive more attention, the more clinically relevant parameter is a CA's kinetic stability – particularly in relation to transmetallation by Ca<sup>2+</sup>, Cu<sup>2+</sup> and Zn<sup>2+</sup>.<sup>26,27</sup> A Mn<sup>2+</sup>-based CA (Teslascan) with inferior kinetic stability was approved for liver imaging and used clinically.<sup>28</sup> Manganese (in the form of Mn<sup>2+</sup>) has a lower magnetic moment but an even longer electronic relaxation time than Gd<sup>3+</sup>. However, the contrast mechanism for Teslascan relies on the slow release of Mn<sup>2+</sup> ions from the polydentate chelate, and the marketing of this CA was discontinued by 2005 in

the U.S and in 2012 in the E.U.<sup>29</sup>  $Gd^{3+}$  on its own leads to significant contrast enhancement, but non-chelated lanthanide ( $Ln^{3+}$ ) ions, or those in kinetically labile chelates, are toxic<sup>30</sup> as they mimic  $Ca^{2+}$  and disrupt various ion pumps. Furthermore,  $Ln^{3+}$  ions have a long residence time in the body, eventually leading to skin and bone deposition. Clinically approved MRI CAs, which are all polyaminocarboxylate  $Gd^{3+}$  chelates (Figure 1.1), must be eliminated from the body at a rate much faster than their dissociation rate.<sup>31</sup> Optimizing the contrast-generating ability and the kinetic and thermodynamic stabilities of Gd-based CAs requires knowledge of the unique chemistries of the lanthanides.

### 1.2 Chemistry of the lanthanides and their DOTA chelates

**Rare Earth Elements**

<b>La</b> 57	<b>Ce</b> 58	<b>Pr</b> 59	<b>Nd</b> 60	<b>Pm</b> 61	<b>Sm</b> 62	<b>Eu</b> 63	<b>Gd</b> 64	<b>Tb</b> 65	<b>Dy</b> 66	<b>Ho</b> 67	<b>Er</b> 68	<b>Tm</b> 69	<b>Yb</b> 70	<b>Lu</b> 71
-----------------	-----------------	-----------------	-----------------	-----------------	-----------------	-----------------	-----------------	-----------------	-----------------	-----------------	-----------------	-----------------	-----------------	-----------------

**Lanthanides**

H																	He
Li	Be											B	C	N	O	F	Ne
Na	Mg											Al	Si	P	S	Cl	Ar
K	Ca	Sc	Ti	V	Cr	Mn	Fe	Co	Ni	Cu	Zn	Ga	Ge	As	Se	Br	Kr
Rb	Sr	<b>Y</b>	Zr	Nb	Mo	Tc	Ru	Rh	Pd	Ag	Cd	In	Sn	Sb	Te	I	Xe
Cs	Ba	<b>Lu</b>	Hf	Ta	W	Re	Os	Ir	Pt	Au	Hg	Tl	Pb	Bi	Po	At	Rn
Fr	Ra	Ac	Lr														

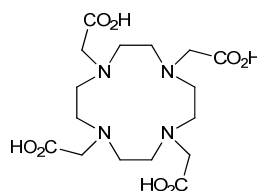
**Figure 1.2:** Lanthanides on the periodic table<sup>32</sup>

Lanthanides (abbreviated Ln) are the series of elements 57-71 (Figure 1.2). Their electronic configurations are that of  $[Xe]6s^25d^14f^n$ , varying only by the number of electrons in the 4f shell. The 4f electrons are highly shielded by the 5s and 5p electrons

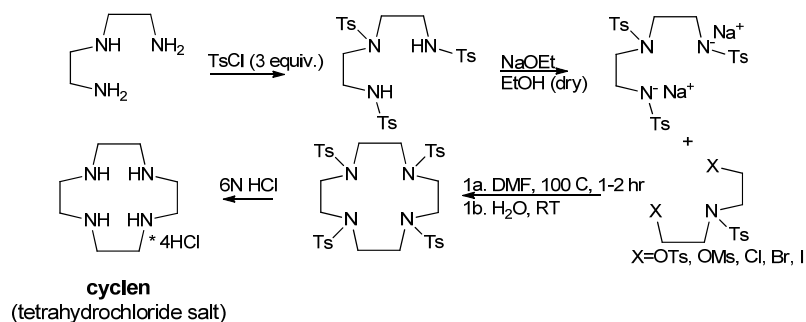
and interact only minimally with other ions or ligating groups. Lanthanides are almost universally found in the (3+) oxidation state, due to the low energies of ionization of the 6s and 5d electrons. Due to the identical oxidation state and increased nuclear charge across the series, lanthanide ions contract linearly from  $\text{La}^{3+}$  (about 105 pm ionic radius) to  $\text{Lu}^{3+}$  (about 85 pm). These ionic radii are large, leading to high coordination numbers (typically 8 or 9). The high oxidation state and limited accessibility of valence electrons make  $\text{Ln}^{3+}$  ions hard Lewis acids.  $\text{Ln}^{3+}$  ions form coordination compounds mainly with hard bases such as water, hydroxide, nitrate, triflate, acetate, phosphate, and some halides. These compounds are formed mainly due to electrostatic (charge/dipole) interactions, and ligand exchange is very rapid (the ligands are labile). The lack of strong electronic orbital overlap between  $\text{Ln}^{3+}$  4f electrons and ligands gives the complexes more geometric flexibility than complexes of *d* block metals. As ligand displacement is accompanied by a distortion in geometry, the less a ligand is able to distort, the more stable the chelate. Due to entropic effects, the greater the denticity of a ligand, the less labile the chelate becomes and the more constrained its coordination geometry becomes. Coordination compounds of  $\text{Ln}^{3+}$  generally adopt tri-capped trigonal prismatic (TTP) geometry. Exceptions to TTP geometry arise from the structural rigidity of certain polydentate ligands. The lack of interaction between the 4f electrons and ligands also means that compounds of  $\text{Ln}^{3+}$  across the series are effectively isostructural. Thus, the chemistries of the lanthanides are extremely similar.<sup>33</sup> The physical properties, rather than the chemical properties, of an individual lanthanide are the source of interesting behavior and applications.

## 1.2.1 Synthesis of the macrocyclic ligand DOTA

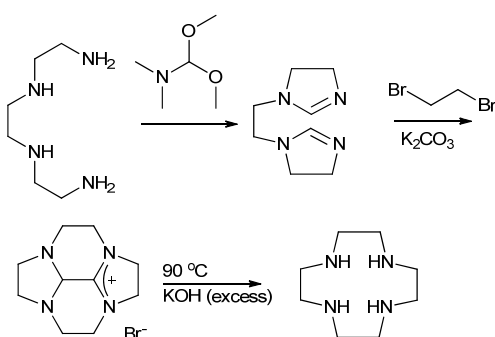
CAs based on macrocyclic ligands are more rigid and much more stable than those of their acyclic counterparts.<sup>34</sup> The macrocyclic ligand 1,4,7,10-tetraazacyclododecane-1,4,7,10-tetraacetic acid (H<sub>4</sub>DOTA) is the starting point for our CA design and research efforts. It forms some of the most stable Ln<sup>3+</sup> chelates ever observed.<sup>35</sup> Chelates of DOTA have been thoroughly studied to date.<sup>36-42</sup>

1,4,7,10-tetraazacyclododecane-1,4,7,10-tetraacetic acid (H<sub>4</sub>DOTA)

The main challenge in preparing 12-membered tetraaza crowns (as seen in the structures of Dotarem, ProHance, Gadovist, and in the study of many non-clinical Ln<sup>3+</sup> chelates) is the kinetic unfavorability of macrocyclic ring closure. Cyclen (1,4,7,10-tetraazacyclododecane) was produced previously on a commercial scale using the synthesis method published by Richman and Atkins,<sup>43</sup> shown in Scheme 1.1 below.

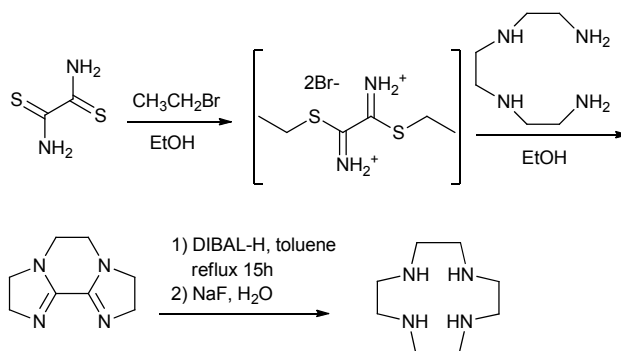
**Scheme 1.1:** Richman-Atkins synthesis of cyclen

This approach employs bulky tosyl protecting/activating groups which led to low atom economy. Furthermore, relatively high dilutions were necessary in the cyclization step, which meant that the product had to be recovered from large volumes of dimethylformamide. Today cyclen is produced by a more effective route, which was developed by Kiefer and Athey<sup>44</sup>, and is shown in Scheme 1.2. Upon commercial implementation of the Kiefer/Athey method, the price of cyclen as a reagent dropped substantially.



**Scheme 1.2:** Kiefer/Athey route to cyclen

A second high efficiency route to cyclen was developed by Weisman and co-workers, although this procedure is less amenable to large scale reactions (Scheme 1.3).<sup>45</sup>



**Scheme 1.3:** Weisman synthesis of cyclen





the end product has a separate absorption peak which grows in gradually. The rate data indicate overall first-order kinetics of formation. There is therefore a rapid formation of an intermediate chelate  $H_2LnL^+$ , where only the four oxygen atoms bind to the metal, partially encapsulating it. A slower step involves the metal “dropping into the cage” so it coordinates to the nitrogen atoms of the ligand, which is then fully deprotonated (Figure 1.3).

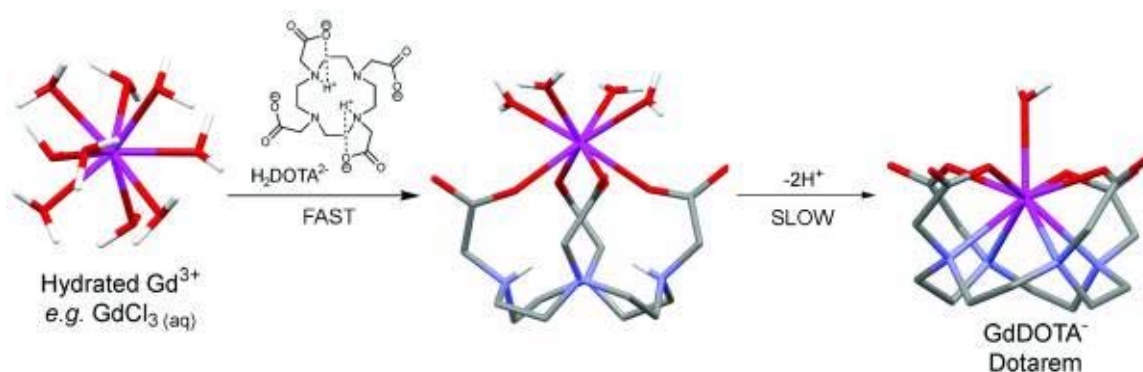


**Figure 1.3:** Chelation mechanism of  $Ln[DOTA]^{27}$

The formation of  $H_2LnL^+$  is slower for conformationally rigid systems.<sup>38</sup>

### 1.2.3 Coordination geometry of $Ln[DOTA]^-$ and conformational exchange

The coordination geometry of  $Ln[DOTA]^-$  is shown in Figure 1.4. The four nitrogen atoms are coplanar, as are the four coordinating oxygen atoms. The  $Ln^{3+}$  atom is located between the two planes, and a single coordinated water molecule is located axially above the ligand oxygen atoms' plane (Fig. 1.4a). The macrocyclic cyclen ring adopts a square [3333] arrangement<sup>46</sup> (Fig. 1.4b) – each side of the square is formed by 3 bonds (2 C-N

and 1 C-C).<sup>47</sup> The ethylene bridges on the macrocyclic ring can adopt one of two chiral (helical,  $\delta$  or  $\lambda$ ) configurations (Fig 1.4c).

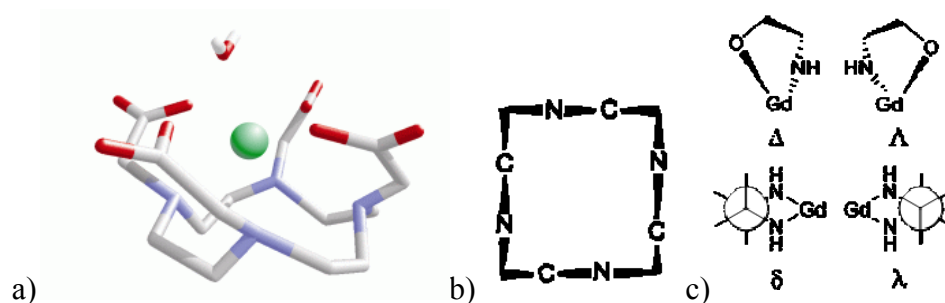


**Figure 1.4:** Structure and geometry of  $\text{Ln}[\text{DOTA}]^-$ , where a) shows the position of the metal ion between the nitrogen and oxygen planes and the position of the water molecule, b) shows the square arrangement of the macrocycle, and c) shows the possible helicities of the chelate rings formed by the pendant arms (top) and of the ethylene bridges (bottom)

For a  $\text{Ln}^{3+}$  chelate of DOTA, the ethylene bridges all adopt the same helicity ( $\delta\delta\delta\delta$  or  $\lambda\lambda\lambda\lambda$ , Fig. 1.4c, bottom).<sup>48,49</sup> The chelate rings formed from  $\text{Ln}^{3+}$  binding to the arms also have helical chirality. The arms wrap around the metal cooperatively (they also all have the same helicity), and the two resulting isomers are denoted as  $\Delta$  or  $\Lambda$  (Fig. 1.4c, top). These elements of helical chirality mean that for  $\text{Ln}[\text{DOTA}]^-$ , more than one stereoisomer is available in solution. Two coordination geometries are available to DOTA-based chelates – square antiprism (SAP) and twisted-square antiprism (TSAP) as seen in Fig. 1.5.<sup>37,50</sup> TSAP geometry results from the arms and the bridges adopting the same helicity (*i.e.*,  $\Lambda(\lambda\lambda\lambda\lambda)$ ), and SAP geometry results from the arms and the bridges adopting opposite helicities.

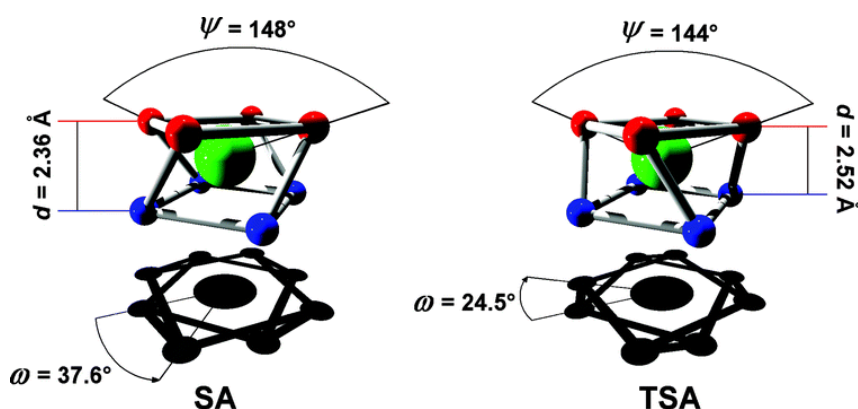


**Figure 1.5:** Structures of the coordination geometries available to  $\text{Ln}[\text{DOTA}]^-$  chelates<sup>51</sup>

The two main differences between SAP and TSAP are the twist angle ( $\omega$ ) between the nitrogen (N4) and oxygen (O4) planes and the distance ( $d$ ) between the two planes (greater in TSAP). There is a modest difference in the “openness” ( $\psi$ , also referred to as the “bite” angle) of the O4 plane that is related to how closely a water molecule can approach the metal ion. SAP and TSAP isomers cannot be isolated from one another in Ln-DOTA as the energy barriers to conformational isomerism (the processes of reversing helicity *via* ring inversion and arm rotation) are too low under physiological conditions (Figure 1.9). The possible coordination geometries  $\Lambda(\lambda\lambda\lambda\lambda)$ ,  $\Lambda(\delta\delta\delta\delta)$ ,  $\Delta(\lambda\lambda\lambda\lambda)$ , and  $\Delta(\delta\delta\delta\delta)$  are two enantiomeric pairs. A reversal of helicity of either the four ethylene bridges or of the four pendant arms will convert a SAP isomer to a TSAP or *vice versa*. A particular conformation can be converted to its geometric pair (SAP-to-SAP or TSAP-to-TSAP) by a dual arm-flip, ring-inversion process. This exchange has been observed by exchange NMR spectroscopy (EXSY).<sup>50,52</sup> It should be noted that this conversion will move a carbon which was previously on the corner of the [3333] macrocyclic ring (Fig. 1.6) to a position on the side of the ring. These 2 carbons are not chemically equivalent if

chemical substitution on the basic DOTA ligand restricts the conformational equilibria, or breaks the 4-fold symmetry of the chelate.

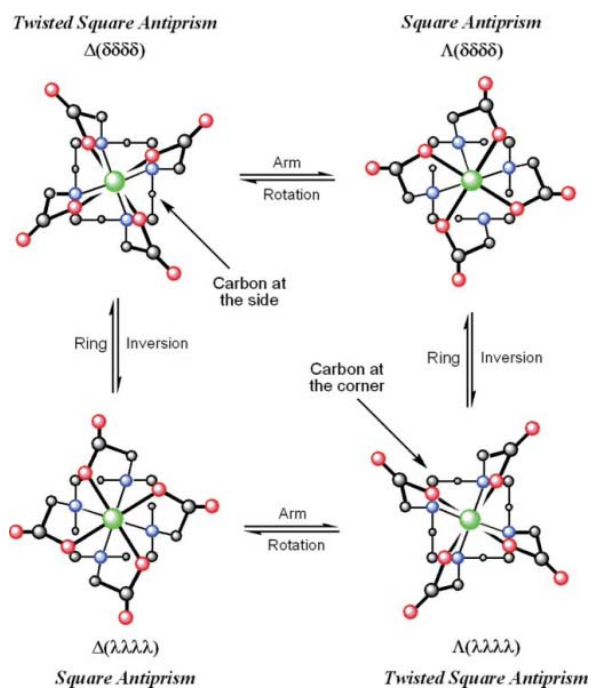


**Figure 1.6:** Conformational equilibria of Ln[DOTA]<sup>-</sup> chelates in solution<sup>53</sup>

### ***1.3 The efficacy of Gd<sup>3+</sup> chelates as CAs***

Presently, Gd<sup>3+</sup>-based CAs require high intravenous doses (0.03 – 0.1 mmol/kg) to improve MR contrast appreciably. These doses of Dotarem™ (Gd[DOTA]) and other market-established macrocyclic Gd-based CAs are considered safe.<sup>54</sup> However, the doses of CAs could be much lower – these clinically approved CAs enhance contrast by a small fraction of what is theoretically possible. To understand optimization of per-dose efficacy in CAs, it is necessary to consider the prevailing theory of paramagnetic relaxation of nearby nuclear spin momenta.

#### *1.3.1 Relaxivity of Gd<sup>3+</sup> chelates as a measure of MRI CA efficacy*

Our understanding of how paramagnetic CAs function is based on Solomon-Bloembergen-Morgan (SBM) theory.<sup>55-59</sup>  $R_1$ , the longitudinal relaxation rate observed ( $R_1 = 1/T_1$ ), changes from its base value (that of pure water) when a reorientation restriction (such as a solution with high concentration of macromolecule, which increases the solution viscosity) or an ion or compound which interacts strongly with nuclear spins (*i.e.*, a paramagnetic species) is introduced.  $R_1$  differences in the magnetic behavior of nuclei as a function of local molecular environment are exploited for imaging purposes. A tissue sample with more “restricted” water will have a shorter  $T_1$ . Thus, if appropriate imaging protocols are used, contrast is inherently apparent. However, the image quality is often greater with a contrast agent. The superior contrast provided by Gd<sup>3+</sup> agents stems from the agents’ effect on the longitudinal relaxation rate of nuclear magnetic momenta of nearby water protons; contrast is thus enhanced by an indirect mechanism.

$R_1$  of an aqueous solution is increased upon the addition of a CA. This relaxation enhancement “arises from time fluctuation of the dipolar coupling between the electron magnetic moment of the metal ion and the nuclear magnetic moment of the solvent nuclei.”<sup>20,60</sup> The primary measure of the efficacy of a magnetic resonance contrast agent is its relaxivity, the per-millimolar concentration (of  $Gd^{3+}$ ) decrease of longitudinal relaxation time ( $T_1$ ) of protons in the system. Typically, in the context of MRI CAs, the longitudinal component of relaxivity ( $r_1$ ) is measured and reported.<sup>61</sup> The relationship between  $R_1$  and paramagnetic relaxivity ( $r_{1p}$ ) is described in Equation 1.2.

$$R_{1obs} = [CA]r_{1p} + R_{1w}$$

**Equation 1.2:** The observed relaxation rate is a function of the contrast agent concentration and its experimentally determined relaxivity.  $R_{1w}$  is the relaxation rate of the water protons prior to introduction of a paramagnetic species.

### *1.3.2 The central role of water (solvent) exchange in $Ln^{3+}$ -chelate CAs in generating contrast*

In order to mathematically describe the behavior of a particular type of water proton and how it is affected by paramagnetic relaxation, SBM theory treats water molecules associated with a paramagnetic chelate as divided into three distinct “spheres” (Figure 1.7).

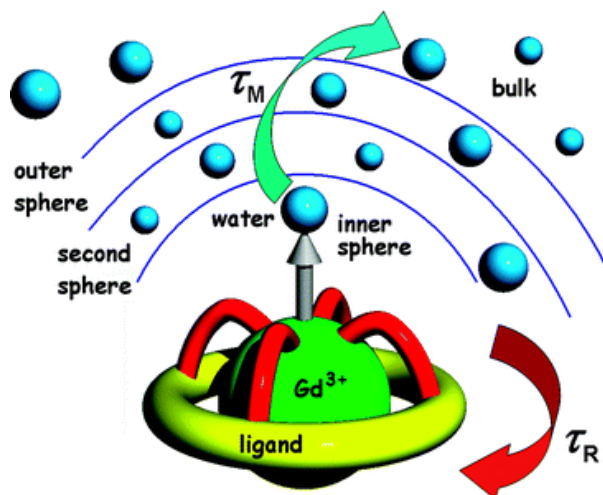


**Figure 1.7:** Water exchange of Ln[DOTA]-type chelates<sup>51</sup>

An inner-sphere water molecule is directly bound to the gadolinium ion in a CA. Water molecules in the second sphere are closely associated with the metal ion but not directly coordinated; these have hydrogen bonding interactions with the oxygen atoms of the chelate. There is a third “shell” of pre-organized water associated with the chelate, known as the outer sphere, where the water molecules have weak bonding interactions with those in the second sphere. There are inner-, second-, and outer-sphere contributions to relaxivity (Equation 1.3). The second- and outer-sphere contributions to relaxivity arise from water protons not directly coordinated to  $Gd^{3+}$  but sufficiently close for their spin states to be affected. These contributions, though significant (up to 10-30% of the overall relaxivity, depending on the agent and its surroundings)<sup>62</sup>, are difficult to improve upon through rational design, so researchers typically focus on the inner sphere.



$$r_1^{Observed} = r_1^{Inner-sphere} + r_1^{Second-sphere} + r_1^{Outer-sphere}$$

**Equation 1.3:** The longitudinal relaxivity observed contains contributions from each hydration sphere

Water molecules in each sphere are constantly and rapidly undergoing chemical exchange. Due to this rapid solvent exchange, the nuclear relaxation times of many water protons in the vicinity of the agent are affected. The inner-sphere component of relaxivity is a function of the number of  $Gd^{3+}$ -bound water molecules ( $q$ ), the rate of water exchange ( $1/\tau_M$ ), and longitudinal inner-sphere water proton relaxation time ( $T_{1M}$ ) (Equation 1.4). Though relaxivity scales directly with  $q$  (the number of inner-sphere water molecules), clinical agents are limited to  $q = 1$  due to stability/safety concerns. A few chelates have been studied in the laboratory that may prove sufficiently stable with  $q > 1$ .<sup>63,64</sup> DOTA and its derivatives are octacoordinate, leaving a single free coordination site available for water to bind. The exchange of inner-sphere water molecules in DOTA-type chelates of all but the largest lanthanides is known to occur by a dissociative mechanism.<sup>65-68</sup>

$$r_{1p} = \frac{q}{55.6} \left( \frac{1}{T_{1M}} + \frac{1}{\tau_M} \right)$$

**Equation 1.4:** The inner-sphere dependence of paramagnetic relaxivity is a function of  $T_{1M}$  and  $\tau_M$

### 1.3.3 Inner-sphere relaxivity and its dependence on molecular reorientation, water exchange, and electronic relaxation

The overall effect on  $T_1$  is governed by a so-called “characteristic correlation time” ( $\tau_c$ )<sup>69</sup>, which is a function of water exchange, rotational correlation time (related to the size of the agent), and electron spin relaxation. This relationship is shown in the SBM equations 1.5 and 1.6.  $\tau_c$  is a time constant (the inverse of a rate constant) and characterizes the interactions of a given nucleus with other sub-atomic particles with “spin” and how that nucleus behaves with respect to applied magnetic fields.  $T_1$  of the inner-sphere water molecule ( $T_{1M}$ ) is proportional to  $r_{Ln-H}^{-6}$  and on both the longitudinal ( $\tau_{c1}$ ) and transverse ( $\tau_{c2}$ ) correlation time constants.

$$\frac{1}{T_{1M}} = \frac{2}{15} \frac{\gamma_H^2 g^2 S(S+1) \beta^2}{r_{Ln-H}^6} \left[ \frac{3\tau_{c1}}{1 + \omega_H^2 \tau_{c1}^2} + \frac{7\tau_{c2}}{1 + \omega_S^2 \tau_{c2}^2} \right]$$

**Equation 1.5:** SBM equation describing the longitudinal relaxation time of a CA-bound water proton, where  $\gamma_H$  is the proton magnetogyric ratio,  $g$  is an electronic factor usually close to 2,  $S$  is the electron spin quantum number,  $\beta$  is the Bohr magneton, and  $r_{Ln-H}$  is the distance between the metal and water proton(s). The terms  $\omega_S$  and  $\omega_H$  are the electronic and proton Larmor frequencies, respectively. The Larmor frequency is the frequency at which the nuclear spin momenta resonate in a magnetic field of particular strength.

$$\frac{1}{\tau_{ci}} = \frac{1}{T_{ie}} + \frac{1}{\tau_R} + \frac{1}{\tau_M}$$

**Equation 1.6:**  $\tau_c$  is a correlation time constant associated with interactions at the Larmor frequency.  $i = 1$  (longitudinal relaxation) or  $2$  (transverse relaxation).  $T_{ie}$ ,  $\tau_R$ , and  $\tau_M$  are the electronic, rotational, and water exchange components, respectively

The rotational correlation time ( $\tau_R$ ) is a measure of how rapidly the CA “tumbles” in solution, reorienting itself continuously with respect to the magnetic field.  $\tau_R$  is a function of the molecule’s size and shape, and is longer for bulkier compounds.  $T_{1e}$  ( $i = 1$  or  $2$ ) are the longitudinal or transverse electron spin relaxation times, and  $Gd^{3+}$  has the longest  $T_{1e}$  of any lanthanide.<sup>70</sup> The electron spin relaxation component’s effect on  $\tau_c$  is related to the static zero-field splitting (ZFS) interaction ( $\Delta^2$ ) and the ZFS modulation ( $\tau_v$ ).<sup>71</sup> According to empirical findings, SBM theory does not predict  $T_{1e}$  effects on relaxivity with a great deal of accuracy. It has been determined that a more symmetric, rigid chelate (such as Gd-DOTA, compared with Gd-DTPA) has more favorable electronic relaxation, particularly for systems with longer  $\tau_R$ .<sup>72,73</sup> Efforts have been made recently to better understand the effects of  $T_{1e}$  on relaxivity.<sup>74,75</sup>

Using these equations, the influence of  $\tau_R$  and  $\tau_M$  on inner-sphere relaxivity have been modeled holding other relaxation parameters, such as  $q$  and  $r_{Gd-H}$  (or simply  $r$ , the distance between the lanthanide ion and inner-sphere water protons) constant.<sup>72,76</sup> A plot of one such model at a field strength of 0.5 T is shown in Figure 1.8.

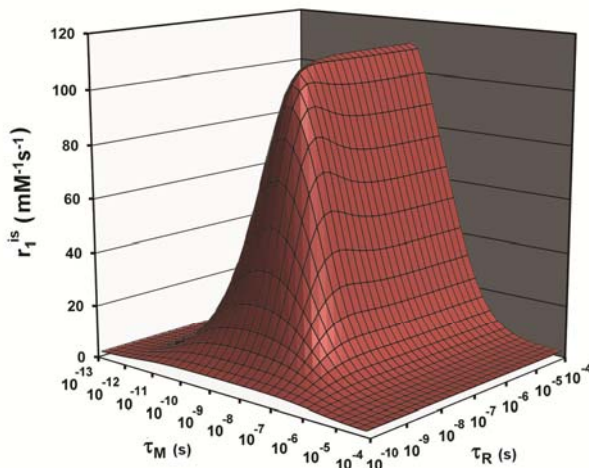


**Figure 1.8:** Inner-sphere paramagnetic relaxivity ( $r_1^{is}$ ) dependence on  $\tau_R$  and  $\tau_M$  at 0.5 T imaging field

As is evident from the curve, there is an optimal range for  $\tau_M$ . If a water molecule does not spend enough time close to the paramagnetic  $\text{Gd}^{3+}$ , the proton spin momenta do not experience the full effect of  $T_1$  reduction. A water molecule which spends too much time close to the metal ion prevents other water molecules from displacing it to have their own spin momenta relaxed efficiently. The optimal  $\tau_M$  range for CAs has been calculated to be  $\sim 20\text{-}40$  ns at 0.5 T, and  $\tau_M$  values above 1  $\mu\text{s}$  or below 10 ps (which is not physically attainable in solution) should lead to very poor relaxivity.

Values of  $\tau_R$  greater than 1 ns are desirable, which is an order of magnitude larger than  $\tau_R$  values of clinical agents.<sup>77</sup> The agents in use clinically today have relaxivities of 4 - 5  $\text{mM}^{-1} \text{s}^{-1}$  at 25°C and 0.5 T.<sup>24</sup> Relaxivities of novel compounds which contain  $\text{Gd}^{3+}$  chelates are commonly reported at 0.5 T (corresponding to a  $^1\text{H}$  Larmor frequency of approximately 20 MHz) for historical comparison, though MR imaging is now performed largely at 1.5 or even at 3 T. A maximum relaxivity surface has the same basic shape as

the one in Figure 1.8 at these fields but is shifted slightly towards faster water exchange.<sup>78</sup> The optimal  $\tau_M$  value has been calculated to be  $\sim 6$  ns at 1.5 T, the most commonly used field strength of MRI instruments for medical diagnosis.<sup>79</sup>

Because of the large improvements in relaxivity that could be achieved by optimizing these parameters, the rate of water exchange ( $1/\tau_M$ ) between a small-molecule, lanthanide-based agent and the bulk matrix is important to study (and to control, as much as is feasible). Many researchers in the field of medical imaging are working toward the goal of molecular imaging, a way to observe the molecular processes indicative of specific pathologies and diseases. For low molecular weight chelates, water exchange is not the relaxivity-limiting parameter ( $\tau_R$  is limiting), but will play a defining role in the efficacy of a CA that is bound to a macromolecular target. The excellent spatial resolution obtainable by MRI is advantageous for molecular imaging, but chemical probes available cannot currently be detected by MRI at the concentration of the involved biological markers.<sup>80</sup> This fact demonstrates the need to develop higher-relaxivity (more effective) agents, which will in part be accomplished by optimizing  $\tau_M$ .

## ***1.4 Structural characterization of Ln<sup>3+</sup> chelates and MRI CAs***

### *1.4.1 Measuring relaxivity of CAs over a range of magnetic field strengths by nuclear magnetic relaxation dispersion (NMRD)*

Nuclear magnetic relaxation dispersion (NMRD) is the standard technique for measuring relaxivity as a function of magnetic field strength, and is useful in comparing the likely efficacy of existing and potential CAs.<sup>81,82</sup> Measuring the relaxation properties of paramagnetic species in solution by NMRD yields information about both electronic and nuclear relaxation rates (Figure 1.9). These rates can provide insight about the relaxation mechanism and which factor(s) are the prime determinant(s) of relaxation rate under specific conditions. The wide range of magnetic field strengths probed in NMRD allows the experimenter to analyze how the factors that govern relaxation behavior vary over this range, as described in Table 1.1. By looking at the shape of an NMRD curve, the experimenter can narrow down which parameter or parameters limit the relaxivity for a given magnetic field strength range. The most influential factors are conformational or coordination changes (including  $\tau_M$ ), reorientation ( $\tau_R$ ), and electron-spin relaxation ( $T_{1e}$ ). The fastest of the above processes will dominate (and limit) the relaxation rates observed, and the field dependence of relaxivity can allow estimation of the relaxation rate due to that parameter alone.

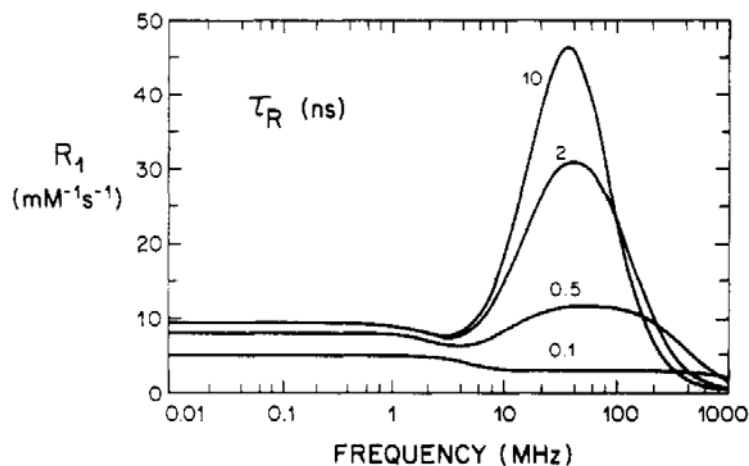


**Figure 1.9:** NMRD profile of a non-specified, typical  $\text{Gd}^{3+}$  chelate with varying  $\tau_R$  values<sup>61</sup>

It is important to note that the relaxivity measured has contributions from all protons in the sample that undergo rapid diffusion and chemical exchange. The inner- and outer-sphere contributions to relaxivity cannot be separated in an NMRD fit. In practice, an assumed value for outer-sphere relaxivity is fixed based on the profile of a  $q = 0$   $\text{Gd}^{3+}$  chelate. A diamagnetic equivalent of the chelate of interest is free from a substantial  $T_{1e}$  contribution and its relaxivity is dominated by  $\tau_R$  for small molecules.  $\tau_R$  can be estimated from the NMRD profile of such a diamagnetic species, using  $\text{Y}^{3+}$ ,  $\text{La}^{3+}$ , or  $\text{Lu}^{3+}$  in place of a paramagnetic  $\text{Ln}^{3+}$ . Electronic relaxation due to  $\text{Gd}^{3+}$  is longer in viscous solutions, or when  $\text{Gd}^{3+}$  is bound to a species with long  $\tau_R$ , which leads to a peak or “hump” in the NMRD profile at a field strength of approximately 20-50 MHz (Figures 1.9, 1.10).<sup>83</sup>

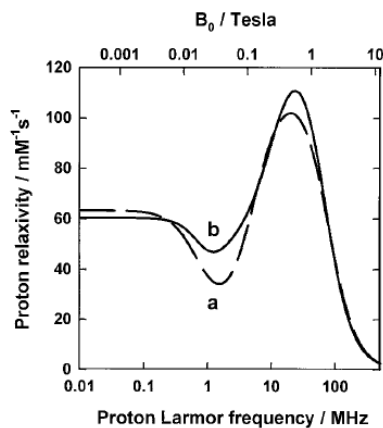


**Figure 1.10:** NMRD profile of  $\text{Gd}(\text{H}_2\text{O})_9^{3+}$  in ethylene glycol using two different electron relaxation fitting values  $a$  and  $b$ .<sup>84</sup>

There are many parameters necessary to account for when generating a fit to the experimental NMRD data, and these all must be fit to values that have physical meaning. The universally used approach is to constrain certain parameters to values previously and/or independently measured for related systems, and to vary one or a few parameters that the experimenter believes characterize his or her unique system. The parameters that receive the most attention due to their strong influence on relaxivity are summarized in Table 1.1. A recent review on the search for improved Gd-based contrast agents was used to construct this table.<sup>20</sup>



Parameter	Independent measurement technique	Accepted range of values for Gd <sup>3+</sup> chelates	B <sub>0</sub> field dependence
	Luminescence lifetime of Eu <sup>3+</sup> or Tb <sup>3+</sup> chelate <sup>85,86</sup>		
$q$	Dy <sup>3+</sup> -induced <sup>17</sup> O NMR shift <sup>87</sup>  Variable-temperature Eu <sup>3+</sup> UV-Vis. absorption <sup>77</sup>	0,1*, rarely 2 or 3	Relaxivity scales linearly with $q$ at low field (<0.05 T)
$r_{\text{Gd-H}}$	None, assumed values from X-ray crystallography are typically used.‡ <sup>88</sup>	2.9 - 3.25 Å, typically 3.1 Å	Relaxivity scales proportionally to $1/r^6$ at all fields
$\tau_{\text{R}}$	Usually determined by NMRD by trying logical values for $\tau_{\text{R}}$ once all other parameters have been established/fixed, or by Curie relaxation§	0.1 ns for small chelates, up to 30 ns for large macromolecular adducts	A longer $\tau_{\text{R}}$ will exhibit a larger peak and at a lower field due to T <sub>1e</sub> limit**
$\tau_{\text{M}}$	Variable-temperature ( <sup>17</sup> O and Dy <sup>3+</sup> ) NMR shift and T <sub>2</sub> <sup>89,90</sup>	1 ns to 1 ms	For otherwise analogous species, the entire curve will be offset, but not proportionally
T <sub>1e</sub> and T <sub>2e</sub>	Comparison of EPR, NMR and NMRD data to obtain the best fit <sup>71,91</sup>	<sup>‡</sup> T <sub>1e</sub> ≥ 2 × 10 <sup>-10</sup> s at 25°C <sup>70</sup>	Only obvious when $\tau_{\text{R}}$ and $\tau_{\text{M}}$ are non-limiting

**Table 1.1:** Influence of the most important parameters in fitting experimental NMRD data. \*The empirical value of  $q$  is usually a non-integer due to an  $r_{\text{Ln-H}}$  value outside of what is predicted by Horrocks' method for calculating  $q$  based on luminescent lifetimes. ‡Values extrapolated from ENDOR<sup>92</sup> or EXAFS(Gd-O)<sup>93</sup> measurements are sometimes used. §Determined by the Debye-Stokes equation<sup>77</sup> if the microviscosity and molecular radius are known, alternatively by diffusion measurement (DOSY) or <sup>13</sup>C T<sub>1</sub>/NOE measurements.<sup>94</sup> \*\*See examples in Figures 1.9 and 1.10. †Not directly obtainable from NMRD, the parameters  $\tau_{\text{v}}$  (zero-field splitting) and  $\Delta^2$  (mean-square zero-field-splitting energy) are used instead.

When a curve that fits poorly to the data results, it is not necessarily obvious which parameter(s) must be adjusted to generate a more optimal fit. Measuring the relaxivity-influential properties of  $\text{Ln}^{3+}$  chelates by independent techniques aids in the optimization of parametric fitting. By combining NMRD with as many complementary studies as are feasible, it is possible to measure how effective a putative CA will be and ascertain how to potentially improve the agent further. Relaxivities obtained from NMRD are in good agreement with  $R_1$  values and contrast enhancement measured for CAs in biological systems, including *in vivo* studies. The relationship between  $r_1$ , field strength, and contrast agent dose has also been studied *in vivo*.<sup>95</sup>

#### 1.4.2 Probing structure by taking advantage of lanthanides' electronic properties

Crystallography is a valuable tool for studying the structures of  $\text{Ln}^{3+}$  chelates. However, solid-state techniques, including crystallography and ENDOR (electron-nuclear double resonance), cannot provide a complete picture of the critical dynamic processes described by  $\tau_R$  and  $\tau_M$ . It is difficult to study the structures of  $\text{Gd}^{3+}$  chelates in solution directly due to their unique electronic properties. As  $\text{Ln}^{3+}$  chelates of a particular ligand are practically isostructural, other lanthanides with more favorable electronic behavior are used as surrogates in structural characterization of chelates of the ligand(s) of interest. It is preferable to use  $\text{Ln}^{3+}$  whose atomic radii are closest to  $\text{Gd}^{3+}$  ( $\text{Eu}^{3+}$  and  $\text{Tb}^{3+}$ ) for the most accurate structural comparison, although there are drawbacks to using these particular lanthanides as well. NMR is a valuable technique for structural characterization in solution, and allows the determination of distances (from  $\text{Ln}^{3+}$ ) and  $\tau_R$  for individual nuclei in a chelate, particularly protons.

For the lanthanides, the ligand field in their chelates is much smaller in energy in comparison with their spin-orbit coupling, a coupling between the electronic orbital angular momentum  $L$  and spin angular momentum  $S$ .<sup>96</sup> An approach to describe the combination of spin and orbital angular momenta into one term symbol  $J$  is known as Russell-Saunders coupling, which explains and predicts the electronic behavior of lanthanides to a good approximation. This approach assigns each lanthanide a specific ground state electronic configuration and allows the effective magnetic moment of each ion to be calculated. The effect of the electronic configuration and magnetic moment of a  $\text{Ln}^{3+}$  ion on nearby nuclei can be broken down into three contributions: diamagnetic, contact ( $\delta^c$ ) and pseudo-contact or dipolar ( $\delta^d$ ). The diamagnetic contribution is small for nuclei not directly coordinated to the  $\text{Ln}^{3+}$ . Through-bond transmission of unpaired electron spin density to a nucleus produces  $\delta^c$ . Through-space dipole-dipole interaction between nuclear and electronic magnetic momenta is the cause of the  $\delta^d$  contribution. The sum of these contributions will affect the nuclear spin properties of a given proximal nucleus and induce a particular NMR shift.<sup>97</sup> The paramagnetic contributions to an NMR shift are expressed by proportionality constants particular to the lanthanide and independent of ligand(s) in Equations 1.7 and 1.8.

$$\text{Equation 1.7: } \Delta_c \text{ (ppm)} = \langle S_z \rangle \cdot \frac{\beta}{3kT\gamma_1} \cdot \frac{A}{\hbar} \cdot 10^6$$

$$\text{Where } \langle S_z \rangle = J(J+1)g(g-1) \text{ and } g = \frac{3J(J+1) - L(L+1) + S(S+1)}{2J(J+1)}$$

and  $\langle S_z \rangle$  is a constant (the reduced value of the average spin polarization),  $\beta$  is the Bohr magneton,  $k$  is Boltzmann's constant,  $T$  is absolute temperature,  $\gamma_1$  is the magnetogyric ratio of the nucleus acted upon,  $A/\hbar$  is a hyperfine coupling constant, and  $g$  is the Landé factor.

$$\text{Equation 1.8: } \Delta_d = C_j \cdot \frac{\beta^2}{(60k^2 T^2)} \cdot \frac{\langle r^2 \rangle A_2^0 (3\cos^2\theta - 1) + \langle r^2 \rangle A_2^2 (\sin^2\theta \cdot \cos 2\varphi)}{r^3}$$

Where  $C_j$ , Bleaney's constant, is equal to  $g^2 J(J+1)(2J-1)(2J+3)\langle J | a | J \rangle$  and is also characteristic to the lanthanide ion.  $\langle r^2 \rangle A_2^0$  and  $\langle r^2 \rangle A_2^2$  are the zero and second order ligand field coefficients,  $r$ ,  $\theta$ , and  $\psi$  are the polar coordinates of the ligand nucleus with respect to the principal magnetic axis of the complex with the lanthanide ion at the origin, and  $\langle J | a | J \rangle$  is a numerical coefficient

The constants  $C_j$ <sup>98</sup> and  $\langle S_z \rangle$ <sup>99</sup> and  $g$  factors have been determined for each of the paramagnetic lanthanides.

#### 1.4.3 Structure determination by NMR

The spin density of the electrons is primarily centered on the metal ion and not in the bonds or donor ligand atoms, so the contact contribution is relatively small in magnitude. Most of the lanthanide ions are known to cause large chemical shifts in nearby nuclei in NMR experiments.<sup>100</sup> For this type of shift to occur, the lanthanide must have an anisotropic  $g$  factor in the liquid at room temperature as first described by Bleaney *et al.*<sup>98,101</sup> This means that the paramagnetic energy levels must be degenerate in the

absence of a magnetic field, and that the Zeeman interaction of the levels depends on the orientation of a magnetic field relative to the local axis of the paramagnetic complex. This interaction only leads to large dipolar ( $\delta^d$ ) shifts when the ligand field is asymmetric.  $Gd^{3+}$  has an isotropic ligand field, so its chelates cannot be used for the study of relaxation of individual ligand protons. This magnetic dipole interaction is strongly distance- ( $r^{-3}$ ) and temperature dependent ( $T^{-2}$ , except for  $Sm^{3+}$  and  $Eu^{3+}$ , when it is between  $T^{-1}$  and  $T^{-2}$ ). The exceptions for  $Sm^{3+}$  and  $Eu^{3+}$  arise due to the population of low-lying electronic excited states for these ions. The sign and magnitude of the induced shifts stem from the spin angular momenta of the unpaired electrons and the local magnetic field they produce. Analysis of these shifts can yield important structural details about the chelate of interest.<sup>102,103</sup>

The dipolar shift component is non-zero for an anisotropic electron configuration (all paramagnetic lanthanides except  $Gd^{3+}$ ), and for those  $Ln^{3+}$  it is the dominant contributor to induced NMR shift. By assuming that the ligand field does not vary across the lanthanide series, the  $\langle r^2 \rangle A_2$  terms can be neglected. The chelates of interest are axially symmetric or nearly enough so that the  $\psi$  term (polar coordinate, not the O4 plane opening angle) can be discounted as well. This reduces the major contribution of lanthanide-induced shifts (LIS) to  $\Delta = D \frac{(3 \cos^2 \theta - 1)}{r^3}$ , where D is a lanthanide-dependent proportionality constant and r and  $\theta$  are polar coordinates.

SAP and TSAP chelates can be distinguished from one another by any technique which probes the magnitude of the axial ligand field,  $A_2^0$ .<sup>104-106</sup> This parameter is larger for

SAP chelates, and the  $\text{Ln}^{3+}$  ion induces a wider frequency range of shifts in the spectra of SAP chelates than in the TSAP analogues in the case of  $\text{Eu}^{3+}$  and  $\text{Yb}^{3+}$ . The geometry is identifiable by the large downfield shift of the protons positioned axially on carbons on the sides ( $ax^S$  protons) of the macrocyclic ring. These  $ax^S$  protons have the largest induced downfield chemical shift due to their proximity to the principal magnetic axis in the chelates.<sup>40,107</sup> However, 2-dimensional spectroscopy is necessary to characterize multiple isomers of the same geometry. Quantitative structural analysis<sup>108,109</sup> is possible for those lanthanides for which  $C_j$  is large (the later lanthanides, such as  $\text{Yb}^{3+}$ ), but the contact and diamagnetic contributions cannot be neglected for lanthanides where  $C_j$  is small, or for lanthanides that have populated electronic excited states at ambient temperature ( $\text{Sm}^{3+}$  and  $\text{Eu}^{3+}$ ). In the case of these elements we are restricted to qualitative interpretation.

The width of a proton resonance gives a relative measure of relaxation time in the absence of chemical exchange, and line-width at half height can be used to approximate  $T_2$  of a particular resonance.  $T_2$  also has a strong spatial dependence relative to  $\text{Ln}^{3+}$ , and can inform on the relative symmetry and electronic relaxation of a chelate.

#### 1.4.4 Determination of $q$ and $\tau_M$

Direct excitation of the f-f electronic transitions of  $\text{Ln}^{3+}$  ions gives rise to distinctive luminescence emission. The luminescent lifetimes are long (on the order of ms) because these transitions are parity-forbidden. The vibrational energy of -OH oscillators in water is very close to the energy of the  $^5D_0$ - $^7F_1$  ( $\Delta J = 0-6$ ) f-f transitions in  $\text{Eu}^{3+}$ . Using the

similarity of these energy levels as a basis, Horrocks and co-workers developed a luminescence-based method to measure the number of water molecules interacting with  $\text{Eu}^{3+}$  or  $\text{Tb}^{3+}$ .<sup>110,111</sup> The  $\text{Ln}^{3+}$  excited electrons can return to their ground state *via* non-radiative energy transfer to the -OH bonds, where the degree of vibrational quenching is proportional to the number of proximal oscillators. The quenching by water is far more efficient than that by  $\text{D}_2\text{O}$ , whose vibrational energies do not match up as closely with f-f transitions. A plot of the mole fraction of water in  $\text{D}_2\text{O}$  against the difference in quenching rate by  $\text{D}_2\text{O}$  and  $\text{H}_2\text{O}$  ( $\Delta k$ ) yields a straight line. The value of  $q$  can be determined based on the slope ( $A$ ) of the line where  $q = A \cdot \Delta k$ . There is a degree of error in this determination due to outer-sphere quenching, which can be corrected for.<sup>86,112</sup> It has been shown that  $r_{\text{Eu-O}}$  is fairly consistent among crystal structures of  $\text{Eu}^{3+}$  complexes with varying charge and number of inner-sphere water molecules, approximately  $2.45 \pm 0.4 \text{ \AA}$ .<sup>49,113-115</sup> A  $q$  value between 0 and 1 is reported when a water molecule has been determined to be in the vicinity of the metal, but with a longer Gd-H distance (greater than  $\sim 2.9 \text{ \AA}$ ) than the accepted  $r_{\text{Ln-H}}$  for inner-sphere water.<sup>86</sup> Based on known  $q$  values of various  $\text{Ln}^{3+}$  chelates, the magnitude of  $\Delta k$  due to non-inner-sphere interactions was determined.

The measurement of inner-sphere water exchange rates ( $k_{\text{ex}}$ ) and water residence lifetime ( $\tau_{\text{M}}$ ) by variable-temperature  $^{17}\text{O}$  NMR methods was first published by Swift, Connick, and co-workers,<sup>116,117</sup> using the Bloch equations modified for chemical exchange as described by McConnell.<sup>118</sup> These methods were later extended to gadolinium complexes.<sup>119</sup> The measured shift difference ( $\Delta\omega$ ) between inner-sphere water and bulk

water is a function of  $T_2$ ,  $\tau_M$ , and an outer-sphere contribution that can be neglected. These parameters and others which describe the system (including electronic relaxation parameters, which can be determined from electron paramagnetic resonance (EPR)) are fit in a way analogous to NMRD to yield plots  $1/T_1$ ,  $1/T_2$ , and  $\Delta\omega$  vs. temperature<sup>-1</sup>.<sup>120,121</sup> From these data, accurate values of  $k_{ex}$  and  $\tau_M$  can be obtained.

#### *1.4.5 Examination of the motion and angle of a coordinated water molecule with respect to the lanthanide*

The “internal motion” of an inner-sphere water molecule has been examined recently by Dunand *et al.*<sup>122</sup> Based on the Curie (dipolar) relaxation of  $Tb^{3+}$  and quadrupolar (contact) relaxation of  $^{17}O$  and  $^2H$  of Eu-bound water,  $\tau_R$  values of Ln-O and Ln-H were calculated for DOTAM chelates. The calculation of  $\tau_R$  relies on several assumptions, including that  $r_{Ln-H}$  in solution is the same as in the crystal. The justifications for this assumption are based on data from a paper by Aime *et al.*,<sup>123</sup> discussed below, and on X-ray absorbance spectroscopy (XAFS or EXAFS) determination in solid state and solution by Bénazeth *et al.*<sup>124</sup>

The Ln-H distances of the 6 types of ligand proton in DOTA were calculated for Tb, Dy, and  $Ho[DOTA]^-$ .<sup>123</sup> These are based on  $T_2$  determinations from the line-widths of the proton peaks at half height. Due to the geometric exchange processes in DOTA, though, the lines could be broadened by non- $T_2$  factors. The authors neglect the contributions to the line-widths from the minor TSAP isomer observed in the NMR spectra. The Ln-H values determined also rely on calculated  $\tau_R$  values from NMRD,  $^{13}C$   $T_1$  and NOE data.



Data underlying the calculations of  $\tau_R$  are based on an incomplete description of sources of line-broadening, which leads to systematic errors in the calculations.

The Ln-H distances were also calculated separately by measuring the line-widths at 3 different magnetic fields and plotting line-width vs. the square of the field. The line-width of an internal standard (t-butanol) was subtracted from the line-width of each of the DOTA shifts. The authors acknowledge that a chemical exchange process may affect the shifts, and measure them at different temperatures. Good agreement of calculated  $r_{\text{Ln-H}}$  values is claimed at 3 temps: 275, 285, 295 K. In this study, Ln-H was measured only for the DOTA ligand hydrogen atoms, not for bound water.

Dunand *et al.* took Ln-H distances directly from the crystallographic data and postulated 2 different orientations of the water molecule with respect to Ln: H's oriented upward, furthest from the  $\text{Ln}^{3+}$ , and H's angled downward, somewhat towards the  $\text{Ln}^{3+}$  (Figure 1.11).

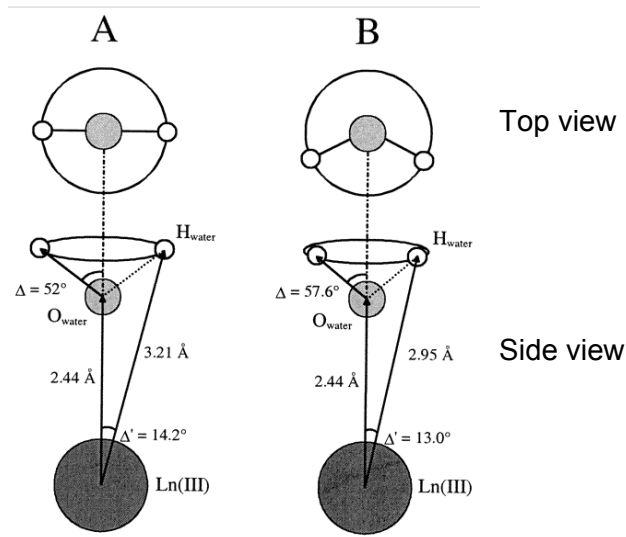


**Figure 1.11:** Distances and angles calculated for crystal structures of Gd[DOTA]<sup>-</sup> with the water molecule positioned A) such that the protons are furthest from the metal ion, and B) such that the protons are angled downward slightly towards the metal.<sup>122</sup>

They determined  $\tau_R$  values for  $r_{Ln-H}$  and  $r_{Ln-O}$ , and  $\tau_R$  ratios of  $r_{Ln-H}/r_{Ln-O}$  were calculated to be 1 and 0.6 respectively using the 2 angles. They also took quadrupolar relaxation data by measuring line-widths for the Eu<sup>3+</sup> complex, which is expected to be inexact due to low-lying Eu<sup>3+</sup> excited states.

They defend the use of 2.44 Å for  $r_{Ln-O}$  based on XAFS measurements<sup>124</sup> performed in solution, which gives  $r_{Ln-O} = 2.46$  Å (not 2.447 as claimed by Dunand *et al.* The 2.447 value is from the solid state XAFS data). In a later paper<sup>93</sup>, there is not an adequate explanation of why the determined XAFS solution values for Eu-O and Tb-O are 2.5 Å, but 2.44 Å for Gd-O in Ln[TCE-DOTA].

The assumptions made by Dunand *et al.* do not invalidate their conclusion that the local motion of water should not significantly affect relaxivity in compounds with long  $\tau_R$ .

However, the data cited from the other work to support the assumed Ln-O and Ln-H distances does not seem wholly applicable. There are small  $r_{\text{Ln-O}}$  differences between solid and solution state structures, leading to a small degree of error in using the Ln-O distance as a fixed parameter. There is a great deal of uncertainty about the Ln-H distance due to the unknown “tilt” angle of the water molecule, and the low degree of H-atom position prediction in crystallography. The two Ln-H distances calculated (3.21 vs. 2.95 Å) as shown in Figure 1.11 might reasonably be expected to be the possible maximum and minimum. However, the “tilt” angle of the water molecule is likely fluctuating between these extremes due to the continual motion of water (including water exchange). A thorough structural characterization of any  $\text{Ln}^{3+}$  chelate proposed for study as an MRI CA is prudent for measuring and optimizing parameters including  $\tau_{\text{M}}$ , though with techniques available today we are still limited to educated guesses with respect to values for  $r_{\text{Ln-H}}$  for inner-sphere water.

### ***1.5 The scope of this work: increasing the efficacy of MRI CAs***

The scope of this work is to design, synthesize, and test the properties of relaxivity-optimized  $\text{Ln}^{3+}$  chelates having high kinetic stability.

### 1.5.1 Strategy for decreasing $\tau_M$ via coordination isomer selection

Since  $r_{\text{Ln-H}}$  cannot be measured directly,  $r_{\text{Ln-O}}$  is measured in many studies of CA-applicable chelates and the two  $r$  values are assumed to be proportional. A greater Gd-OH<sub>2</sub><sup>(inner-sphere)</sup> distance ( $r$ ) has a strong correlation with faster water exchange. Strategies to accelerate water exchange have been pursued by a number of researchers in efforts to prepare more effective contrast agents. These strategies mainly involve modifying the overall charge of the chelate and/or increasing steric hindrance about the water coordination site.<sup>66,125-127</sup> The results, however, have been disappointing – the resultant relaxivities have not increased as much as would be predicted by SBM theory.<sup>80,128,129</sup> Many of these studies are complicated by the existence of multiple coordination geometries and/or conformations for a given chelate, making it difficult to isolate the effects of  $\tau_M$  on relaxivity.

$\tau_M$  for Gd[DOTA]<sup>-</sup> has been determined to be 244 ns, which is much slower than optimal according to SBM theory. It has been demonstrated that water exchange rates depend strongly on the coordination geometry of the chelate.<sup>73,130</sup> The TSAP isomer has water exchange kinetics in the optimal range predicted by SBM theory. However, the SAP isomer is the major isomer (~85%) in solution under physiological conditions, and its water residence lifetime is approximately 50 times longer.<sup>131</sup>

It would be advantageous to synthesize a DOTA derivative with only the coordination geometry yielding the desired water exchange kinetics. To do this, chiral substituents on the arms and on the ring can be added to increase steric hindrance to reversal of helicity

(Figure 1.12). These steric modifications should increase the energy barriers to arm rotation and ring inversion.<sup>132-134</sup>

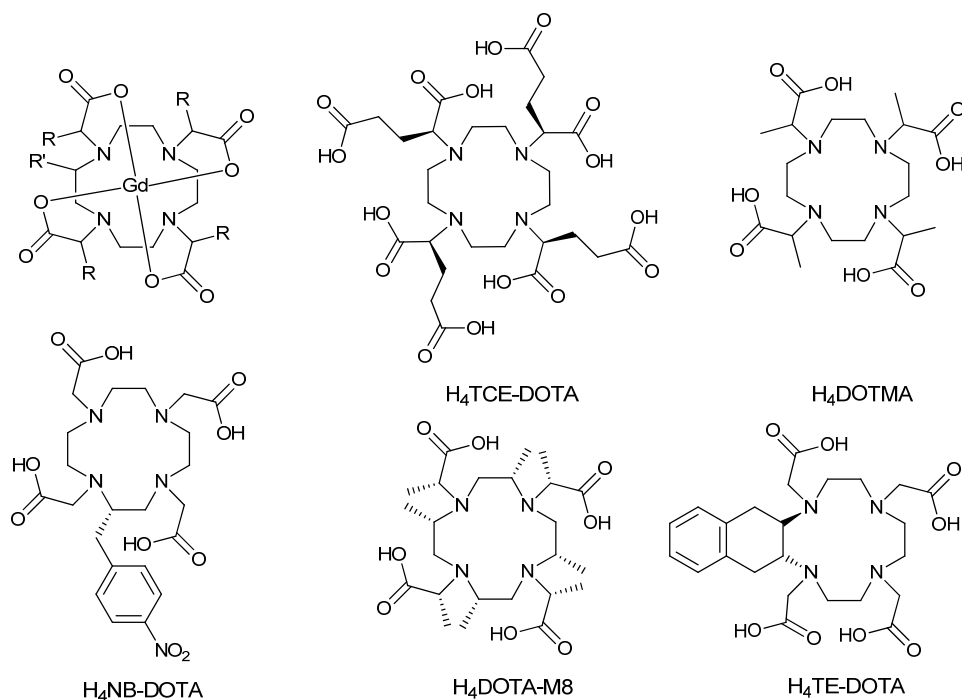


**Figure 1.12:** Examples of DOTA derivatives with arm (R) and ring (R') substituents.<sup>115,134-137</sup>

Synthesis of the DOTA derivative TCE-DOTA with chiral arms has been described.<sup>132</sup> The ratio of TSAP and SAP isomers have been measured in solution, and the chelates were mostly SAP, with pendant arms having mixed chiralities (*RSRS*-, etc.) leading to a minor isomer in TSAP form. The chelates with greater percent TSAP geometry had faster water exchange.<sup>137</sup> When both bulky ring and arm substituents were added, these were found to “lock” the chelate into a single conformational isomer in solution.<sup>53</sup> A specific configuration at each substituted carbon was found to be necessary to select for a given helicity; racemic mixtures led to multiple products and geometries.

Understanding the isomeric preference and/or interconversion is crucial to preparative efforts and potential clinical use of the relaxivity-optimized isomer for a particular macrocyclic chelate. If  $\tau_R$  of DOTA-type chelates were made longer (*i.e.* by binding to a macromolecule), the relaxivities would be limited by  $\tau_M$  unless the geometry is TSAP, according to the SBM model in Figure 1.8. By carefully selecting the chirality at the stereogenic centers in arm and ring substituted DOTA-type chelates, we attempted to prepare  $\tau_M$ -optimized chelates and to study their structural and relaxometric properties.

### 1.5.2 Strategies for increasing relaxivity based on $\tau_R$

All clinical MRI CAs are extracellular and non-specific, exhibiting a distribution within the vasculature.<sup>138</sup> Of particular current interest in CA development are potential diagnostic agents that are administered as low molecular weight agents and bind to macromolecules in blood or tissue or are covalently conjugated to macromolecules, both leading to more optimal  $\tau_R$ . For example, MS-325 (marketed as Ablavar™) has a Gd<sup>3+</sup> chelate covalently linked to a lipophilic, human serum albumin-binding moiety<sup>139</sup> and has been approved in the E.U. and other countries as a MR blood-pool agent. The small-molecule agent circulates freely in the blood until its bicyclohexyl group binds to albumin, enhancing relaxivity by slowing  $\tau_R$  (due to restricted local and global rotation) of the agent.<sup>140-142</sup>

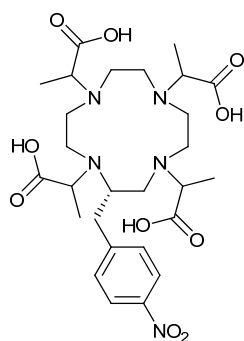
Dendrimer, nanoparticulate, micelle, or liposome-based formulations of Ln-based CAs have been envisioned and show great promise for imaging.<sup>143-147</sup> Their large size increases  $\tau_R$  (at least due to the global rotation limitation), but there are concerns that

water exchange may be negatively affected. Also, the larger size changes the biodistribution and pharmacokinetics compared with the parent chelate.<sup>36,148,149</sup> In order to maximize the relaxivity gains from this slower tumbling, extracellular water must be able to diffuse to, and exchange freely with, the inner-, second-, and outer-sphere water molecules for all  $Gd^{3+}$  sites, most of which are on the inside of nanoparticles or liposomes by design. Alternatively, the Ln-water exchangeable sites could be placed on the surface of the large particles. It would be valuable to know whether the rate of water exchange between the inner-sphere and bulk water limits the observed relaxivity of these putative agents. In micelles, the local concentration of  $Gd^{3+}$  may even be too high, leading to disruption of the water relaxation mechanism.<sup>150,151</sup>

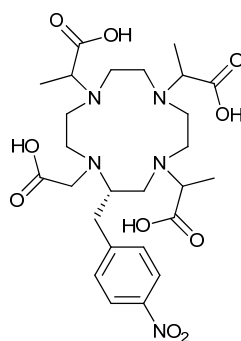
No clinical agents are currently available with the capability of targeting specific pathologies, such as a CA which binds only to certain types of extracellular protein (for example, on the outside of tumor cells). Work on a macrocycle with phosphonate monoester pendant arms by another lab has shown that its  $Tb^{3+}$  chelate binds selectively to certain types of tumor cells.<sup>152</sup> Assuming rapid, pervasive biodistribution and high specificity, this targeted binding approach would provide contrast enhancement only at that site, reducing the required dose. The research of cancer-cell-targeting MR agents is starting to receive a great deal of interest. Injecting a CA that is as stable as possible is particularly important when designing an agent which will bind to a molecular target, due to the increased residence time in the body.<sup>153-155</sup> We attempted to prepare  $Gd^{3+}$  chelates with macromolecular binding capability and to study their properties when bound to a

slowly tumbling target. One of these chelates could become the active component in a potential CA.

Arm and ring substituted DOTA chelates are characterized by fast water exchange and are interesting candidates for high relaxivity. Though chelates of NB-DOTMA (**2**) have been synthesized and studied before,<sup>53,106,137</sup> there seemed to be merit in further characterization of these systems. In particular, the structure and subtle structural variations between isomeric chelates were targeted for study. Questions concerning the origin of multiple isomers in this system, which had implications for relaxivity behavior, had remained unanswered prior to this work. Chelates of **2** also are very similar to those of NB-DO3MA-1A (**3**), whose relaxometric properties when bound to slowly tumbling species have previously been investigated.<sup>156</sup>



H<sub>4</sub>NB-DOTMA (H<sub>4</sub>[**2**])



H<sub>4</sub>NB-DO3MA-1A (H<sub>4</sub>[**3**])

Ligands whose chelates were studied in this work



**1.6 References**

- (1) Iglehart, J. K. *New England Journal of Medicine* **2006**, 354, 2822.
- (2) Brenner, D. J.; Hall, E. J. *New England Journal of Medicine* **2007**, 357, 2277.
- (3) de González, A. B.; Darby, S. *The Lancet* **2004**, 363, 345.
- (4) Rothkamm, K.; Balroop, S.; Shekhdar, J.; Fernie, P.; Goh, V. *Radiology* **2007**, 242, 244.
- (5) Kwong, R. Y.; Yucel, E. K. *Circulation* **2003**, 108, e104.
- (6) Tatlisumak, T. *Stroke* **2002**, 33, 2144.
- (7) Gupta, R. T.; Kauffman, C. R.; Polascik, T. J.; Taneja, S. S.; Rosenkrantz, A. B. *Oncology-Ny* **2013**, 27, 262.
- (8) Li, X.; Priest, R. A.; Woodward, W. J.; Siddiqui, F.; Beer, T. M.; Garzotto, M. G.; Rooney, W. D.; Springer Jr, C. S. *Journal of Magnetic Resonance* **2012**, 218, 77.
- (9) Li, X.; Priest, R. A.; Woodward, W. J.; Tagge, I. J.; Siddiqui, F.; Huang, W.; Rooney, W. D.; Beer, T. M.; Garzotto, M. G.; Springer, C. S. *Magnetic Resonance in Medicine* **2013**, 69, 171.
- (10) Lauterbur, P. C. *Nature* **1973**, 242, 190.
- (11) Damadian, R. *Science* **1971**, 171, 1151.
- (12) Andrew, E. R.; Bottomley, P. A.; Hinshaw, W. S.; Holland, G. N.; Moore, W. S.; Simaraj, C. *Physics in Medicine and Biology* **1977**, 22, 971.
- (13) Damadian, R.; Goldsmith, M.; Minkoff, L. *Physiol Chem Phys* **1977**, 9, 97.
- (14) Hinshaw, W. S.; Bottomley, P. A.; Holland, G. N. *Nature* **1977**, 270, 722.
- (15) Kumar, A.; Welte, D.; Ernst, R. R. *Journal of Magnetic Resonance (1969)* **1975**, 18, 69.
- (16) Harris, R. K.; Grant, D. M. *Methods in Biomedical Magnetic Resonance Imaging and Spectroscopy*; John Wiley & Sons, Inc, 2000; Vol. 1.
- (17) *Magnetic Resonance in Medicine*; 4 ed.; Rinck, P. A., Ed.; Wiley-Blackwell, 2001.
- (18) Canet, D. In *Advances in Inorganic Chemistry*; Academic Press: 2005; Vol. Volume 57, p 3.
- (19) *2007 MRI Market Summary Report*, IMV, Ltd., 2007.
- (20) Aime, S.; Botta, M.; Terreno, E. In *Advances in Inorganic Chemistry*; Academic Press: 2005; Vol. Volume 57, p 173.
- (21) Huang, W.; Tudorica, L. A.; Li, X.; Thakur, S. B.; Chen, Y.; Morris, E. A.; Tagge, I. J.; Korenblit, M. E.; Rooney, W. D.; Koutcher, J. A.; Springer, C. S. *Radiology* **2011**, 261, 394.
- (22) Eisinger, J.; Shulman, R. G.; Blumberg, W. E. *Nature* **1961**, 192, 963.
- (23) Cohn, M.; Leigh, J. S. *Nature* **1962**, 193, 1037.

- (24) Caravan, P.; Ellison, J. J.; McMurry, T. J.; Lauffer, R. B. *Chemical Reviews* **1999**, *99*, 2293.
- (25) Brucher, E.; Sherry, A.; Merbach, A. E., Tóth, E. v., Eds.; John Wiley & Sons: Chichester, 2001, p 243.
- (26) Cacheris, W. P.; Quay, S. C.; Rocklage, S. M. *Magnetic Resonance Imaging* **1990**, *8*, 467.
- (27) Sherry, A. D.; Caravan, P.; Lenkinski, R. E. *Journal of Magnetic Resonance Imaging* **2009**, *30*, 1240.
- (28) Elizondo, G.; Fretz, C. J.; Stark, D. D.; Rocklage, S. M.; Quay, S. C.; Worah, D.; Tsang, Y. M.; Chen, M. C.; Ferrucci, J. T. *Radiology* **1991**, *178*, 73.
- (29) Frydrychowicz, A.; Lubner, M. G.; Brown, J. J.; Merkle, E. M.; Nagle, S. K.; Rofsky, N. M.; Reeder, S. B. *Journal of Magnetic Resonance Imaging* **2012**, *35*, 492.
- (30) Bousquet, J. C.; Saini, S.; Stark, D. D.; Hahn, P. F.; Nigam, M.; Wittenberg, J.; Ferrucci, J. T. *Radiology* **1988**, *166*, 693.
- (31) Shellock, F. G.; Spinazzi, A. *American Journal of Roentgenology* **2008**, *191*, 1129.
- (32) Lanthanide. <http://www.daviddarling.info/encyclopedia/L/lanthanide.html> (accessed June 21st, 2013).
- (33) Kaltsoyannis, N.; Scott, P. *The f elements*; Oxford University Press, Inc.: New York, 1999; Vol. 76.
- (34) Tweedle MF, E. S., Eckelman WC, Gaughan GT, Hagan JJ, Wedeking PW, Yost FJ. *Invest. Radiol.* **1988**, Suppl 1:S236.
- (35) Loncin, M. F.; Desreux, J. F.; Merciny, E. *Inorganic Chemistry* **1986**, *25*, 2646.
- (36) Meyer, D.; Schaefer, M.; Bonnemain, B. *Investigative Radiology* **1988**, *23*.
- (37) Aime, S.; Botta, M.; Ermondi, G. *Inorganic Chemistry* **1992**, *31*, 4291.
- (38) Wang, X.; Jin, T.; Comblin, V.; Lopez-Mut, A.; Merciny, E.; Desreux, J. F. *Inorganic Chemistry* **1992**, *31*, 1095.
- (39) Toth, E.; Brucher, E.; Lazar, I.; Toth, I. *Inorganic Chemistry* **1994**, *33*, 4070.
- (40) Marques, M. P. M.; Geraldès, C. F. G. C.; Sherry, A. D.; Merbach, A. E.; Powell, H.; Pubanz, D.; Aime, S.; Botta, M. *Journal of Alloys and Compounds* **1995**, *225*, 303.
- (41) Viola-Villegas, N.; Doyle, R. P. *Coordination Chemistry Reviews* **2009**, *253*, 1906.
- (42) Boulon, M.-E.; Cucinotta, G.; Luzon, J.; Degl'Innocenti, C.; Perfetti, M.; Bernot, K.; Calvez, G.; Caneschi, A.; Sessoli, R. *Angewandte Chemie International Edition* **2013**, *52*, 350.
- (43) Richman, J. E.; Atkins, T. J. *Journal of the American Chemical Society* **1974**, *96*, 2268.
- (44) Athey, P. S.; Kiefer, G. E. *The Journal of Organic Chemistry* **2002**, *67*, 4081.
- (45) Weisman, G. R.; Reed, D. P. *The Journal of Organic Chemistry* **1996**, *61*, 5186.

- (46) Anet, F. A. L.; Krane, J.; Dale, J.; Daasvatn, K.; Kristiansen, P. O.; Swahn, C.-G. *Acta Chemica Scandinavica* **1973**, *27*, 3395.
- (47) Meyer, M.; Dahaoui-Gindrey, V.; Lecomte, C.; Guillard, R. *Coordination Chemistry Reviews* **1998**, *178–180, Part 2*, 1313.
- (48) Desreux, J. F. *Inorganic Chemistry* **1980**, *19*, 1319.
- (49) Spirlet, M. R.; Rebizant, J.; Desreux, J. F.; Loncin, M. F. *Inorganic Chemistry* **1984**, *23*, 359.
- (50) Aime, S.; Botta, M.; Fasano, M.; Marques, M. P. M.; Geraldès, C. F. G. C.; Pubanz, D.; Merbach, A. E. *Inorganic Chemistry* **1997**, *36*, 2059.
- (51) Hermann, P.; Kotek, J.; Kubicek, V.; Lukes, I. *Dalton Transactions* **2008**, 3027.
- (52) Jacques, V.; Desreux, J. F. *Inorganic Chemistry* **1994**, *33*, 4048.
- (53) Woods, M.; Botta, M.; Avedano, S.; Wang, J.; Sherry, A. D. *Dalton Transactions* **2005**, 3829.
- (54) Ishiguchi, T.; Takahashi, S. *Drugs in R&D* **2010**, *10*, 133.
- (55) Solomon, I. *Physical Review* **1955**, *99*, 559.
- (56) Solomon, I.; Bloembergen, N. *The Journal of Chemical Physics* **1956**, *25*, 261.
- (57) Bloembergen, N. *The Journal of Chemical Physics* **1957**, *27*, 572.
- (58) Morgan, L. O.; Nolle, A. W. *The Journal of Chemical Physics* **1959**, *31*, 365.
- (59) Bloembergen, N.; Morgan, L. O. *Journal of Chemical Physics* **1961**, *34*, 842.
- (60) Bertini, I.; Luchinat, C. *NMR of Paramagnetic Molecules in Biological Systems*; Benjamin/Cummings: Menlo Park, CA, 1986.
- (61) Lauffer, R. B. *Chemical Reviews* **1987**, *87*, 901.
- (62) Chen, J. W.; Belford, R. L.; Clarkson, R. B. *The Journal of Physical Chemistry A* **1998**, *102*, 2117.
- (63) Datta, A.; Raymond, K. N. *Accounts of Chemical Research* **2009**, *42*, 938.
- (64) Aime, S.; Calabi, L.; Cavallotti, C.; Gianolio, E.; Giovenzana, G. B.; Losi, P.; Maiocchi, A.; Palmisano, G.; Sisti, M. *Inorganic Chemistry* **2004**, *43*, 7588.
- (65) Moreau, G.; Helm, L.; Purans, J.; Merbach, A. E. *The Journal of Physical Chemistry A* **2002**, *106*, 3034.
- (66) Laus, S.; Ruloff, R.; Tóth, É.; Merbach, A. E. *Chemistry – A European Journal* **2003**, *9*, 3555.
- (67) Nicolle, G. M.; Yerly, F.; Imbert, D.; Böttger, U.; Bünzli, J.-C.; Merbach, A. E. *Chemistry – A European Journal* **2003**, *9*, 5453.
- (68) Lincoln, S. F.; Merbach, A. E. In *Advances in Inorganic Chemistry*; Sykes, A. G., Ed.; Academic Press: 1995; Vol. Volume 42, p 1.
- (69) Koenig, S. H.; Schillinger, W. E. *Journal of Biological Chemistry* **1969**, *244*, 3283.
- (70) Stephens, E. M.; Grisham, C. M. *Biochemistry* **1979**, *18*, 4876.

- (71) Powell, D. H.; Merbach, A. E.; González, G.; Brücher, E.; Micskei, K.; Ottaviani, M. F.; Köhler, K.; Von Zelewsky, A.; Grinberg, O. Y.; Lebedev, Y. S. *Helvetica Chimica Acta* **1993**, *76*, 2129.
- (72) Aime, S.; Botta, M.; Fasano, M.; Terreno, E. *Chemical Society Reviews* **1998**, *27*, 19.
- (73) Powell, D. H.; Dhubhghaill, O. M. N.; Pubanz, D.; Helm, L.; Lebedev, Y. S.; Schlaepfer, W.; Merbach, A. E. *Journal of the American Chemical Society* **1996**, *118*, 9333.
- (74) Benmelouka, M.; Borel, A.; Moriggi, L.; Helm, L.; Merbach, A. E. *The Journal of Physical Chemistry B* **2007**, *111*, 832.
- (75) Senn, F.; Helm, L.; Borel, A.; Daul, C. A. *Comptes Rendus Chimie* **2012**, *15*, 250.
- (76) Caravan, P.; Farrar, C. T.; Frullano, L.; Uppal, R. *Contrast Media & Molecular Imaging* **2009**, *4*, 89.
- (77) Tóth, E. v.; Helm, L.; Merbach, A. E.; Wiley: New York, 2001, p 45.
- (78) Sherry, A. D.; Wu, Y. *Current Opinion in Chemical Biology* **2013**, *17*, 167.
- (79) Werner, E. J.; Datta, A.; Jocher, C. J.; Raymond, K. N. *Angewandte Chemie International Edition* **2008**, *47*, 8568.
- (80) Terreno, E.; Castelli, D. D.; Viale, A.; Aime, S. *Chemical Reviews* **2010**, *110*, 3019.
- (81) Muller, R. N.; Elst, L. V.; Rinck, P. A.; Vallet, P.; Maton, F.; Fischer, H.; Roch, A.; Haverbeke, Y. V. *Investigative Radiology* **1988**, *23*.
- (82) Bertini, I.; Luchinat, C.; Parigi, G. In *Advances in Inorganic Chemistry*; Academic Press: 2005; Vol. Volume 57, p 105.
- (83) Banci, L.; Bertini, I.; Luchinat, C. *Inorganica Chimica Acta* **1985**, *100*, 173.
- (84) Strandberg, E.; Westlund, P.-O. *Journal of Magnetic Resonance, Series A* **1996**, *122*, 179.
- (85) Horrocks, W. D.; Sudnick, D. R. *Accounts of Chemical Research* **1981**, *14*, 384.
- (86) Beeby, A.; M. Clarkson, I.; S. Dickins, R.; Faulkner, S.; Parker, D.; Royle, L.; S. de Sousa, A.; A. Gareth Williams, J.; Woods, M. *Journal of the Chemical Society, Perkin Transactions 2* **1999**, 493.
- (87) Alpoim, M. C.; Urbano, A. M.; Geraldès, C. F. G. C.; Peters, J. A. *Journal of the Chemical Society, Dalton Transactions* **1992**.
- (88) Koenig, S. H.; Brown Iii, R. D. *Progress in Nuclear Magnetic Resonance Spectroscopy* **1990**, *22*, 487.
- (89) Frey, U.; Merbach, A. E.; Powell, D. H.; Delpuech, J.-J., Ed.; John Wiley & Sons Ltd.: Chichester, 1995, p 263.
- (90) Zech, S. G.; Eldredge, H. B.; Lowe, M. P.; Caravan, P. *Inorganic Chemistry* **2007**, *46*, 3576.
- (91) Rast, S.; Borel, A.; Helm, L.; Belorizky, E.; Fries, P. H.; Merbach, A. E. *Journal of the American Chemical Society* **2001**, *123*, 2637.

- (92) Astashkin, A. V.; Raitsimring, A. M.; Caravan, P. *The Journal of Physical Chemistry A* **2004**, *108*, 1990.
- (93) Moreau, J.; Guillon, E.; Aplincourt, P.; Pierrard, J.-C.; Rimbault, J.; Port, M.; Aplincourt, M. *European Journal of Inorganic Chemistry* **2003**, *2003*, 3007.
- (94) Aime, S.; Botta, M.; Ermondi, G. *Journal of Magnetic Resonance (1969)* **1991**, *92*, 572.
- (95) Rooney, W. D.; Johnson, G.; Li, X.; Cohen, E. R.; Kim, S.-G.; Ugurbil, K.; Springer, C. S. *Magnetic Resonance in Medicine* **2007**, *57*, 308.
- (96) Dirac, P. A. M. *Proceedings of the Royal Society of London. Series A* **1928**, *117*, 610.
- (97) Peters, J. A.; Huskens, J.; Raber, D. J. *Progress in Nuclear Magnetic Resonance Spectroscopy* **1996**, *28*, 283.
- (98) Bleaney, B. *Journal of Magnetic Resonance (1969)* **1972**, *8*, 91.
- (99) Golding, R. M.; Halton, M. P. *Australian Journal of Chemistry* **1972**, *25*, 2577.
- (100) Piguet, C.; Geraldes, C. F. G. C. In *Handbook on the Physics and Chemistry of Rare Earths*; Gschneidner, K. A., Bünzli, J.-C., Pecharsky, V. K., Eds.; Elsevier: 2003; Vol. Volume 33, p 353.
- (101) Bleaney, B.; Dobson, C. M.; Levine, B. A.; Martin, R. B.; Williams, R. J. P.; Xavier, A. V. *Journal of the Chemical Society, Chemical Communications* **1972**, 791b.
- (102) Horrocks, W. D.; Sipe, J. P. *Journal of the American Chemical Society* **1971**, *93*, 6800.
- (103) Reuben, J. *Journal of Magnetic Resonance (1969)* **1982**, *50*, 233.
- (104) Muller, G.; Kean, S. D.; Parker, D.; Riehl, J. P. *The Journal of Physical Chemistry A* **2002**, *106*, 12349.
- (105) Dickins, R. S.; Parker, D.; Bruce, J. I.; Tozer, D. J. *Dalton Transactions* **2003**, 1264.
- (106) Borel, A.; Bean, J. F.; Clarkson, R. B.; Helm, L.; Moriggi, L.; Sherry, A. D.; Woods, M. *Chemistry – A European Journal* **2008**, *14*, 2658.
- (107) Ren, J.; Zhang, S.; Sherry, A. D.; Geraldes, C. F. G. C. *Inorganica Chimica Acta* **2002**, *339*, 273.
- (108) Platas-Iglesias, C. *European Journal of Inorganic Chemistry* **2012**, *2012*, 2023.
- (109) Di Pietro, S.; Piano, S. L.; Di Bari, L. *Coordination Chemistry Reviews* **2011**, *255*, 2810.
- (110) Horrocks, W. D.; Schmidt, G. F.; Sudnick, D. R.; Kittrell, C.; Bernheim, R. A. *Journal of the American Chemical Society* **1977**, *99*, 2378.
- (111) Horrocks, W. D.; Sudnick, D. R. *Journal of the American Chemical Society* **1979**, *101*, 334.

- (112) Beeby, A.; S. Dickins, R.; Faulkner, S.; Parker, D.; A. Gareth Williams, J. *Chemical Communications* **1997**, 0, 1401.
- (113) Parker, D.; Williams, J. A. G. *Journal of the Chemical Society, Dalton Transactions* **1996**, 0, 3613.
- (114) Dickins, R. S.; Howard, J. A. K.; Lehmann, C. W.; Moloney, J.; Parker, D.; Peacock, R. D. *Angewandte Chemie International Edition in English* **1997**, 36, 521.
- (115) A. K. Howard, J.; M. Kenwright, A.; M. Moloney, J.; Parker, D.; Woods, M.; Port, M.; Navet, M.; Rousseau, O. *Chemical Communications* **1998**, 1381.
- (116) Swift, T. J.; Connick, R. E. *Journal of Chemical Physics* **1962**, 37, 307.
- (117) Swift, T. J.; Connick, R. E. *The Journal of Chemical Physics* **1964**, 41, 2553.
- (118) McConnell, H. M. *The Journal of Chemical Physics* **1958**, 28, 430.
- (119) Southwood-Jones, R. V.; Earl, W. L.; Newman, K. E.; Merbach, A. E. *The Journal of Chemical Physics* **1980**, 73, 5909.
- (120) Micskei, K.; Powell, D. H.; Helm, L.; Brücher, E.; Merbach, A. E. *Magnetic Resonance in Chemistry* **1993**, 31, 1011.
- (121) Gonzalez, G.; Powell, D. H.; Tissieres, V.; Merbach, A. E. *The Journal of Physical Chemistry* **1994**, 98, 53.
- (122) Dunand, F. A.; Borel, A.; Merbach, A. E. *Journal of the American Chemical Society* **2002**, 124, 710.
- (123) Aime, S.; Barbero, L.; Botta, M.; Ermondi, G. *Journal of the Chemical Society, Dalton Transactions* **1992**, 0, 225.
- (124) Bénazeth, S.; Purans, J.; Chalbot, M.-C.; Nguyen-van-Duong, M. K.; Nicolas, L.; Keller, F.; Gaudemer, A. *Inorganic Chemistry* **1998**, 37, 3667.
- (125) Rudovský, J.; Cígler, P.; Kotecký, J.; Hermann, P.; Vojtíšek, P.; Lukeš, I.; Peters, J. A.; Vander Elst, L.; Muller, R. N. *Chemistry – A European Journal* **2005**, 11, 2373.
- (126) Werner, E. J.; Avedano, S.; Botta, M.; Hay, B. P.; Moore, E. G.; Aime, S.; Raymond, K. N. *Journal of the American Chemical Society* **2007**, 129, 1870.
- (127) Rodríguez-Rodríguez, A.; Esteban-Gómez, D.; de Blas, A.; Rodríguez-Blas, T.; Fekete, M.; Botta, M.; Tripier, R.; Platas-Iglesias, C. *Inorganic Chemistry* **2012**, 51, 2509.
- (128) Laus, S.; Sour, A.; Ruloff, R.; Tóth, É.; Merbach, A. E. *Chemistry – A European Journal* **2005**, 11, 3064.
- (129) Rudovský, J.; Botta, M.; Hermann, P.; Hardcastle, K. I.; Lukeš, I.; Aime, S. *Bioconjugate Chemistry* **2006**, 17, 975.
- (130) Aime, S.; Botta, M.; Fasano, M.; Terreno, E. *Accounts of Chemical Research* **1999**, 32, 941.
- (131) Aime, S.; Barge, A.; Bruce, J. I.; Botta, M.; Howard, J. A. K.; Moloney, J. M.; Parker, D.; de Sousa, A. S.; Woods, M. *Journal of the American Chemical Society* **1999**, 121, 5762.

- (132) Woods, M.; Aime, S.; Botta, M.; Howard, J. A. K.; Moloney, J. M.; Navet, M.; Parker, D.; Port, M.; Rousseaux, O. *Journal of the American Chemical Society* **2000**, *122*, 9781.
- (133) Pierrard, J.-C.; Rimbault, J.; Aplincourt, M.; Le Greneur, S.; Port, M. *Contrast Media & Molecular Imaging* **2008**, *3*, 243.
- (134) Häussinger, D.; Huang, J.-r.; Grzesiek, S. *Journal of the American Chemical Society* **2009**, *131*, 14761.
- (135) Brittain, H. G.; Desreux, J. F. *Inorganic Chemistry* **1984**, *23*, 4459.
- (136) Comblin, V.; Gilsoul, D.; Hermann, M.; Humblet, V.; Jacques, V.; Mesbahi, M.; Sauvage, C.; Desreux, J. F. *Coordination Chemistry Reviews* **1999**, *185-186*, 451.
- (137) Woods, M.; Kovacs, Z.; Zhang, S.; Sherry, A. D. *Angewandte Chemie International Edition* **2003**, *42*, 5889.
- (138) Bottrill, M.; Kwok, L.; Long, N. J. *Chemical Society Reviews* **2006**, *35*, 557.
- (139) Lauffer, R. B.; Parmelee, D. J.; Dunham, S. U.; Ouellet, H. S.; Dolan, R. P.; Witte, S.; McMurry, T. J.; Walovitch, R. C. *Radiology* **1998**, *207*, 529.
- (140) Muller, R. N.; Radüchel, B.; Laurent, S.; Platzek, J.; Piérart, C.; Mareski, P.; Vander Elst, L. *European Journal of Inorganic Chemistry* **1999**, *1999*, 1949.
- (141) Caravan, P.; Cloutier, N. J.; Greenfield, M. T.; McDermid, S. A.; Dunham, S. U.; Bulte, J. W. M.; Amedio, J. C.; Looby, R. J.; Supkowski, R. M.; Horrocks, W. D.; McMurry, T. J.; Lauffer, R. B. *Journal of the American Chemical Society* **2002**, *124*, 3152.
- (142) Zhou, X.; Caravan, P.; Clarkson, R. B.; Westlund, P.-O. *Journal of Magnetic Resonance* **2004**, *167*, 147.
- (143) Løkling, K.-E.; Fosshem, S. L.; Klaveness, J.; Skurtveit, R. *Journal of Controlled Release* **2004**, *98*, 87.
- (144) Gianolio, E.; Porto, S.; Napolitano, R.; Baroni, S.; Giovenzana, G. B.; Aime, S. *Inorganic Chemistry* **2012**, *51*, 7210.
- (145) Kielar, F.; Tei, L.; Terreno, E.; Botta, M. *Journal of the American Chemical Society* **2010**, *132*, 7836.
- (146) Polášek, M.; Hermann, P.; Peters, J. A.; Geraldès, C. F. G. C.; Lukeš, I. *Bioconjugate Chemistry* **2009**, *20*, 2142.
- (147) Botta, M.; Tei, L. *European Journal of Inorganic Chemistry* **2012**, *2012*, 1945.
- (148) Kobayashi, H.; Brechbiel, M. W. *Advanced Drug Delivery Reviews* **2005**, *57*, 2271.
- (149) Tweedle, M. F.; Eaton, S. M.; Eckelman, W. C.; Gaughan, G. T.; Hagan, J. J.; Wedeking, P. W.; Yost, F. J. *Investigative Radiology* **1988**, *23*.
- (150) Nicolle, G. M.; Helm, L.; Merbach, A. E. *Magnetic Resonance in Chemistry* **2003**, *41*, 794.
- (151) Gianolio, E.; Giovenzana, G. B.; Longo, D.; Longo, I.; Menegotto, I.; Aime, S. *Chemistry – A European Journal* **2007**, *13*, 5785.

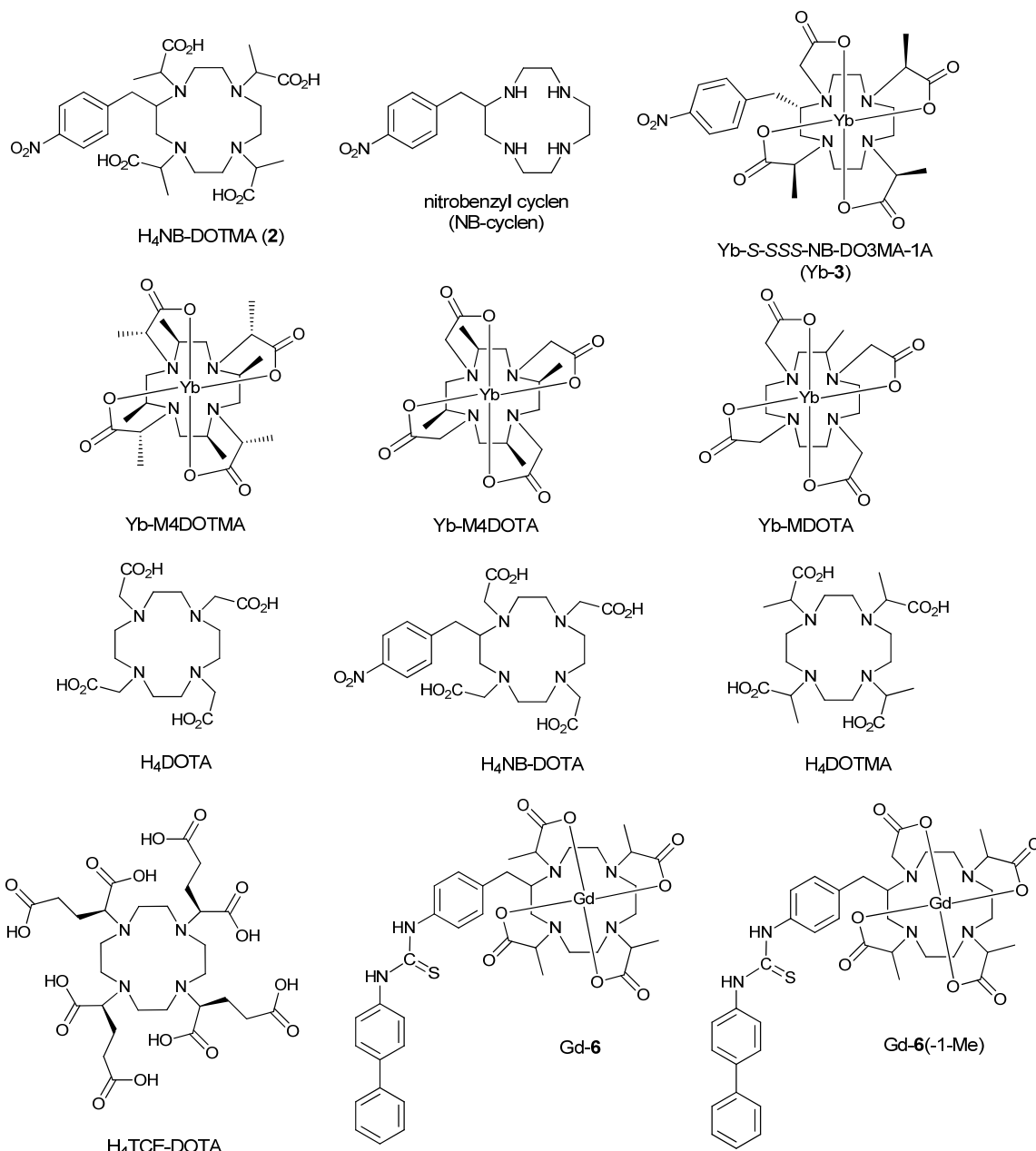
- (152) Bornhop, D. J.; Hubbard, D. S.; Houlne, M. P.; Adair, C.; Kiefer, G. E.; Pence, B. C.; Morgan, D. L. *Analytical Chemistry* **1999**, *71*, 2607.
- (153) Sarka, L.; Burai, L.; Brücher, E. *Chemistry – A European Journal* **2000**, *6*, 719.
- (154) White, G. W.; Gibby, W. A.; Tweedle, M. F. *Invest Radiol* **2006**, *41*, 272.
- (155) Aime, S.; Caravan, P. *Journal of Magnetic Resonance Imaging* **2009**, *30*, 1259.
- (156) Avedano, S.; Botta, M.; Haigh, J.; Longo, D.; Woods, M. *Inorganic Chemistry* **2013**, *52*, 8436.



**CHAPTER 2. REGIOISOMERISM IN CONFORMATIONALLY RIGID NB-DOTA-TYPE CHELATES**

***2.1 Utility of conformationally rigid chelates for probing subtle, structurally related differences in solution behavior***

Most studies of contrast agents and prototypical agents have been performed on chelates that undergo conformational exchange. The presence of multiple conformational isomers and coordination geometries makes it difficult or impossible to separate the effects of the various structural contributions to the relaxation properties of the compound of interest.<sup>1</sup> It is often the case that the properties which govern relaxivity can only be determined as weighted averages in the case of a sample with two or more isomers. Deconvolution of these weighted averages requires that we know the distribution of coordination isomers, which is not always possible. It has been found that many important properties of Gd<sup>3+</sup> chelates differ greatly between conformational and geometric isomers. Isomer ratios and rates of interconversion can be heavily dependent on temperature<sup>2</sup>, solvent<sup>3</sup>, pH<sup>4</sup>, counter ion<sup>5</sup>, and concentration. In order to understand the relationship between structure and MRI-relevant properties in detail, it is advantageous to use conformationally rigid Ln<sup>3+</sup> chelates for which it is possible to extract small differences between fully resolved, isomeric structures. The arm- and ring-substituted DOTA derivative Ln[NB-DOTMA]<sup>-</sup> (**2**) (in Scheme 2.1), which is characterized by a single coordination geometry and rapid water exchange<sup>6</sup>, is the focus of these studies.



**Scheme 2.1:** Structures of ligands and chelates referenced in this chapter

The nitrobenzyl (NB) group is an important modification to the DOTA scaffold due to its ability to “lock” the helicity of the macrocyclic ring. In addition, the nitro group can be converted to the isothiocyanate *via* facile synthesis without affecting the rest of the chelate, enabling the attachment of a covalent linker that can bind to a macromolecular

target. This functionizable group allows for a “bifunctional” chelate – one with relaxivity enhancing and targeted binding potential.<sup>7,8</sup> When a prototypical agent binds to a macromolecular target,  $\tau_R$  should increase as described above.<sup>9,10</sup> This binding interaction slows molecular tumbling for the agent and increases accumulation of the agent, producing greater contrast per total injected dose at the site of interest. Because of its aromaticity, the nitrobenzyl group is also useful as a chromatographic handle throughout synthesis and purification. An aromatic ring can act as an “antenna” for directing lanthanide luminescence (another potential way of generating contrast *in vivo*) as well.<sup>11,12</sup>

## ***2.2 Rationalizing the appearance of multiple isomers in a conformationally rigid chelate of single stereochemistry***

In the synthesis of Ln-*S-RRRR-2*, the arm- and ring-substitution locks the chelate into only one coordination geometry. If the ligand is *S-RRRR*, only the SAP geometry should be possible. It was expected that only one isomer would be obtained, yet two isomers of Yb-*S-RRRR-2* were isolated by HPLC purification.<sup>13,14</sup> These isomers had identical mass and elemental analyses. NMR spectra for the two isomers had peaks in the  $ax^S$  region indicating SAP geometry (Figure 2.1).

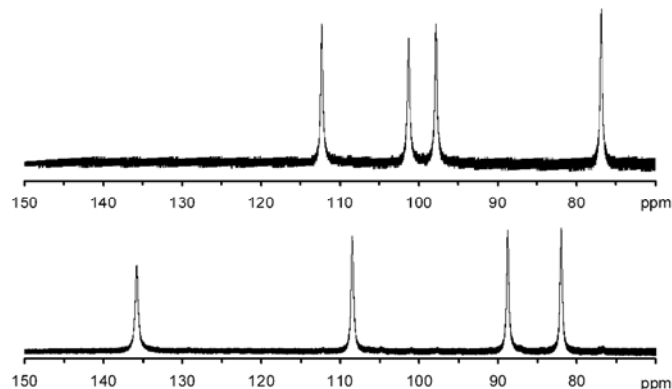
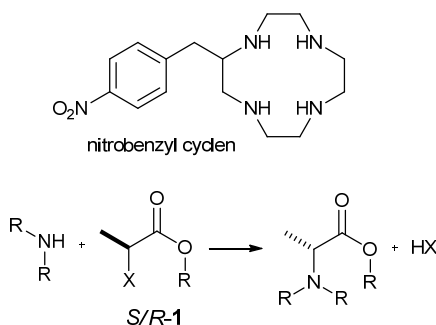


**Figure 2.1:** Partial  $^1\text{H}$  NMR spectra of the two isomers of Yb-S-RRRR-2 showing the  $ax^S$  resonances. Both spectra have  $ax^S$  shifts which indicate SAP geometry.

In the synthesis of **2** (Scheme 2.2), alkylation of the amines in NB-cyclen is accomplished by nucleophilic substitution on the  $\alpha$ -carbon of an ester. This substitution proceeds *via* an  $S_N2$  reaction and complete inversion of configuration at this carbon, i.e. an *R*- configuration of the alkylating agent (**1**) is required to form SSSS-**2**.

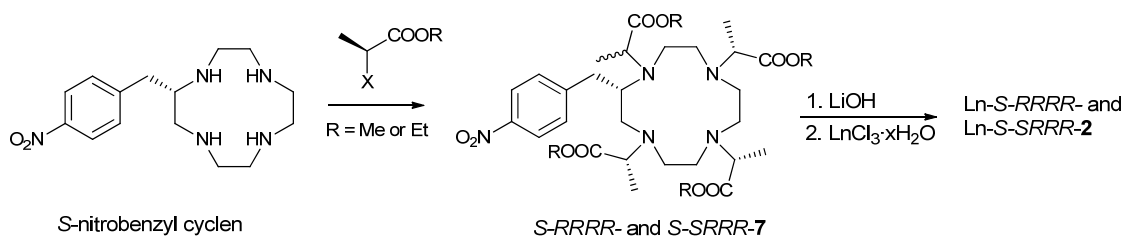


**Scheme 2.2:** Nucleophilic substitution to alkylate nitrobenzyl cyclen amine groups during synthesis of **2**, X=leaving group (bromide or triflate)

NB-cyclen will react to form only the tri-alkylated macrocycle with four equivalents of alkylating agent **1**, even with a triflate (a highly labile leaving group), if the reaction is performed at room temperature. To yield the tetra-alkylated product, extended heating

and reaction times are required. The nitrogen in the 1-position is the poorest nucleophile due to steric crowding from the nearby NB substituent, possibly giving the substitution at that position more  $S_N1$  character. In these syntheses of **2**, two isomers of the tetraester precursor **7** (Scheme 2.3) were identified by NMR and could not be separated at this stage. The authors modified the synthetic procedures leading to Yb-S-RRRR-**2** by changing the leaving group for *N*-alkylation and changing the solvent, but two isomers were obtained in each case.

In this same work<sup>14</sup>, it was speculated that racemization (of the chiral carbon on the (2-methyl)acetate arm adjacent to the NB group) occurred during ligand synthesis, leading to the observation of two isomeric chelates, assigned as Yb-S-RRRR- and Yb-S-SRRR-NB-DOTMA (Scheme 2.3).



**Scheme 2.3:** Racemization of a (2-methyl)acetate arm leading to two chelates, X = Br, OTf

To overcome this synthetic challenge, a ligand (**3**) without the potential for stereoisomerism in the 1-*N* position was synthesized and its  $\text{Ln}^{3+}$  chelates were prepared. Only 3 pendant arms are required to have appropriate chiral substituents to lock the coordination geometry.<sup>15</sup> Both *S*-SSS- and *S*-RRR-**3** were synthesized and did not show multiple isomers at the time of publication.

Due to the apparent poor nucleophilicity of the 1-aza position, racemization was put forth as the likeliest explanation for the observation of two isomeric chelates, where matters stayed until we revisited Ln-2 in this work.

### *2.3 Structural characterization of regioisomeric chelates by correlational NMR spectroscopy (COSY)*

Recent observations have led us to question the racemization explanation. A previous study on isomers of Yb-2 noted that for the isomer previously assigned as the *S*-RSSS isomer, the NB group appeared to be located on a carbon on the side of the ring based on 2D NMR and modeling data.<sup>16</sup> Analysis of the COSY NMR spectra of resolved Yb-2 isomers showed that axial protons were missing an expected geminal couple to a proton on a carbon on the corner and on a carbon on the side of the macrocyclic ring, respectively. Unfortunately, a complete assignment of the cross peaks of both isomers was not made in previous studies of Yb-2. Additionally, later syntheses of Ln-3 afforded two isomers of single coordination geometry (unpublished data).

#### *2.3.1 Previous studies of two-dimensional NMR spectra of arm- and ring-substituted DOTA-type chelates*

Crystallography is a convenient method for understanding conformation and structure. To probe the nature of the two isomers directly, it would be beneficial to examine crystal structures of the resolved chelates. However, crystal structures of NB-DOTA or NB-DOTMA chelates have never been obtained; these ligands and their chelates could not be induced to crystallize. Instead, they form amorphous solids. Nonetheless, a great deal of

structural information can be extracted from the NMR spectra of conformationally rigid chelates in solution.

Desreux and colleagues proposed the existence of regioisomers for structures of conformationally rigid chelates.<sup>17</sup> Chelates of the highly rigid, symmetric ligand M4DOTMA were synthesized. The substitutions of each type of ring proton with a methyl substituent group were modeled individually and the lowest-energy conformations were determined. The methyl group could occupy an equatorial position either on the corner or the side of the ring, but the difference in energies between these indicated only 1 species should be observed in solution. The correlational NMR spectroscopy (COSY) spectrum of Yb-M4DOTMA includes only one peak for each type of ring substituent (3 proton peaks and a peak for the methyl group) and arm substituent (1 proton on the arm and 1 peak for the methyl arm substituent). This indicates that only one isomer is present. In the spectrum of YbM4DOTA, the two geometries available (due to ring inversion) appear. The peaks for these structures broaden and coalesce as the temperature is increased. No cross-coupling peaks between the two sets of resonances are observed. These spectral features show that the structures are distinct from one another but interconvert, and that the rate of exchange is fast on the NMR time-scale at elevated temperatures. The methyl arms on the ring are assigned as being positioned in the *eq* corner position. However, a third set of shifts is apparent in the spectrum of YbM4DOTA that are not in exchange with the shifts of the first two structures. This spectrum is assigned as having the arm substituents in the *eq* side position. Isomers with

*eq* substitution on the corner and side were observed in the spectrum of YbMDOTA as well.

An alternative explanation for the production of two isomers of Yb-*S-RRRR-2* is as follows. On the cyclen ring, the configuration of the NB carbon is *S*-, and the more favorable conformation ( $\delta\delta\delta\delta$ ) places the large ring substituent into an equatorial position. There are two chemically distinct carbon atoms in a 12-*N*-4 crown, carbons on the corner and carbons on the side of the ring. The equatorial protons on both the carbons on the corner and the side of the [3333] macrocyclic ring are pro-*S* in a  $\delta\delta\delta\delta$  conformation. This means that a ring substituent of single configuration could occupy one of two chemically distinct positions and still adopt an equatorial conformation (Figure 2.2). Thus, for any singly substituted cyclen there are two possible *regioisomeric* structures, referred to hereafter as corner and side isomers of Ln-**2** (Figure 2.3).



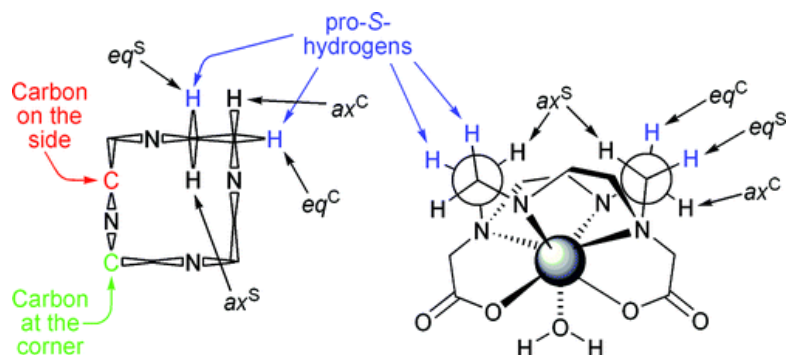


**Figure 2.2:** Two possible sites of ring substitution, both pro-S. eq = equatorial proton, ax = axial. For example, an equatorial proton on a carbon on the side of the ring is abbreviated eq<sup>S</sup>

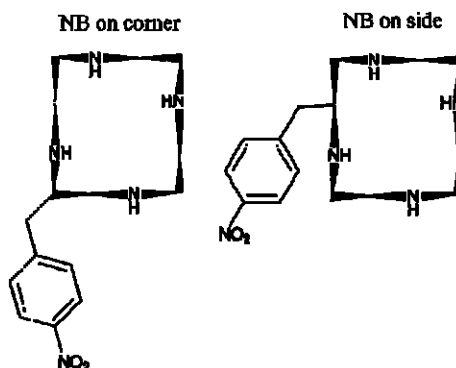


**Figure 2.3:** Two possible arrangements for the macrocyclic ring in 2

The substituent group positioned equatorially on a “corner carbon” would be evident from a lack of proton-proton coupling to the axial proton on that same carbon – the  $ax^C$  proton would not show a geminal coupling when characterized by COSY. One of the challenges in acquiring NMR spectra, particularly 2-dimensional spectra, of  $Ln^{3+}$  chelates, is the extraordinarily large frequency range of the resulting proton shifts. This large spectral window necessitates scanning parameters that limit the signal-to-noise for coupling peaks of interest.  $Eu^{3+}$  gives rise to relatively sharp line-widths and a narrow frequency range of  $^1H$  shifts in its chelates compared with other lanthanides. A more

complete structural characterization by NMR of individually purified isomers of Eu-**2** was undertaken in this work. This work demonstrates evidence supporting structures with the substituents positioned in both corner and side *eq* positions as described in the work of Desreux and colleagues.<sup>18</sup>

### *2.3.2 Structural characterization of isomeric Eu-S-SSSS-2 chelates by correlational spectroscopy (COSY)*

Eu-S-SSSS-**2** was prepared according to the literature procedures<sup>14</sup> and the two isomers produced were resolved by HPLC. Mass spectrometry was used to confirm that both compounds had the same molecular mass and <sup>1</sup>H NMR was used to confirm that both isomers had  $\alpha\chi^S$  shifts indicative of TSAP geometry. COSY spectra were acquired for the two isomers of Eu-S-SSSS-**2** at 278.15 (in the figures that follow) and 313.15 K (data not shown) at 600 MHz. The wider spectral window of the low temperature data more readily allows for analysis of individual shifts and their cross-peaks, and is presented here. The COSY spectrum of the major isomer of Eu-S-SSSS-**2** is shown in Figure 2.4.

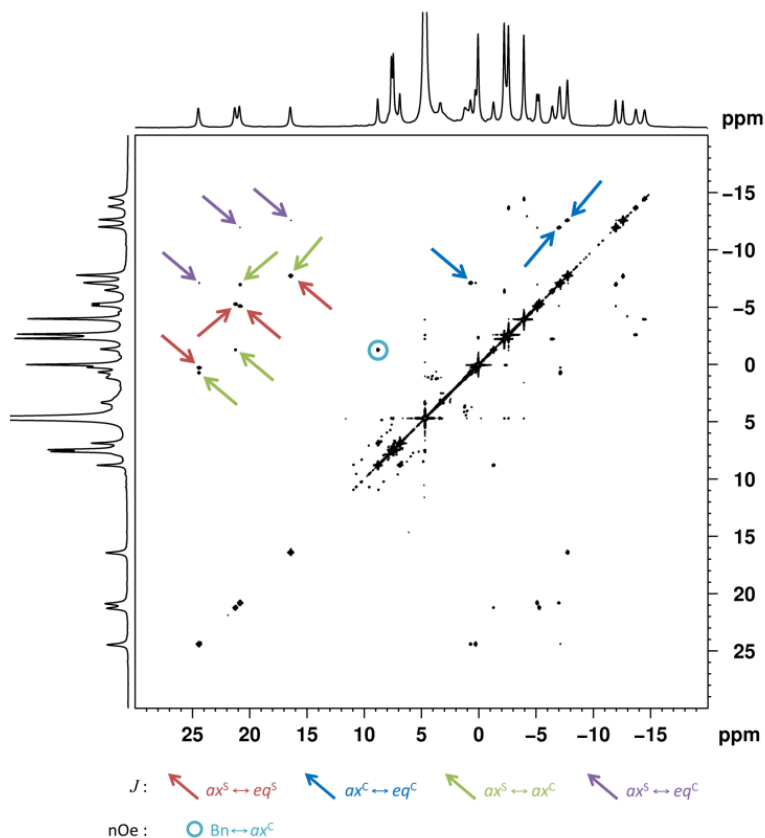


**Figure 2.4:** COSY spectrum of the major isomer of Eu-S-SSSS-2. Off-diagonal peaks indicate through-bond proton-proton coupling ( $J$ -coupling). Cross-peaks assigned to coupling of the same type of protons are indicated by the same colored arrow. Peaks that cannot be explained by  $J$ -coupling are circled.

Assignments for the cross-peaks in the spectrum of the major isomer of Eu-S-SSSS-2 (Figure 2.4) were made as follows. For Eu-S-SSSS-2, it could not be determined which ethylene bridge a given set of shifts corresponded to as there is no cross-coupling observed through the nitrogens on the macrocyclic ring. We can, however, group the protons for a particular bridge together – each ring proton has a distinct shift owing to the asymmetry ( $C_1$ ) of the chelate. The axial side ( $ax^S$ ) protons exhibit the greatest downfield shift in the spectrum due to their position close to the  $z$ -axis of the electron paramagnetic

field. Each axial proton on an ethylene bridge can experience  $J$ -coupling to the other three protons: one each with the other axial and the two equatorial protons. The starting point for the assignment of all cross-peaks begins with  $J$ -coupling to the  $ax^S$  peaks. The geminal ( $^2J$ ) couplings are the strongest (red arrows), so the most intense cross-peaks correspond to coupling of the  $ax^S$  protons with the equatorial side protons ( $eq^S$ ). The next strongest cross peaks are  $ax^S$ - $ax^C$  (axial proton on a corner carbon, green arrows) based on the Karplus relationship.<sup>19</sup> The H-C-C-H angle between axial protons approaches  $180^\circ$  giving a strong vicinal coupling.

The least intense cross-peaks correspond to coupling of the  $ax^S$  protons to the equatorial proton on a corner carbon ( $eq^C$ ) protons (purple arrows). The  $ax^C$ - $eq^C$  couplings (blue arrows) are assigned based on the cross-peaks from  $ax^S$  to  $ax^C$  and  $eq^C$ , respectively, and have intensities similar to the  $ax^S$ - $eq^S$  peaks, which have already been assigned. For the NB group, the two peaks for  $p$ -substituted aromatic protons are identified by their slight downfield shift,  $^3J$  coupling to one another, and relative integration area of two. The two peaks for the benzylic protons (1H,  $^2J$ ) are identified on the basis of shift as well. The methyl peaks on the pendant arms are identified by their number (4) and relative integration areas (3). Each methyl proton is vicinally coupled to its corresponding  $ac$  proton. One of the  $ax^C$  resonances should have a  $^2J$  coupling (to an equatorial proton on a corner carbon) which is notably absent. This observation is consistent with an  $eq^C$  proton having been replaced by the  $S$ -nitrobenzyl substituent.

Some peaks were observed in the spectrum that could not be assigned to through-bond cross-coupling. Under certain conditions in COSY spectroscopy, cross-peaks are observed due to the nuclear Overhauser effect (NOE). The NOE arises from dipole-dipole interactions between nuclei close together in space. For a system of two nuclei  $\alpha$  and  $\beta$ , there are multiple possible transitions between nuclear spin states (Figure 2.5).

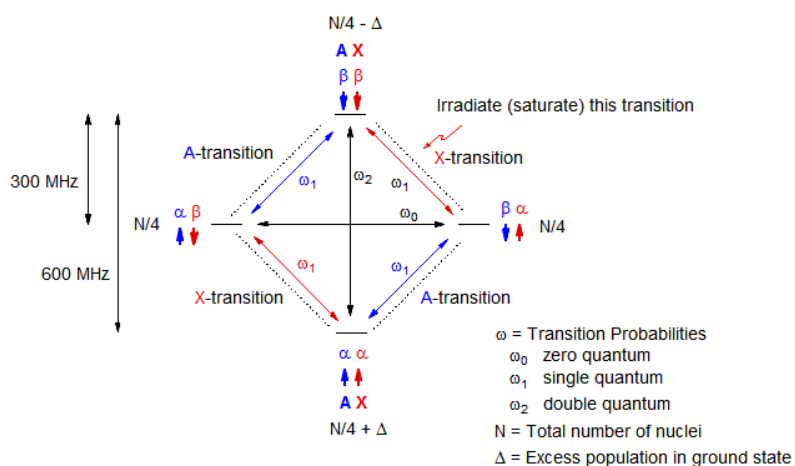


**Figure 2.5:** Transitions between nuclear spin states which may give rise to NMR peaks due to the nuclear Overhauser effect<sup>20</sup>

Each nucleus can have its spin state aligned parallel or antiparallel to the main magnetic field, resulting in four possible populations – one each with both states parallel and both states antiparallel, and two states where the nuclei are oppositely aligned. Upon irradiation with an RF pulse with sufficient energy to excite the transition, one nucleus could flip the direction of its spin, leaving the other unchanged (illustrated by  $\omega_1$ , a single quantum transition). At a different RF frequency, a transition could be excited where the two nuclei each flip the alignment of their spin momenta (illustrated by  $\omega_0$  or  $\omega_2$ , either a net zero quantum transition or a double quantum transition). If the incidences of  $\omega_0$  and

$\omega_2$  are unequal, and if the dipolar interactions between these two nuclei are the dominant  $T_1$  relaxation pathway, NOE peaks can be observed in an NMR spectrum. The large frequency range of the COSY spectra of Eu-*S*-SSSS-2 increases the chances that RF pulses include the energies leading to the available transitions. The cross peaks arising from the NOE are through-space interactions indicating protons which are proximal yet not closely connected through bonds. The presence of a peak resulting from through-space interaction of a coupled  $ax^C$  proton and a benzyl proton (circled in teal) is one such NOE peak. This peak indicates a close spatial relationship between the substituted corner carbon and the NB group.

There are key differences between the COSY spectrum in Figure 2.4 and the spectrum in Figure 2.6, which was acquired for the minor isomer of Eu-*S*-SSSS-2.

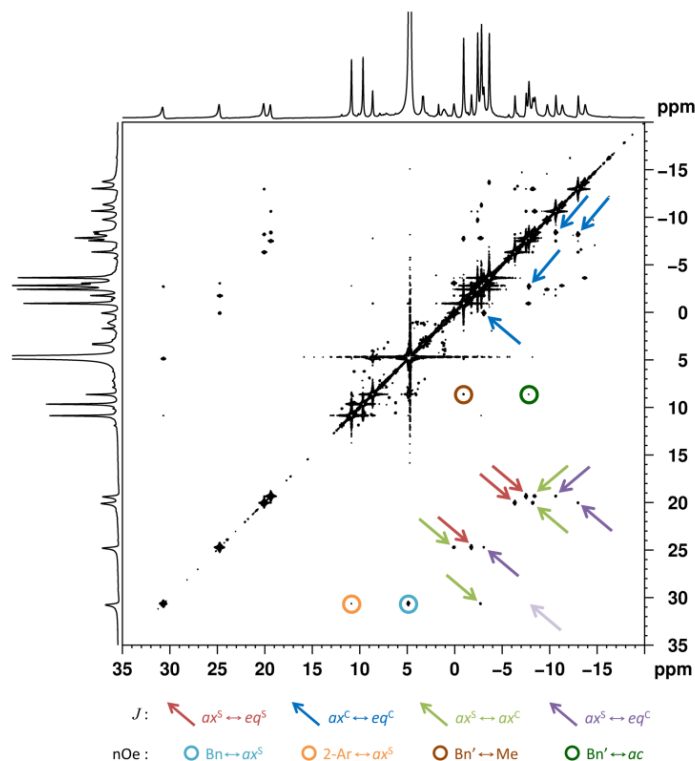


**Figure 2.6:** COSY spectrum of the minor isomer of Eu-S-SSSS-2. Off-diagonal peaks indicate through-bond proton-proton coupling ( $J$ -coupling). Cross-peaks assigned to coupling of the same type of protons are indicated by the same colored arrow. Peaks that cannot be explained by  $J$ -coupling are circled.

In the COSY spectrum in Figure 2.6, the same number of  $^1\text{H}$  peaks are observed over essentially the same spectral window as in Figure 2.4. The shifts, though, are different. The  $ax^S$  peaks (in the 20-30 ppm region) indicate TSAP geometry, yet based on differing chemical shifts, a distinctly different chelate from that shown in Figure 2.4. There are the same number of off-diagonal COSY peaks that arise from through-bond coupling. The assignments of the cross-peaks are as follows.

Three of the  $ax^S$  protons have three cross-peaks each of varying intensity. These have been assigned to geminal ( $ax^S-eq^S$ , indicated by red arrows) and vicinal ( $ax^S-ax^C$ , green arrows and  $ax^S-eq^C$ , purple arrows) couplings based on the cross-peak intensity in the same manner as described above.  $ax^S$  coupling assignments were used to identify the corresponding  $ax^C-eq^C$  cross-peaks (blue arrows) on the same ethylene bridge.

The peaks at 10.8 and 9.8 ppm are minimally affected by  $Eu^{3+}$  in terms of their shift and line-width broadening. These peaks each have an integration area of 2H and show a cross-peak between them. These are assigned as protons on the *p*-NB aromatic ring (*Ar* and *Ar'*). The peak at 8.4 ppm is similarly narrow and shows a cross-peak to a resonance hidden under the HOD peak (4.7 ppm). The peak at 8.4 ppm has an integration area of 1H and is assigned to a benzylic proton (*Bn'*).

The fourth and most highly-shifted  $ax^S$  proton shows NOE peaks to an aromatic proton (orange circle) and a benzylic proton (teal circle). The remaining off-diagonal peak for this  $ax^S$  proton is assigned as an  $ax^S-ax^C$  cross-peak (green arrow) based on its intensity. This assignment is confirmed by an intense  $eq^C-ax^C$  peak (blue arrow) on the same ethylene bridge. Based on these cross-peaks, the location of where the  $ax^S-eq^C$  peak should appear (but does not appear) is indicated by a washed-out purple arrow. No  $eq^S$  proton is evident for this ethylene bridge.

The methyl and acetate protons on the pendant arms show cross-peaks and are identified in the same manner as in Figure 2.4.



Ethylene bridges with no substituents adopt almost ideal gauche conformations ( $60^\circ$ ). Replacing one hydrogen with a bulky NB group could distort the conformation of the ethylene bridge, increasing the angle between the NB group and the hydrogen substituents on the vicinal carbon. The more steric strain induced by coordination and substituent effects, the larger this angle will distort from an idealized gauche geometry (Figure 2.7). The  $ax^S$  peak with no coupling to equatorial protons is broad and highly shifted, indicating a close proximity to  $Eu^{3+}$ . Its ethylene bridge, if substituted with a NB group, would show the most torsional strain due to steric interaction and the most distortion from an ideal gauche conformation. Depending on the angle, distortion could increase or decrease the intensity of a cross-peak due to the Karplus relationship. This is the likely explanation for the missing  $ax^S$ - $eq^C$  coupling (washed-out purple arrow).

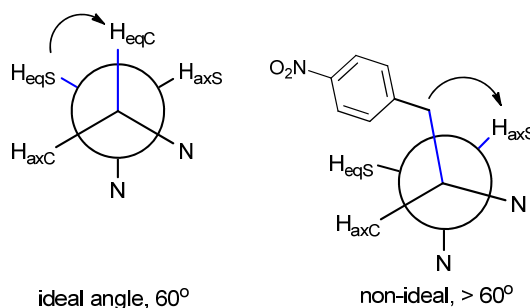


**Figure 2.7:** Newman projection (not to scale) showing distortion of the dihedral angle from ideal gauche conformation between adjacent carbons on an  $eq^C$ -substituted ethylene bridge

The lack of a cross-peak corresponding to  $J$ -coupling between the 30 ppm  $ax^S$  peak and an  $eq^S$  proton leads us to conclude that this carbon on the side of the ring has been substituted by the nitrobenzyl group.

The spectra and structures in this work were compared to those of Yb-M4DOTMA, -M4DOTA, and -MDOTA. This analysis showed that the chelate in Fig. 2.4 is the corner regioisomer and Fig. 2.6 is the side regioisomer. The evidence from the COSY analysis demonstrates that the Yb-S-RRRR-2 chelates assigned as diastereoisomers in earlier work are instead, in fact, regioisomers.

*2.3.3 Molecular mechanics simulation of the NB position and orientation based on NOE peaks observed in the COSY spectra*

There are more NOE peaks (circled) observed in the COSY spectrum of the  $eq^S$ -NB-substituted chelate in Fig. 2.6 than in the  $eq^C$ -substituted isomer in Fig. 2.4. There are proximal through-space relationships in evidence between the  $ax^S$  and benzylic ( $Bn$ )/aromatic protons, and between the other benzylic ( $Bn'$ ) and pendant arm protons ( $Me$  or  $ac$ ). The NOE peaks observed in the COSY spectra of these chelates enable us to use MM+ geometry optimization for each chelate. These models were constructed to predict the approximate time-averaged position of the nitrobenzyl substituent with respect to the chelate (Fig 2.8).

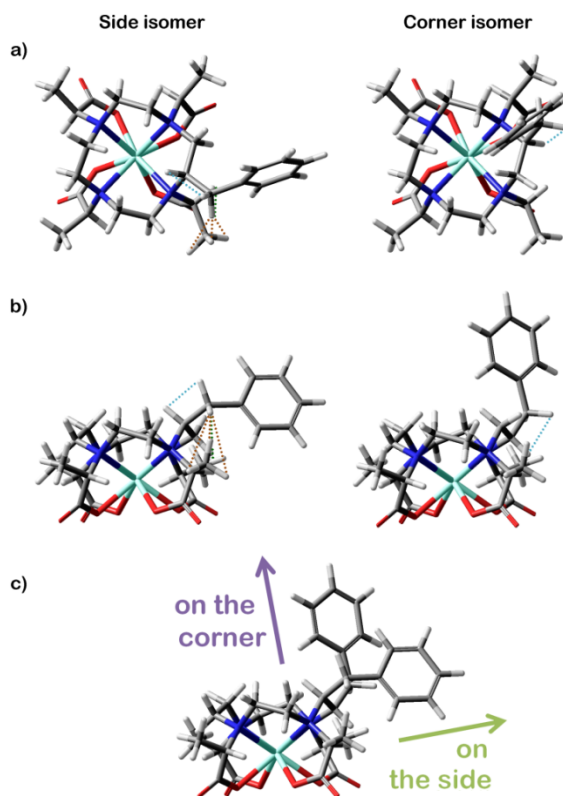


**Figure 2.8:** Molecular models of the proposed regioisomeric structures. a) is the view from the top of the chelate, looking down the principal axis at the  $\text{Eu}^{3+}$  ion. b) is the view from the side of the chelate. c) shows the two chelates superimposed in the “side” view. The dotted lines correspond to NOE peaks observed in the COSY spectra (Figures 2.4 and 2.6). Bn- $ax^S$  interactions are in teal and Bn'-Me interactions are in gold. The nitro groups are not shown.

In the model, the positions of the substituents relative to the macrocycle are based on the number and type of cross couplings alone. There is only one NOE peak in the corner isomer, suggesting that the remaining protons in the NB group are farther away from the macrocycle. In contrast, from Fig. 2.6, NOE peaks indicate the proximity of  $ax^S$ , Bn/Bn' and  $ac$  protons to the macrocyclic ring. In the model of the corner isomer, this reasoning led to the placement of the NB substituent above the chelate, oriented away from the

macrocycle, whereas the location of the NB substituent in the side isomer was placed facing away from the macrocycle but more or less in plane with the ring. Any deviation from the idealized 60° C-H-C-H angle will change the size of the  $^3J_{\text{H-H}}$  couplings, according to the Karplus relationship, as observed in Figure 2.6 (washed-out arrows). Since the torsional angles cannot be determined from the strength of the couplings alone (particularly for peaks which are absent), it is not possible to take the magnitude of the distortion of the ring caused by the NB substituent into account in the model. The model is based on a symmetric, unsubstituted cyclen ring. Finally, in the COSY spectra acquired at 313 K, there are no NOE peaks observed. This may reflect either or both increased intramolecular motion and a slightly different time-averaged chelate geometry, or a nuclear relaxation mechanism other than dipole-dipole which is dominant. These findings suggest that the nitrobenzyl group is oriented differently depending on the substitution position. The NB group appears to be closer to the chelate ring (and to one of the pendant arms) in the side isomer (Figure 2.6) than in the corner isomer (Figure 2.4).

#### *2.3.4 Structural characterization of isomeric Eu-S-RRRR-2 chelates*

Chelates of Eu-S-RRRR-2 were also synthesized and studied. Surprisingly, 4 isomeric chelates were isolated from purification of the chelate synthesis instead of the expected two (regioisomers). The COSY spectrum of the chelate isolated in greatest yield is shown in Figure 2.9. In this spectrum, the  $^1\text{H}$  peaks are observed over a larger spectral window than in Figures 2.4 and 2.6. The  $ax^S$  peaks (in the 40-50 ppm region) in each of

Figures 2.9, 2.10, 2.11 and 2.12 indicate SAP geometry and each spectrum is unique, indicating a distinct chelate. The number and type of peaks in Figure 2.9 closely resemble those observed in Figure 2.4, the corner-substituted isomer of Eu-S-SSSS-2.

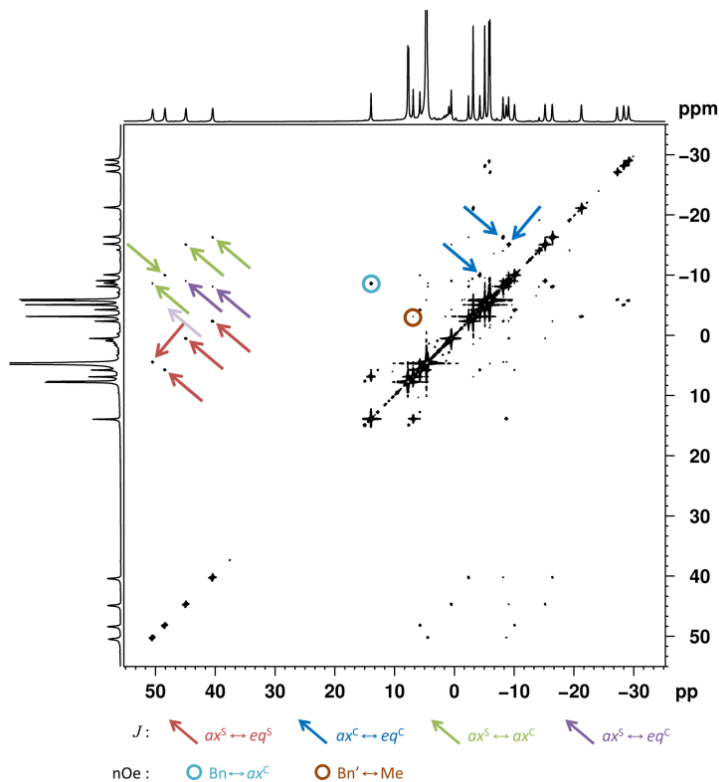


**Figure 2.9:** COSY spectrum of the major isomer of Eu-S-RRRR-2. Off-diagonal peaks indicate through-bond proton-proton coupling ( $J$ -coupling). Cross peaks of the same type are indicated by the same colored arrow. Peaks that cannot be explained by  $J$ -coupling are assumed to be due to NOE interactions and are circled.

Cross-peaks each of varying intensity have been assigned to geminal ( $ax^S$ - $eq^S$ ) and vicinal ( $ax^S$ - $ax^C$  and  $ax^S$ - $eq^C$ ) couplings based on the cross-peak intensity in the same manner as described previously. Each  $ax^S$  peak in Figure 2.9 has an intense cross-peak that is assigned to a geminal ( $ax^S$ - $eq^S$ ) coupling. The vicinal ( $ax^S$ - $ax^C$ ) couplings are

observed for each of the four ethylene bridges as well. Only three  $ax^C$ - $eq^C$  peaks are identified, again consistent with substitution of an  $eq^C$  proton. Only two  $ax^S$ - $eq^C$  vicinal couplings are observed. The position of where the third should appear based on the  $ax^C$ - $eq^C$  and  $ax^S$ - $ax^C$  assignments is shown by a washed-out purple arrow. Steric interaction causing distortion of this ethylene bridge from an ideal gauche conformation is again the likely explanation for the missing  $ax^S$ - $eq^C$  coupling (washed-out purple arrow).

The peaks at 12.7 and 6.8 ppm show minimal line-width broadening and show cross-peaks to one another. These peaks have an integration area of 1H each and are assigned to benzylic protons ( $Bn$  and  $Bn'$ ). The methyl and acetate protons on the pendant arms show cross-peaks and are identified in the same manner as in Figure 2.4.

Due to the missing  $eq^C$  peak and presence of the remaining expected protons, the predominant isomer therefore has the NB group positioned on the corner of the ring.

The COSY spectrum (Figure 2.10) of one of the three minor isomers isolated from the synthesis of Eu-*S*-RRRR-2 is shown below.

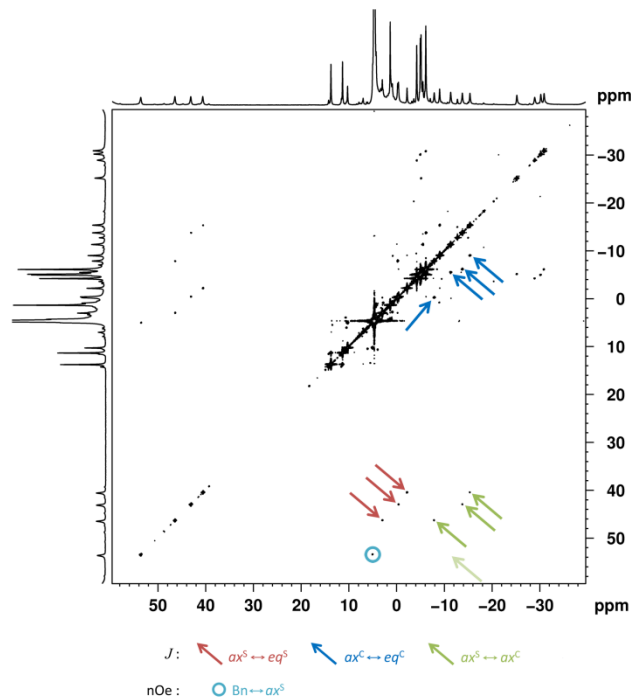


**Figure 2.10:** COSY spectrum of a minor isomer isolated from the synthesis of Eu-S-RRRR-2. Off-diagonal peaks indicate through-bond proton-proton coupling ( $J$ -coupling). Cross peaks of the same type are indicated by the same colored arrow. Peaks that cannot be explained by  $J$ -coupling are assumed to be due to NOE interactions and are circled.

Three of the  $ax^S$  protons in this spectrum show two cross-peaks each. A third set of  $ax^S$  cross-peaks was not observed – the  $ax^S$ - $eq^C$  peaks are presumably too weak to be seen under the conditions tested. The strongest coupling is to a geminal proton, so these are again assigned as  $ax^S$ - $eq^S$ . The next strongest coupling is  $ax^S$ - $ax^C$ , which was assigned to the remaining cross-peak for each ethylene bridge. Three of the  $ax^C$ - $eq^C$  peaks are assigned based on their cross-coupling to  $ax^S$ . An additional cross-peak in the same region of the spectrum (0 to -10 ppm) corresponds to protons with similar peak shape and

was assigned to the fourth  $ax^C-eg^C$  coupling. The aromatic, benzylic, and pendant arm protons were identified in the same manner as for the above chelates.

Except for the missing  $ax^S-eg^C$  peaks, the cross-peaks observed and their assignments are similar to that of the side isomer of Eu-S-SSSS-2. The chelate which yielded the COSY in Figure 2.10 is assigned as the side isomer of Eu-S-RRRR-2. The reason for the absence of these cross-peaks is probably the minimal amount of sample available and the 2D NMR spectral limitations described above, and not due to any structural differences. COSY spectra were acquired for the remaining two minor isomers (Figures 2.11 and 2.12).



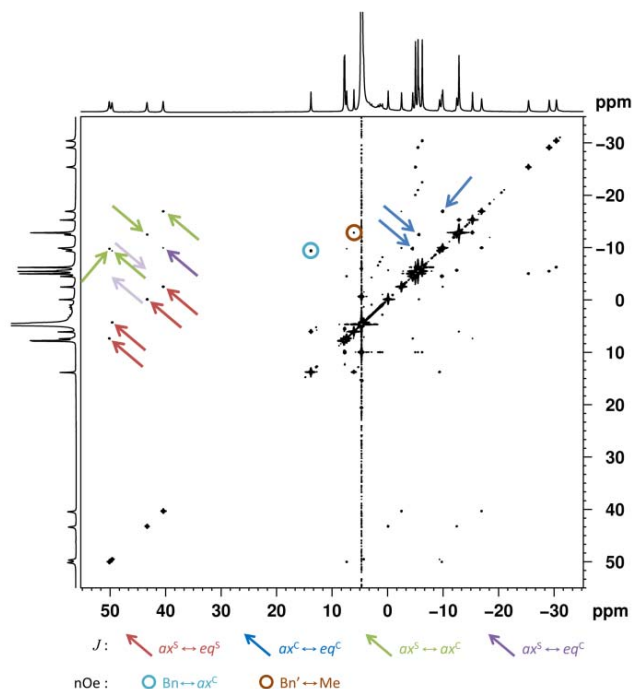


**Figure 2.11:** COSY spectrum of a minor isomer from the synthesis of Eu-S-RRRR-2. Off-diagonal peaks indicate through-bond proton-proton coupling ( $J$ -coupling). Cross peaks of the same type are indicated by the same colored arrow. Peaks that cannot be explained by  $J$ -coupling are assumed to be due to NOE interactions and are circled.

In Figure 2.11, four strong cross-peaks are in evidence and were assigned to  $ax^S$ - $eq^S$  coupling. The four cross-peaks of intermediate intensity were assigned to  $ax^S$ - $ax^C$  coupling. This allowed the assignment of strong cross-peaks to  $ax^C$ - $eq^C$  coupling, of which only three were observed. Only one  $ax^S$ - $eq^C$  cross-peak could be assigned, the remaining positions where these couplings would show up are noted based on the  $ax^S$ - $eq^S$ ,  $ax^S$ - $ax^C$ , and  $ax^C$ - $eq^C$  assignments. Based on the peak assignments, this structure is consistent with another isomer with NB-substituent having replaced an equatorial proton on a corner carbon.

The axial-axial cross-peaks are not of uniform intensity. The  $ax^S$  proton with the weakest  $ax^C$  coupling is the one missing an  $eq^C$  cross-peak on its ethylene bridge. This  $ax^C$  proton is coupled to a benzylic proton. One of the peaks corresponding to a methyl group on a pendant arm is shifted upfield significantly compared with the other three methyl resonances. These observations would be explained by an arm “forced” into a helicity which is opposite to the preferred orientation for its chirality. Since the arms in DOTA-type chelates must bind cooperatively; three arms in a particular orientation ( $\delta$  or  $\lambda$ ) are enough to select for a particular geometry regardless of the chirality of the fourth arm. The cross-peak observations are indicative of an ethylene bridge which is significantly distorted, strongly suggesting an inverted ( $S$ -) stereocenter on the pendant arm closest to the nitrobenzyl group. The chelate in this spectrum was assigned as Eu- $S$ - $SRRR$ -2, corner regioisomer.

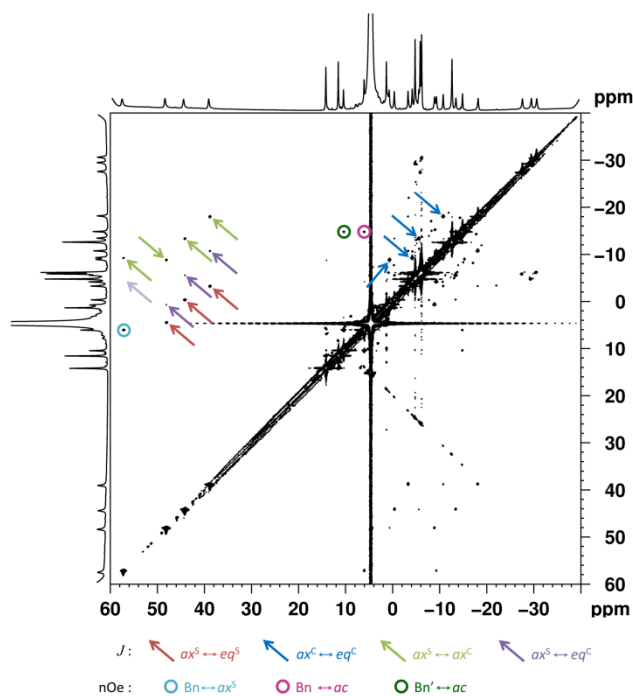


**Figure 2.12:** COSY spectrum of a minor isomer isolated from the synthesis of Eu-S-RRRR-2. Off-diagonal peaks indicate through-bond proton-proton coupling ( $J$ -coupling).

Cross peaks of the same type are indicated by the same colored arrow. Peaks that cannot be explained by  $J$ -coupling are assumed to be due to NOE interactions and are circled.

The final isomeric chelate isolated from the synthesis of Eu-S-RRRR-2 has three cross-peaks assigned to  $ax^S-eg^S$  coupling and four peaks assigned to  $ax^C-eg^C$  coupling. Three NOE peaks were identified. This spectrum also shows an arm methyl substituent which is shifted significantly away from the peaks corresponding to the other methyl-substituted arms. Based on these observations, the chelate whose COSY spectrum appears in Figure 2.12 was assigned to Eu-S-SRRR-2, side isomer.

In Figure 2.9, the uncoupled  $ax^C$  proton shows an NOE peak to a benzylic proton (teal circle). The presence of a  $Bn'$ -Me NOE peak as well, based on the above assignments, indicates a similar yet not equivalent spatial relationship between the NB group and the macrocyclic ring as for the corner isomer of Eu-S-SSSS-2 (Figure 2.4). Either or both the smaller distance between N-O planes and the larger twist angle between the arms and the macrocycle may be the source of this additional NOE peak. The  $ax^C-Bn$  and  $Bn'$ -Me NOE peaks are also observed in Figure 2.11. The  $ax^S-eg^C$  cross peaks are notably weak or absent in this isomer, suggesting a more strained ring. The similarity of the NOE coupling peaks in the COSY spectra of each corner isomer studied indicates a structural similarity among the orientations of the NB groups in each of these chelates.

MM+ geometry models were again employed for the SAP chelates (Figure 2.11). The positions of the substituents reflect the particular NOE cross-peaks observed and their

respective intensities. The position of the NB group was again placed above the macrocycle but close to it, reflecting the greater number of NOE peaks in SAP vs. TSAP corner isomers. The less intense *Me-ax*<sup>C</sup> peaks support the increased distance between the NB group and the ring in the second isomer. The *Me-Bn'* peaks show the interaction between the NB group and the 1-*N* arm in both isomers. The models are in good agreement with the racemization hypothesis, with the *S* arm positioned further from the nitrobenzyl substituent than its homochiral analogue. From these models it is predicted that the corner isomers each have the NB substituent above and perpendicular to the macrocyclic ring, as in the case of the TSAP corner chelate of Eu-2.

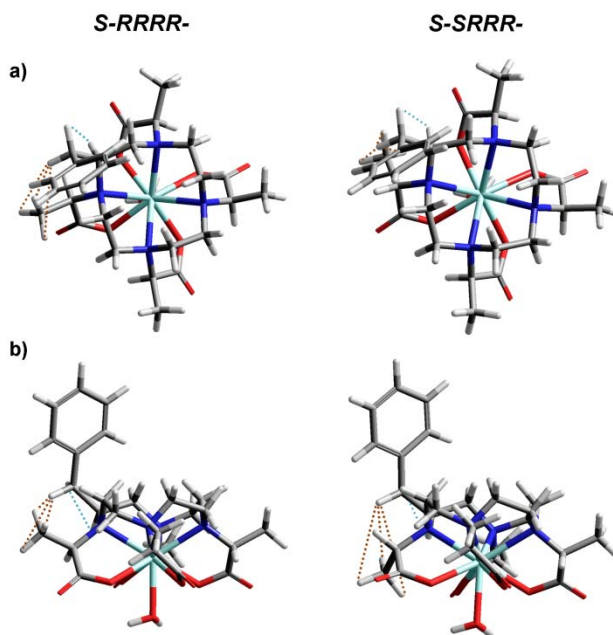


**Figure 2.13:** Molecular models of the proposed diastereoisomeric structures. a) is the view from the top of the chelate, looking down the principal axis at the  $\text{Eu}^{3+}$  ion. b) is the view from the side of the chelate. The dotted lines correspond to NOE peaks observed

in the COSY spectra (Figures 2.9 and 2.10). Bn- $ax^S$  interactions are in teal and Bn'-Me interactions are in gold. The nitro groups are not shown.

The synthesis of **2** and its chelates yielded two different outcomes depending on the stereochemistry of the starting materials. For Eu-*S*-SSSS-**2** (TSAP), only regioisomers were observed. For the SAP chelates, the second-most abundant species is the product of racemization during ligand species, Eu-*S*-SRRR-**2**. Two isomers each were identified in which the NB substituent in an equatorial conformation is located on a corner carbon or side carbon, respectively.

We have unambiguously shown that conformationally rigid Ln-DOTA-type chelates can form regioisomers with the bulky ring substituent on the corner or on the side of the macrocyclic ring. The  $ax^S$  peak patterns in the  $^1H$  NMR data were found to differ between corner and side isomers of the same chelate, but are similar between corner isomers (or side isomers) of related chelates. Three pairs of regioisomeric Eu-**2** chelates were obtained and thoroughly characterized. For a cyclen ring in which a single proton is replaced by another substituent, there are 7 possible  $^1H$  geminal through-bond ( $^2J$ ) couplings. All but one of the 8 carbons in the macrocycle should show a cross-peak in the COSY between  $ax$  and  $eq$  protons. Though absence of some expected cross-peaks does not prove that the anticipated coupling is not occurring, it is telling that in the COSY spectrum of each isomer of Eu-**2** obtained, 7 cross-peaks are present which represent  $^2J$  coupling. There are either three  $ax^S$ - $eq^S$  (red arrows) and four  $ax^C$ - $eq^C$  (blue arrows) peaks, representing a side isomer, or four and three, representing a corner isomer, respectively.

Even though two coordination geometries complicate the spectra of Ln-NB-DOTA chelates, it can be determined that regioisomers are not present.<sup>21</sup> It appears that the previous racemization hypothesis was correct but incomplete. Diastereoisomeric chelates were observed to form in syntheses of Eu-*S-RRRR-2*, but not for Eu-*S-SSSS-2* by the author. The isomeric chelates of Yb-*S-SSSS-2* studied previously are now believed to be regioisomers rather than diastereoisomers.<sup>14,16</sup> In prior syntheses of Ln-**2** or related chelates where only one (major) isomer was reported, regioisomers may have formed, but were not resolved or efforts were not made to purify them by HPLC. To our knowledge, no further study of the phenomenon has been published since Desreux and co-workers in 2002. Regioisomerism could also explain the presence of two non-exchanging isomers from a ligand of single stereochemistry which were observed for Cu-1,4,7-triazanonane-*N,N',N''*-triacetate (Cu-NOTA) with a ring substituent.<sup>22</sup>

Additionally, the NOE peaks allow us to model the positions of the nitrobenzyl substituents for the regioisomers – the positions are appreciably different for the corner isomer *versus* the side isomer. This becomes noteworthy if we explore functionalizing the nitrobenzyl group with a molecular “probe” and study the chelate when bound to a slowly rotating system. A functional group linked to the NB substituent pointing closer to or further from, and parallel *versus* perpendicular to the ring, will likely have different binding behavior with respect to its macromolecular target. This behavior may include but is not limited to binding kinetics (the likelihood and duration of a binding event) and  $\tau_M$  of the chelates in the system. The relaxation properties of regioisomeric chelates may differ depending on the local and global rotation of the chelate and the orientation of the

exchangeable inner-sphere water site when bound to a macromolecular target. These possible variations in binding,  $\tau_R$ , and  $\tau_M$  would each influence the observed relaxivity.

## **2.4 Investigation of the chelation mechanism as it relates to regioisomer formation**

### **2.4.1 $pK_a$ and conformational changes of the ligand **2** in solution**

An earlier paper describes  $\text{Ln}^{3+}$  chelates of *S*-NB-DOTA (Scheme 2.1).<sup>21</sup> Two isomeric chelates were identified by  $^1\text{H}$  NMR – one SAP and one TSAP chelate. Analysis of the isomeric mixture by COSY confirmed that for both isomers, the NB substituent is on a carbon on the corner of the macrocycle, having replaced an  $eq^C$  proton. The EXSY spectrum shows exchange between the two types of axial proton ( $ax^S$ - $ax^C$ ) and between the two types of equatorial proton. No exchange peaks between axial and equatorial protons are observed. These findings confirm the hypothesis that SAP and TSAP geometries can interconvert *via* arm rotation ( $\Delta$  to  $\Lambda$ ) but not *via* ring inversion. No other isomers of *S*-NB-DOTA were observed for any of the lanthanide chelates. To investigate why regioisomers of Ln-**2** form but regioisomers of NB-DOTA do not, the synthetic conditions, stability constants, and conformational analysis were considered for these and related chelates.<sup>23</sup> A recent study to determine the stability constants of  $\text{Ln}^{3+}$  ions with two stereoisomeric ligands led to an interesting result which may be related to regioisomerism. Titration studies with KCl were performed to determine the protonation constants of **2** and **3** (Table 2.1). These analyses were performed in the laboratory of Prof. Gyula Tircso at the University of Debrecen in Debrecen, Hungary. The fourth  $pK_a$

is higher than the third for **3** and for NB-DOTA, a highly unusual result that at first seems impossible.



	S-RRRR-2	S-SSS-3	DOTA <sup>b</sup>	NB-DOTA	NB-DOTA <sup>c</sup>
Titration medium	1.0 M KCl	1.0 M KCl	1.0 M KCl	1.0 M KCl	0.1 M Me <sub>4</sub> NCl
log K <sub>1</sub> <sup>H</sup>	11.81	11.30	12.09	10.00	10.93
log K <sub>2</sub> <sup>H</sup>	8.23	9.96	9.68	9.54	9.14
log K <sub>3</sub> <sup>H</sup>	4.00	<b>4.60</b>	4.55	<b>4.29</b>	4.5
log K <sub>4</sub> <sup>H</sup>	3.46	<b>5.41</b>	4.13	<b>4.72</b>	4.19
log K <sub>5</sub> <sup>H</sup>	2.13	1.99		2.28	2.33
log K <sub>6</sub> <sup>H</sup>					1.4
Σ log K <sub>i</sub> <sup>H</sup>	29.62	33.26	30.45	30.83	32.49

**Table 2.1:** Acid dissociation constants ( $K_a$ ) of DOTA-type ligands. (b),(c) data taken from respective references<sup>21,24</sup> Chelates with determined 4<sup>th</sup> p $K_a$  with higher values than the 3<sup>rd</sup> p $K_a$  are highlighted in bold.

This p $K_a$  “inversion” suggests that *via* successive addition of acid, protonating the ligand a third time makes it more basic. One possible explanation for this increased basicity is a change in conformation as a result of the third protonation step. The chance of observing a conformational change due to protonation is greater in rigid systems. The conformation adopted following a third protonation could be more basic than the conformation adopted prior to the third protonation. Specifically, a conformational change could render the 4<sup>th</sup> protonation site on the ligand more basic than in its conformation prior to titrating to the 3<sup>rd</sup> p $K_a$ .

An apparent p $K_a$  inversion in related (polyaza crown) ligands has been published previously.<sup>25</sup> The authors report a significant ring strain in their molecular mechanics simulation upon addition of a third proton to the ligand due to electrostatic and van Der

Waals repulsion. The  $pK_a$  inversion was interpreted as leading to a conformational change after the third  $pK_a$  was reached. If this conformational change is leading to the  $pK_a$ s determined, the pH at any point in the chelation reaction will affect the basicity of the ligand and may affect the conformation of the ligand. The rates of formation for regioisomeric chelates may depend on what conformation the ligand is in during the chelation steps. However, the  $pK_a$  “inversion” is not observed for *S-RRRR-2*.

We investigated chelate formation of Yb-*S-RRRR-2* to determine whether different ligand conformations in solution arising from different protonation states give rise to different isomers. The mechanism for  $Ln^{3+}$  chelate formation with **2** was assumed to mimic that of Ln-DOTA. The intermediate chelate, where  $Gd^{3+}$  binds only to the carboxylate groups of the ligand, was identified by Prof. Tirso by potentiometric titration for the reaction of  $Gd^{3+}$  with **2**, **3**, and NB-DOTA.

The following experiments were designed to examine whether formation of regioisomers of Yb-*S-RRRR-2* was due to different ligand conformations in solution, and if conditions could be found which produced only one regioisomer. It was hypothesized that if the pH determined the conformation of the ligand, regioisomer production could be controlled by maintaining the chelation reaction at the proper pH. *S-RRRR-2* was synthesized according to established procedures and purified by preparative HPLC. From the HPLC, this ligand is isolated in the acid form  $H_6NB-DOTMA$ . Yb-*S-RRRR-2* formation at a variety of pH and concentration conditions was assayed to see if the chelation (and resulting isomerism) is dependent on these factors.

There is an optimal pH range to produce  $\text{Ln}^{3+}$  tetraacetate complexes. A pH below 3 results in very slow chelate formation (ligation is much stronger with free carboxylates than their protonated analogues), and the chelation reaction releases protons from the ligand. *Le Châtelier's* principle thus favors the forward reaction more strongly at higher pH.  $\text{Ln}^{3+}$  salts have low water solubility at pH higher than 6.0, constraining the efforts to prepare DOTA-type chelates at high pH. The apparent pH range for the inverted  $\text{pK}_{\text{a}}$ s determined by Tircso *et. al.* is approximately 4-6. The pH range 3.0-6.0 in increments of 0.5 pH units was chosen for the study.

For each sample, the concentration of  $\text{Yb}^{3+}$  was twice the concentration of *S-RRRR-2*, which was the case for prior syntheses of Ln-2. A single buffer system could not be found for the entire range of pH conditions tested where the counter ion does not chelate  $\text{Ln}^{3+}$ , so various non-coordinating buffers were used (as described in the Experimental) depending on the desired pH. Each solution was buffered at 1M to control against pH changes resulting from  $\text{H}^+$  released as a result of chelate formation. All solutions were sealed in vials and incubated for 64 days at 70°C. An LC/MS method was developed in order to resolve isomeric chelates present following this incubation period and to calculate their relative proportions. The proportion of each regioisomer produced in each reaction was determined by monitoring at  $m/z = 765$ . The sample set from the incubation study was analyzed, paying specific attention to the isomeric peak ratios. These ratios were computed using the areas under the appropriate peaks on the LC trace. In order to confirm which peak corresponds to which regioisomer, the concentration study samples were combined and freeze-dried, and an NMR spectrum of the combined sample showed

multiple chelate. These chelates were separated by prep. HPLC, and the identity of each HPLC peak was confirmed by NMR. Two chelates were resolved, each with a distinctive peak pattern in the  $ax^S$  region matching earlier Yb-*S-RRRR*- and Eu-*S-RRRR-2* chelates (Figures 2.1, 2.9 and 2.10, previously identified as regioisomers). The effect of pH on the distribution of isomers produced during chelate formation is shown in Figure 2.14.

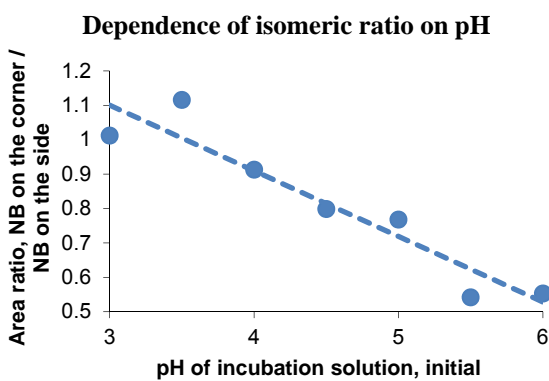


**Figure 2.14:** The relationship between pH and regioisomeric ratio, holding  $[Yb^{3+}]$  and  $[S-RRRR-2]$  constant;  $[2] = 7.1$  mM

The ratio of corner/side regioisomers produced after the incubation study was approximately 0.5:1 at the highest pH, increasing to approximately 1:1 at the lowest pH tested. There is a gradual change in isomer ratio with a change in chelation reaction pH. If the  $pK_a$  inversion is due to a conformational change, and if the conformation of the ligand determines which regioisomer is formed, there should be an abrupt change in the regioisomer ratio at a pH around the  $pK_a$ . We did not observe this to be the case. It appears that the pH does play some role in chelate formation, and possibly the buffer used as well. It is likely that the protonation states of the various amines and carboxylates affect the solution configuration of the ligand, slightly favoring one

nitrobenzyl position over the other. The high concentrations of salts may be competing with **2** and  $\text{Yb}^{3+}$  for electron density, altering the kinetics relative to an unbuffered reaction.

The results of the concentration dependence study are shown in Figure 2.15.

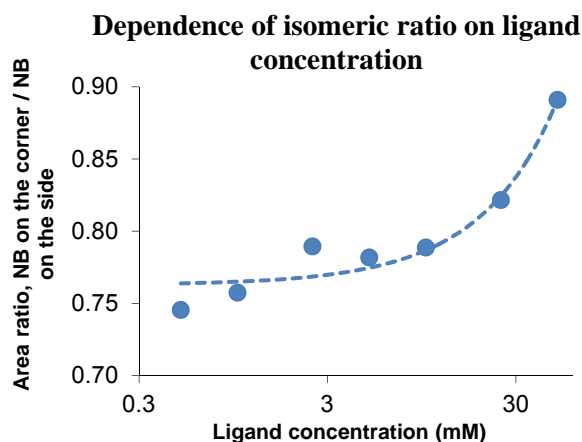


**Figure 2.15:** The relationship between the  $\log_{10}$  of *S*-RRRR-**2** concentration and regioisomeric ratio, holding  $[\text{Yb}^{3+}]:[\mathbf{2}]$  constant and pH at 5.0

The relative amounts of regioisomeric Yb-**2** chelates formed indicate a clear trend between the concentrations of  $\text{Yb}^{3+}$  and *S*-RRRR-**2** and the regioisomeric ratio obtained (Figure 2.15). A high concentration of both leads to a greater portion of corner isomer formed. None of the conditions assayed select for a single regioisomer or even a large excess of one regioisomer.

A  $\text{pK}_a$ -dependent conformational change may be related to regioisomerism, but the data above do not suggest that this is the cause of regioisomerism. Also, the chelation reaction was allowed to progress over a much longer time than in prior syntheses, which

were done over less than a week. The rate of formation of corner regioisomer is likely faster than that of side isomer at first: a higher corner : side ratio resulted from a shorter reaction time, and from a higher concentration of both reactants. The rate of de-chelation is extremely slow for substituted Ln[DOTA] chelates, but de-chelation and reincorporation of Yb<sup>3+</sup> occur on a time scale which is fast enough relative to the 64 day study duration. The results provide some insight into the kinetic and thermodynamic preference between corner and side isomer, but it cannot be determined from the above study whether the reaction conditions truly produce the kinetically or thermodynamically-favored isomer.

In a later experiment<sup>23</sup>, the pK<sub>a</sub> determination was repeated, titrating with Me<sub>4</sub>NCl in place of KCl (Table 2.2, not all data are shown). For this ionic system, a decrease of pK<sub>a</sub> was observed for each protonation step for each ligand. Association of the non-protonated amines in the ligands with K<sup>+</sup> is a more likely explanation for the inverted pK<sub>a</sub> behavior than conformation dependence, so the reason for regioisomer formation must be found elsewhere.

2.4.2 Modeling the solution conformation and the position of the NB substituent to gain insight into the chelation mechanism.

As mentioned earlier, crystal structures of NB-DOTA and -DOTMA are unavailable. In order to analyze the conformation of **2** in solution, molecular models were constructed based on the crystal structures of  $H_6DOTMA$  or  $H_2DOTMA^{2-}$ .  $H_6DOTMA$  and  $H_2DOTMA^{2-}$  are the maximum and minimum protonation state of the ligand during chelate synthesis.

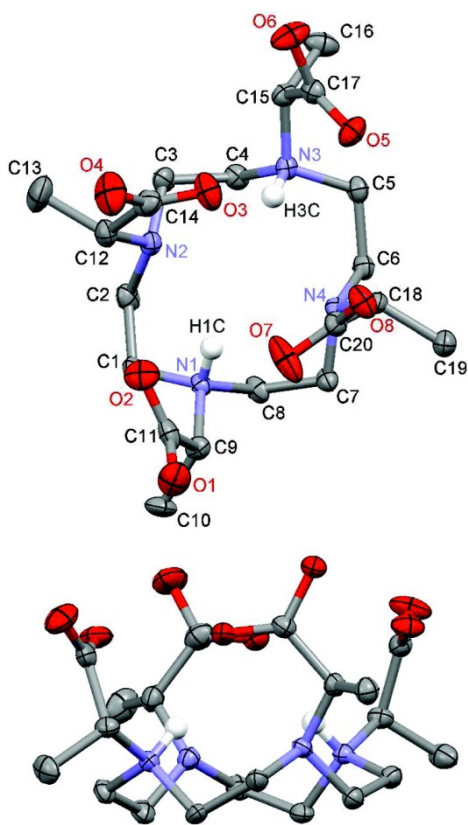


**Figure 2.16:** Crystal structure of  $H_4DOTMA \cdot 2HCl \cdot 3H_2O$ , 50% thermal ellipsoid plot. Hydrogen atoms, water molecules and counter ions are omitted for clarity. All carboxylates are protonated on O2, O4, O6, and O8.

A nitrobenzyl substituent was placed on each equatorial position for each carbon on the macrocycle, and the energies were computed. According to modeled configuration energies, positioning the NB (or other large) group on the C3 or C7 carbon on the corner of the ring is most favorable. To form logical structures which minimize configuration energies, these models assume that all four pendant arms cannot be located on one side of the macrocyclic ring (unlike in Figure 2.16 and in the crystal structure of H<sub>4</sub>DOTA).<sup>26</sup> Having the Ln<sup>3+</sup> ion approach 4 arms on a single face of the macrocycle was thought to be essential in the first step of DOTA-type chelate formation. Again, there is no explanation for the observed regioisomerism in the models based on crystal structure. The modeled energies of substituents positioned on a side carbon are still much higher than for the corner position. One aspect the model does not take into account is distortion of the macrocyclic ring due to the steric strain from the NB group. The structure of TCE-DOTA (Figure 2.17)<sup>15</sup>, a ligand which affords predominantly SAP Ln<sup>3+</sup> chelates, related to **2**, was considered for a configuration which fits with the models above and our observations of the prevalence of two isomers.



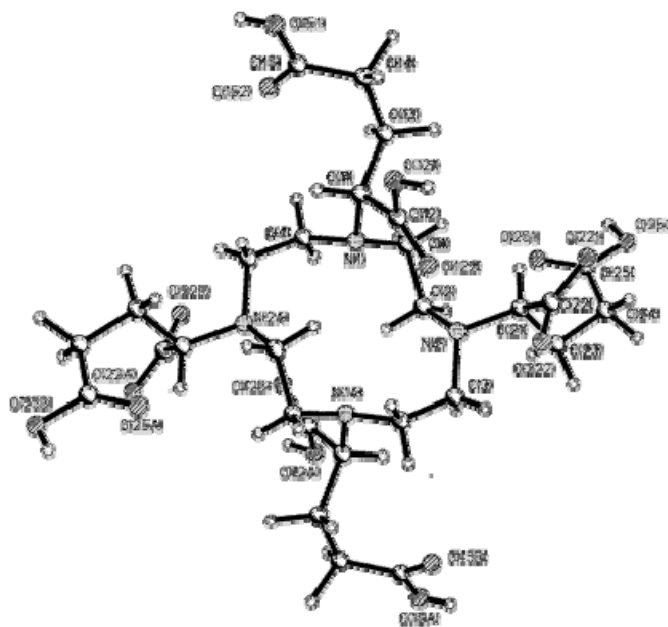


**Figure 2.17:** Crystal structure of (*RRSS*)-TCE-DOTA

In this structure, there are two arms above and two arms below the macrocyclic ring, a possible conformation of  $H_42$  in solution. In this arrangement, two of the ethylene bridges on the macrocycle have  $\delta$  helicity and two bridges have  $\lambda$  helicity. Let's assume that the  $Ln^{3+}$  ion approaches this ligand from the face opposite the NB substituent (the "bottom," Fig. 2.18). If this metal ion approach and ligand conformation, or something akin to it, resembles the predominant solution state collision leading to chelation, then two pendant arms must flip over to the other side of the ring to generate the  $H_2LnL^+$  species. The chelate can only exist in the  $\Lambda(\delta\delta\delta\delta)$  conformation with all arms adopting the same helicity, and all ethylene bridges doing the same. For a pendant arm to flip to the other side of the ring to chelate the metal, its ethylene bridge must reverse helicity from  $\lambda$  to  $\delta$ . Once all four arms are coordinated to the metal, no further conformational changes can take place – the geometry is locked at this stage. The regiochemistry must

be determined in this first chelation step; even for the intermediate chelate, the arms and rings cannot invert their helicities.

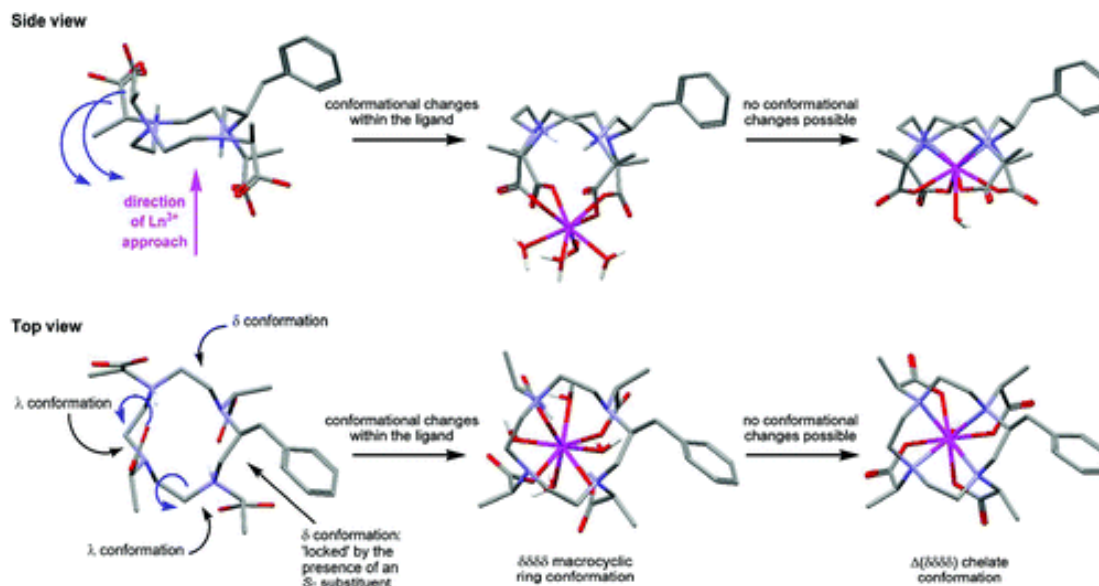


**Figure 2.18:** Proposed chelation mechanism when  $\text{Ln}^{3+}$  approaches the ligand from the face opposite the NB group. The solution conformation of *S*-SSSS-2 is modeled after the crystal structure of *RRSS*-TCE-DOTA. The NB group is in the lowest energy substitution position ( $eq^C$ ) according to the modeling study with  $\text{H}_x\text{DOTMA}$ . The two pendant arms on the face opposite the  $\text{Ln}^{3+}$  direction of approach must flip around *via* inversion of helicity for their ethylene bridge. This is shown in the first structure of the “top view” (blue arrows).

But there is a chance the  $\text{Ln}^{3+}$  approaches from the opposite direction relative to the macrocycle (the “top”, Fig 2.19). The ethylene bridges are still locked into the  $\delta$  orientation by the equatorial NB substituent. In this case, the two opposite-face arms would have to flip their ethylene bridges to  $\lambda$  in order to reorient and ligate the metal, which they are sterically unable to do as the *S*-NB group would be forced into an axial position. A positional shift must occur, retaining the orientation of the two arms initially

bound to the metal, but ensuring the ring helicity is  $\delta\delta\delta\delta$ . This shift moves each of the atoms in the [3333] arrangement one position counterclockwise, as shown in the figure. The “face-of-approach” explanation is the most logical one which yields two regioisomeric chelates of single coordination geometry. It is possible that one face of the macrocycle has 3 arms, not two, but this possibility does not invalidate the previous explanation. The ligand and  $\text{Ln}^{3+}$  ions are diffusing and tumbling freely in solution, so the chance of approach of the metal should be equal from either side. Since the ratio of isomers was not 50:50 in all cases, there must be another factor or factors which determine chelate formation other than direction of  $\text{Ln}^{3+}$  approach. It was concluded that the regioisomer formed depends on the direction of approach of the metal – via the “top” or “bottom” of the plane of the ring (Figures 2.18, 2.19).<sup>23</sup>

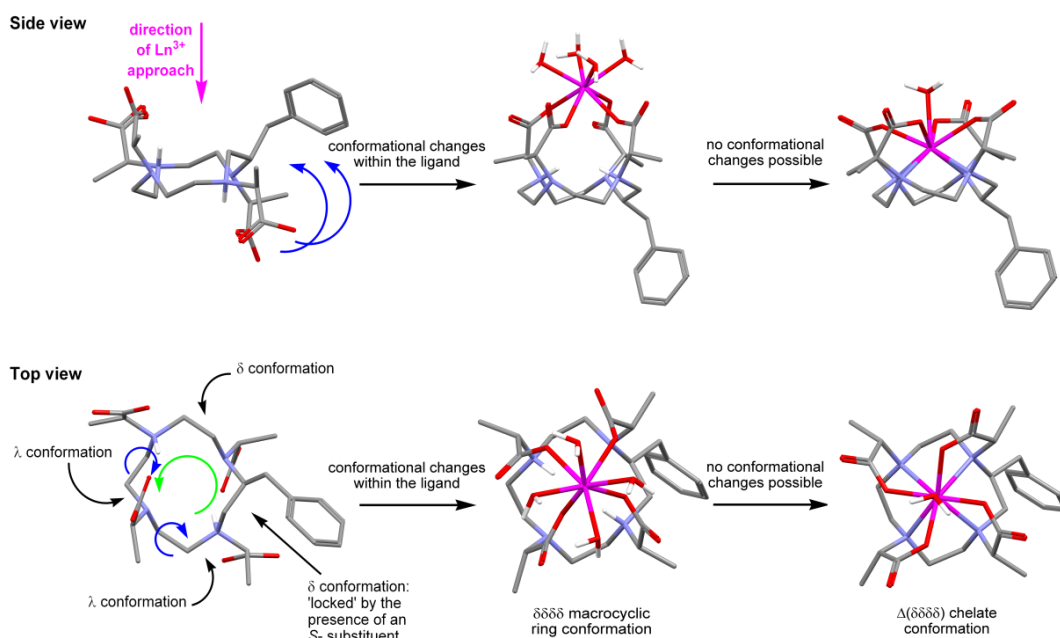


**Figure 2.19:** Mechanism for forming Ln-S-SSSS-2 with nitrobenzyl group on the side. Each atom in the [3333] square must rotate one position to accommodate a  $\delta$ , equatorial nitrobenzyl group on the side.

*2.4.3 Thermodynamic stability of conformationally rigid SAP and TSAP Ln<sup>3+</sup> chelates*

The later lanthanides show a preference for the smaller coordination “cage” of SAP geometry. TSAP geometry is preferred for the earlier lanthanides (Table 2.2) – Yb-S-RRRR-2 (SAP) has a stability constant more than two orders greater than Yb-S-SSS-3 (TSAP).

Ln <sup>3+</sup>	S-RRRR-2	S-SSS-3	DOTA <sup>‡</sup>
	SAP	TSAP	SAP
Ce <sup>3+</sup>	19.79	24.04	23.4
Gd <sup>3+</sup>	23.86	21.53	24.7
Yb <sup>3+</sup>	24.12	21.91	25

**Table 2.2:** log values of thermodynamic stability constants of Ln[DOTA]-type chelates.<sup>23</sup>

‡Data for DOTA taken from the reference.<sup>27</sup>

A Yb<sup>3+</sup> chelate known to adopt TSAP geometry (Yb-S-SSS-3) was selected for study to see if it could be converted to the more thermodynamically stable SAP geometry. The possibility for geometric isomer conversion arises *via* epimerization. Previously, it has been shown that the chiral centers on substituted acetate pendant arms can be epimerized in TCE-DOTA via acid-induced epimerization (Figure 2.20).<sup>15</sup>

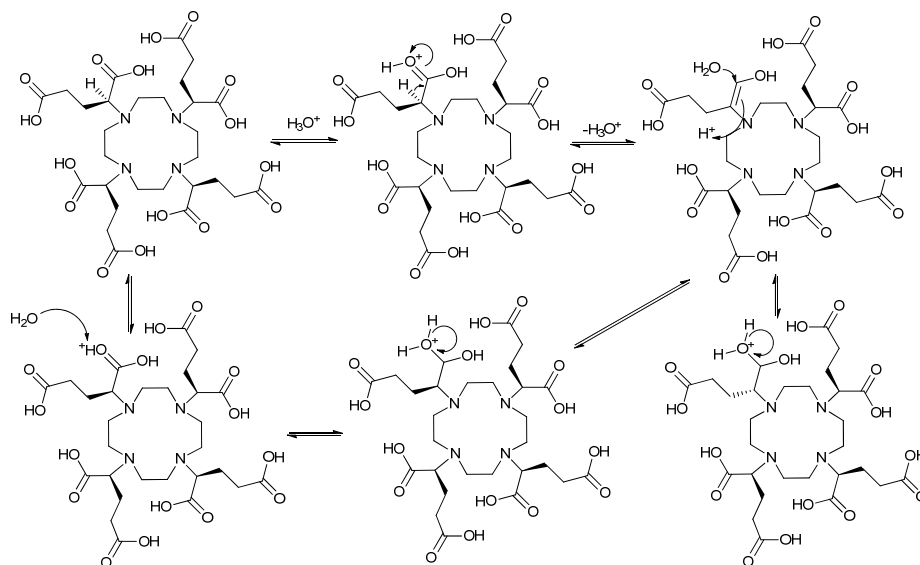


**Figure 2.20:** reversal and retention of configuration at the  $\alpha$ -carbonyl carbon due to acid-induced epimerization in H<sub>4</sub>TCE-DOTA

Over time, this can allow conversion of any other diastereoisomer to the most stable homochiral stereoisomer. It was hypothesized that this mechanism would facilitate conversion of the TSAP isomer of Yb-S-SSS-**3** to the more thermodynamically stable<sup>28</sup> SAP isomer.

The corner isomer of Yb-S-SSS-**3** was purified by HPLC. A 20 mM sample of this chelate was sealed in an NMR tube to ensure that the concentration of chelate solution did not change. The sample tube was then heated in acid (DCl in D<sub>2</sub>O, pD ~1) at 90°C. NMR spectra of this sample were acquired at regular intervals for 15 weeks – every week for the first 7 weeks, and every two weeks thereafter until the NMR peaks and their respective areas appeared to stabilize. A second set of peaks was observed to grow in over the duration of the study (Fig. 2.21). This species also showed  $ax^S$  shifts indicating a TSAP Yb<sup>3+</sup> chelate. It was expected that either no new species would be produced, or that TSAP→SAP conversion would be observed. Instead, an apparent TSAP→TSAP conversion occurred. The evidence for regioisomerism in Ln-**2** chelates points to the side isomer of Yb-S-SSS-**3** as the second species formed.

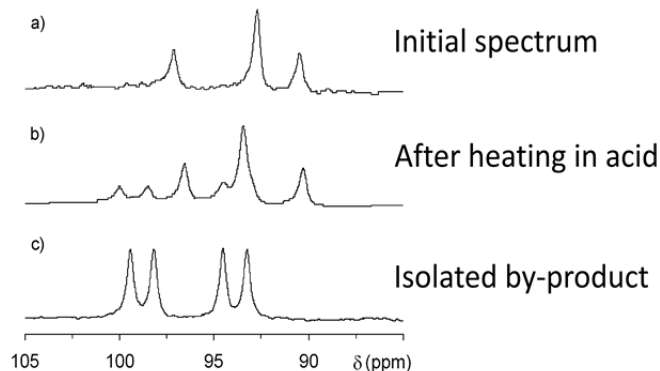


**Figure 2.21:** A second Yb-S-SSS-3 chelate increases in intensity over time, as seen by the methyl arm peak pattern in the hyperfine shift region. Spectrum 2.21c was a different TSAP chelate isolated as a byproduct of Yb-S-SSS-3 synthesis.

The area ratio of methyl peaks between the two species was calculated. This ratio seemed to stabilize at ~1:0.8 after 15 weeks (Fig. 2.22).

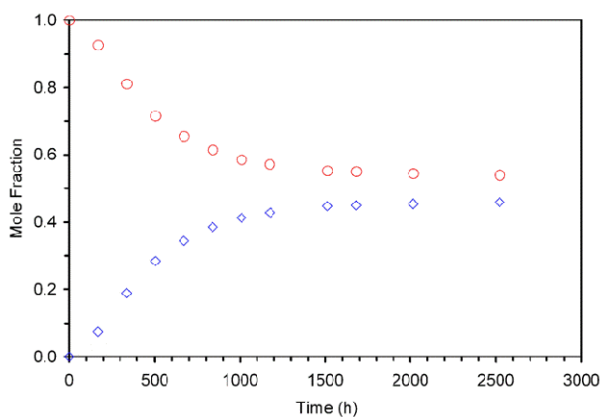


**Figure 2.22:** Ratio of Yb-S-SSS-3 TSAP isomers as a function of time, heating under acidic conditions

The acid-catalyzed epimerization method breaks the *ac* C-H bond at the stereogenic center. By conducting the experiment in deuterated solvent, the occurrence of acid-catalyzed enolization can be assessed by examining for deuteration of the chelates.

Epimerization would induce chemical exchange of the *ac* protons. If the first reaction in Figure 2.23 (forming the tautomer) occurs, the *ac* proton lost from the  $\alpha$ -methyl carbon can be replaced with either  $H^+$  or  $D^+$ , and there is much more  $D^+$  available. Epimerization would be indicated by the loss of *ac* proton peaks in the NMR spectrum from deuterium incorporation.

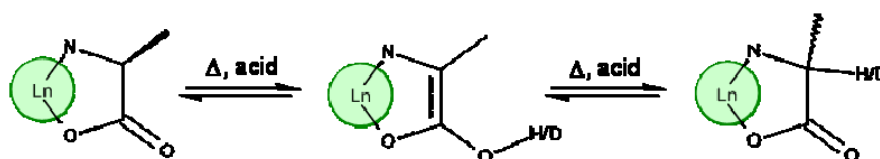


**Figure 2.23:** Acid-induced epimerization mechanism of a Ln-NCCO chelate ring

The intensity of the *ac* proton resonances remained constant throughout the experiment, indicating that no incorporation of deuterium, and therefore enolization, was occurring. This observation was verified by mass spectrometry at the conclusion of the experiment, which showed no increase in the mass of the chelate, again consistent with no deuterium incorporation. These results explain why no conversion of the TSAP Yb-*S*-SSS-**3** to the more thermodynamically stable Yb-*S*-RRR-**3** was observed, even under these relatively harsh conditions. A mechanism involving removal and re-chelation of the metal was proposed as the only logical explanation of the above observations.<sup>23</sup> If the metal is removed, it can either form the original regioisomer, or reapproach the ligand in such a way that the NB position shifts as in Figure 2.19. The two regioisomers will eventually reach equilibrium *via* acid-induced displacement of the metal and re-chelation. The relative proportions of the two regioisomers appear to approach 1:1, similar to the



regioisomeric ratios of Yb-2 in Figures 2.14 and 2.15. Whereas the regioisomer ratios found in the concentration/pH dependence study cannot be said to be definitively kinetically or thermodynamically driven, the ratio in Figure 2.22 is indicative of a thermodynamic relationship.

The significance of regioisomeric chelates arises from the possibility of tuning of the physical properties of a prototypical MRI CA. These regioisomeric chelates of Gd-2 and Gd-3 have stability constants on the order of those of Gd-DOTA, which is considered safe for clinical applications.

### **2.5 Conclusions and future directions**

To date, it has not been possible to find conditions for synthesizing a single regioisomer of Ln-2. Though the regioisomers can be resolved by HPLC, this requires multiple purification steps and is expensive and time-consuming. For a CA based on Ln-2 to be viable for clinical use, it must both be cost-effective to make and be safe and effective *in vivo*. If a potential clinical compound is to be administered as multiple isomers (i.e. regioisomers), it must be demonstrated that the isomers on the whole generate better per-dose contrast than existing treatments, and are stable and viable both separately and as formulated under physiological conditions. It is possible to produce the majority of the chelate as either corner or side regioisomer by optimizing pH, reactant concentration, and reaction time. The relative proportions, though, vary depending on the coordination geometry formed (SAP vs. TSAP) and the lanthanide used (Yb<sup>3+</sup> yields more of the side isomer than Eu<sup>3+</sup>). Our current understanding of maximizing relaxivity in

conformationally rigid chelates is incomplete but was studied further as described in the next chapters.

## **2.6 References**

- (1) Aime, S.; Botta, M.; Ermondi, G. *Inorganic Chemistry* **1992**, *31*, 4291.
- (2) Bénazeth, S.; Purans, J.; Chalbot, M.-C.; Nguyen-van-Duong, M. K.; Nicolas, L.; Keller, F.; Gaudemer, A. *Inorganic Chemistry* **1998**, *37*, 3667.
- (3) Miller, K. J.; Saherwala, A. A.; Webber, B. C.; Wu, Y.; Sherry, A. D.; Woods, M. *Inorganic Chemistry* **2010**, *49*, 8662.
- (4) Aime, S.; Barge, A.; Batsanov, A. S.; Botta, M.; Castelli, D. D.; Fedeli, F.; Mortillaro, A.; Parker, D.; Puschmann, H. *Chemical Communications* **2002**, 1120.
- (5) Barge, A.; Botta, M.; Parker, D.; Puschmann, H. *Chemical Communications* **2003**, 1386.
- (6) Merbach, A. E.; Helm, L.; Tóth, E. v. *The Chemistry of Contrast Agents in Medical Magnetic Resonance Imaging*; 2nd ed. ed.; Wiley, 2013.
- (7) Brechbiel, M. W.; Gansow, O. A.; Atcher, R. W.; Schlom, J.; Esteban, J.; Simpson, D.; Colcher, D. *Inorganic Chemistry* **1986**, *25*, 2772.
- (8) Moi, M. K.; Meares, C. F.; DeNardo, S. J. *Journal of the American Chemical Society* **1988**, *110*, 6266.
- (9) Aime, S.; Botta, M.; Fasano, M.; Crich, S. G.; Terreno, E. *Journal of Biological Inorganic Chemistry* **1996**, *1*, 312.
- (10) Elst, L. V.; Maton, F.; Laurent, S.; Seghi, F.; Chapelle, F.; Muller, R. N. *Magnetic Resonance in Medicine* **1997**, *38*, 604.
- (11) Horrocks, W. D.; Sudnick, D. R. *Accounts of Chemical Research* **1981**, *14*, 384.
- (12) Faulkner, S.; Pope, S. J. A. *Journal of the American Chemical Society* **2003**, *125*, 10526.
- (13) Woods, M.; Kovacs, Z.; Zhang, S.; Sherry, A. D. *Angewandte Chemie International Edition* **2003**, *42*, 5889.
- (14) Woods, M.; Botta, M.; Avedano, S.; Wang, J.; Sherry, A. D. *Dalton Transactions* **2005**, 3829.
- (15) Woods, M.; Aime, S.; Botta, M.; Howard, J. A. K.; Moloney, J. M.; Navet, M.; Parker, D.; Port, M.; Rousseaux, O. *Journal of the American Chemical Society* **2000**, *122*, 9781.
- (16) Di Bari, L.; Pescitelli, G.; Sherry, A. D.; Woods, M. *Inorganic Chemistry* **2005**, *44*, 8391.

- (17) Ranganathan, R. S.; Raju, N.; Fan, H.; Zhang, X.; Tweedle, M. F.; Desreux, J. F.; Jacques, V. *Inorganic Chemistry* **2002**, *41*, 6856.
- (18) Webber, B. C.; Woods, M. *Inorganic Chemistry* **2012**, *51*, 8576.
- (19) Karplus, M. *Journal of the American Chemical Society* **1963**, *85*, 2870.
- (20) The Nuclear Overhauser Effect. <http://www.chem.wisc.edu/areas/reich/nmr/08-tech-02-noe.htm> (accessed June 17th, 2013).
- (21) Woods, M.; Kovacs, Z.; Kiraly, R.; Brücher, E.; Zhang, S.; Sherry, A. D. *Inorganic Chemistry* **2004**, *43*, 2845.
- (22) Schlesinger, J.; Rajander, J.; Ihalainen, J. A.; Ramesh, D.; Eklund, P.; Fagerholm, V.; Nuutila, P.; Solin, O. *Inorganic Chemistry* **2011**, *50*, 4260.
- (23) Tircso, G.; Webber, B. C.; Kucera, B. E.; Young, V. G.; Woods, M. *Inorganic Chemistry* **2011**, *50*, 7966.
- (24) Delgado, R.; da Silva, J. J. R. F. *Talanta* **1982**, *29*, 815.
- (25) Hancock, R. D.; Motekaitis, R. J.; Mashishi, J.; Cukrowski, I.; Reibenspies, J. H.; Martell, A. E. *Journal of the Chemical Society, Perkin Transactions 2* **1996**, *0*, 1925.
- (26) Aime, S.; Barge, A.; Bruce, J. I.; Botta, M.; Howard, J. A. K.; Moloney, J. M.; Parker, D.; de Sousa, A. S.; Woods, M. *Journal of the American Chemical Society* **1999**, *121*, 5762.
- (27) Cacheris, W. P.; Nickle, S. K.; Sherry, A. D. *Inorganic Chemistry* **1987**, *26*, 958.
- (28) Aime, S.; Botta, M.; Fasano, M.; Marques, M. P. M.; Geraldes, C. F. G. C.; Pubanz, D.; Merbach, A. E. *Inorganic Chemistry* **1997**, *36*, 2059.

**CHAPTER 3. TEMPERATURE DEPENDENCE OF THE PARAMAGNETIC SHIFTS OF LN-2 AND EVIDENCE FOR TIME-AVERAGED STRUCTURAL CHANGES AS A FUNCTION OF WATER EXCHANGE RATE**

The isolation of conformationally rigid chelates with well-defined coordination geometries afforded a unique opportunity to study subtle differences between coordination isomers, free from complications arising due to coordination and/or geometric exchange processes. As described previously, a great deal of useful structural and electronic information about  $\text{Ln}^{3+}$  chelates can be determined by NMR. The broadened lines of the  $^1\text{H}$  NMR peaks in the spectra of  $\text{Ln}^{3+}$  chelates with anisotropic ligand fields (such as  $\text{Eu}^{3+}$ ) are indicative of fast proton relaxation. The transverse relaxation ( $T_2$ ) of an individual proton in these chelates can be estimated by measuring its line-width in NMR spectra at different temperatures. Narrower lines would indicate longer values of  $T_2$ , corresponding to greater flexibility in that portion of the molecule. The line-widths of the  $^1\text{H}$  NMR peaks of Eu-2 chelates are not uniform. It was speculated that comparison of the NMR spectra of Eu-2 chelates (Figure 3.1) at different temperatures might bring to light some novel insight into their structural and/or electronic behavior, including detection of the relative rigidity of portions of the chelate (whether parts of molecule were more susceptible to movement or less so). This might lead to a greater understanding about chelate motion, specifically changes in the conformation of the molecule. It was initially thought that these motions might be due to intermolecular collisions, but these changes could be due to any process causing a conformational change. If geometric isomers (SAP and TSAP) can interconvert, a process which occurs

for all other very rapidly exchanging  $Gd^{3+}$  chelates reported, the small differences in line-widths or shift that could give insights into the structural behavior of the chelates would be obscured. Due to the inverse relationship between Eu-induced shifts (LIS) and temperature (scales as  $T^{-1}$  up to  $T^{-2}$ ), it was expected that each peak's shift would decrease proportionately and uniformly with an increase in temperature.

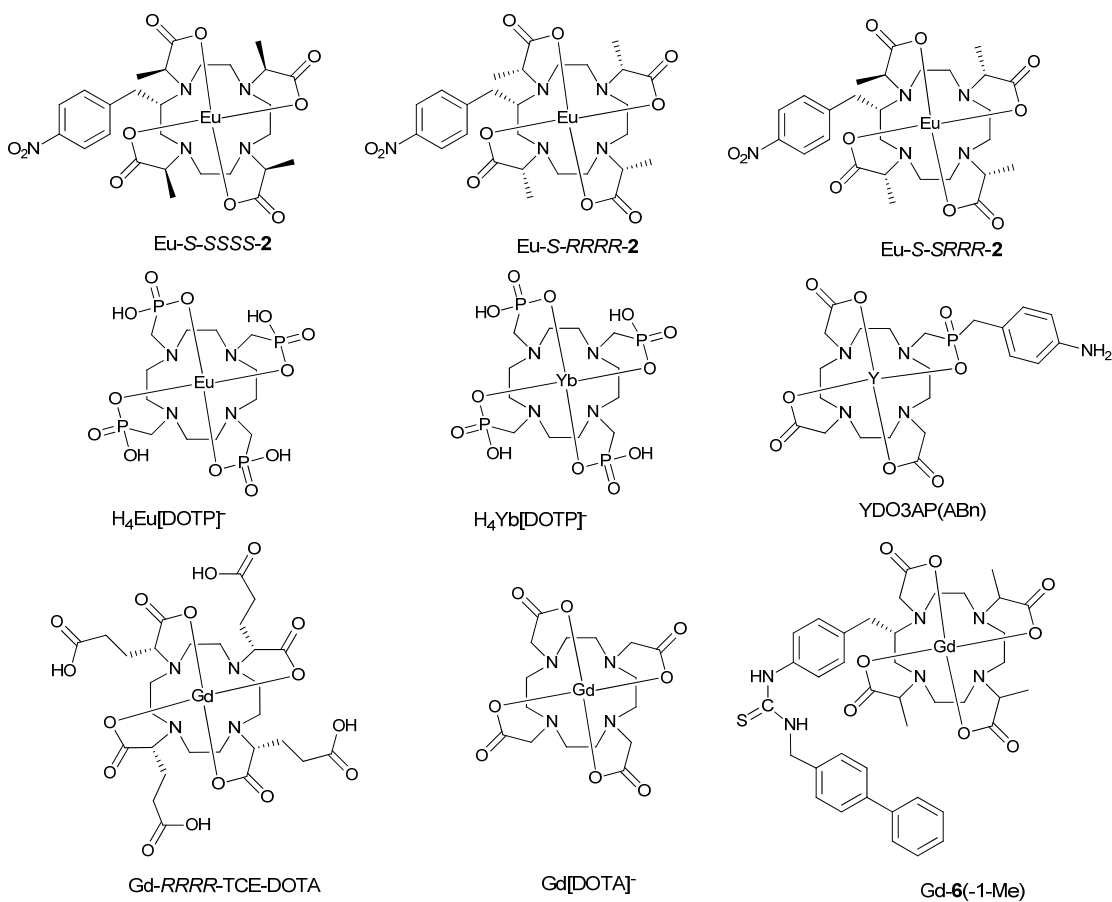


**Figure 3.1:** Chelates referred to in this chapter

### *3.1 Unexpected trends in $^1\text{H}$ NMR spectra of Eu-2 chelates at varying temperatures*

Six isomeric  $\text{Eu}^{3+}$  chelates of **2** were isolated and characterized as described in Chapter 2. A variable-temperature (VT) study of these chelates by  $^1\text{H}$  NMR was then initiated. Proton spectra were acquired for each available Eu-**2** isomer from 5 to 40 °C in 5 degree increments. All VT spectra for a given isomer were acquired using the same prepared NMR sample to avoid observing shift differences due to pH or concentration. The pD of the Eu-**2** NMR samples was not adjusted but was found to lie between 3 - 4. Tetraacetate chelates are known to be the conjugate bases of strong acids and no protonation equilibria occur in this pH range. The temperatures of the NMR probe and sample tube were equilibrated for 5 minutes before acquiring spectra, and the temperature was controlled to within 0.05 °C over the course of an acquisition. Longer equilibration times prior to acquisition did not lead to statistically significant differences in the resultant spectra.

Each peak in each NMR spectrum was assigned to a proton in the structure of Eu-**2** based on the COSY analysis detailed previously. The  $ax^S$ ,  $ax^C$ ,  $eq^S$ ,  $eq^C$ ,  $Me$ , and  $ac$  resonances were tracked carefully across the temperature series based on their shift frequency at 5 °C, peak area, and peak width (Figures 3.2 and 3.3).

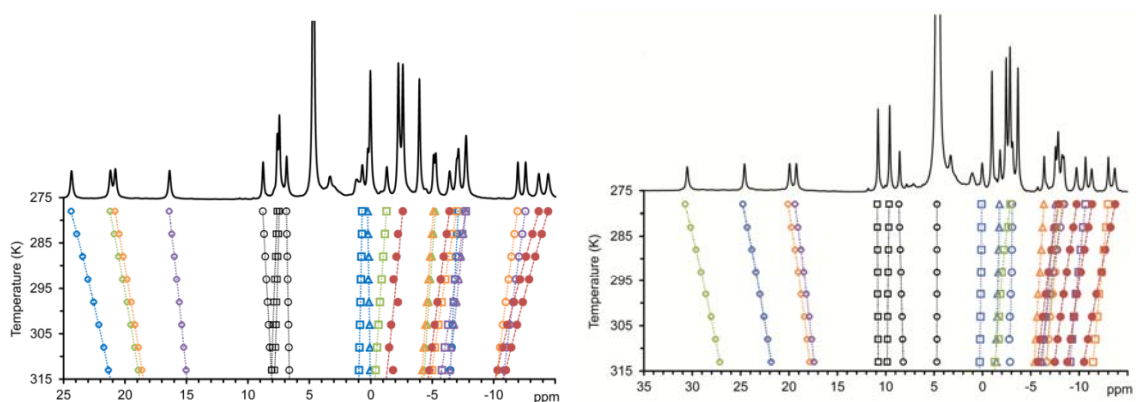


**Figure 3.2:** Variable temperature  $^1\text{H}$  NMR spectra recorded in  $\text{D}_2\text{O}$  at 400 MHz of the ‘corner’ (left) and ‘side’ (right) isomers of Eu-S-SSSS-2. The spectral assignment from COSY data (Chapter 2) was used to show the shifts each proton on a particular ethylene bridge in the same color using open symbols according to the scheme:  $ax^S$  (diamond),  $eq^S$  (square),  $ax^C$  (triangle), and  $eq^C$  (circle). The acetate protons,  $ac$ , are shown as closed red circles; the benzylic protons as black open circles; and the aromatic protons as black open squares. For clarity the temperature dependence of the methyl substituents is not shown.

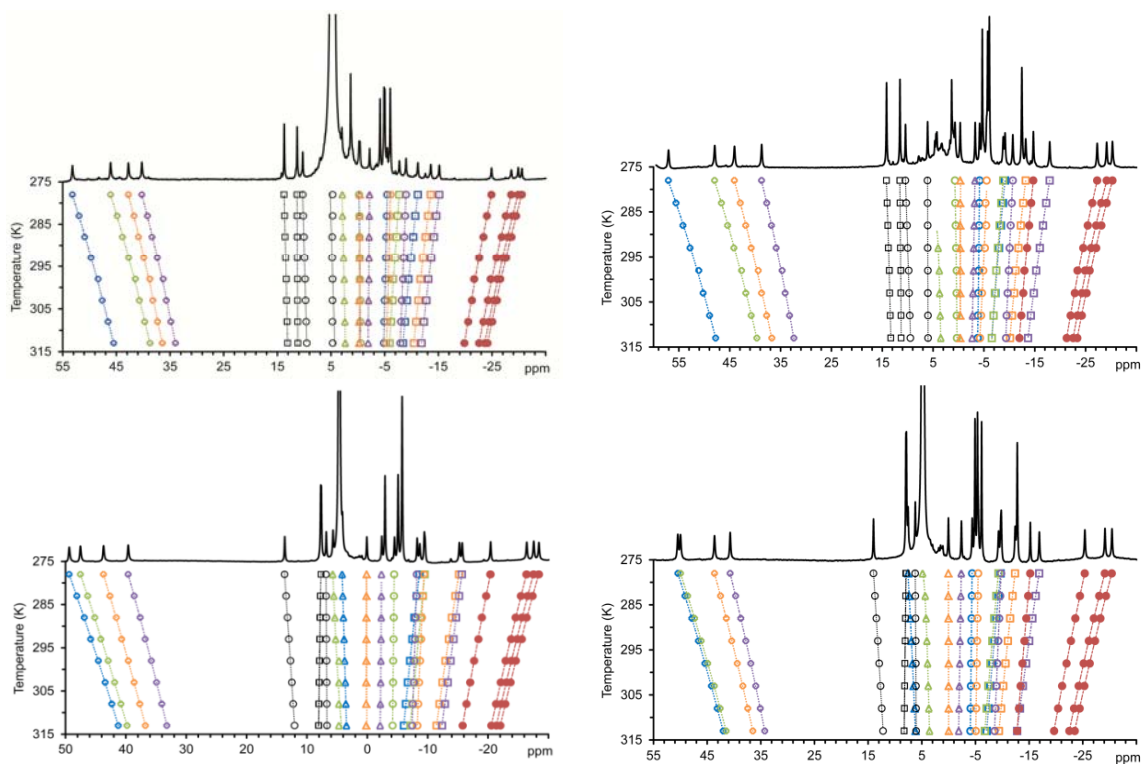


**Figure 3.3:** Variable temperature  $^1\text{H}$  NMR spectra of the side isomer of Eu-S-RRRR-2 (top left), the corner isomer of Eu-S-RRRR-2 (bottom left), the side isomer of Eu-S-SRRR-2 (top right), and the corner isomer of Eu-S-SRRR-2 (bottom right).



Each proton peak showed an extraordinarily linear temperature dependence over the range of temperature values studied. After careful examination of the spectra, it was observed that the sequences of the resonances for Eu-S-SSSS-2 corner and side isomers were changing over the range of temperatures studied. Multiple peaks were observed to change places in the upfield region over the temperature series. The assignments of the rearranged peaks were confirmed by COSY at 40 °C. For each  $ax^S$ ,  $ax^C$ ,  $eq^S$ ,  $eq^C$ ,  $Me$ , and  $ac$  peak, the absolute difference in the shift (in ppm) from 5 to 40 °C was calculated. This difference value was plotted against the chemical shift (in ppm) at 25 °C of each peak for the two Eu-S-SSSS-2 isomers (Figure 3.4).

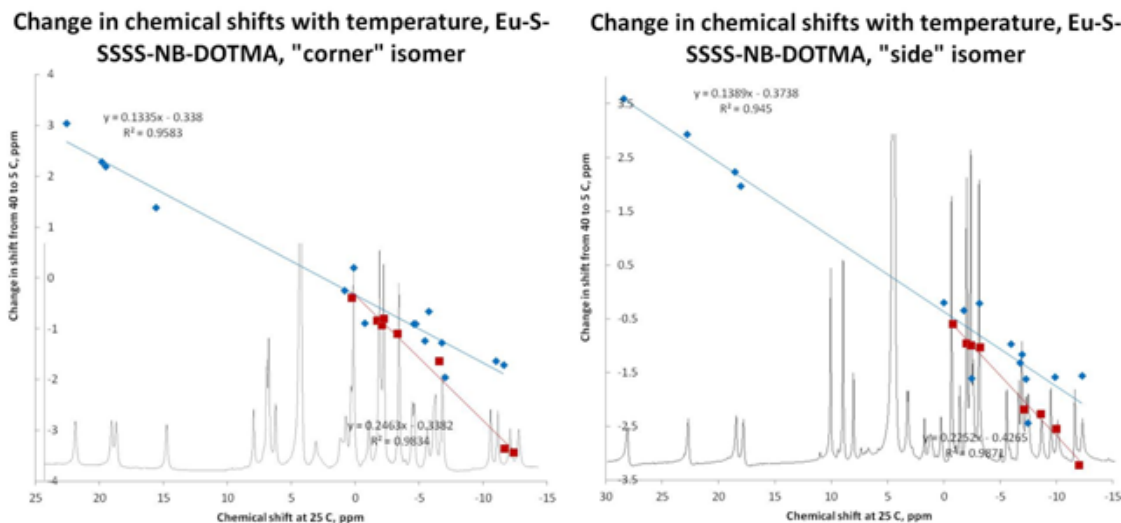


**Figure 3.4:** Absolute change of chemical shift, 5 – 40 °C, as a function of shift at 25 °C. Macrocyclic ring protons ( $ax^S$ ,  $ax^C$ ,  $eq^S$ , and  $eq^C$ ) and their regression fits are shown in blue. Arm protons ( $Me$  and  $ac$ ) and their regression fits are in red.

Further analysis led to the recognition of a pattern where the percent change in shifts of the arm protons with changing temperature was significantly greater than the percent

change in shifts of the ring protons over the same temperature range. The percent change of the shifts follow the trends particularly closely for the most highly shifted (to either lower or higher frequency)  $ax^S$  and  $ac$  proton resonances. The shifts of Eu-S-RRRR-2 and Eu-S-SRRR-2 chelates were observed to change with a lesser temperature dependence than for the Eu-S-SSSS-2 chelates.

### ***3.2 Changes in Eu<sup>3+</sup>-induced <sup>1</sup>H NMR shifts between closely related structures have a spatial dependence***

Variable-temperature NMR studies of Ln[DOTA]-type chelates have been reported previously, for chelates that undergo conformational exchange.<sup>1,2</sup> These chelates, which possess both carboxylate and phosphonate pendant arms on the same ligand, were observed to exchange by <sup>1</sup>H and <sup>31</sup>P NMR spectroscopy between SAP and TSAP forms, and in some cases, between hydrated and dehydrated forms.

There is only one set of shifts in each spectrum of Eu-2. The shifts do not broaden toward coalescence as the temperature increases. These observations indicate that only one chelate is present and not in exchange with any other chelate over the temperature range studied. However, the differing rates of change of the proton shifts cannot be explained solely by the temperature dependence of nuclear relaxation by paramagnetic electrons. Subtle structural changes that occur rapidly and do not change the positions of the shifts substantially could explain the line-width and temperature-dependent shift change behavior. Prototopic exchange and solvent (water) exchange occur too rapidly for distinct structures to be observed by NMR.

*3.2.1 A crystal structure containing a unique type of unit cell provides a basis for structural comparison of  $q = 1$  and  $q = 0$  chelates*

Crystal structures of  $\text{Ln}^{3+}$  chelates having both acetate and phosphonate pendant arms on the same ligand can be found in the literature.<sup>3-7</sup> Some of these chelates are structurally related to Ln-S-SSSS-2 in that they adopt TSAP geometry; like Ln-S-SSSS-2 they also have fast water exchange relative to  $\text{Ln}[\text{DOTA}]$ .

Chelates of the same ligand have been studied across the  $\text{Ln}^{3+}$  series. With decreasing  $\text{Ln}^{3+}$  ionic radius,  $r_{\text{Ln-O}}$  increases until there is no inner-sphere water molecule. Crystal structures of chelates have been found that are effectively isostructural over the course of this change in  $q$  and  $r$ . Several interesting aspects of the coordination geometry of these chelates came to light. There are at least four examples of crystals with a unit cell containing two structures with slightly different geometries (one each for  $\text{Pr}^{3+}$ ,  $\text{Nd}^{3+}$ ,  $\text{Sm}^{3+}$ , and  $\text{Y}^{3+}$ , which typically exist as  $q = 1$  DOTA-type chelates). These structures differ in the length of  $r_{\text{Ln-O}}$ , the “bite” angle of the axial water coordination site, and the relative position of the metal ion between the plane containing the macrocyclic nitrogen atoms (the N4 plane) and the plane containing the chelating pendant arm oxygen atoms (the O4 plane). An explanation for the apparent paramagnetism-temperature anomaly described above was found in crystal structures of a chelate related to Eu-2 and in our understanding of the solution behavior of  $q = 0$  and  $q = 1$   $\text{Ln}^{3+}$  chelates of DOTA derivatives.

Hermann, Lukeš, and co-workers obtained a crystal structure of YDO3AP(ABn) (Figure 3.1) with both  $q = 1$  and  $q = 0$  TSAP chelates in the same unit cell, a previously unknown phenomenon.<sup>4</sup> The two chelates in the crystal are structures which differ with respect to  $q$  and the  $Y^{3+}$  position within the coordination cage. In these chelates, the  $Y^{3+}$  ion is closer to the N4 plane and further from the O4 plane in the dehydrated chelate in comparison to the  $Y^{3+}$  position in the hydrated chelate. Presumably, without a coordinated water molecule, the  $Y^{3+}$  has shifted position closer to the N atoms to satisfy its demand for electron density.

### *3.2.2 Comparison of the structural information given by the LIS with the principal axis of a $Ln^{3+}$ chelate and its paramagnetic field*

Interpretation of the LIS trends in the variable-temperature NMR data yielded qualitative structural information about the chelates. As described previously, the lanthanides' contact and dipolar contributions to NMR shifts have spatial and temperature dependence, according to the equation  $\delta^{obs} = \delta^{dia} + \delta^c + \delta^d$ . For  $Eu^{3+}$  there is a modest through-bond nuclear spin interaction (the contact contribution ( $\delta^c$ )).<sup>8,9</sup> The contact contribution precludes a quantitative calculation of Eu-H distances from the NMR shifts. It has been shown, however, that the most strongly shifted  $ax^S$  and  $ac$  protons in a Eu-DOTA-type chelate are only minimally affected by the contact contribution.<sup>10</sup> For the axial component of the predominating dipolar contribution  $\delta^d$ , the spatial dipolar contribution dependence is described by Equation 3.1:

$$\delta_{ax}^d \propto D \frac{(3 \cos^2 \theta - 1)}{r^3}$$

**Equation 3.1:** where  $D$  is a ligand-field dependent parameter, and  $r$  and  $\theta$  are the distance from the metal center and the angle from the axis of the nucleus affected by the dipole shift.

We can superimpose the dipolar magnetic field induced by the  $\text{Ln}^{3+}$  paramagnetic electrons upon the central axis of the chelate. Consider the relevant protons in the hydrated *versus* dehydrated YDO3AP(ABn). Changing from the former structure to the latter moves ligand protons with respect to the orientation of the Ln's magnetic dipole – some shifts will move upfield and some downfield in the NMR. The nuclei in the blue regions of NMR spectra will experience a shift to lower frequency (upfield), and the nuclei in the red will shift to higher frequency (downfield); the extent of the shift is proportional to the color intensity. By extension, this assumption is applied to the conformationally rigid chelates Eu-2. The protons whose dipolar contributions to their chemical shifts will be affected most are the  $ax^S$  and  $ac$  protons, due to their respective positions in the magnetic field induced by the paramagnetic electrons (superimposed density map, Figure 3.5).

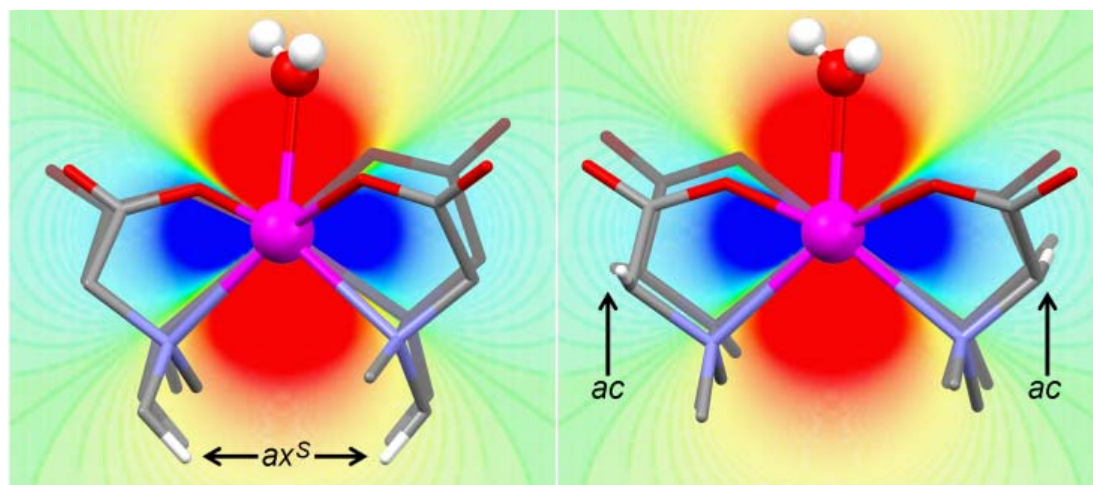
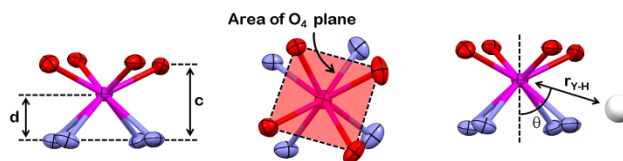


**Figure 3.5:** Structural comparison of the isomeric  $q = 1$  and  $q = 0$  YDO3AP(ABn) chelates contained in the crystal structure. The axial contribution of the dipolar shift is shown superimposed in a “heat map.” The hydrated structure is shown in front and the shadowed structure (rear) is the  $q = 0$  structure.

The angle and distances of hydrated and dehydrated YDO3AP(ABn) relative to the central axis of the chelate have been computed, and combined into one axial geometric parameter ( $G$ ) (Table 3.1), where  $G = (3\cos^2\theta - 1)/r^3$ , the same axial dependence as  $\delta^d$ :



	mono-hydrated	dehydrated
$q$	1	0
Y-OH <sub>2</sub> (Å)	2.485	N/A
$c$ (Å)	2.421	2.559
$d$ (Å)	1.660	1.531
$d/c$	0.69	0.60
N <sub>4</sub> -O <sub>4</sub> (°)	26.79	-26.08
N-C-C-N (°)	56.67	-57.95
Area of O <sub>4</sub> plane (Å <sup>2</sup> )	9.55	8.31
<b>ac</b>		
$r_{Y-H}$ (Å)	3.43	3.47
$\theta$ (°)	81.68	82.85
$G$ ( $\times 10^3$ )	-22.88	-23.21
$G_{q=1} - G_{q=0}$ ( $\times 10^3$ )		-0.33
<b>ax<sup>s</sup></b>		
$r_{Y-H}$ (Å)	3.66	3.68
$\theta$ (°)	14.55	25.07
$G$ ( $\times 10^3$ )	29.26	36.88
$G_{q=1} - G_{q=0}$ ( $\times 10^3$ )		7.62

**Table 3.1:** Calculation of geometric parameters in the crystal structures of YDO3AP(ABn). The values represent averages of the four ax<sub>s</sub> and ac protons.

With respect to the central chelate axis, it is apparent from the table that the average position of the *ac* protons (described by the *G* value) changes little from hydrated to dehydrated chelate compared with the average position (*G* value) of the  $ax^S$  protons. A  $q = 1$  DOTA-type chelate is not hydrated all of the time; it is rapidly exchanging water molecules in solution. There must be some point in time at which this  $q = 1$  chelate is dehydrated. If the two solid state structures of YDO3AP(ABn) above are representative of the solution structures, the dehydrated version of a  $q = 1$  chelate in solution closely resembles its hydrated structure but differs by *G* values calculated as above. Though there are a limited number of data points, the line-widths of the *ac* proton peaks are greater than those of the  $ax^S$  peaks in Eu-*S*-SSSS-**2**, indicative of faster relaxation and a closer spatial relationship (compared with average  $r_{Y-H}$  values of 3.43 Å (*ac*) vs. 3.66 Å ( $ax^S$ ) in the hydrated YDO3AP(ABn) chelate).

### *3.2.3 Comparison of the temperature dependence of Eu-2 chelates to a chelate with no inner-sphere water exchange*

To examine whether the shift change patterns were related to an exchange process in Eu-**2** chelates, the variable-temperature spectra of the  $q = 0$  chelate  $\text{Eu}[\text{DOTP}]^{5-}$  (Figure 3.1), were acquired. The DOTP ligand was purchased as its acid ( $\text{H}_8\text{DOTP}$ ) from which the corresponding  $\text{Eu}^{3+}$  and  $\text{Yb}^{3+}$  chelates were synthesized as described in the experimental section. For each NMR sample of  $\text{Ln}[\text{DOTP}]^{5-}$ , the pD was set in the range 10-11 to ensure complete deprotonation of the phosphonates, eliminating the possibility that protonation equilibria of the phosphonates could interfere with the change in shifts of the



chelate.<sup>7</sup> The percent shift change (calculated using the average shift, in ppm) of the  $ax^S$  (ring) and  $ac$  (arm) protons from the 278 K shifts was plotted against temperature for each of the 6 isomeric Eu-**2** chelates studied, as well as for  $\text{Eu}[\text{DOTP}]^{5-}$  (Figure 3.6). Error bars represent the variance across the four protons for each type being averaged.

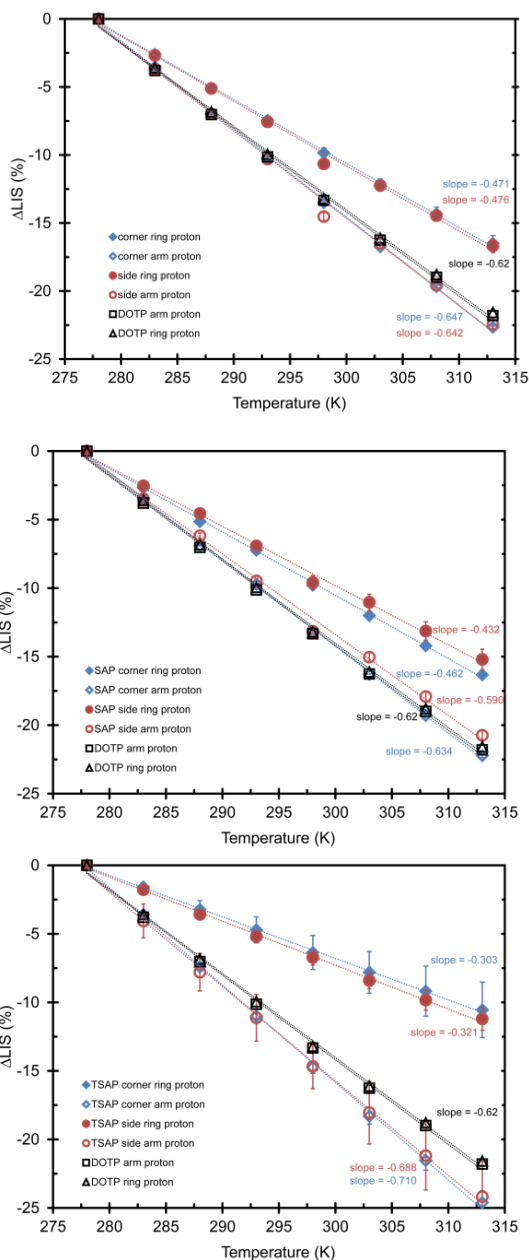


**Figure 3.6:** Comparison of the temperature dependence of SAP S-SRRR (top), SAP S-RRRR (middle), and TSAP S-SSSS (bottom) regioisomeric Eu-2 chelates with Eu[DOTP]<sup>5-</sup>. Peaks from the side isomers are in red, from the corner isomers are in blue, and for DOTP are in black. The arm (*ac*) protons are the open symbols and the ring protons (*ax<sup>S</sup>*) are the closed symbols.

$\Delta LIS$  is the percent difference of the average magnitude of the *ax<sup>S</sup>* or *ac* shifts between the 278 K spectrum of a particular isomer and the average of the same proton shifts at a higher temperature. For example,

$$\Delta LIS_{ax^S}(\%) = \frac{\sum_1^4 ax^S \delta(T) - \sum_1^4 ax^S \delta(278)}{\sum_1^4 ax^S \delta(278)} \times 100\%$$

where  $(\sum ax^S \delta)/4$  gives the average of four shifts of a particular proton type, either *ax<sup>S</sup>* or *ac* at a specific temperature. Dividing each sum term in the above expression by 4 reduces to the same equation.

For the non-water-exchanging chelate Eu[DOTP]<sup>5-</sup>, shifts of both arm and ring protons vary uniformly as a function of temperature. The temperature-shift dependence of the *ax<sup>S</sup>* and *ac* protons for chelates undergoing water exchange deviated from the shift

dependence of the continuously dehydrated chelate. The average temperature dependence of the  $ax^S$  shifts are similar for all 6 Eu-2 chelates studied, changing at a lesser rate with temperature than the  $\text{Eu}[\text{DOTP}]^{5-}$   $ax^S$  protons. The temperature dependence of the  $ac$  proton shifts are similar for all 6 Eu-2 chelates studied, changing at a nearly identical or slightly greater rate with temperature than the  $\text{Eu}[\text{DOTP}]^{5-}$   $ac$  protons. The regiochemistry does not seem to affect the overall trends observed. The  $G_{q=1} - G_{q=0}$   $ac$  values in YDO3AP(Bn) are of opposite sign and an order of magnitude smaller than for the  $ax^S$   $G$  value difference. Comparison of the VT data with the  $G$  value and  $\delta^d$  relationship above suggests that temperature-dependent structural changes are occurring in Eu-2 which are not occurring for  $\text{Eu}[\text{DOTP}]^{5-}$ .

### **3.3 VT data for Yb-2**

If it were possible to use the NMR data to calculate the  $G$  values of each proton using Equation 3.1, the structure of the ligand in solution could be determined. The structures of SAP and TSAP isomers of Eu-2, or of the same isomer at different temperatures, could be calculated and compared with the crystallographic data of YDO3AP(ABn) above. In this way, the progression of time-averaged  $r_{\text{Ln-O}}$  could be estimated based on the relationship between  $d/c$  ratio and  $r$ .<sup>11</sup> It is unfortunately not possible to calculate  $T_2$  values from the line-widths of  $\text{Eu}^{3+}$  chelates, but it is possible for  $\text{Yb}^{3+}$  chelates.

A VT series of  $^1\text{H}$  NMR data for Yb-2 (corner isomers, SAP and TSAP) were analyzed to see if the same trends in  $\% \Delta \text{LIS}$  vs. temperature would be observed. If so, quantifying the average position of the lanthanide in the coordination cage with changes in water

exchange rate might be possible. In  $\text{Yb}[\text{DOTP}]^{5-}$ , the percent change in arm and ring shifts are also identical as a function of temperature. A plot (Figure 3.7) of percent shift change of  $ax^S$  and  $ac$  protons compared with the 5 °C spectrum shows a trend similar to that of Eu-2.

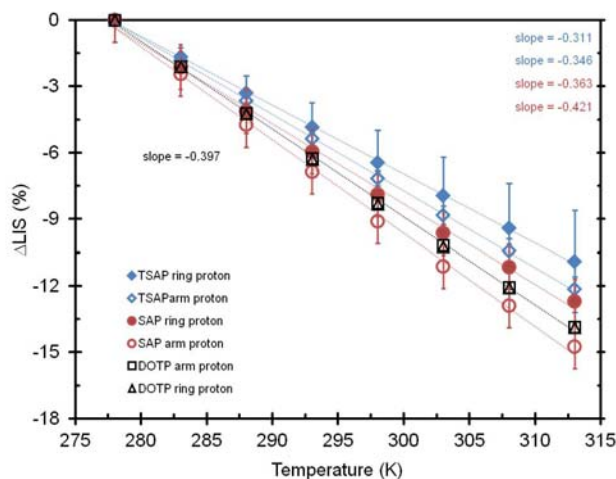


**Figure 3.7:** Shift change as a function of temperature in Yb-2 vs.  $\text{Yb}[\text{DOTP}]^{5-}$

The difference between the slopes obtained for the arm ( $ac$ ) and ring ( $ax^S$ ) protons of Yb-2 chelates are not as great as for the Eu-2 chelates, but the difference in the change in the shifts of each are statistically significant. As the  $\text{Yb}^{3+}$  ion is approximately 10% smaller than  $\text{Eu}^{3+}$ , it is likely that increasing the temperature over the same relatively narrow range does not accelerate water exchange proportionally for complexes of the two lanthanides, even considering the same geometric and regio- isomer. The water exchange rate for Yb-2 is already very fast and cannot be accelerated much further. Unfortunately, the data do not tell us anything about the relative activation energies for water exchange in  $\text{Eu}^{3+}$  vs.  $\text{Yb}^{3+}$  chelates. The macrocyclic ring may be significantly more distorted about a smaller ion from the steric strain induced by the nitrobenzyl group, leading to the

large variability of the four  $ax^S$  and  $ac$  shifts relative to the average shift temperature dependence. The VT data of the  $Yb^{3+}$  analogues are more difficult to interpret with respect to solution-state structural parameters in Gd-2 owing to the smaller ionic radius of  $Yb^{3+}$ .

### *3.4 Examination of the prevailing view of hydration state of MRI CAs in light of new evidence*

The exchange of water molecules in Ln[DOTA]-type chelates is known to occur by a dissociative mechanism.<sup>12,13</sup> The picture (Figure 3.8) of solvent exchange by dissociative mechanism in inorganic chemistry has held constant for over 40 years.<sup>14</sup> In this picture, the following occurs in discrete steps: a solvent molecule is lost, reducing the coordination number by one, to form an intermediate that closely resembles the initial state. Then, a new solvent molecule is bound, increasing the coordination number to its original value. There is no mention in this mechanism of the time or distance progression of the leaving solvent molecule or of the newly ligating solvent molecule. It is almost as if the water molecule transitions between two quantum states. The dissociative mechanism picture is the widely accepted way in which Ln[DOTA]-type chelates behave in solution.<sup>15-17</sup>

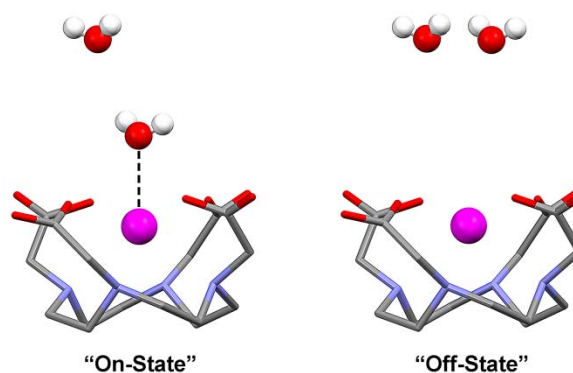


**Figure 3.8:** Dissociative exchange of a water molecule from Ln[DOTA]<sup>-</sup>

Under our current understanding, NMRD data are interpreted in terms of single values for each parameter<sup>18</sup> and rarely are fits using more than one value reported.<sup>19</sup> The parameter  $r_{\text{Ln-H}}$  in particular is treated as a constant in development of Ln[DOTA]-type chelates except in a few isolated studies.<sup>20,21</sup> However, solution structure is never without motion for Ln<sup>3+</sup> chelates which are bound by electrostatic forces, even in highly ordered, symmetric, rigid systems.

#### 3.4.1 The treatment of $q$ and $r$ as separate, static parameters provides an incomplete description of solution structure and dynamics

The properties of the chelates examined above can be used as a model to help us to revise our understanding of the relationships between temperature, water exchange, structure, and <sup>1</sup>H shifts. Let us assume that the  $q = 1$  and  $q = 0$  crystal structures of YDO3AP(ABn) represent the structural extremes of the dissociative exchange model. In solution, the water exchange process would lead to a transformation of the  $q = 1$  structure to resemble the  $q = 0$  structure on the time scale of  $\tau_M$ . The Ln<sup>3+</sup> “drops” in the

coordination “cage” from its position closest to the O4 plane to its position closest to the N4 plane in this same time span.

We can look at the differences between  $q$  and  $r_{Ln-H}$  in slower and faster exchanging chelates in attempt to fill the gaps in our understanding of how these parameters are related. Using what information could be gained from the crystal structures, the  $r_{Ln-O}$  values for structurally related TSAP and SAP chelates were compared in Table 3.2.<sup>22,23</sup> These data were compared with  $Eu^{3+}$  (as a surrogate for  $Gd^{3+}$ ) luminescence data in solution, in which  $r_{Ln-O}$  is slightly longer than in the crystal, regardless of chelate.<sup>24,25</sup>

Chelate	Coordination Geometry	$r_{Gd-O}$ (Å)	$q$
Gd-TCE-DOTA	SAP	2.43	-
Eu-S-RRRR-2	SAP		0.97
Gd-DOTMA	TSAP	2.50	-
Eu-S-SSSS-2	TSAP		0.74

**Table 3.2:** Differences in  $q$  and  $r_{Ln-O}$  dependent on coordination geometry.  $r^{TSAP}/r^{SAP} = 102.8\%$  in the crystal.

How can we rationalize a  $q$  value of approximately 0.75? One explanation which gives this value physical meaning is if a chelate has an inner-sphere water molecule only 75% of the time. To look at another way, by the ergodic principle, at a given moment  $3/4$  of the chelates in the solution are hydrated. This population explanation has been given as a reason for the coordination chemistries of some smaller lanthanide ions<sup>26</sup>, but never

before for  $Gd^{3+}$  or for the larger lanthanides including  $Pr^{3+}$ ,  $Nd^{3+}$  or  $Sm^{3+}$ . Work from Parker and co-workers provides an alternate explanation for the luminescence data – that the quenching of  $Eu^{3+}$  excited states is dependent on both  $q$  and  $r_{Ln-O}$ .<sup>25</sup> The -OH oscillators proximal to Eu used to determine  $q$  by Horrocks' method also have an  $r^{-6}$  distance dependence. On this basis we can calculate that  $r_{Ln-O}$  is approximately 4.5% longer in the TSAP vs. SAP chelates in solution by data in Table 3.2 and Equation 3.2:

$$\frac{r^{TSAP}}{r^{SAP}} = \left( \frac{q^{TSAP}}{q^{SAP}} \right)^{-6}$$

**Equation 3.2:**  $q^{SAP}/q^{TSAP} = 131.1\%$  from the data in Table 3.2.  $q$  and  $r_{Ln-O}$  were determined to have a direct relationship based on Horrocks' method and modifications to correct for other luminescence quenching mechanisms.

Clearly there are difficulties in measuring  $q$  and  $r_{Ln-H}$  separately. When the Ln-OH<sub>2</sub> interaction is in the process of a bond “breaking” or “forming” event (Figure 3.9), one can consider the hydration state of the metal as a function of  $r_{Ln-O}$  in two ways – both descriptions of the same process. The chelate is either always  $q = 1$  as the water molecule moves further away from Ln<sup>3+</sup> until it is no closer to the metal than the next closest water molecule. Or, the value of  $q$  decreases proportionately with  $r_{Ln-O}$  during this process. The first view does not provide a complete description of the hydration state during water exchange, while the second describes parameters that cannot be measured independently in solution.



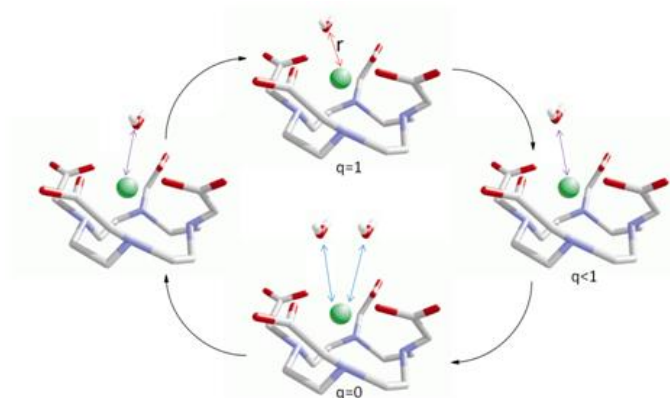


**Figure 3.9:** A representation of the dissociative inner-sphere water exchange mechanism in Ln[DOTA]-type chelates

However, a single parameter could be used to describe both aspects of the inner-sphere water molecule. The parameter  $q/r^6$  is appropriate for describing the hydration state of Ln[DOTA]-type chelates in solution. Precedent for this parameter exists<sup>27</sup>, and can be used to differentiate between geometries which exchange water at different rates.

#### 3.4.2 Variable-temperature NMR data yield a time-averaged coordination geometry and hydration state

The length of time a chelate which exchanges inner-sphere water is in the fully dehydrated state (the structure which has the maximum  $r$  value, represented in the bottom structure in Figure 3.9) is very short (but finite). The amount of time a particular chelate spends in the fully dehydrated state is not expected to change substantially with changes in the water exchange rate. This picture of hydration equilibrium also means that  $\tau_M$  is not exactly the inverse of water exchange rate where water exchange ( $1/k_{ex}$ ) is extremely fast, as is commonly assumed in these systems.  $\tau_M$  will be slightly shorter as it does not

include the time in the  $q = 0$  state;  $k_{ex}$  includes the time required for a new water molecule to “bind.” The  $k_{ex}$  of any ligand increases with increasing temperature, and there will be more dissociative events for a fast-water-exchanging complex than a slow-water-exchanging complex in a given amount of time (Figure 3.10).

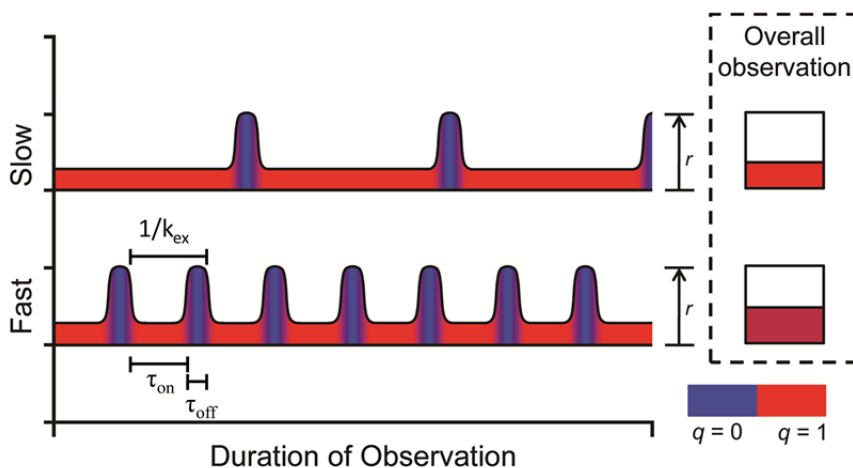


**Figure 3.10:** Color bars representing the distance of the inner-sphere water molecule from  $\text{Ln}^{3+}$  as a function of time. The color in the overall observation represents an

average  $r$  across the entire hypothetical time window.  $\frac{1}{k_{ex}} = \tau_{on} + \tau_{off}$

We are not making any claims about the progression of metal-water distance; the simplistic model above accounts only for the fact that there is a minimum and maximum  $r_{\text{Ln-O}}$  and that the water molecule’s position cycles between the two more often with faster water exchange. The modeled distance ( $r_{\text{Ln-O}}$ ) over a hypothetical time interval ( $t$ ) was averaged (depicted in the final bar in Figure 3.10 with color matching the time-averaged  $r_{\text{Ln-O}}$ ). Regardless of  $r_{\text{Ln-O}}$  and  $t$ , it is clear that the chelate spends more time in the state with the water furthest from the metal ion when the exchange rate is increased (due to coordination geometry of the ligand or due to temperature).

Changing the water exchange rate, either by changing the temperature or selecting a different coordination geometry, is assumed to be the prime determinant of the portion of time the chelate spends in its maximum hydration state (distance of closest inner-sphere water molecule approach). The relative amounts of time the water is in the hydrated *versus* the dehydrated state over the entire chelate population is what leads to the observed time-averaged structure and  $r_{\text{Ln-H}}$  (alternatively,  $q/r^6$ ) and by extension the observed LIS. The  $ax^S$  and  $ac$  shifts would only vary uniformly with temperature provided that the coordination geometry does not change with changes in temperature (a static structure). We propose that the differing LIS temperature dependence of the  $ax^S$  and  $ac$  protons are direct evidence for a time-averaged coordination geometry that does change with changes in temperature. As the temperature increases, the water exchange rate increases and the time-averaged conformation of the chelate becomes closer to that of the dehydrated structure (Figure 3.11).

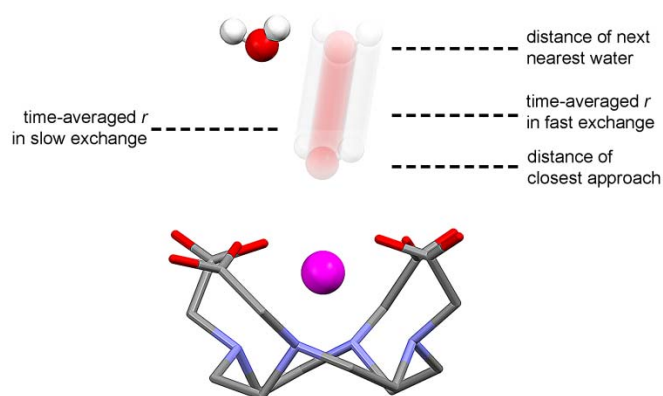


**Figure 3.11:** A model for average Ln-OH<sub>2</sub> distance as a function of exchange rate under dissociative exchange conditions.

The time-averaged conformation of the chelate is dependent upon the water exchange rate, which has a temperature dependence. The main force acting upon the temperature dependence of the shifts of protons in Eu-2 is a geometry-specific dynamic behavior (the percent of the time the chelate exists in the dehydrated state or the state with the largest value of  $r_{\text{Eu-O}}$ ). It is unsurprising that the  $ac$  shifts in Eu-2 follow a temperature dependence close to  $\text{Eu}[\text{DOTP}]^{5-}$  – the  $G$  value does not change significantly from the hydrated to the dehydrated form of YDO3AP(ABn). However, there is a more substantial change in  $ax^S$   $G$  value between the hydrated and dehydrated chelates. This is manifest in the overall structure of the population of chelates, averaged over time, bearing greater resemblance to a structure with longer  $r$ . Therefore, there is greater deviation of the temperature dependence of the  $ax^S$  shifts in Eu-2 from those of  $\text{Eu}[\text{DOTP}]^{5-}$  with a greater change in water exchange rate from the reference point for shift change calculation. Further, the divergence of the Eu-2 shifts from  $\text{Eu}[\text{DOTP}]^{5-}$  shifts with increasing temperature is more pronounced in the TSAP chelates (which exhibit faster water exchange) than in the SAP chelates. In summary, the deviance in the shifts from simple temperature-dependent paramagnetic behavior indicates a change in time-averaged structure due to changes in water exchange rate. These observations are the first, to our knowledge, to provide evidence for movement of the  $\text{Ln}^{3+}$  within the macrocyclic cage for an isostructural chelate in solution.

$\text{Eu}^{3+}$  luminescence can also be used to determine the number of hydrated species in solution.<sup>28</sup> Each luminescence spectrum of Eu-2 reported<sup>29</sup> shows only one  ${}^5\text{D}_0 \rightarrow {}^7\text{F}_0$  transition, meaning either that the hydration equilibrium is fast in comparison to the

luminescent time scale, or the energies of multiple species are not sufficiently different to distinguish between hydration states. This finding coincides with the argument for the structural similarity and rapid equilibrium between  $q = 0$  and  $q = 1$  chelates above. The analytical techniques employed can be compared to the use of a camera. It has become clear that the difficulty of observing and quantifying structural changes in solution relating to  $q$  and  $r$  is a problem of “shutter-speed.” Water exchange and the corresponding structural changes of ligand and metal ion are occurring too rapidly to be observed directly by NMR and luminescence spectroscopy for the Ln-2 chelates studied. We can see only a time-averaged “snapshot” of these dynamic processes. Due to the lack of other motions (such as conformational or coordination geometry changes) on the same time scale in our “rigid” chelates, the picture we see is sharply defined as opposed to poorly resolved.

The Yb<sup>3+</sup> VT data suggest that the generally held assertion that TSAP Yb-DOTA-type complexes are  $q = 0$  (primarily stemming from crystallographic studies) is incomplete ( $q$  values of up to 0.54 have been determined for these chelates by luminescence studies).<sup>25,30,31</sup> The time-averaged hydration state ( $q/r^6$ ) for Yb-DOTA-type chelates may be too small to be considered as having an inner-sphere water molecule. However, our data suggest that the coordination cage is “breathing” in solution in a similar way to that of an inner-sphere water-exchanging Eu<sup>3+</sup> chelate. The likeliest explanation for this dynamic behavior is an exchanging inner-sphere water molecule which does not approach the metal closely, and for any given moment in time, the population of chelates with an inner-sphere water molecule is small compared to chelates without.

Crystallographic data for the heavier (smaller) lanthanides in mixed acetate/phosphonate chelates, as mentioned earlier, and in Ln[DOTMA]<sup>-</sup> complexes<sup>32</sup> provide additional support for these interpretations. It would be interesting to look for a trend across the lanthanide series of VT changes in LIS for  $ax^S$  and  $ac$  protons in Ln-2 or another conformationally rigid chelate. The magnetic susceptibilities of most of the paramagnetic lanthanides make this impractical; the resonances are significantly broadened in comparison with those of Yb<sup>3+</sup> and Eu<sup>3+</sup> LIS and would lend a great deal of inaccuracy to plots of absolute shift changes.

### *3.4.3 Reviewing the relaxivity behavior of conformationally rigid SAP and TSAP chelates bound to slowly tumbling species*

Two isomeric, conformationally rigid chelates (Gd-S-SSS- and Gd-S-RRR-6(-1-Me)) having differing water exchange rates were prepared and their relaxivities measured.<sup>33</sup> The slower-exchanging isomer afforded greater relaxivity, in direct opposition to models derived from SBM theory and accepted by the MRI CA community at large. The plots of relaxivity *versus* magnetic field strength (NMRD profiles, Figure 3.12), make it clear that the relevant difference arises from a parameter which scales with  $r_1$  at all fields; either  $q$  or  $r_{Ln-H}$  (top spectrum).

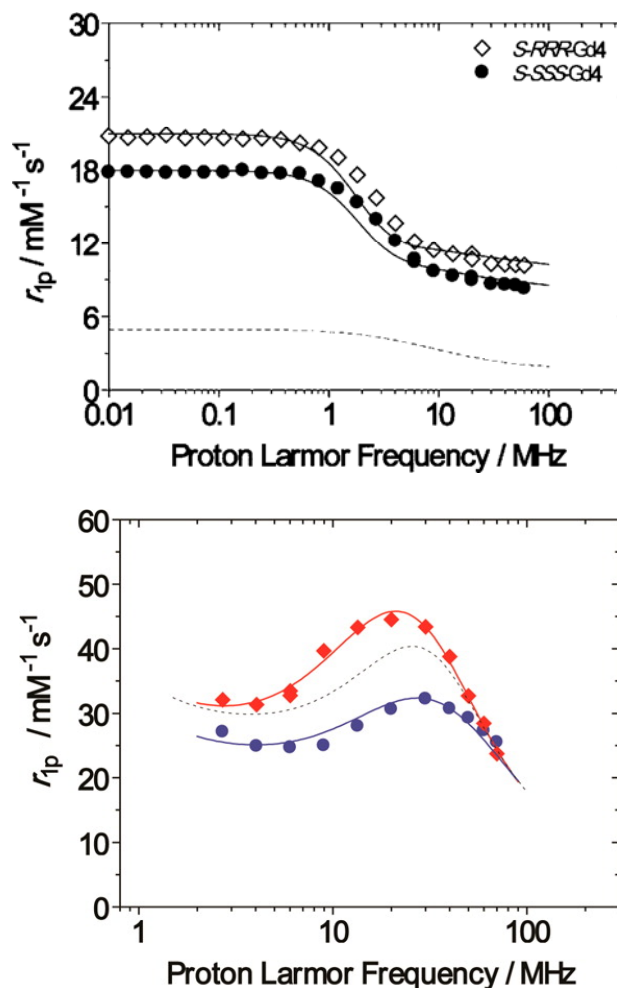


**Figure 3.12:** The NMRD profiles of  $S\text{-RRR-Gd-6(-1-Me)}$  (SAP, diamonds) and  $S\text{-SSS-Gd-6(-1-Me)}$  (TSAP, circles). The top profiles were obtained at  $0.2 \text{ mM Gd}^{3+}$ . The dashed line in the top profile is the diamagnetic relaxation rate of pure water. The bottom profiles were obtained at  $0.17 \text{ mM Gd}^{3+}$  and in the presence of  $6 \text{ mM poly-}\beta\text{-CD}$  at  $25 \text{ }^\circ\text{C}$ . The bottom dashed line is a simulated profile using the fitting parameters from the profile of  $S\text{-RRR-Gd6(-1-Me)}$  but applying the water exchange parameters  $\tau_M$  and  $r_{\text{Gd-H}}$  from the  $S\text{-SSS-Gd6(-1-Me)}$  profile. The ligand is referred to as compound **4** in the reference.<sup>33</sup>

When bound to slowly tumbling molecules human serum albumin (HSA) and poly- $\beta$ -cyclodextrin, the slower-exchanging isomer again showed higher relaxivity (bottom

spectrum). Our results show that the time-averaged  $q/r^6$  may be longer than was previously assumed, particularly for the fastest-exchanging Ln[DOTA]-type chelates, and this is almost certainly leading to depressed  $r_1$  values in comparison to that which is predicted by SBM theory. In light of this evidence, it is not wholly accurate to assign values to the parameters  $q$ ,  $r$ , and  $\tau_M$  based on static structures. To optimize, fit, or treat  $q$ ,  $r$ , and  $\tau_M$  independently in solution relaxation measurements is an incomplete description of the system; they should be considered ensemble. A major consequence of this work is the realization is that the optimum water exchange rate may be slower than previously calculated for a given imaging field strength, and that it may not be possible to achieve the maximum relaxivity gains modeled in the SBM curve (Figure 1.8). This realization is likely the explanation for the higher relaxivities observed for the SAP isomers of Gd-6(-1-Me)<sup>33</sup> and Gd-6 (this work) in comparison to those of the TSAP isomers when bound to slowly tumbling species. Additionally, the temperature and isomer dependence of water exchange rates should vary differently between systems; the optimal value for  $\tau_M$  for contrast agents based on Ln[DTPA]<sup>2-</sup> or other chelates should be determined independently and cannot be predicted based on the Ln[DOTA]<sup>-</sup> system. A thorough understanding of how the critical parameters  $q$ ,  $r_{Ln-H}$ , and  $\tau_M$  may vary and be interrelated in a compound undergoing exchange is necessary for the design of more effective CAs.



### **3.5 Further research/future directions**

#### *3.5.1 Measuring $q/r^6$ by variable-temperature luminescence and X-ray absorbance spectroscopy*

In an attempt to obtain additional evidence for a change in time-averaged  $q$  as a function of water exchange rate, homochiral corner SAP and TSAP isomers of Eu-**2** were sent to the laboratory of Dr. Ana de Betancourt-Dias for variable-temperature luminescence lifetime analysis. Using Parker's modifications to Horrocks' method,  $q$  values will be calculated for these chelates in solution.<sup>28,29</sup> These data may confirm our theory that  $q/r^6$  varies differently in solution with differing coordination geometry and temperature. We believe that the inner-sphere water molecule spends increasingly less time associated with the lanthanide as the temperature is increased, and that these changes will be more evident for the TSAP isomer, both leading to lower experimental values for  $q$ .

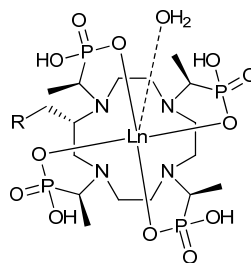
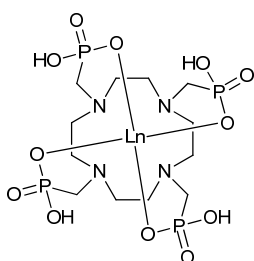
Further research into the structural changes due to varying water exchange rates will be conducted on the conformationally rigid Gd-**2** chelates. These chelates, purified as single regio- and diastereoisomers, were sent to the laboratory of Dr. N. Blackburn at Oregon Health and Sciences University. Collection of EXAFS data will be attempted at the Stanford synchrotron (SSRL) in collaboration with Dr. Blackburn's lab, and the median Gd-O distance as well as the Gaussian distribution could be determined for isomeric Gd-**2** species. The resolution of this technique may or may not be sufficient to distinguish between isomeric chelates.  $q$  and  $r_{\text{Gd-H}}$  (estimated from  $r_{\text{Gd-O}}$ ) parameters obtained from these measurements could be used to re-fit NMRD profiles and from variable temperature

$^{17}\text{O}$  NMR data determined in collaboration with Dr. M. Botta. Activation volumes (from variable-pressure NMR data) will be determined in the laboratory of Dr. L. Helm at the École Polytechnique Fédérale de Lausanne in Lausanne, Switzerland, and the energetics of water exchange will be computed.

*3.5.2 Assessment of water exchange rate and molecular probe capability of a DOTA-type chelate with phosphonate pendant arms*

DOTA-derivatives with four phosphonate pendant arms show very fast water exchange. Previous phosphonate/phosphinate chelates possessing achiral pendant arms were studied and determined to be octacoordinate and adopt TSAP geometry. They do not have an inner-sphere relaxivity contribution as they are  $q = 0$  chelates. If a macrocyclic ligand with phosphonate pendant arms of appropriate chirality could be synthesized, it might be possible to “force” the chelate to adopt SAP geometry (Figure 3.13). In addition to the relaxivity benefits of a conformationally rigid,  $\tau_{\text{M}}$ -optimized chelate, changing the ligating group from carboxylate to phosphonate monoester arms is projected to endow the agent with molecular ‘probe’ capabilities.

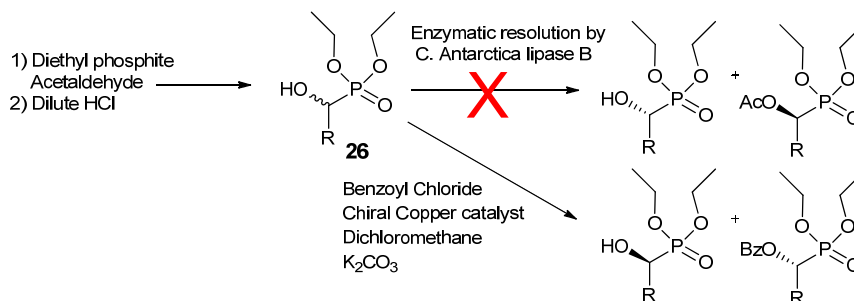
$\text{H}_4\text{Ln}[\text{DOTP}]$ , fluxional helicity,  
TSAP,  $q = 0$



$\text{H}_4\text{-S-RRRR-Ln}[\text{DOTP}]$ , conformationally rigid,  
expected SAP,  $q = 1$ ?

**Figure 3.13:** Design of a DOTP-type chelate with possible SAP geometry and  $q = 1$

The SAP geometry has a more “open” O4-plane in general for DOTA-type chelates and a SAP analogue of  $\text{Ln}[\text{DOTP}]^{5-}$  is predicted to have a greater hydration state than the TSAP  $\text{Ln}[\text{DOTP}]^{5-}$ , which could increase the relaxivity. Work was begun on the synthesis of a chiral phosphonate arm (Scheme 3.1). The first step in this synthesis was to prepare enantiomerically pure ( $> 98\%$  enantiomeric excess (*ee*)) phosphonate esters. The resulting  $\alpha$ -hydroxy chiral phosphonates would be activated and used to alkylate macrocyclic ligands. Enantiomeric enrichment was attempted by converting one stereoisomer of the racemic alcohol to an acetate (in the presence of an enzyme)<sup>34</sup> or benzoate (in the presence of a chiral catalyst).<sup>35</sup>



**Scheme 3.1:** Preparation of enantiomerically enriched phosphonate esters where R = Methyl or Phenyl. Note that the reaction is not enantiospecific – several enrichment steps and subsequent purifications are required to obtain >98% ee.

The percent *ee* could not be verified for the enzymatic resolution experiment. The benzoyl chloride route leads to enantiomeric enrichment on a very small scale, but is not applicable to scaling up. Future work on chiral phosphonates will employ different starting materials.

### 3.6 References

- (1) Polášek, M.; Kotek, J.; Hermann, P.; Císařová, I.; Binnemans, K.; Lukeš, I. *Inorganic Chemistry* **2008**, *48*, 466.
- (2) Vitha, T.; Kubicek, V.; Kotek, J.; Hermann, P.; Vander Elst, L.; Muller, R. N.; Lukes, I.; Peters, J. A. *Dalton Transactions* **2009**, 3204.
- (3) Rohovec, J.; Vojtisek, P.; Hermann, P.; Ludvik, J.; Lukes, I. *Journal of the Chemical Society, Dalton Transactions* **2000**, *0*, 141.
- (4) Kotek, J.; Rudovský, J.; Hermann, P.; Lukeš, I. *Inorganic Chemistry* **2006**, *45*, 3097.
- (5) Klimentová, J.; Vojtíšek, P. *Journal of Molecular Structure* **2007**, 826, 82.
- (6) Campello, M. P. C.; Lacerda, S.; Santos, I. C.; Pereira, G. A.; Geraldes, C. F. G. C.; Kotek, J.; Hermann, P.; Vaněk, J.; Lubal, P.; Kubíček, V.; Tóth, É.; Santos, I. *Chemistry – A European Journal* **2010**, *16*, 8446.
- (7) Rudovský, J.; Cígler, P.; Kotek, J.; Hermann, P.; Vojtíšek, P.; Lukeš, I.; Peters, J. A.; Vander Elst, L.; Muller, R. N. *Chemistry – A European Journal* **2005**, *11*, 2373.
- (8) Ren, J.; Sherry, A. D. *Journal of Magnetic Resonance, Series B* **1996**, *111*, 178.

- (9) Ren, J.; Zhang, S.; Sherry, A. D.; Geraldès, C. F. G. C. *Inorganica Chimica Acta* **2002**, 339, 273.
- (10) Dickins, R. S.; Parker, D.; Bruce, J. I.; Tozer, D. J. *Dalton Transactions* **2003**, 1264.
- (11) Payne, K. M.; Woods, M. *unpublished results*.
- (12) Powell, D. H.; Dhuhghaill, O. M. N.; Pubanz, D.; Helm, L.; Lebedev, Y. S.; Schlaepfer, W.; Merbach, A. E. *Journal of the American Chemical Society* **1996**, 118, 9333.
- (13) Tóth, E. v.; Helm, L.; Merbach, A. E.; Wiley: New York, 2001, p 45.
- (14) Langford, C. H.; Gray, H. B. *Ligand Substitution Processes*; W.A. Benjamin: New York, 1966.
- (15) Gonzalez, G.; Powell, D. H.; Tissieres, V.; Merbach, A. E. *The Journal of Physical Chemistry* **1994**, 98, 53.
- (16) Laus, S.; Ruloff, R.; Tóth, É.; Merbach, A. E. *Chemistry – A European Journal* **2003**, 9, 3555.
- (17) Datta, A.; Raymond, K. N. *Accounts of Chemical Research* **2009**, 42, 938.
- (18) Koenig, S. H.; Epstein, M. *The Journal of Chemical Physics* **1975**, 63, 2279.
- (19) Muller, R. N.; Radüchel, B.; Laurent, S.; Platzek, J.; Piérart, C.; Mareski, P.; Vander Elst, L. *European Journal of Inorganic Chemistry* **1999**, 1999, 1949.
- (20) Dunand, F. A.; Borel, A.; Merbach, A. E. *Journal of the American Chemical Society* **2002**, 124, 710.
- (21) Caravan, P.; Astashkin, A. V.; Raitsimring, A. M. *Inorganic Chemistry* **2003**, 42, 3972.
- (22) Woods, M.; Aime, S.; Botta, M.; Howard, J. A. K.; Moloney, J. M.; Navet, M.; Parker, D.; Port, M.; Rousseaux, O. *Journal of the American Chemical Society* **2000**, 122, 9781.
- (23) Aime, S.; Botta, M.; Garda, Z. n.; Kucera, B. E.; Tireso, G.; Young, V. G.; Woods, M. *Inorganic Chemistry* **2011**, 50, 7955.
- (24) Woods, M.; Botta, M.; Avedano, S.; Wang, J.; Sherry, A. D. *Dalton Transactions* **2005**, 3829.
- (25) Beeby, A.; M. Clarkson, I.; S. Dickins, R.; Faulkner, S.; Parker, D.; Royle, L.; S. de Sousa, A.; A. Gareth Williams, J.; Woods, M. *Journal of the Chemical Society, Perkin Transactions 2* **1999**, 493.
- (26) Lebduskova, P.; Hermann, P.; Helm, L.; Toth, E.; Kotek, J.; Binnemans, K.; Rudovsky, J.; Lukes, I.; Merbach, A. E. *Dalton Transactions* **2007**, 0, 493.
- (27) Banci, L.; Bertini, I.; Luchinat, C. *Inorganica Chimica Acta* **1985**, 100, 173.
- (28) Horrocks, W. D.; Arkle, V. K.; Liotta, F. J.; Sudnick, D. R. *Journal of the American Chemical Society* **1983**, 105, 3455.

- (29) Borel, A.; Bean, J. F.; Clarkson, R. B.; Helm, L.; Moriggi, L.; Sherry, A. D.; Woods, M. *Chemistry – A European Journal* **2008**, *14*, 2658.
- (30) Woods, M. Ph.D. Dissertation, University of Durham, 1998.
- (31) Faulkner, S.; Pope, S. J. A. *Journal of the American Chemical Society* **2003**, *125*, 10526.
- (32) Payne, K. M.; Valente, E. J.; Aime, S.; Botta, M.; Woods, M. *Chemical Communications* **2013**, *49*, 2320.
- (33) Avedano, S.; Botta, M.; Haigh, J.; Longo, D.; Woods, M. *Inorganic Chemistry* **2013**, *52*, 8436.
- (34) Persson, B. A.; Larsson, A. L. E.; Le Ray, M.; Bäckvall, J.-E. *Journal of the American Chemical Society* **1999**, *121*, 1645.
- (35) Demizu, Y.; Moriyama, A.; Onomura, O. *Tetrahedron Letters* **2009**, *50*, 5241.

**CHAPTER 4: RELAXOMETRIC STUDIES OF REGIOISOMERIC GD-NB-DOTMA CHELATES**

The relaxivities of clinical agents are comparatively low (4-8 mM<sup>-1</sup>s<sup>-1</sup> under physiological conditions). From previous studies of slowly rotating TSAP isomers, it was not expected that high relaxivities would be observed for Gd-2.<sup>1</sup> The goal of measuring relaxivities was not to obtain a chelate with the highest relaxivity. Studying the NMRD profiles of isomers of Gd-2 should allow subtle differences between chelates, such as variations in electron spin relaxation and  $\tau_R$ , to be extracted from the data. It was expected that this set of experiments would lead to some understanding about the coordination chemistries of each regioisomer and how they might vary in terms of their structure and dynamics.

The regioisomeric Eu-2 chelates studied exhibited very similar NMR spectra. Due to the spatial relationship ( $\delta = D[3\cos^2\theta/r^3]$ ) between the ligand protons and their NMR shifts and line-widths, it was anticipated that the Ln<sup>3+</sup> coordination environment in regioisomers of the same coordination geometry would differ only slightly. Therefore, it seemed likely that regioisomeric chelates would possess similar physicochemical properties. The properties of regioisomeric Gd<sup>3+</sup> chelates with macromolecule-binding functionalities were investigated. The strategy was to look at the regio-, diastereo-, and geometric isomers of Gd-2 to assess their relaxation behavior relative to one another and then to investigate how any differences manifest when rotation is slowed.

*4.1 Relaxometric studies of Gd-2 chelates*

The two regioisomers of each diastereoisomer of Gd-2 were prepared as previously described for the Eu<sup>3+</sup> analogues. Isomeric assignments following HPLC purification were made on the basis of the retention times of their respective Eu<sup>3+</sup> analogues. These chelates were sent to the laboratories of Prof. M. Botta (Università del Piemonte Orientale, Alessandria, Italy), a leading expert in the analysis of <sup>17</sup>O NMR and NMRD measurements of Gd<sup>3+</sup> chelates. These methods are the established techniques for analysis of water exchange and relaxation behavior. For  $\tau_M$  determination by <sup>17</sup>O NMR, spherical NMR sample containers and a probe that can accommodate them are necessary to ensure homogeneity of the sample, diffusion, and magnetic field. NMRD requires the use of a field-cycling relaxometer.

According to SBM theory, low field (<1 MHz) relaxivity is primarily determined by  $\tau_R$  and the electron spin relaxation characteristics of the chelate.<sup>2</sup> The Gd-2 chelates studied are isomeric, have the same mass and are therefore expected to have identical hydrodynamic volumes and  $\tau_R$  values. For chelates that undergo fast water exchange, relaxivity scales with hydration state across all fields. In terms of the electronic relaxation components  $\Delta^2$  (a measure of mean zero-field-splitting (ZFS) energy) and  $\tau_v$  (the ZFS), even if the coordination environments are similar, the shifts of the Eu<sup>3+</sup> complexes are distinct from one another and therefore their differences in the ligand field, which affects the ZFS. Based on the difference in shifts and coupling patterns, the position and orientation of the NB group is expected to be different between regioisomers, which could also have some influence on electronic relaxation.



Due to the complexity of simultaneously fitting at least 7 parameters in an NMRD profile, some of these are usually constrained. The constrained parameters typically chosen do not vary significantly between systems, or fluctuate seemingly at random to values outside of the physically plausible if allowed to vary in the fit. In our experiments,  $q$ ,  $a$  (second-sphere Gd-water distance),  $A/\hbar$  (the scalar coupling constant), and  $D$  (diffusion coefficient) were constrained.  $R$  values were constrained and the difference in hydration states, as evidenced by the VT NMR studies of Eu-2 and the luminescence studies of Eu-2 and related chelates as described in Chapter 3, was taken into consideration. It could not be determined whether  $q$  is smaller for the TSAP chelates (compared with the SAP chelates), or if  $r$  is larger. By constraining both  $q$  and  $r$  for fitting the NMRD profiles, we have accounted for the difference in hydration state as much as possible from the available data. Values for  $r$  were constrained to  $3.0 \text{ \AA}$  for SAP chelates and  $3.1 \text{ \AA}$  for TSAP chelates. The NMRD measurements performed and respective fitting curves generated are shown in Figures 4.1 and 4.2.

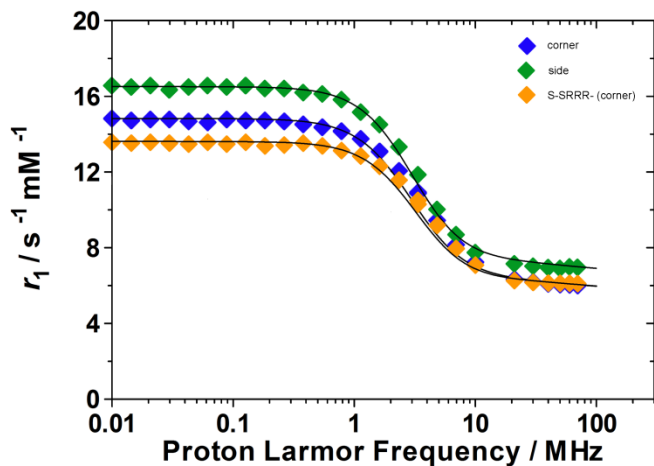


**Figure 4.1:** NMRD profiles of the SAP chelates Eu-S-RRRR-2 corner (blue diamonds) and side (green) isomers, and Eu-S-SRRR-2 corner isomer (yellow) at 25 °C.

From inspection of the NMRD profiles, relaxivity is greatest at low fields ( $< 1$  MHz), goes through a dispersion between 1 and 10 MHz, and is lowest at high fields ( $> 20$  MHz). These data are typical of low-molecular-weight (rapidly tumbling)  $Gd^{3+}$  chelates. Since the regioisomers have the same mass,  $\tau_R$  values are very similar as expected. The profiles of the three SAP isomers analyzed have a largely uniform difference in magnitude in Figure 4.1 at low fields. The SAP side isomer (green diamonds) has higher relaxivity than the corner isomer (blue), which has a higher relaxivity than the diastereoisomer (*S-SRRR*, orange) below 1 MHz. The low-field relaxivity data are indicative of a parameter which scales independently from magnetic field strength, possibly indicating a difference in hydration state between the three isomers. The side isomer could have the largest  $q/r^6$  with the *S-SRRR* isomer having the smallest. At high fields, the relaxivities observed for the two corner isomers have nearly identical values, with a somewhat greater value observed for the side isomer. The fact that the NMRD curves are not offset at all fields indicate that the corner and side isomers could have different electronic relaxation properties. Recent NMR data indicate that corner and side regioisomers are distorted from idealized square antiprismatic geometry differently<sup>3</sup> – the degree of symmetry of the ligand field affects the ZFS. Or, the rigidity of the chelate for the side isomer's NB orientation may lead to more favorable  $\tau_v$ . Lastly, some combination of the above explanations could be the cause of the difference in relaxivity.

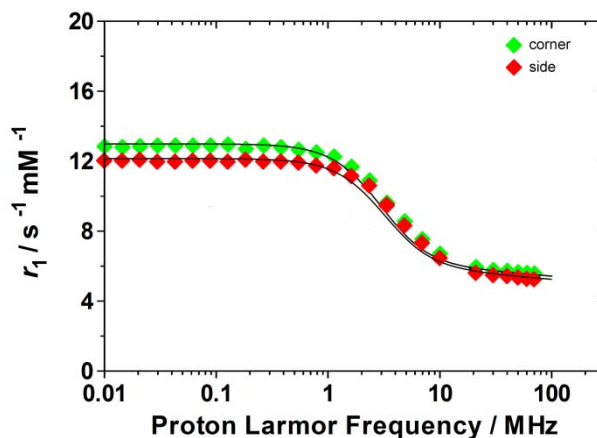


**Figure 4.2:** NMRD profiles of the TSAP chelates Eu-S-SSSS-2 corner (green diamonds) and side (red) isomers at 25 °C.

Similar relaxation behavior was observed over the range of magnetic field strengths for the TSAP isomers. The curves are offset at low fields, but the corner isomer has higher relaxivity than the side isomer, the opposite result from the SAP. It is therefore unlikely that the shape of corner or side isomer intrinsically leads to higher relaxivity. The high-field relaxivity values are slightly greater for corner vs. side isomer, but the difference is not nearly as large as for the regioisomeric SAP chelates. The hydration states are thus likely to be very similar, and the differences in the profiles are probably due to electronic factors. Unexpectedly, the relaxivities for SAP isomers are slightly higher than those of the TSAP isomers.

Based on these observations, values for the five non-constrained parameters were optimized to generate fitting curves to the above data, and these values are shown in Table 4.1. Values for the parameters varied to produce the fits are based on data from related systems<sup>4</sup> and not on independent measurements.

Gd <sup>III</sup> complexes	$r_1^{[a]}$ mM <sup>-1</sup> s <sup>-1</sup>	$\Delta^2$ 10 <sup>19</sup> s <sup>-2</sup>	$\tau_V$ ps	$\tau_R$ ps	$\tau_M$ ns	$r$ Å
Gd-S-SRRR-2 (corner isomer)	6.3	2.0	18	112	70	3.0
Gd-S-RRRR-2 (corner isomer)	6.3	1.6	16	111	70	3.0
Gd-S-RRRR-2 (side isomer)	7.1	1.6	18	112	70	2.9
Gd-S-SSSS-2 (corner isomer)	5.9	1.7	18	118	8	3.1
Gd-S-SSSS-2 (side isomer)	5.6	1.8	20	112	8	3.1

<sup>[a]</sup> recorded at 20 MHz

For all the complexes  $q = 1$ ,  $a$  (second-sphere Gd-water distance) = 4.0 Å and  $D = 2.24$  (298 K) and  $3.10$  (310K)  $\times 10^{-5}$  cm<sup>2</sup> s<sup>-1</sup>.

**Table 4.1:** Relaxometric parameters obtained from the fit of the <sup>1</sup>H NMRD profiles

The relaxivities observed are statistically distinct from one another. The SAP (RRRR) side isomer has slow water exchange (but faster than Gd[DOTA]<sup>-</sup>), and higher relaxivity than the SAP corner isomers (RRRR and SRRR). The TSAP (SSSS) side isomer has fast water exchange, but lower relaxivity than the TSAP corner isomer. The fits reflect the belief that  $\tau_R$  values are essentially the same. Though dominated by similar, rapid fitted values for  $\tau_R$  and  $\tau_M$ , the relaxation properties of regioisomeric chelates were shown to be subtly different. The difference in structure could alter ligand rigidity and therefore  $\tau_V$  – the structure of the side isomer may lead to more favorable electronic relaxation in the SAP chelates but slightly less favorable electronic relaxation in the TSAP chelates (which have different rigidity and distortion from idealized geometry). Differences in  $\tau_M$  affect relaxivity at 20 MHz, with the slower-exchanging isomer predicted to have lower relaxivity. Though there seemed no reasonable cause to expect that there would be differences in  $q/r^6$  or the water exchange kinetics of regioisomeric chelates, the NMRD

data suggest that these differences are real. A lower  $r$  value for the  $S$ -RRRR side isomer yielded the best fit to the NMR data. There is no way to tell just from the NMRD profiles above if this isomer actually has a higher hydration state than the other isomers, or if the fit is due to inaccuracies in values for the other parameters.

The fits to the NMRD data indicate that electronic properties lead to relaxivity differences between the 5 Gd-2 isomers studied, but the high field differences cannot be due to electronic relaxation differences alone. These findings indicate that a difference in hydration state is affecting relaxivity. There is no explanation in the NMRD data of Gd-2 for the SAP chelates possessing higher relaxivity than the TSAP chelates. The potential differences in relaxivity behavior between regioisomers should be more clearly observable and interpretable when bound to a slowly tumbling species in comparison to the rapidly tumbling chelates.

#### **4.2 Measurement of $\tau_M$ in Gd-2 chelates by variable-temperature $^{17}\text{O}$ NMR shift and $T_2$**

The  $^{17}\text{O}$  NMR measurements inform on whether  $\tau_M$  is affecting the relaxivity of isomeric Gd-2 chelates (Figures 4.3).  $\tau_M$  values were measured by  $^{17}\text{O}$  NMR spectroscopy if sufficient amount of a given isomer was present. The fitting data are shown in Table 4.2.

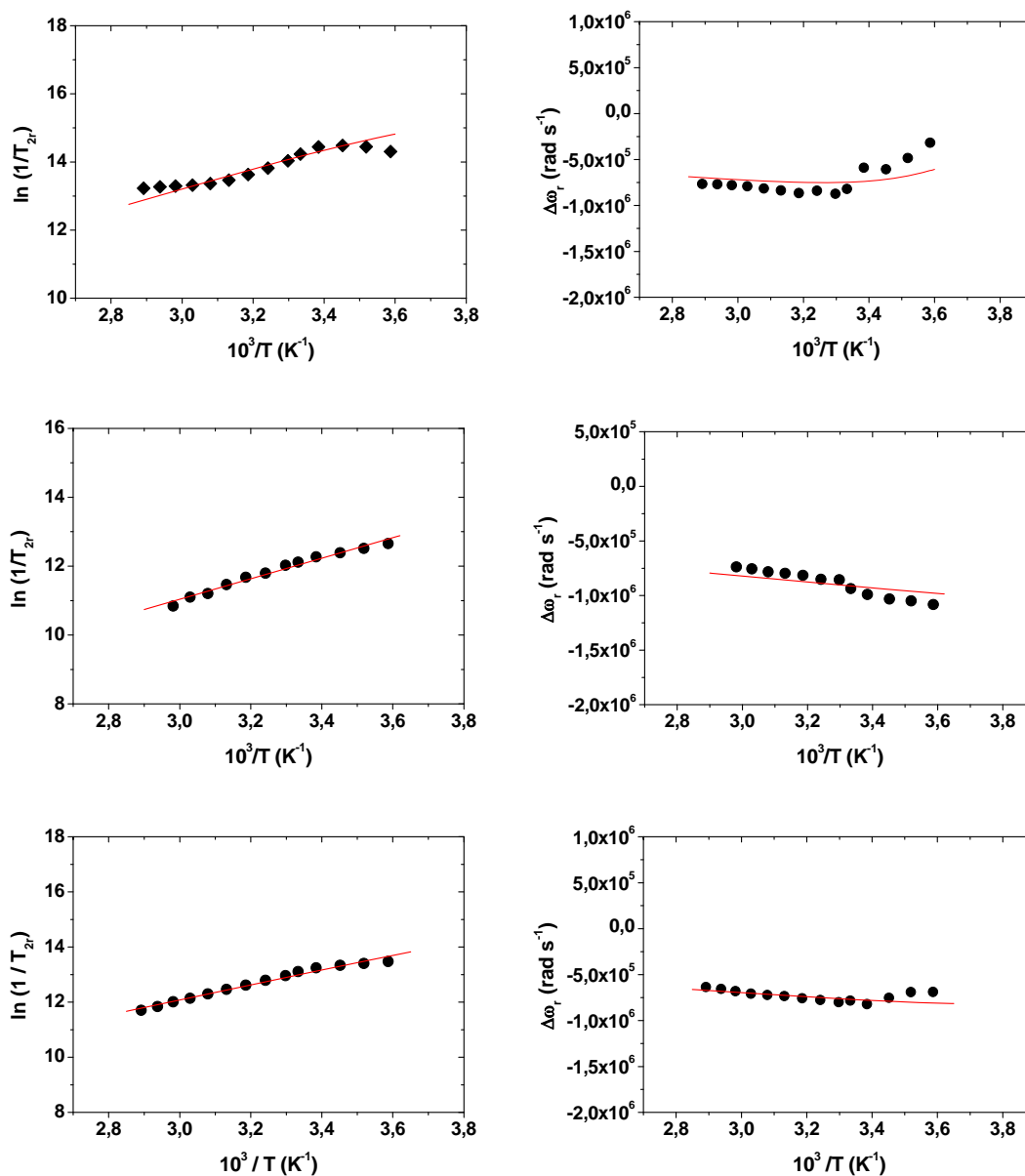


**Figure 4.3:** Variable temperature  $T_2$  (left) and chemical shift (right)  $^{17}O$  data for Gd-S-RRRR-2 corner isomer (top), Gd-S-SSSS-2 side isomer (middle), and Gd-S-SSSS-2 corner isomer (bottom)

	RRRR-corner (SAP)	SSSS-corner (TSAP)	SSSS-side (TSAP)
$r_{\text{Gd-H}} (\text{\AA})^a$	3.00	3.10	3.10
$\tau_{\text{M}} (\text{ns})$	24	7	3
$\Delta H_{\text{M}} (\text{kJmol}^{-1})$	22.5	20.6	23.5
$10^{19} \Delta^2 (\text{s}^{-2})$	1.6	1.7	1.8
$\tau_{\text{V}} (\text{ps})$	16	18	20
$\tau_{\text{R}} (\text{ps})$	112	118	112
$\Delta H_{\text{V}} (\text{kJmol}^{-1})^a$	1.0	1.0	1.0
$a (\text{\AA})^a$	4.0	4.0	4.0
$10^{-5} D (\text{cm}^2 \text{s}^{-1})^a$	2.24	2.24	2.24
$A/\hbar (10^6 \text{ rad s}^{-1})$	-3.5	-3.5	-3.1

**Table 4.2:** Fitting parameters used in the fitting of the NMRD and  $^{17}\text{O}$  relaxation profiles of the complexes. a) parameter fixed during fitting

$^{17}\text{O}$  data could not be acquired for Gd-RRRR-2 side or Gd-SRRR-2 chelates due to insufficient amounts of sample. It is important to note that the data analyses of these  $^{17}\text{O}$  NMR profiles are only preliminary. For instance, the shape of the  $R_2$  profile for S-RRRR-isomer, which reaches a maximum and begins to decrease at lower temperatures, indicates that exchange is actually slower than reflected in the fitting, in line with previously published work.<sup>5</sup> Nonetheless, these data confirm that the TSAP isomers indeed have the fastest water exchange kinetics as expected. Interestingly, the  $^{17}\text{O}$  data for Gd-S-SSSS-2 chelates show that the side isomer and corner isomers do not have identical  $\tau_{\text{M}}$  values, though the NMRD profiles in section 4.1 were fit with  $\tau_{\text{M}} = 10$  ns as those values were the best available data at the time. The TSAP corner isomer has a water residence lifetime that is twice as long as that of the side isomer. However, owing

to very fast exchange and to the  $1/(\tau_{\text{on}} + \tau_{\text{off}}) = k_{\text{ex}}$  relationship outlined in Chapter 3, the exchange *rates* are actually very similar. There is a field dependence for the optimal water exchange rate.<sup>6</sup> This is a possible explanation for the slightly higher relaxivities observed for the SAP chelates over the TSAP (Table 4.1). Faster water exchange appears to lead to a decrease in the hydration state and this in turn affects relaxivity over the whole NMRD profile.

### ***4.3 Relaxometric properties of regioisomeric, slowly tumbling biphenyl analogues of Gd-2***

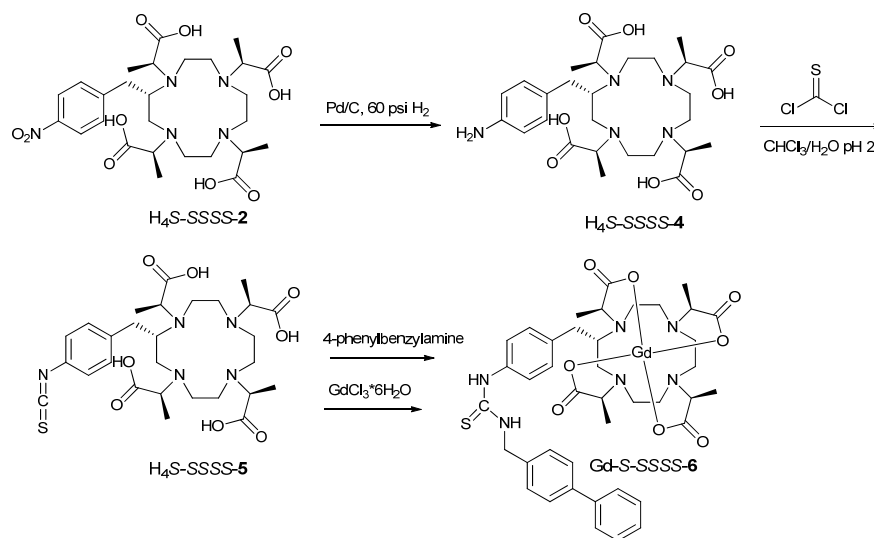
A recent paper detailed the investigation of two slowly tumbling chelates with very similar electronic relaxation properties but different water exchange kinetics.<sup>1</sup> Though fast water exchange and slow tumbling led to high relaxivities, the more slowly exchanging (SAP) chelate unexpectedly showed higher relaxivity than its TSAP isomer. The relaxivity differences observed between coordination geometries have thus been investigated for conformationally rigid chelates with similar electronic relaxation, but no studies are known where the relaxivities of regioisomers were compared. It was expected that for slowly tumbling derivatives of Gd-2, a difference in macromolecular binding would be evident due to the predicted orientations of the NB group and the question of whether this could result in differences in relaxivity was probed.

One complication with using human serum albumin (HSA) to quantify relaxivity enhancement of different chelates is that HSA does not exhibit 1:1 binding of a Gd<sup>3+</sup> chelate with binding functionality.<sup>7,8</sup> The conformation of HSA changes upon binding



and at least one of the binding sites could accommodate more than one chelate. This can obscure the contributions of a particular chelate to observed relaxation rate. Polymers of cyclodextrins have also shown to be useful for demonstrating increased relaxivity of slowly-tumbling complexes.<sup>9-11</sup> The biphenyl group has been shown to bind to biological macromolecules *in vivo* within detectable limits (nM range).<sup>12,13</sup>

Biphenyl conjugates of Gd-S-SSSS-2 were prepared based on literature procedures<sup>1</sup> for study by NMRD. The nitrobenzyl group in **2** was reduced to the corresponding amine **4** by catalytic hydrogenation. Subsequent reaction with thiophosgene converted the amine **4** to the isothiocyanate **5** which could then be coupled to 4-phenylbenzylamine, yielding the biphenyl substituted ligand **6**. This ligand was used to form the Gd<sup>3+</sup> chelate, generating an amphiphilic molecular probe (Scheme 4.1).



**Scheme 4.1:** Conversion of the nitrobenzyl group in **2** to confer macromolecular binding ability

An HPLC method was developed to resolve regioisomers of Gd-*S-SSSS-6*. The corner and side isomers of Gd-*S-SSSS-6* (biphenyl-conjugated) chelates were purified by HPLC. The isomers of Gd-*S-SSSS-6* were again identified by synthesizing and purifying the Eu<sup>3+</sup> analogues, which were analyzed by <sup>1</sup>H NMR. The order of HPLC elution and the *ax<sup>S</sup>* peak patterns in the downfield region of the spectra of Eu-*S-SSSS-6* clearly align with corner and side isomers of Eu-*S-SSSS-2* (data not shown), as characterized above. This also shows that the coordination environment and ligand field between the same regioisomer of Gd-**2** and Gd-**6** are analogous for the purposes of comparing relaxation properties.

To test if the orientation of the bulky ring substituent with respect to N/O planes affects the binding and relaxation properties of regioisomeric Gd-**6** chelates (*via* potential differences in  $\tau_R$  and  $\tau_M$ ), NMRD profiles of the free and poly- $\beta$ -cyclodextrin-bound complexes were analyzed. With faster water exchange, the relaxation properties of the TSAP biphenyl conjugates of Gd-**2** (Gd-**6**) should be more sensitive to changes in water exchange rate than the SAP, and should have  $\tau_M$  values closer to the optimal predicted by SBM theory. Or, the relaxivities may be limited by  $\tau_M$  for slowly tumbling species if water exchange rate is not optimal. In the event of varying binding behavior between regioisomers, water exchange or local rotation (as evidenced by differences in  $\tau_R$ ) could be more restricted in one isomer over the other.

The longitudinal relaxation rate was determined at a series of concentrations to find the critical micelle concentration (cmc) for each isomer (Fig. 4.4). Chelates conjugated to

biphenyl or other hydrophobic groups have previously been shown to form micelles above a certain concentration in solution. These micelles act as higher-relaxivity (via long  $\tau_R$ ) “clusters” with their hydrophilic (Gd-acetate) groups facing the bulk water, and the hydrophobic (biphenyl) groups forming the core.<sup>14-16</sup> It is important to determine the cmc<sup>17,18</sup> for each chelate to separate the relaxivity effects of  $\tau_R$  due to binding from effects due to micelle formation, particularly when the aim is to then titrate in a binding target and measure  $r_1$ .

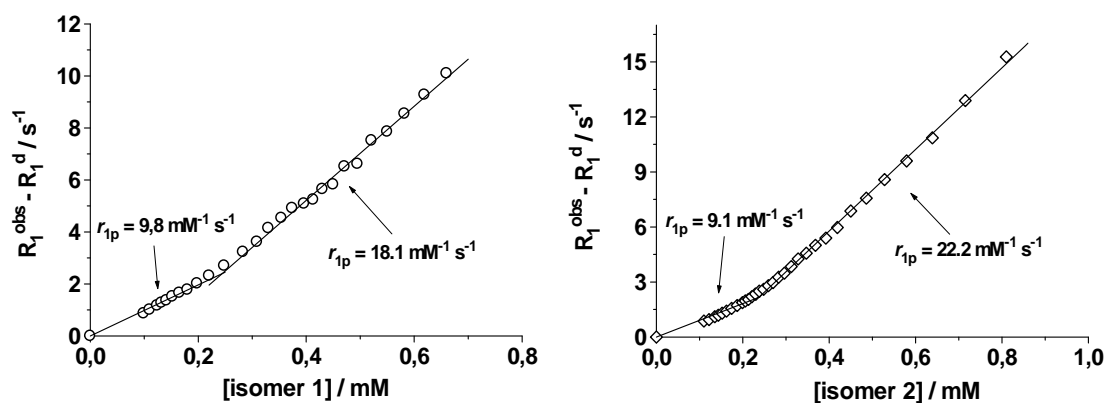


**Figure 4.4:** Relaxation properties of Gd-S-SSSS-6 above and below critical micelle concentration (cmc). Isomer 1 = Gd-S-SSSS-6 corner (left) and Isomer 2 = Gd-S-SSSS-6 side (right). The cmc was determined to be 0.24 mM ( $\pm 0.01$ ) for both corner and side isomers. The y-axis is the background relaxation rate ( $\frac{1}{T_1}$ ) of water subtracted from the observed relaxation rate with the chelate ( $R_1^{\text{obs}} - R_1^{\text{d}}$ )

The cmc was determined to be 0.24 mM for both corner and side isomers of Gd-S-SSSS-6. Above this concentration, the relaxivity is substantially higher due to micelle formation. The regiochemistry does not seem to substantially affect the concentration range at which micelles form. The relaxivity is higher for the corner TSAP isomer than

for the side isomer below the cmc, consistent with the TSAP Gd-2 NMRD data above. This again could be related to differences in electronic relaxation properties between regioisomers. Above the cmc, however, the relaxivities are higher for the side isomer. Micelles of the side isomer may be larger or have a different shape, leading to greater  $\tau_R$ . Or, micelles of the corner isomer may orient the inner-sphere water site in such a way that  $\tau_M$  is restricted or the hydration state is smaller in comparison to the free chelate or to micelles of the side isomer.

It was assumed that the relaxivities of both chelates will be greater with increasing concentration of macromolecule, due to binding of the chelate and reduced rate of molecular tumbling, until no further binding can occur with a subsequent increase in macromolecular concentration. NMRD profiles for the samples were determined for Gd-S-SSSS-6 (Figure 4.5).

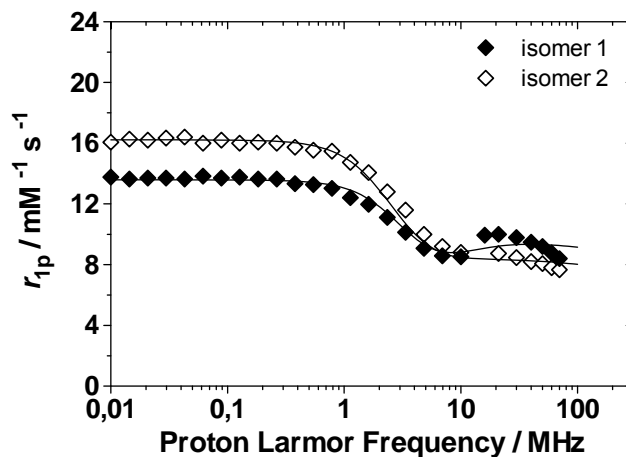


**Figure 4.5:** NMRD profiles of Gd-S-SSSS-6 corner (filled diamonds) and -side (open diamonds) at 0.15 mM and 298 K

The relaxivity of the TSAP corner isomer is lower than the relaxivity of the side isomer at low fields, in contrast to the Gd-2 data. The “hump” around 20 MHz in the relaxation data for the corner isomer indicates that the chelate continues to aggregate to some degree even at 0.15 mM, below the cmc. At that same concentration, the lack of a hump for the side isomer indicates no aggregation. Now the picture we are getting is one where the hydration state is greater, or  $\tau_M$  or electronic relaxation is more favorable for the side isomer, dominating the low field behavior, but the greater  $\tau_R$  of the corner isomer (due to aggregation) dominates the relaxivity at high fields. The cmc profiles in Figure 4.4 and the NMRD profile in Figure 4.5 suggest that if the concentration of the chelates were low enough, the side isomer would have greater relaxivity at all fields. Optimized fitting values for the NMRD profiles of the biphenyl chelates are shown in Table 4.3.

[Gd <sup>3+</sup> ] = 0.15 mM		
	Gd-S-SSSS-6 corner (isomer 1)	Gd-S-SSSS-6 side (isomer 2)
$r_{\text{Gd-H}} / \text{\AA}^b$	3.0	3.0
$\tau_M / \text{ns}^b$	10	10
$\Delta^2 / 10^{19} \text{ s}^{-1}$	2.4	1.7
$\tau_V / \text{ps}$	27	23
$\tau_R / \text{ps}$	200	168

**Table 4.3:** Best-fit parameters<sup>a,b</sup> of the NMRD profiles of Gd-S-SSSS-6 (corner, isomer 1) and Gd-S-SSSS-6 (side, isomer 2) a) Fitting used  $a = 4.0 \text{ \AA}$ ,  $^{298}D = 2.24 \times 10^{-5} \text{ cm}^2 \text{ s}^{-1}$  and  $q = 1$ . b) parameter fixed during fitting.

The fitting of the NMRD profile gives the corner isomer a significantly larger value for  $\tau_R$ . This may indicate that the side isomer is more compact and therefore has less restricted tumbling. However, the  $\tau_R$  values obtained from the fit may be due to the assumed values of other parameters, or are more reflective of an aggregate rather than a monomeric chelate. The low-field relaxivities are overall slightly higher than the TSAP Gd-2 values, which is to be expected as Gd-6 chelates are more massive and therefore tumble more slowly.  $\tau_M$  values were again fixed to 10 ns for both regioisomers as those were the best available data to produce a fit at the time. The  $^{17}\text{O}$  NMR data indicate that the regioisomers should have different  $\tau_M$  values, but the poor fits to the NMRD profiles of Gd-S-SSSS-6 are more likely due to aggregation.

The potential difference in binding between regioisomeric Gd-S-SSSS-6 chelates was probed by titration of chelate solutions with poly- $\beta$ -CD. The degree of binding of the two isomers of Gd-S-SSSS-6 was assayed by titration with poly- $\beta$ -cyclodextrin (Figure 4.6). The binding constant and relaxivity data are shown in Table 4.4.

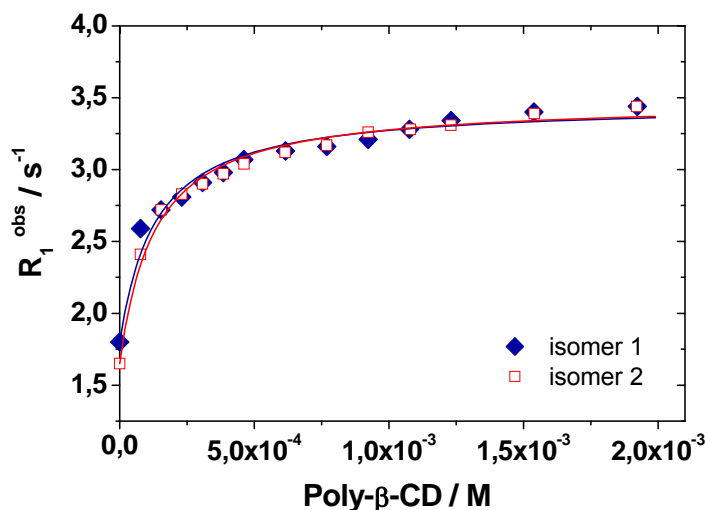


Figure 4.6: Interaction with poly-β-cyclodextrin (20 MHz, 298 K)

	$K_a / M^{-1}$	$r_1^{\text{bound}} / mM^{-1} s^{-1a}$
Gd-S-SSSS-6 corner	$0.61 \pm 0.09 \times 10^3$	$21.7 \pm 0.3$
Gd-S-SSSS-6 side	$0.63 \pm 0.06 \times 10^3$	$21.3 \pm 0.2$

a) Measured at 20 MHz and 25 °C.

Table 4.4: Fitting parameters for the binding of the two isomers of Gd to poly-β-CD

The initial rapid rise in relaxation rate is due to the  $Gd^{3+}$  chelates' strong relaxation enhancement when bound to a slowly tumbling species. The more gradual rise as the poly-β-cyclodextrin concentration increases further indicates an increase in viscosity of the overall solution. The shape of the curve indicates 1:1 binding. The binding differences between the two regioisomers are not statistically significant. The NMRD profiles of Gd-S-SSSS-6 bound to poly-β-cyclodextrin (poly-β-CD) are shown in Figure 4.7.

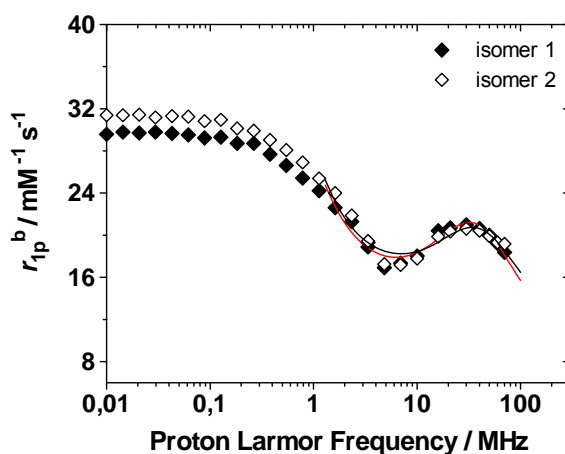


Figure 4.7: NMRD of the supramolecular adducts (298 K)

The difference in relaxation behavior of the poly- $\beta$ -CD-bound chelates are similar to those of the free chelates. At low fields, the side isomer has higher relaxivity due to a difference in hydration state or electronic relaxation; at high fields, the relaxivities are similar and typical of long  $\tau_R$  values from macromolecular binding. Optimized fitting values for the NMRD profiles of poly- $\beta$ -CD-bound chelates are shown in Table 4.5.



	Gd-S-SSSS-6 corner (isomer 1)	Gd-S-SSSS-6 side (isomer 2)
$r_{\text{Gd-H}} / \text{\AA}^b$	3.0	3.0
$\tau_{\text{M}} / \text{ns}^b$	10	10
$\Delta^2 / 10^{18} \text{s}^{-1}$	5.9	6.3
$\tau_{\text{V}} / \text{ps}$	11	9
$\tau_{\text{g}} / \text{ns}$	2.9	2.8
$\tau_1 / \text{ns}$	0.37	0.42
$S^2$	0.14	0.12

**Table 4.5:** Best-fit parameters of the NMRD profiles (25 °C) of the inclusion complexes of the two isomers of Gd with poly- $\beta$ -CD. a) Fitting used  $a = 4.0 \text{ \AA}$ ,  $^{298}D = 2.2 \times 10^{-5} \text{ cm}^2 \text{ s}^{-1}$  and  $q = 1$ . b) parameter fixed during fitting.  $\tau_{\text{g}}$  is the global reorientation time constant,  $\tau_1$  is the local reorientation time constant, and  $S^2$  represents the extent to which local and global rotation are coupled. From the Lipari-Szabo model,<sup>19</sup> 1 means entirely coupled and 0 entirely decoupled<sup>8</sup>

With poly- $\beta$ -cyclodextrin, the peak centered around 35 MHz indicates binding of Gd-S-SSSS-6, increasing relaxivity at moderately high fields via  $\tau_{\text{R}}$  increase and  $T_{1e}$  limitation before decreasing again. The constraining of  $r$  and  $\tau_{\text{R}}$  to identical values for regioisomers could be erroneous.  $\tau_{\text{V}}$  values are larger for the corner isomer for both free and bound chelates, and larger in the free species, suggesting that this isomer is more rigid with respect to vibrational and collisional motions (larger values are more favorable for increasing relaxivity).  $\Delta^2$  values are larger in the bound chelates indicating a more asymmetric ligand field. The chelates likely distort from idealized geometry further upon binding, having a small negative impact on relaxivity.

The data indicate that the relaxivities of the macromolecular adducts of corner and side isomers are not limited by possible differences in shape, binding kinetics, local rotation, electronic factors, differences in water exchange, or differences in hydration state at 20 MHz and 25 °C. Alternatively, the differences in local rotation, electronic factors, water exchange rates, or hydration state may be canceling one another out for the regioisomers under these conditions, leading to very similar relaxivities at high fields.

#### *4.4 Conclusions and future directions*

The NMRD data indicate that the electronic relaxation properties do, as anticipated, appear to differ between regioisomers. Unfortunately, our understanding of the relationship between ZFS,  $\tau_v$ , and coordination chemistry is currently quite limited and it is not currently possible to optimize these factors *via* rational design. The differences in relaxivities observed for both Gd-**2** and Gd-**6** chelates were shown to be proportional to differences in  $\tau_M$  (or possibly hydration state, since these parameters were shown to be related in Chapter 3). It is interesting that the side isomer has higher relaxivity in the SAP regioisomers, and lower relaxivity in the TSAP regioisomers. We can speculate that this is the result of differences in  $\tau_M$  and the inherently linked hydration state.  $\tau_M$  is shorter and, according to our results in Chapter 3, associated with a lower hydration state ( $q/r^6$ ) in the side isomer of Gd-S-SSSS-**2**. This leads to lower relaxivity for the side isomer. In contrast, the side isomer of Gd-S-RRRR-**2** exhibits higher relaxivity at all fields in the NMRD profile, and using the same reasoning could be associated with slightly slower water exchange and therefore an increased hydration state. The

relaxivities of Gd-2 and their respective water exchange rates are in the following order: SAP corner (moderately high relaxivity, slowest water exchange), SAP side (highest, slightly faster), TSAP corner (moderately low, even faster), and TSAP side (lowest, fastest). This evidence suggests that the TSAP chelates have faster water exchange than optimal at 0.5 T, and the faster the exchange is in comparison to that of the SAP side isomer, the further away from optimal relaxivity. Additionally, the SAP corner isomer may exchange water too slowly for optimal relaxivity. These are all minor differences for the rapidly tumbling chelates, but have major implications for CA design and may show significant differences when bound to macromolecular targets. Gd-6 analogues of the SAP isomers have not yet been prepared, but the SAP and TSAP properties of closely related chelates have been analyzed (for which regioisomer data are not available).<sup>1</sup>

Since it is not possible to measure  $r_{\text{Gd-H}}$  directly in solution, Gd-O measurements will be assumed to be proportional to Gd-H. Regioisomerically pure Gd-2 chelates were sent for X-ray fluorescence analysis at the Stanford Synchrotron Radiation Lightsource, which can probe Gd-O distances, and we hope that the resolution is sufficient to observe differences between isomers. If these data are obtained, the NMRD data will again be re-fit using the most accurate values obtainable. Analysis of the  $\tau_{\text{M}}$  vs.  $r$  data may tell us which parameter is affecting the relaxivity.

The relaxivities obtained are still below optimal as predicted by SBM theory and are surprisingly higher for the longer- $\tau_{\text{M}}$  SAP isomers. Our understanding of how to maximize relaxivity in conformationally rigid chelates by rational design has been

improved by the study of hydration state, water exchange, and relaxivity by comparing regioisomeric and macromolecular-binding conformationally rigid chelates.

#### **4.5 References**

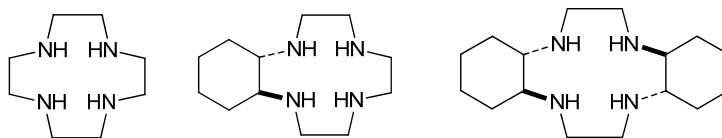
- (1) Avedano, S.; Botta, M.; Haigh, J.; Longo, D.; Woods, M. *Inorganic Chemistry* **2013**, *52*, 8436.
- (2) Powell, D. H.; Dhubhghaill, O. M. N.; Pubanz, D.; Helm, L.; Lebedev, Y. S.; Schlaepfer, W.; Merbach, A. E. *Journal of the American Chemical Society* **1996**, *118*, 9333.
- (3) Slack, J.; Woods, M., unpublished results.
- (4) Woods, M.; Botta, M.; Avedano, S.; Wang, J.; Sherry, A. D. *Dalton Transactions* **2005**, 3829.
- (5) Woods, M.; Kovacs, Z.; Zhang, S.; Sherry, A. D. *Angewandte Chemie International Edition* **2003**, *42*, 5889.
- (6) Werner, E. J.; Datta, A.; Jocher, C. J.; Raymond, K. N. *Angewandte Chemie International Edition* **2008**, *47*, 8568.
- (7) Caravan, P.; Cloutier, N. J.; Greenfield, M. T.; McDermid, S. A.; Dunham, S. U.; Bulte, J. W. M.; Amedio, J. C.; Looby, R. J.; Supkowski, R. M.; Horrocks, W. D.; McMurry, T. J.; Lauffer, R. B. *Journal of the American Chemical Society* **2002**, *124*, 3152.
- (8) Zhou, X.; Caravan, P.; Clarkson, R. B.; Westlund, P.-O. *Journal of Magnetic Resonance* **2004**, *167*, 147.
- (9) Aime, S.; Botta, M.; Frullano, L.; Crich, S. G.; Giovenzana, G. B.; Pagliarin, R.; Palmisano, G.; Sisti, M. *Chemistry – A European Journal* **1999**, *5*, 1253.
- (10) Aime, S.; Botta, M.; Fedeli, F.; Gianolio, E.; Terreno, E.; Anelli, P. *Chemistry – A European Journal* **2001**, *7*, 5261.
- (11) Gianolio, E.; Napolitano, R.; Fedeli, F.; Arena, F.; Aime, S. *Chemical Communications* **2009**, *0*, 6044.
- (12) Kuduk, S. D.; Ng, C.; Feng, D.-M.; Wai, J. M. C.; Chang, R. S. L.; Harrell, C. M.; Murphy, K. L.; Ransom, R. W.; Reiss, D.; Ivarsson, M.; Mason, G.; Boyce, S.; Tang, C.; Prueksaritanont, T.; Freidinger, R. M.; Pettibone, D. J.; Bock, M. G. *Journal of Medicinal Chemistry* **2004**, *47*, 6439.
- (13) Feng, D.-M.; Wai, J. M.; Kuduk, S. D.; Ng, C.; Murphy, K. L.; Ransom, R. W.; Reiss, D.; Chang, R. S. L.; Harrell, C. M.; MacNeil, T.; Tang, C.; Prueksaritanont, T.; Freidinger, R. M.; Pettibone, D. J.; Bock, M. G. *Bioorganic & Medicinal Chemistry Letters* **2005**, *15*, 2385.

- (14) André, J. P.; Tóth, É.; Fischer, H.; Seelig, A.; Mäcke, H. R.; Merbach, A. E. *Chemistry – A European Journal* **1999**, *5*, 2977.
- (15) Nicolle, G.; Tóth, É.; Eisenwiener, K.-P.; Mäcke, H.; Merbach, A. *JBIC* **2002**, *7*, 757.
- (16) Torres, S.; Martins, J. A.; André, J. P.; Geraldes, C. F. G. C.; Merbach, A. E.; Tóth, É. *Chemistry – A European Journal* **2006**, *12*, 940.
- (17) Gianolio, E.; Giovenzana, G. B.; Longo, D.; Longo, I.; Menegotto, I.; Aime, S. *Chemistry – A European Journal* **2007**, *13*, 5785.
- (18) Schühle, D. T.; Schatz, J.; Laurent, S.; VanderElst, L.; Muller, R. N.; Stuart, M. C. A.; Peters, J. A. *Chemistry – A European Journal* **2009**, *15*, 3290.
- (19) Dunand, F. A.; Tóth, É.; Hollister, R.; Merbach, A. E. *JBIC* **2001**, *6*, 247.

**CHAPTER 5. OVERCOMING REGIOISOMERISM: A POTENTIAL PATH TOWARD SYNTHETICALLY EFFICIENT, CONFORMATIONALLY RIGID CHELATES**

**5.1 Motivation for study and summary of synthetic research plan**

Although the corner regioisomer of Ln-2 is generally the more favored position formed under typical reaction conditions, we have been unable to find synthetic conditions which yield only one regioisomer. The difference in substituent orientation between corner and side isomers means that they could function differently as targeted imaging agents, and it may therefore be necessary to isolate them as single compounds, greatly complicating the synthesis of agents. Synthetic efficiency is poor since one regioisomer must be discarded, and NB-cyclen is an expensive (\$2500/g) precursor. The HPLC purification of regioisomers is impractical on a large scale. Optimizing the synthetic process of preparing a potential MRI CA would be valuable from a scientific and an economical point of view. A conformationally rigid chelate (such as one based on the macrocycles **8** or **9**) which eliminates the potential challenge of regioisomerism would be preferable for synthetic efficiency.



Cyclen, Cyclohexylcyclen (**8**) and Bicyclohexylcyclen (**9**)

*Trans* fusion of a cyclohexyl ring to one ethylene bridge of cyclen would occupy both equatorial positions equivalently and yield a single chelate. A *trans*-2,3-cyclohexane-

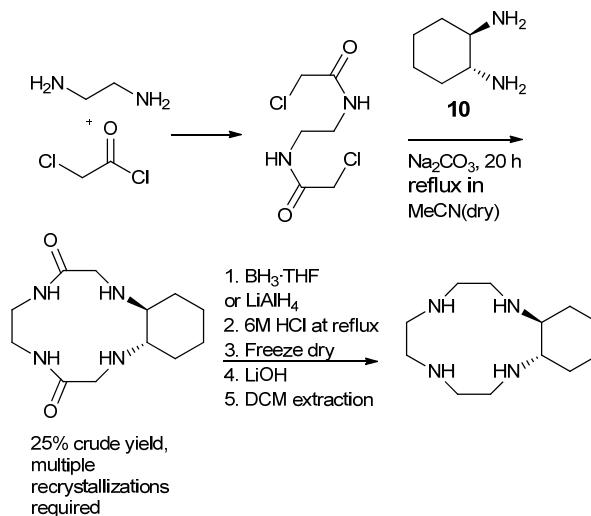
fused tetraazacrown such as **8** or **9** with appropriately substituted pendant arms would not be expected to be able to form regioisomers. In this way it should be possible to synthesize a conformationally rigid chelate with no possibility for regioisomerism. A synthesis of compound **8** has been reported in a patent, and some synthetic conditions, yields, and/or characterization data were not reported.<sup>1</sup> The major drawback of this work is the low yield, and ways to improve upon that were explored. Other 2,3-substituted tetraazacyclododecane compounds have been reported<sup>2-7</sup>, but are either unsuitable for converting to a stable  $\text{Ln}^{3+}$  chelate which won't undergo conformational exchange, or have low yields and/or a large number of synthetic steps. Considerable effort was put forth toward synthesizing a conformationally rigid, cyclohexyl-bridged macrocycle. The primary motivation for this work was to achieve an economical, relatively simple synthesis of a conformationally rigid tetraazacrown for use in development of prototypical CAs.

## *5.2 Attempted synthesis of a 1,4,7,10 tetraaza-crown with no potential for regioisomerism*

### *5.2.1 Efforts to synthesize cyclohexylcyclen based on the Richman-Atkins method*

Multiple synthetic routes to **8** were tested, and the approaches were based on successful syntheses of cyclen and the one reported synthesis of **8**. The synthesis of **8** by Desreux and colleagues (Scheme 5.1), similar to the Richman-Atkins synthesis of cyclen and based on the synthesis of cyclen published earlier by Stetter and co-workers,<sup>8</sup> uses chloride as the leaving group rather than triflate or tosylate. Compound **10**, (1*S*,2*S*)- or

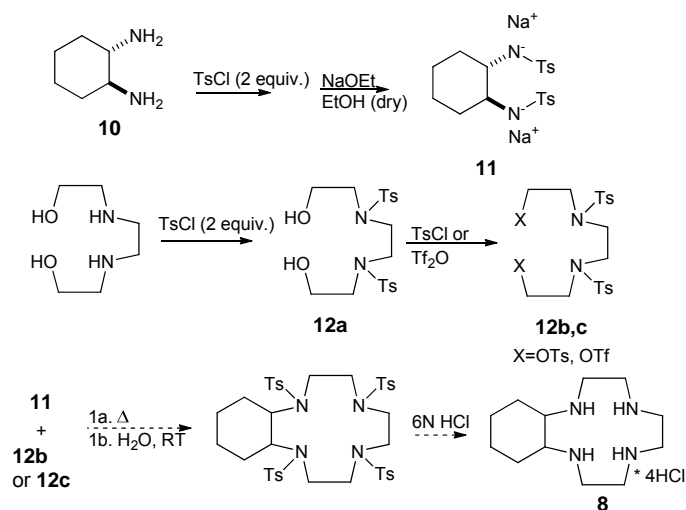
(1*R*,2*R*)-1,2-diaminocyclohexane, is advantageous because it is a commercially available, enantiomerically pure starting material. The *S,S* and *R,R* isomers of **10** would yield  $\Delta$  or  $\Lambda$  chelate geometries, respectively.



**Scheme 5.1:** Experimental details of the synthesis from the patent by Desreux and co-workers, as best as can be determined.

We attempted to modify the Richman-Atkins cyclen synthesis<sup>9</sup> in order to prepare **8**. In the cyclization step, we tried using both a stronger nucleophile and a more active leaving group than employed in scheme 5.1. The di-*N*-tosyl derivatives of *trans*-1,2-diaminocyclohexane (**11**) and of *N,N'*-bis(2-hydroxyethyl)-ethylenediamine (**12a**) were produced (Scheme 5.2). The di-triflic-ester of *N,N'*-bis(2-hydroxytoluenesulfonyl)-ethylenediamine (**12b**) was formed and then reacted with **11** in DMF/DCM under inert atmosphere.



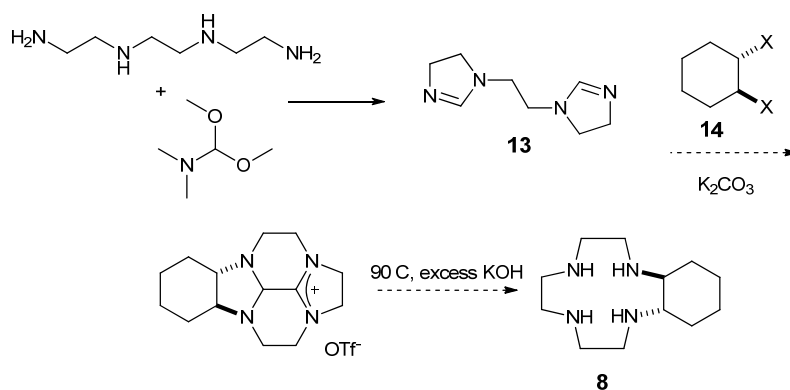


**Scheme 5.2:** Attempted adaptation of the Richman-Atkins method to yield **8**

This procedure did not lead to cyclization *via N*-alkylation of **12b**; the triflate esters were instead hydrolyzed back to the *N*-tosyl diol **12a**. In light of this result, it was hypothesized that a poorer leaving group might afford the nucleophilic substitution with the *N*-tosyl amides to out-compete hydrolysis. In attempt to increase the nucleophilicity of **11**, the disodium salt was pre-prepared using sodium ethoxide. This compound was again reacted with triflic (**12b**) or tosyl (**12c**) esters of **12a**, but no macrocycles were formed. Using equivalent building blocks, cyclization was not achieved using various solvents, heating times, and leaving groups. Scheme 5.2 was shown to be unreliable, particularly the cyclization step. It was decided that effort would be more fruitfully spent developing a more modern, higher yielding synthesis of substituted cyclen derivatives to try to produce the target macrocycle.

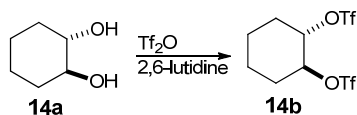
## 5.2.2 Efforts based on the Kiefer-Athey method

As described in the introduction, diimine **13** is reacted with dibromoethane to form a bridged cyclen macrocycle as reported by Kiefer and Athey. The proposed scheme for cyclohexane-bridged macrocyclic ring formation started with the reaction of **13** with an electrophilic *trans*-1,2-substituted cyclohexane (Scheme 5.3).



**Scheme 5.3:** Attempted adaptation of Kiefer-Athey method using **14**. X is a leaving group – Br, OTf, or OMs

Triethylene tetramine was reacted neat with *N,N*-dimethylformamide dimethyl acetal to form **13** according to the literature procedure. Any remaining volatiles were removed *in vacuo*, and the crude product was recrystallized from dry THF, and then isolated by filtration, all under  $N_2$ . This procedure was repeated and scaled up successfully several times. Care must be taken upon scaling up to use gradual heating and an appropriately large flask; bumping is a problem otherwise. Low yields were obtained when attempting the reaction with a solvent.



The ditriflate **14b** of *trans*-1,2-cyclohexanediol (**14a**) was prepared under N<sub>2</sub> by reacting with triflic anhydride in the presence of 2,6-lutidine and dry dichloromethane. The solvent was removed *in vacuo* and the salts precipitated by adding ether. The ether-soluble ditriflate was separated by filtering the salts off, then dried *in vacuo* and stored under N<sub>2</sub> at -20 °C until use.

The diimine **13** and ditriflate **14b** were heated under reflux for 3 hours in dry acetonitrile in the presence of 1 equivalent of potassium carbonate (Scheme 5.4). The salts were filtered off under N<sub>2</sub>, and solvent removed *in vacuo*. The resultant oil was used directly in the next step. It was dissolved in water and transferred drop-wise to a boiling solution of potassium hydroxide (5.7 M). The solution was heated under reflux for an additional 30 minutes, allowed to cool, and concentrated *in vacuo*, yielding an aqueous solution with precipitate. Both the solution and precipitate were analyzed by MS. The target mass of **8** (227, [M+H]<sup>+</sup>) was observed in each spectrum, but is not the major ion. Extraction of **8** from the hydrolysis mixture into chloroform or dichloromethane was attempted. Recrystallization was also attempted by slow diffusion of ethanol or diethyl ether into the aqueous mixture. Sublimation of a small portion of the lyophilized residue was also attempted. None of these techniques resulted in successful isolation of the target mass.

As attempts to isolate the product from the hydrolysis step were unsuccessful, an effort was made to isolate the cyclization product prior to the hydrolysis step. The reaction of **13** and **14b** was repeated, but not taken on to the hydrolysis step. Unsuccessful attempts were made to crystallize **8** or its ethylene-bridged precursor from toluene or water.

Instead, the crude solid was rinsed with cold acetonitrile, and both the solid and extract were analyzed by MS (representative spectrum in Figure 5.1). A variety of species are present, including peaks which appear to correspond to the target macrocycle (247,  $[M]^+$ ), the suspected hydrolysis product **8** (226,  $[M]^+$ ), and a proposed mono-N-alkylated species (266,  $[M+H]^+$ ) where the second triflate had been hydrolyzed rather than displaced by a nucleophilic nitrogen. Ions with larger  $m/z$  are probably acyclic dimer or trimer combinations of **13** and **14b**.

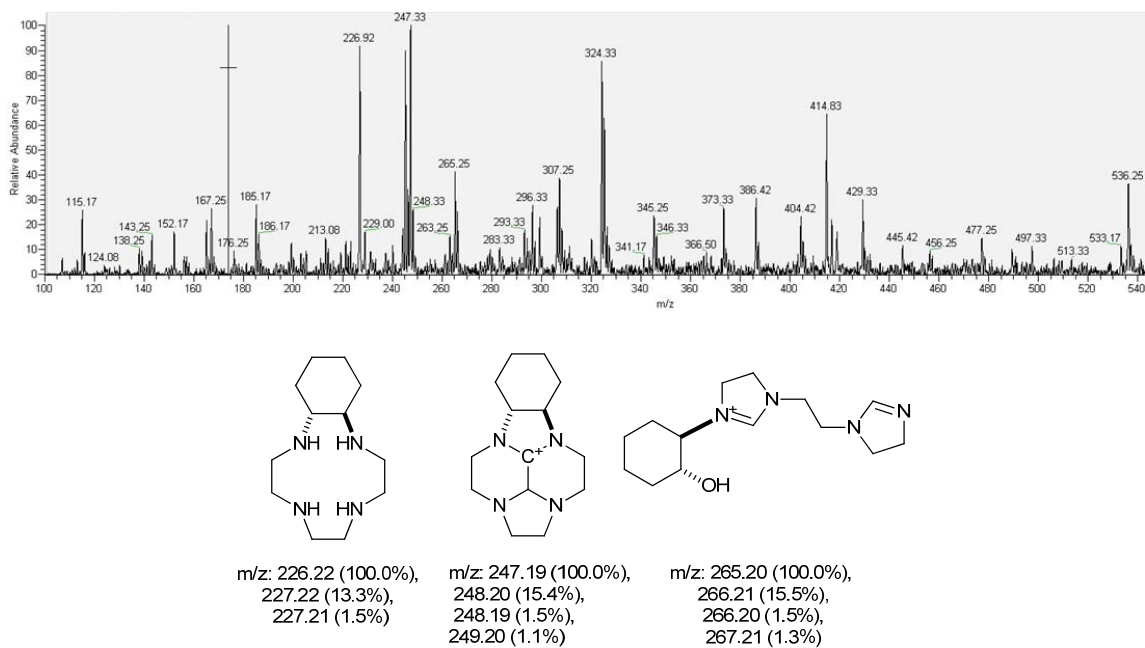
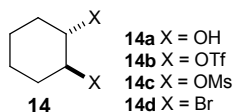


**Figure 5.1:** Representative mass spectrum of the reaction of **13** and **14b** and proposed structures corresponding to observed  $m/z$  peaks

Following the suspicion that water was inhibiting successful synthesis at some stage, procedural modifications were adopted to exclude air and moisture over the course of the reaction and work-up.

After running the cyclization reaction and preparing its precursors using the above changes, mass spectrometric analysis of the isolated solid again reveals an ion at  $m/z$  227. If this product is in fact a 12-membered tetra-aza crown, it should readily form a stable complex with copper. The material possessing  $m/z$  227 was stirred with Cu(II) triflate overnight. This substance, however, does not form a polydentate complex with Cu(II) after heating in water; the solution remained the pale blue-green of copper triflate and did not turn the deep blue of a copper ethylenediamine species. The product is likely a non-macrocyclic isomer of the target (cyclohexyl)cyclen **8**. Subsequent experiments were performed on the effect of changing the leaving group and the solvent for the cyclization reaction.

#### Effect of the leaving group



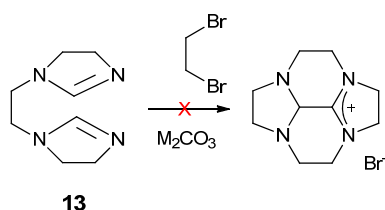
The di-mesylate (**14c**) of *trans*-1,2-cyclohexanediol showed no reaction with diimine **13** in either dry acetonitrile or dry dimethylformamide after heating at reflux for approximately 40 h. The use of *trans*-1,2-dibromocyclohexane (**14d**) also did not result in cyclization.

Effect of the solvent

Chloroform was substituted for acetonitrile in the cyclization reaction. The reaction progress was monitored by NMR after 3h and 19h. The NMR data showed that almost exclusively starting materials are present after 3h, and no longer present after 19h. The organic-insoluble residue was subjected to the hydrolysis procedure, but none of the intended product was observed by mass spectrometry.

Effect of cyclohexyl group

In order to gain evidence for or against intrinsic problems related to the experimenter or scale, the reference procedure<sup>10</sup> (Scheme 5.4) was performed, forming the diimine **13** and reacting with dibromoethane in MeCN. Characterization of the resultant material was performed with similar results to that of the solvent effect experiments – the bridged tetraamide in Scheme 5.4 is not clearly observed from NMR or MS data, and could not be extracted with hot toluene.

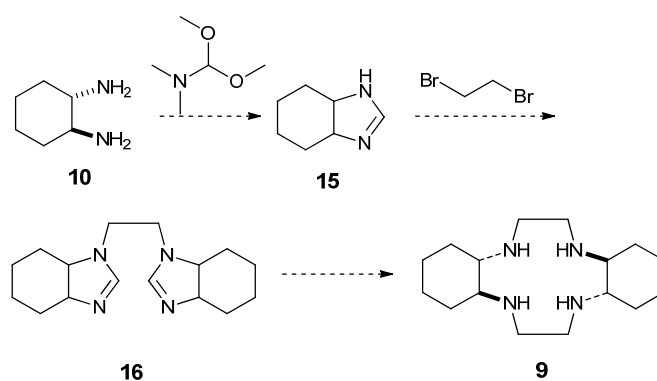


**Scheme 5.4:** Attempt to prepare **8** from 1,2-substituted ethylene

Substituting dibromoethane for 1,2-difunctionalized cyclohexane did not yield cyclen or its cyclized intermediate, nor did changing other reaction conditions including solvent,

temperature, duration, or salt. Owing to our inability to reproduce the Kiefer/Atthey cyclization method for cyclen, this approach was not investigated further.

A synthetic strategy was tested in which the imine would be formed from the cyclohexyl portion. In our lab, diamine **10** was reacted neat with *N,N*-dimethylformamide dimethyl acetal (scheme 5.5) in dry methanol under nitrogen.



**Scheme 5.5:** Formylation of **10** in attempt to prepare **9**

Solvents were removed *in vacuo*, and crystallization of the product (**15**) showed was attempted using THF. A precipitate formed after approximately 1 week stored under argon at -20 °C, but was no more pure than the starting material. The mixture exhibited peaks which appeared to indicate **15**, but a low degree of purity was observed by NMR. Mass spectrometric analysis reveals the target mass (125.25,  $[M+H]^+$ ) to be present, but it is not the major ion; many species are observed. Attempts were made to form an ethylene-bridged dimer (**16**) of the target imine (**15**), using 1,2-dibromoethane (with and without iodine chips), 1,2-dichloroethane, and the ditosyl derivative of ethylene glycol.

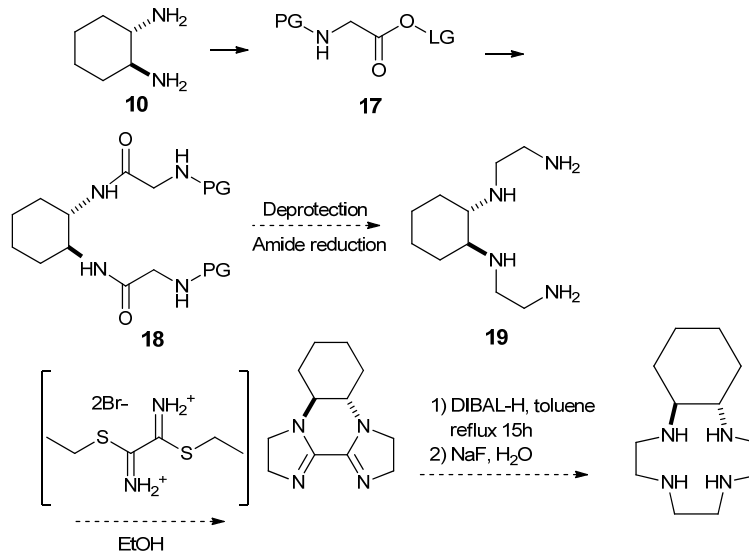
None of the above experiments have resulted in a pure compound. It was postulated that a more pure imine might be necessary to form the bridged dimer.

Purification of the imine **15** was attempted by column chromatography. The crude sample could not be eluted from a silica gel column. TLC studies were performed using cellulose or basic alumina as stationary phases. The major UV-absorbent component had an  $R_f$  which could not be tuned low enough on cellulose with varying solvents. The alumina-based system showed promise, especially after drying the alumina for approximately 15 minutes in a 105 °C oven. The separation method developed consisted of an initial elution using 50/50 hexane/ethyl acetate, followed by a gradient culminating in a 50/50 methanol/dichloromethane secondary elution. An alumina column was run on a large (10 g) batch of crude imine. Mass spectrometric analysis revealed the target mass to no longer be present in any of the fractions collected. It is likely that **15** is unstable in the presence of water/air over time, and/or is unstable on the column or binds irreversibly.

### *5.2.3 Developments based on the cyclen synthesis published by Weisman et al.*

In the cyclen synthesis developed by Weisman and co-workers<sup>11</sup>, a bridged tetramine is formed without passing through an intervening formylation step to yield an imine. Various attempts for preparation of **19** were made, starting with **10**. Compound **19** could lead to cyclization via a Weisman-type synthesis.<sup>12</sup>

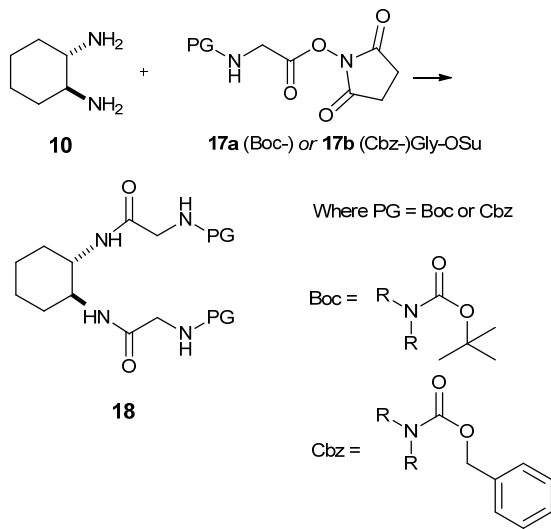




**Scheme 5.6:** approach to tetramine **19** for use in a Weisman-type synthesis using an activated, *N*-protected amino acid, where PG = protecting group and LG = leaving group.

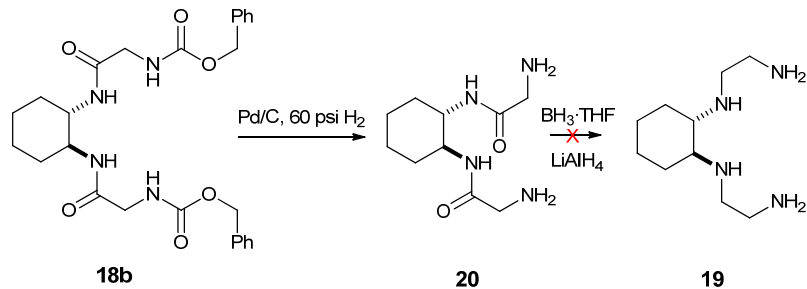
Keys to the success of this scheme are adding a C-C-N chain to **10** with a minimum number of high-yield steps, and avoiding cumbersome purification of intermediates as much as possible. An *N*-protecting group such as *t*-butoxycarbonyl (Boc) or carboxybenzyl (Cbz) was used on the incoming amino acid derivative **17**, and the cyclohexylamine adduct was prevented from further reaction by forming an amide (**18**), (Schemes 5.6 and 5.7) affording mono-alkylation of the amines in **10**.

Initially, synthesis of **18a** was attempted using Boc-glycine and coupling reagents *N*-hydroxysuccinimide (NHS) and *N*-(3-Dimethylaminopropyl)-*N'*-ethylcarbodiimide HCl (EDC) (Scheme 5.7).



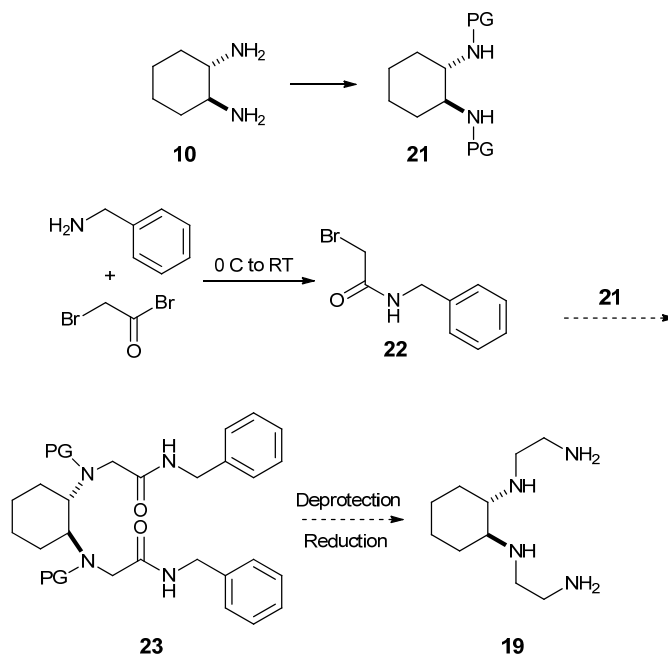
**Scheme 5.7:** Alkylation of **10** using Boc- or Cbz-Gly-OSu (**17a** or **17b**)

The succinimide ester **17a** was isolated as a minor product of this synthesis *via* successive recrystallization, and reacted with **10**. Deprotection of **18a** with trifluoroacetic acid (TFA) was then attempted. However, this did not yield **20**. It was suspected that the strongly acidic conditions (6M HCl) needed to remove the Boc group were also hydrolyzing the amides to some degree. The Boc group was replaced with the Cbz group, which does not require acid deprotection. *N*-(carboxybenzyl)-glycine-succinimidyl ester (Cbz-Gly-OSu, **17b**) was obtained commercially. The diamide **18b** was prepared, and the terminal amines deprotected using catalytic hydrogenolysis as shown in Scheme 5.8. However, it was not possible to reduce the amides in **20** using  $\text{BH}_3 \cdot \text{THF}$  even with extended heating. Reduction of **20** and similar amides by a group member using lithium aluminum hydride resulted in very poor yields.



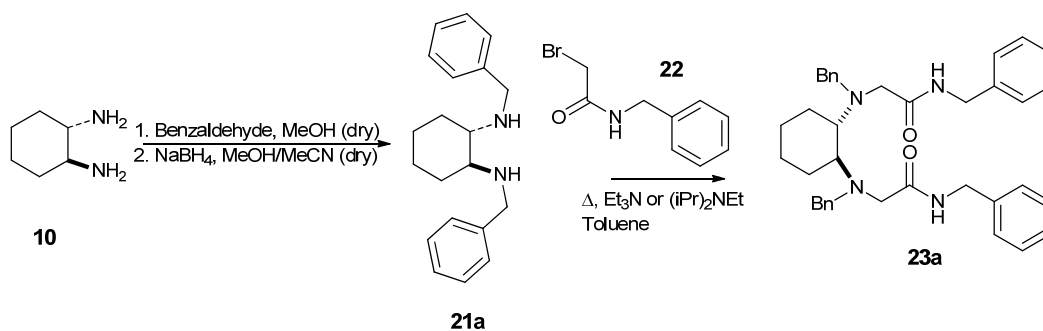
**Scheme 5.8:** Hydrogenation of Cbz groups to yield **20** and subsequent attempts at reduction of the amides

We suspected that the main obstacle to reduction of **20** arose from the steric hindrance of the secondary amides. An alternative route to **19** was devised to lower the energy barrier for ligation of the amide oxygens to boron, as seen in Scheme 5.9.



**Scheme 5.9:** Approach to tetramine **19** for use a Weisman-type synthesis using an N-protected **10** (**21**) and an amide alkylating agent. PG = protecting group

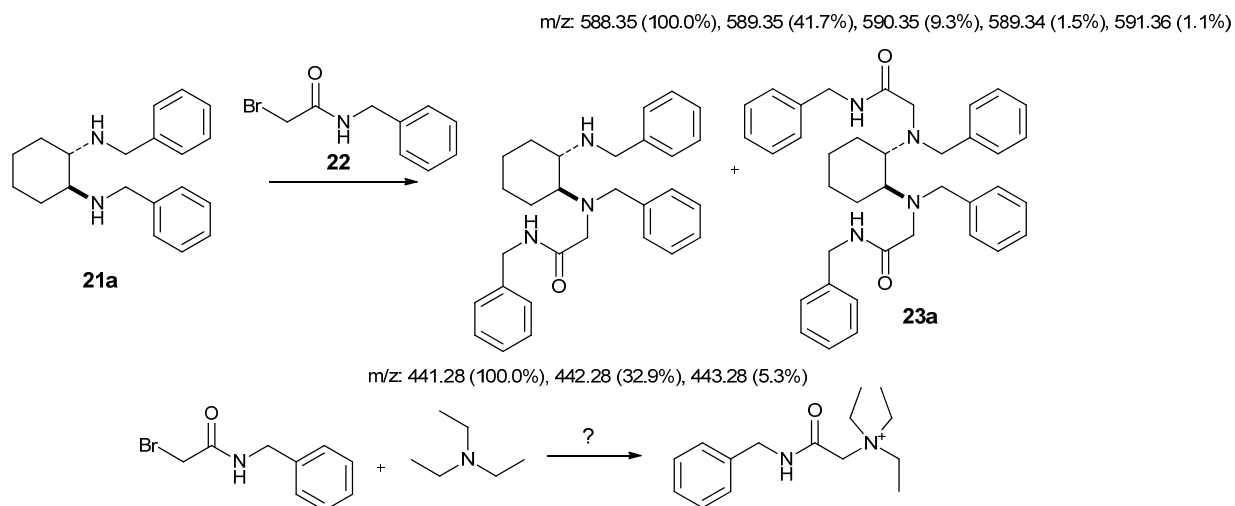
A promising coupling reaction of bromoacetamide **22** to benzyl-protected *trans*-1,2-diaminocyclohexane (**21a**) was developed. Advantages of this approach include cheap, readily available starting materials, a chromatographic handle, and no mechanism for over-alkylation. Compound **10** was protected by reductive amination (Scheme 5.10).



**Scheme 5.10:** Alkylation of N-protected **10** with a  $\beta$ -amide

A sample of **22** was prepared from bromoacetyl bromide and benzylamine and was used as the alkylating agent for the protected amine (**21a**). A series of bases (triethylamine, diisopropylethylamine (Hünig's base), 1,8-Diazabicyclo[5.4.0]undec-7-ene (DBU), sodium ethoxide, and potassium carbonate) and solvents (dry THF, dry MeCN, toluene, and dry methanol) were tested in effort to find optimal reaction conditions. Organic nitrogen bases promoted the reaction more than ethoxide or carbonate. However, mass spectral evidence suggested a tendency for the organic amine bases to also react with the bromoacetamide, especially in more polar solvents (Scheme 5.11). Hünig's base, in theory, is more strongly basic and less nucleophilic than triethylamine, both desirable attributes, and the product-to-base-adduct ratio was higher with Hünig's base (5:2 by ESI-MS ionization intensity) compared with triethylamine (2:5). Complete alkylation of

both amines of **21a** was not observed under any conditions tested. However, the greatest yields were obtained from heating in Hünig's base / toluene at  $\sim 105^\circ\text{C}$ .



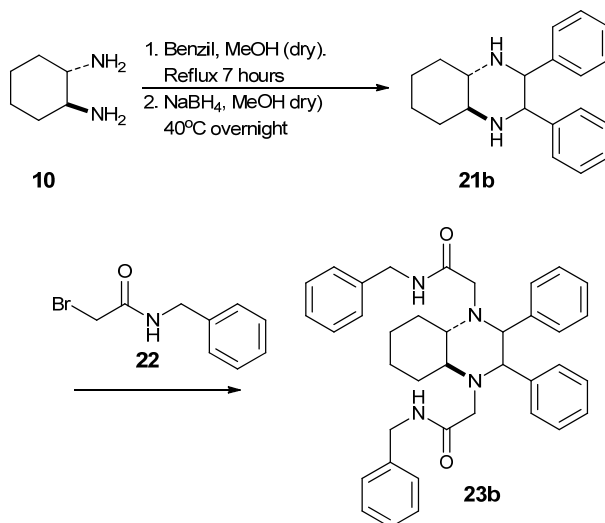
**Scheme 5.11:** Incomplete alkylation of **21a** with **22** and reaction of organic nitrogen base with **22**

Modification of protecting group, reaction time, and workup, and lyophilization of **21**:

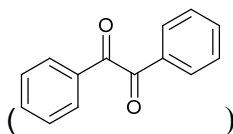
The reaction of **21a** with **22** was monitored by mass spectrometry after 2, 5, 7 and 14 days (**23a** =  $m/z$  589,  $[\text{M}+\text{H}]^+$ ). The peak at  $m/z$  442 (ESI+,  $[\text{M}+(\text{N-benzyl})\text{acetamide}]^+$ ) remained large, indicating that the second alkylation of protected **10** is incomplete even after a two weeks of heating regardless of solvent, base, and reaction temperature.

Benzil was employed as an alternative protecting group (in **21b**) en route to a fused-ring macrocycle (Scheme 5.12). The preferred conformation of the cyclohexane / diazacyclohexane in **21b** likely discourages chelation of alkali metals by the mono-

alkylated species (the adduct of **21b** and 1 equivalent of **22**), which would reduce the *N*-nucleophilicity.



**Scheme 5.12:** Replacement of the benzyl protecting group of **10** with benzil



The benzil-protected diaminocyclohexane **21b** has a slightly greater tendency towards alkylation of both amines (in comparison to **21a**) in toluene with Hünig's base, heating over several days. Additionally, **21b** is readily soluble in hot toluene; the benzyl-protected diamine **21a** requires the addition of water to dissolve.

Freeze-drying is advantageous for making the precursors **21a** and **21b** less colored and less sticky; a substantial amount of mass loss (as water/solvents) was observed following lyophilization. It is assumed that the resulting solid was weighed in closer to the desired stoichiometric amounts when combined with *N*-alkylating agents. It was also discovered

that crystallization of the crude residue from the reaction of **21** with **22** could be accomplished by slow diffusion of hexanes into methanol, but that the crystals are of the bromoacetamide, not the mono- or di-alkylated product. An acid/base workup was attempted on the mother liquor from the recrystallization, but the amines could not be extracted from the aqueous phase, and could not be isolated when this aqueous mixture was freeze-dried.

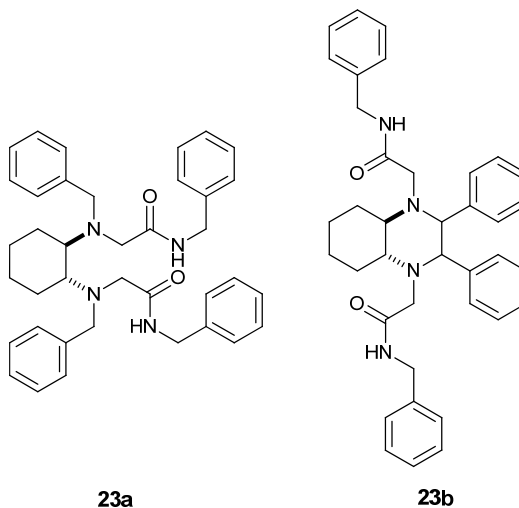
DBU was tested in place of Hunig's base when combined with **21b** and **22** in effort to afford a quicker, cleaner dialkylation. This reaction was done under argon for 4 days. MS of the isolated residue showed mostly starting material and what seems to be an alkylation by-product of DBU and acetamide.

Micro-scale and scale-up batches of **21b** with **22** were performed and reaction progress monitored on alumina TLC plates. The reactions were allowed to run for 5 days. The reaction is observed to progress over 48 hours on alumina plates using 30:70 hexanes/EtOAc. No change in the relative intensity of product is observed between 48 and 120h. The reactants are not completely soluble in toluene at concentrations of ~ 7-30 mM. The reaction seems to produce a greater percent yield when done in dilute fashion. A ~10% impurity is seen by NMR in some scale-up batches of **21b** and **22**, but this could not be removed by extraction or freeze-drying, or separated by TLC. The impurity is not apparent in the mass spectrum of the crude reaction products. A small portion of the reaction of **22** with **21b** crystallized from ether/hexanes/drop of ammonia. These crystals were reacted with **17b** in DCM. It was later discovered by NMR that the crystals were again **22**. Crude **23b** was added to this reaction mixture. TLC indicates that no reaction

between the succinimide ester and the benzil-protected 2° amine took place after several hours. The reaction was refluxed overnight, solvents were removed *in vacuo*, and the crude residue analyzed by MS. No apparent alkylation product mass was observed.

No conditions were found to afford **23a** or **23b** without the incomplete alkylation product present. It was necessary to purify these diamides to remove the partial alkylation product prior to attempts at reduction.

Purification of diamide **23** by column chromatography:



Purifications of **23a** by column chromatography were performed using various solvent systems and stationary phases. For example, 0.7 g **23a** was synthesized and the reaction was terminated after 3 days' heating. Purification was accomplished by silica gel chromatography (~700 mL 70:30 Et<sub>2</sub>O / hexanes, then 250 mL Et<sub>2</sub>O, then ~600 mL 25 : 75 MeOH : Et<sub>2</sub>O). Approximately 0.1 g purified material was obtained from the column. Alternatively, **23a** was eluted from silica using 80:20 ethyl ether/hexanes followed by 75:25 ethyl ether/MeOH.



The use of basic alumina as the stationary phase can result in better elution of amines than use of the silica gel, which is acidic. A column was run on a portion of crude **23b** using a small plug of alumina. The order of eluents for this column was 50:50 Et<sub>2</sub>O:hexanes, 90:10 Et<sub>2</sub>O:hexanes, then 85:15 Et<sub>2</sub>O:methanol. TLC of the resulting fractions suggested that an alumina column using 90:10 Et<sub>2</sub>O:hexanes would resolve the residue into its respective components, and this chromatography was subsequently carried out. Mass spectrometric data of the alumina column fractions confirmed that the reaction is not proceeding to completion, and that the desired product **23** cannot be separated from **22** on alumina using a mixture of Et<sub>2</sub>O/hexanes (it co-elutes).

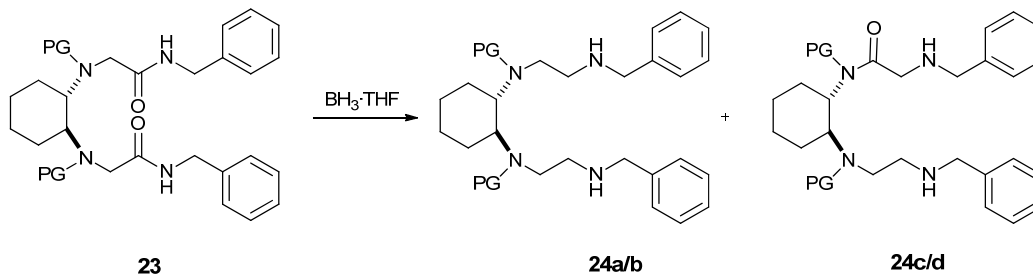
An intermediate-sized batch of the reaction of **21b** with **22** was performed. Ammonium hydroxide was added to the mobile phase to ensure the amines stay de-protonated, which should lead to narrower resolution bands and more complete elution. A small portion of the product was run down a micro-scale column (silica, with 100:6:1 chloroform:MeOH:ammonia. Separation of **22** from the product resulted, but mono- and di-alkylated products co-eluted, and the mono-alkylated was present in much greater abundance. TLC data suggested that these species could be resolved using 80:20:1 Et<sub>2</sub>O:hexanes:ammonia on silica. A column was run using this mobile phase. No pure di-alkylated material was recovered, but mono-alkylated material was obtained from the column.

To test whether impurities in the protected **10** synthesis were affecting the chromatography, a quantity of **21b** was synthesized and isolated by extraction from saturated sodium bisulfite solution with DCM. Much of the product is lost in the aqueous

phase and could not be recovered by freeze drying. The oily residue from the reaction of this material with **22** was purified by silica gel chromatography (~700 mL 70:30 Et<sub>2</sub>O / hexanes, then 250 mL Et<sub>2</sub>O, then ~600 mL 15:85 MeOH:Et<sub>2</sub>O). The compound of interest is not soluble in the mobile phase and was loaded onto the column in THF, which was then partially evaporated with a stream of air. Some of the crude product is carried through with the solvent front, likely because of the method of loading.

Reduction of amides from a purified, dialkylated diaminocyclohexane:

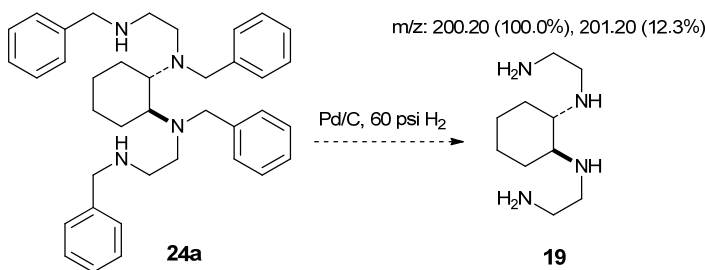
Reduction of **23a** was done using BH<sub>3</sub>·THF solution (Scheme 5.13), followed by MeOH/HCl workup. This reaction is slow – incomplete reduction was still observed after heating at 60 °C for a week.



**Scheme 5.13:** Reduction of the amides in **23**; PG = benzyl (**24a/c**) or benzyl (**24b/d**).

Reaction of **23b** with BH<sub>3</sub>·THF also yielded a mixture of mono- (**24d**) and di-reduced products after 1 week. The residue was neutralized and solvents were removed *in vacuo*. The product could not be recovered from further attempts at reduction of this material with BH<sub>3</sub>·THF.

A mixture of **24a** and **24c** was purified by silica gel chromatography (~700 mL 84:14:3 DCM:MeOH:NH<sub>4</sub>OH, followed by ~100 mL 49:49:3 DCM:MeOH:NH<sub>4</sub>OH, followed by a final flush of the column with MeOH). A group of fractions was identified to have a base peak of  $m/z$  561 ( $[M+H]^+$ ) by MS, indicating the product **24a**. These fractions were combined, solvents removed *in vacuo*, and crystallization was induced from using slow diffusion of hexanes into MeOH/trace HCl. The crystalline **24a** was dissolved in ethanol and reacted on the hydrogenator at 60 psi H<sub>2</sub> for 3 days in attempt to remove the benzylic protecting groups (Scheme 5.14).

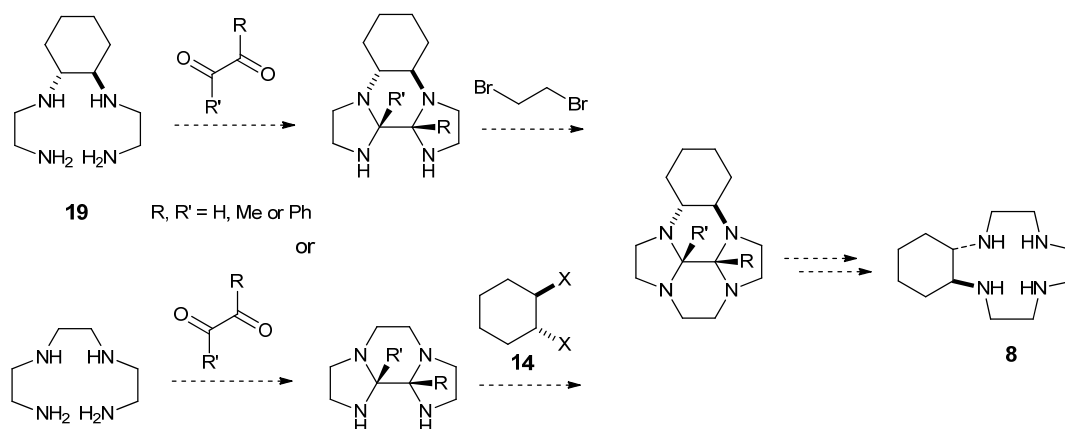


**Scheme 5.14:** Removal of benzylic protecting groups in **24a** via catalytic hydrogenation

The Pd/C catalyst was filtered off and solvents removed *in vacuo*. The mass spectrum of the isolated residue exhibits only one peak at  $m/z = 220$  (positive mode), which does not correspond to a logical product or fragment. It is possible that the crystals isolated in the previous step of the synthesis were actually a more weakly ionizing impurity, rather than the desired above tetramine **24a**. A new sample of **24a** was prepared and again purified by column chromatography. A small amount of what appeared to be **19** (a tetraamine) by NMR was obtained from this reaction by hydrogenation at 60 psi H<sub>2</sub>. This sample was

reacted with  $\text{Cu(II)CO}_3$ , but did not form a complex according to the mass spectrometric data, indicating that this material is not in fact **19**.

In summary, **24** cannot be prepared quickly with a high degree of purity and is poorly resolved from its precursors/byproducts by any chromatographic method tested. The difficulty of preparing suitable starting materials for a Weisman-type synthesis was not initially appreciated. Work on Scheme 5.9 was eventually discontinued as enough material could not be accumulated for de-benzylation of a laboratory-scale batch of **24**. Synthetic developments by Dr. L. Zhao have led us to shelve the approach based on **21** indefinitely. A 1.0 g scale batch of the butanedione/triethylenetetramine bicyclization reaction was attempted based on the procedure first published by Boschetti *et. al.* The synthetic strategy on which this reaction is based is shown in Scheme 5.15.<sup>13</sup>



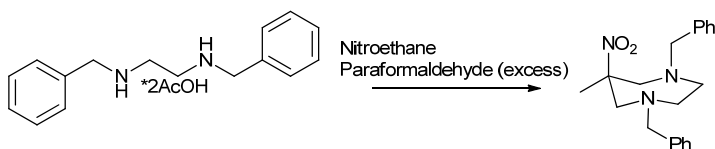
**Scheme 5.15:** A possible pathway to **8** via glyoxal-type cyclization

Interpretation of the resulting NMR proved difficult, but the product appears to be a cycloimine rather than the fully formed tricycloamine. Increasing the reaction

time/temperature is worth exploring, but there are concerns about stability of the bridged tetramine reported.

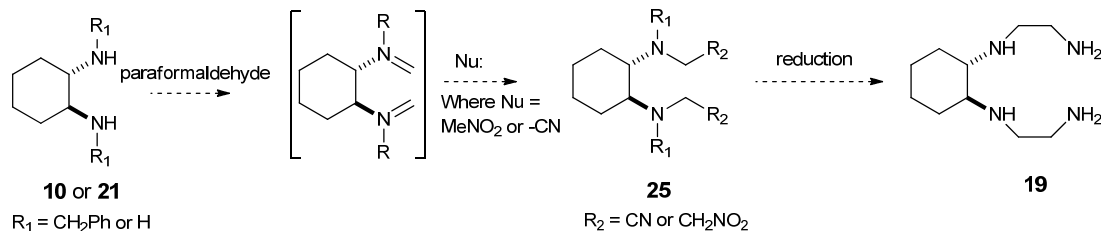
#### 5.2.4 Efforts based on a modified nitro-Mannich reaction

A derivative of the Mannich reaction (modified to replace the enol with an alternate nucleophile like cyanide or nitroethane) has led to successful cyclization by other groups,<sup>14</sup> and Scheme 5.16 has been reproduced in our lab.



**Scheme 5.16:** Nitro-Mannich reaction for *N*-cyclization

Due to the difficulties in reducing **20** and **23**, another approach was investigated based on *N*-cyclization using paraformaldehyde chemistry.<sup>15</sup> A possible alternative pathway to the sterically cumbersome, benzyl-protected alkylation involved CNR<sub>2</sub> addition to an activated imine (Scheme 5.17).



**Scheme 5.17:** A possible pathway to **11** using a modified nitro-Mannich reaction

If an unbranched C-N nucleophile can be added cleanly to a free or protected **10** *via* with C-addition, an alternative synthetic pathway to **19** may be available to us. Deprotection of benzyl amines, reduction of nitriles, and reduction of nitro groups can all be accomplished by (possibly simultaneous) catalytic hydrogenation.

A number of microscale reactions were performed at room temp. overnight using **21a**, paraformaldehyde, and multiple solvents, catalysts, and nucleophiles – see Table 5.1. Nitromethane is more difficult to work with, so nitroethane was used in this exploratory study.

Nu:	Acid/base	Solvent	Notes
KCN	HCl (to adj. to pH 7)	THF/Water	Extracted with ether
KCN	1 drop HCl	THF/Water	
KCN	None	THF/Water	Stirred for 2h before adding KCN
KCN	1 drop HCl	THF	
KCN	1 drop HCl	THF/Water	Added titanium turnings as lewis acid
EtNO <sub>2</sub>	1 drop HCl	THF/Water	
KCN	None	THF	
KCN	None	EtOH	
EtNO <sub>2</sub>	None	THF	

**Table 5.1:** Exploration of Scheme 5.13 using **21a** as a starting point.

None of the possible variations of **25** were clearly formed as a result of any of these trials. Some problems with the above were: paraformaldehyde is not soluble in alcohols or ethers at room temperature. It is sparingly soluble in water/EtOH at elevated temp.  $m/z = 393$  (ESI MS+,  $[M+Na]^+$ (?)) was observed in each reaction mixture, but is probably not the intended product if it is also observed when EtNO<sub>2</sub> was the nucleophile (a different product mass would result). As a result of these trials, it was not possible to isolate the formylation product of **10** by recrystallization or chromatographic purification, which could have given us a route to **19**. A product band was not observed by TLC if water was present, but this may not mean that a reaction is not taking place.

KCN is probably a weak nucleophile by itself (and is not soluble in alcohols or ethers, either). The reverse reaction is almost certainly taking place – the cyano group would be a good leaving group under the above conditions. An activated cyano donor (TMSCN or HCN) and a less sterically hindered electropositive carbon would probably shift the equilibrium more towards the product. A review of the literature also suggests that a better Lewis acid may catalyze the reaction (HBr, transition metal salts). Isolating the imine resulting from reductive amination with a formyl donor may be a workaround for the reversibility/solubility problems seen above.

#### *5.2.5 Other avenues of approach and future directions*

Template-based syntheses of twelve-membered tetraaza rings have been reported.<sup>13,16-19</sup> This approach is based on the premise that the coordination of a metal to the *O*- and/or *N*-atoms in an acyclic precursor leads to “preorganization” of the ligand’s solution structure, favoring cyclization. These template-based procedures were adapted in attempt to synthesize **8**. Dihydroimidazole **13** was combined with copper (II)carbonate/copper (II) hydroxide and *trans*-1,2-dibromocyclohexane under Argon. No reaction was observed. A similar synthesis was attempted with triethylenetetramine and iron (III) chloride hexahydrate. Again, no reaction was observed.

Due to the difficulty in dialkylating **21**, attempts were made to alkylate unprotected **10**. Under varying conditions, the full range of available alkylations (1-4) were detected by MS, with trialkylated predominating. These compounds may be resolvable by column chromatography.



Other approaches that were attempted included reaction of **10** with N-tosyl-aziridine (which polymerized), **10** with glyoxal bisulfite (which failed to form a dimer of **10** akin to **16**), and synthesis of benzylaziridine under Mitsunobu conditions (which failed).

### 5.3 Conclusions

It is evidently more complicated to synthesize **8** or **9** with optimum yield than was originally assumed. In the interest of designing experiments to lead to a logical, scientifically valuable conclusion within a reasonable amount of time, thesis work devoted to cyclohexyl fused rings was discontinued. We have decided to move forward with **2** despite the problem of regioisomerism. There is scientific merit in studying the properties of each individual isomer which can form from chelation of  $\text{Ln}^{3+}$  with **2**.

### 5.4 References

- (1) Desreux, J. F.; F., T. M.; Ratsep, P. C.; Wagler, T. R.; Marinelli, E. R. Hepatobiliary tetraazamacrocyclic magnetic resonance contrast agents Bristol Myers Squibb, Princeton, N.J. 1994
- (2) Comblin, V.; Gilsoul, D.; Hermann, M.; Humblet, V.; Jacques, V.; Mesbahi, M.; Sauvage, C.; Desreux, J. F. *Coordination Chemistry Reviews* **1999**, 185-186, 451.
- (3) Brechbiel, M. W.; Chong, H.-S. Backbone-substituted bifunctional DOTA ligands, complexes and compositions thereof, and methods of using same. United States Dept. of Health and Human Services, USA WO2004021996 (A3) 2004
- (4) Vanasschen, C.; Bouslimani, N.; Thonon, D.; Desreux, J. F. *Inorganic Chemistry* **2011**, 50, 8946.
- (5) Camp, C.; Guidal, V.; Biswas, B.; Pécaut, J.; Dubois, L.; Mazzanti, M. *Chemical Science* **2012**, 3, 2433.
- (6) Scully, C. C. G.; Rai, V.; Poda, G.; Zaretsky, S.; Burns, D. C.; Houliston, R. S.; Lou, T.; Yudin, A. K. *Chemistry – A European Journal* **2012**, 18, 15612.
- (7) Guo, S.; Wang, G.; Ai, L. *Tetrahedron: Asymmetry* **2013**, 24, 480.
- (8) Stetter, H.; Mayer, K.-H. *Chemische Berichte* **1961**, 94, 1410.

- (9) Richman, J. E.; Atkins, T. J. *Journal of the American Chemical Society* **1974**, *96*, 2268.
- (10) Athey, P. S.; Kiefer, G. E. *The Journal of Organic Chemistry* **2002**, *67*, 4081.
- (11) Weisman, G. R.; Reed, D. P. *The Journal of Organic Chemistry* **1996**, *61*, 5186.
- (12) Alexakis, A.; Chauvin, A.-S.; Stouvenel, R.; Vrancken, E.; Mutti, S.; Mangeney, P. *Tetrahedron: Asymmetry* **2001**, *12*, 1171.
- (13) Boschetti, F.; Denat, F.; Espinosa, E.; Guillard, R. *Chemical Communications* **2002**, *0*, 312.
- (14) Aime, S.; Calabi, L.; Cavallotti, C.; Gianolio, E.; Giovenzana, G. B.; Losi, P.; Maiocchi, A.; Palmisano, G.; Sisti, M. *Inorganic Chemistry* **2004**, *43*, 7588.
- (15) Flann, C.; Malone, T. C.; Overman, L. E. *Journal of the American Chemical Society* **1987**, *109*, 6097.
- (16) Fabbrizzi, L.; Licchelli, M.; Manotti Lanfredi, A. M.; Vassalli, O.; Ugozzoli, F. *Inorganic Chemistry* **1996**, *35*, 1582.
- (17) Gèrbélèu, N. V.; Gerbeleu, N. V.; Arion, V. B.; Burgess, J. *Template synthesis of macrocyclic compounds*; Wiley-VCH, 1999.
- (18) Kang, S.-G.; Nam, K.; Kweon, J. K.; Jung, S.-K.; Lee, U. *Bulletin of the Korean Chemical Society* **2006**, *27*, 577.
- (19) Gurumoorthy, P.; Ravichandran, J.; Karthikeyan, N.; Palani, P.; Rahiman, A. K. *Bulletin of the Korean Chemical Society* **2012**, *33*, 2279.

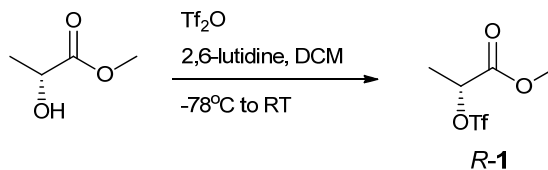
**CHAPTER 6: EXPERIMENTAL SECTION****6.1 General Procedures***6.1.1 Synthesis, purification, and characterization of Ln-2 chelates*

For the synthesis of Ln<sup>3+</sup> chelates, all glassware was acid-washed (H<sub>2</sub>SO<sub>4</sub>) prior to the introduction of organic chelators in order to remove trace metals. All compounds and materials for studies of the Eu<sup>3+</sup>-, Gd<sup>3+</sup>-, Y<sup>3+</sup>-, and Yb<sup>3+</sup> chelates of  $\alpha$ ,  $\alpha'$ ,  $\alpha''$ ,  $\alpha'''$ -tetramethyl [(S)-2-(4-nitrobenzyl)-1,4,7,10-tetraazacyclododecane-1,4,7,10-tetraacetate] (Ln-S-NB-DOTMA; Ln-2) and their biphenyl conjugates (Ln-S-SSSS-6) were prepared according to previously described methods.<sup>1,2</sup> The HPLC system employed was a Waters 2545 Quaternary Gradient Module with a flow rate of 50 mL min<sup>-1</sup> and continuous He sparge. A Phenomenex Luna C18(2) 250 x 50 mm column was used for all preparative separations, with a polar phase of 0.037% HCl (w/w), and an organic phase 100% acetonitrile, with varying gradients as described below. Absorption was monitored at 270 nm (for nitrobenzyl derivatives) or 254 nm (for biphenyl derivatives) using a Waters 2489 UV/Visible detector. All Ln-2 NMR samples were prepared in > 99.9% enriched D<sub>2</sub>O and the pD was not adjusted (unless otherwise noted) but found to lie in the region of 3 – 4 depending upon the concentration of the chelate (each chelate is isolated in its HEuL(H<sub>2</sub>O) form by preparative HPLC). 1-Dimensional <sup>1</sup>H NMR spectra were recorded on a Bruker Avance IIa spectrometer operating at 400.13 MHz using a 5 mm broad-band probe with the temperature controlled using the installed variable-temperature controller model 2416 with BCU-05 chiller. All spectra were referenced with the HOD at 4.7 ppm.

Two-Dimensional  $^1\text{H}$ - $^1\text{H}$  correlational spectroscopy (COSY) data were acquired on a Bruker Avance III spectrometer operating at 600.13 MHz. The temperature was controlled using the installed variable-temperature controller model 2416 with BCU-05 chiller. A 5 mm broad-band probe was used to acquire  $1024 \times 1024$  points. In cases where sample was limited (Eu-*S-SRRR-2* side isomer and Eu-*S-RRRR-2* side isomer), a 1.7 mm microprobe was employed, acquiring  $1024 \times 1024$  points. Coupling constants were not obtainable from  $\text{Ln}^{3+}$  complexes due to the significantly broadened NMR peaks.

### 6.1.2 Organic syntheses

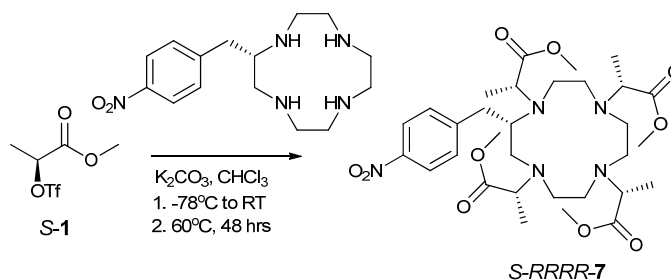
All reagents were obtained commercially except where otherwise noted. Type I water (18.2 M $\Omega$ ·cm) was used in all reactions, workups, and chromatography where applicable. Dry solvents were obtained from a solvent still employing adsorption columns for oxygen and water. Air-free chemistry was performed on a Schlenk line with Virtis vacuum pump and liquid  $\text{N}_2$  trap.  $\text{N}_2$  and argon atmospheres were generated using gas cylinders with 99.998% purity or greater. Positive pressures were maintained and monitored using an oil bubbler. Solvent removal *in vacuo* was accomplished using rotary evaporation unless otherwise noted. NMR samples were prepared in 0.6 - 1.0 mL deuterated solvent without pH adjustment in Norad 507HP sample tubes, and spectra were recorded on a Bruker Avance IIa spectrometer operating at 400.13 MHz using a 5 mm broad-band probe unless otherwise noted. Standard pulse sequences for  $^1\text{H}$ ,  $^{13}\text{C}$ , COSY and HSQC analyses were utilized.

**6.2 Regioisomeric Ln-2-type chelates****6.2.1 Synthesis and characterization****(R)-methyl 2-(((trifluoromethyl)sulfonyl)oxy)propanoate (R-1)**

Methyl D-lactate (0.9 mL, 9.6 mmol) and 2,6-lutidine (1.0 mL, 9.0 mmol) were dissolved in dichloromethane under inert atmosphere (either N<sub>2</sub> or argon). The solution was stirred and cooled in a dry ice/acetone bath. Trifluoromethanesulfonic anhydride (2.5 mL, 14.4 mmol) was added drop-wise. After one hour, the low-temperature bath was removed, and the reaction was stirred under inert atmosphere for an additional 2 - 3 hours. Solvents were then removed *in vacuo*, affording a brown residue. The salts formed as a by-product were precipitated from the remaining residue using diethyl ether or hexanes, and the soluble portion was isolated by decanting. Solvents were again removed *in vacuo*, and the title compound was afforded as a colorless liquid. NMR data were consistent with that previously published:<sup>3</sup> <sup>1</sup>H NMR (400 MHz, CDCl<sub>3</sub>) δ 5.15 (1H, q, <sup>3</sup>J<sub>H-H</sub> = 7 Hz, CH), 3.76 (3H, s, OCH<sub>3</sub>), 1.62 (3H, d, <sup>3</sup>J<sub>H-H</sub> = 7 Hz, CH<sub>3</sub>CH) ppm.

**(S)-methyl 2-(((trifluoromethyl)sulfonyl)oxy)propanoate (S-1)**

The triflate of methyl L-lactate was synthesized following the same protocol as described for synthesis of *R-1* above. NMR data were consistent with that previously published:<sup>4</sup> <sup>1</sup>H NMR (400 MHz, CDCl<sub>3</sub>) δ 5.26 (1H, q, <sup>3</sup>J<sub>H-H</sub> = 7 Hz), 3.87 (3H, s), 1.73 (3H, d, <sup>3</sup>J<sub>H-H</sub> = 7 Hz) ppm.

**Tetramethyl (1*R*,4*R*,7*R*,10*R*)-α, α', α'', α'''-tetramethyl (S)-2-(4-nitrobenzyl)-1,4,7,10-tetraazacyclododecane-1,4,7,10-tetraacetate (H<sub>4</sub>[S-RRRR-7])**

Under argon, *S*-nitrobenzyl cyclen (0.65 mmol, 0.200 g) was added to a suspension of potassium carbonate (1.43 mmol, 0.197 g) in chloroform and the mixture cooled in a dry ice/acetone bath. The triflate *S-1* (2.86 mmol, 0.674 g) was added drop-wise. The solution was stirred at -78 °C for 1 hour, then allowed to warm to room temperature and stirred for 18 hours. The solution was then heated at 60 °C for an additional 48 hours. The reaction mixture was allowed to cool to room temperature and transferred to a separatory funnel. The organic phase was washed three times with potassium carbonate solution, pH ~10. The organic extracts were dried (sodium sulfate), and the solvents were removed *in vacuo*, affording an oily brown residue (0.153 g, 36% yield). The residue was taken up in water/acetonitrile, filtered using a 0.2 μm nylon syringe filter,

and purified by HPLC according to the gradient in Table 6.1. The product was confirmed by mass spectrometry prior to HPLC purification. HPLC: retention time ( $R_T$ ) = 20.8 min.  $m/z$  (ESMS ESI+): 652.4 (80%,  $[M+H]^+$ ), 566.3 (100%,  $[\text{tri-ester}+H]^+$ ). The tri-alkylated macrocycle was isolated as a by-product ( $R_T$  = 16.6 min).

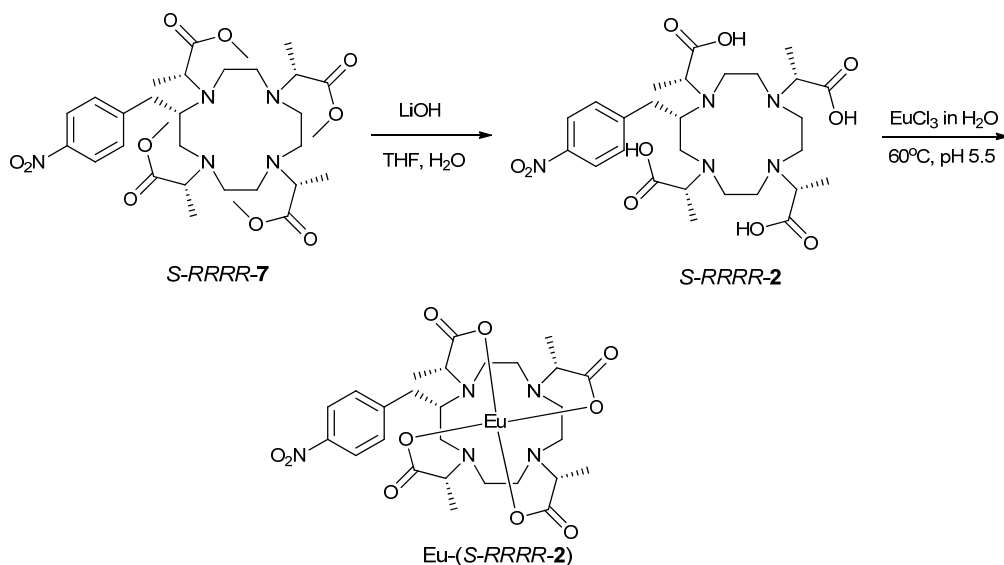
Time (min)	% H <sub>2</sub> O (0.037% HCl)	% MeCN
0	100	0
5	100	0
10	60	40
35	20	80
36	100	0
41	100	0

**Table 6.1:** Gradient for the preparative HPLC purification of H<sub>4</sub>[*S*-RRRR-7]

**Tetramethyl [(1*S*,4*S*,7*S*,10*S*)- $\alpha$ ,  $\alpha'$ ,  $\alpha''$ ,  $\alpha'''$ -tetramethyl (*S*)-2-(4-nitrobenzyl)-1,4,7,10-tetraazacyclododecane-1,4,7,10-tetraacetate] H<sub>4</sub>(*S*-SSSS-7)**

The triflate *R*-1 was used to prepare *S*-SSSS-7 following the same protocol as described for *S*-RRRR-7. The product was purified by HPLC according to the above gradient. HPLC:  $R_T$  = 17.8 min. The mass spectrum was obtained prior to HPLC purification;  $m/z$  (ESMS ESI+): 652.4 (20%,  $[M+H]^+$ ).

**(1*R*,4*R*,7*R*,10*R*)- $\alpha$ ,  $\alpha'$ ,  $\alpha''$ ,  $\alpha'''$ -tetramethyl (*S*)-2-(4-nitrobenzyl)-1,4,7,10-tetraazacyclododecane-1,4,7,10-tetraacetate europium(III) complex H[Eu-(*S*-*RRRR*-2)] corner isomer**



A portion of H<sub>4</sub>[*S*-*RRRR*-7] (0.083 g, 0.127 mmol) was dissolved in tetrahydrofuran (THF, 3 mL) and combined with LiOH solution (3 mL, 5.7 mmol base to neutralize H<sub>4</sub>L and 1 equiv. for each arm) with stirring for 24 - 72 hours at 60 - 80 °C. The product was not isolated; the ligand solution was allowed to cool to room temp., neutralized with HCl (pH 7) and used without further purification

Europium (III) chloride hexahydrate (0.023 mg, 0.064 mmol) was added to approximately one third (1 - 2 mL) of the above *S*-*RRRR*-2 solution. The pH was adjusted to pH 5 - 6 using dilute solutions of HCl or KOH as necessary. The resulting solution was heated for 48 hours at 60 °C and the crude product confirmed by mass spectrometry. The solution was freeze dried, analyzed by <sup>1</sup>H NMR, and found to contain



multiple species. The chelate solution was purified until a single peak remained by reversed-phase preparative HPLC using a step-wise gradient over a 26 min. run according to Table 6.2. The HPLC fraction collected was freeze-dried to constant mass. The title compound was obtained as an off-white amorphous solid.  $R_T = 17.9$  min; NMR data were consistent with that previously published:<sup>1</sup>  $^1\text{H}$  NMR (400 MHz,  $\text{D}_2\text{O}$ ),  $\delta$  44.56 (1H), 42.93 (1H), 39.60 (1H), 35.79 (1H), 12.73 (1H), 7.94 (2H), 7.94 (2H), 6.76 (1H), 4.70 (1H), 3.75 (1H), 0.18 (1H), -2.24 (1H), -2.24 (3H), -4.09 (3H), -4.27 (1H), -4.81 (6H), -7.07 (1H), -7.78 (1H), -8.13 (1H), -8.72 (1H), -12.95 (1H), -13.77 (1H), -17.68 (1H), -22.90 (1H), -23.86 (1H), -24.59 (1H) ppm.  $m/z$  (ESMS ESI-): 744.2, (100%, [M]) with appropriate Eu isotope distribution.

**(1*S*,4*R*,7*R*,10*R*)- $\alpha$ ,  $\alpha'$ ,  $\alpha''$ ,  $\alpha'''$ -tetramethyl (S)-2-(4-nitrobenzyl)-1,4,7,10-tetraazacyclododecane-1,4,7,10-tetraacetate europium(III) complex H[Eu-(S-*SRRR*-2)] corner isomer**

The title compound was prepared according to the method described for Eu-*SRRRR*-2 corner isomer.  $R_T = 15$  min;  $^1\text{H}$  NMR (400 MHz,  $\text{D}_2\text{O}$ ),  $\delta$  45.42 (1H), 44.89 (1H), 39.38 (1H), 36.87 (1H), 12.94 (1H), 8.13 (2H), 8.13 (2H), 6.73 (1H), 6.12 (1H) 3.92 (1H), 0.005 (1H), -2.07 (1H), -4.01 (3H), -4.19 (1H), -4.46 (3H), -5.03 (3H), -5.24 (1H), -7.78 (1H), -8.15 (1H), -9.07 (1H), -10.6 (1H), -10.91 (3H), -13.76 (1H), -14.42 (1H), -21.96 (1H), -25.16 (1H), -26.28 (1H) ppm.

**(1*R*,4*R*,7*R*,10*R*)- $\alpha$ ,  $\alpha'$ ,  $\alpha''$ ,  $\alpha'''$ -tetramethyl (*S*)-2-(4-nitrobenzyl)-1,4,7,10-tetraazacyclododecane-1,4,7,10-tetraacetate europium(III) complex H[Eu-(*S*-*RRRR*-2)] side isomer**

The title compound was prepared according to the method described for Eu-*S*-*RRRR*-2 corner isomer.  $R_T = 19.1$  min;  $^1\text{H}$  NMR (400 MHz,  $\text{D}_2\text{O}$ ),  $\delta$  48.40 (1H), 41.46 (1H), 38.75 (1H), 36.28 (1H), 13.33 (2H), 11.24 (2H), 9.83 (1H), 4.70 (1H), 2.54 (1H), -0.37 (1H), -0.37 (1H), -2.06 (1H), -3.33 (3H), -3.98 (3H), -4.15 (3H), -4.99 (3H), -5.13 (1H), -5.72 (1H), -6.55 (1H), -8.40 (1H), -9.42 (1H), -11.66 (1H), -13.12 (1H), -21.67 (1H), -24.76 (1H), -25.93 (1H), -26.53 (1H) ppm.

**(1*S*,4*R*,7*R*,10*R*)- $\alpha$ ,  $\alpha'$ ,  $\alpha''$ ,  $\alpha'''$ -tetramethyl (*S*)-2-(4-nitrobenzyl)-1,4,7,10-tetraazacyclododecane-1,4,7,10-tetraacetate europium(III) complex H[Eu-(*S*-*SRRR*-2)] side isomer**

The title compound was prepared according to the method described for Eu-*S*-*RRRR*-2 corner isomer.  $R_T = 20.3$  min.;  $^1\text{H}$  NMR (400 MHz,  $\text{D}_2\text{O}$ ),  $\delta$  51.09 (1H), 42.68 (1H), 39.40 (1H), 34.71 (1H), 13.60 (2H), 11.35 (2H), 9.81 (1H), 6.03 (1H), 3.77 (1H), 0.36 (1H), -0.39 (1H), -2.96 (1H), -3.76 (3H), -3.98 (1H), -4.70 (3H), -4.87 (1H), -4.92 (3H), -7.43 (1H), -7.43 (1H), -9.90 (1H), -10.43 (3H), -11.22 (1H), -12.95 (1H), -15.27 (1H), -23.39 (1H), -24.88 (1H), -25.79 (1H) ppm.

Time (min)	% H <sub>2</sub> O (0.037% HCl)	% MeCN
0	78	22
3	78	22
18	65	35
20	65	35
20.1	20	80
21	78	22
26	78	22

**Table 6.2:** Step-wise solvent gradient used during the RP-HPLC purification of Ln-2

**(1*S*,4*S*,7*S*,10*S*)- $\alpha,\alpha',\alpha'',\alpha'''$ -Tetramethyl [(*S*)-2-(4-nitrobenzyl)]-1,4,7,10-tetraazacyclododecane-1,4,7,10-tetraacetic acid europium (III) complex H[(Eu-*S*-SSSS-NB-DOTMA)] H[(Eu-*S*-SSSS-2)] corner isomer**

The title compound was prepared according to the method described for Eu-*S*-RRRR-2 using europium chloride hexahydrate. The chelate was purified to resolve it from its regioisomer according to the gradient used for resolution of Eu-*S*-RRRR-2.  $R_T = 17.6$  min; NMR and  $m/z$  data were consistent with that previously published:<sup>1</sup> <sup>1</sup>H NMR (400 MHz, D<sub>2</sub>O),  $\delta$  22.55 (1H), 19.84 (1H), 19.50 (1H), 15.58 (1H), 8.40 (1H), 7.89 (2H), 7.65 (2H), 6.73 (1H), 0.85 (1H), 0.29 (3H), 0.15 (1H), -0.74 (1H), -1.72 (3H), -2.04 (3H), -2.20 (1H), -3.28 (3H), -4.56 (1H), -4.73 (1H), -5.42 (1H), -5.76 (1H), -6.74 (1H), -6.74 (1H), -6.99 (1H), -10.97 (1H), -11.58 (1H), -11.65 (1H), -12.36 (1H) ppm.  $m/z$  (ESMS ESI-): 744.2 (100%, [M<sup>-</sup>], appropriate isotopic distribution).

**(1*S*,4*S*,7*S*,10*S*)- $\alpha$ , $\alpha'$ , $\alpha''$ , $\alpha'''$ -Tetramethyl [(*S*)-2-(4-nitrobenzyl)]-1,4,7,10-tetraazacyclododecane-1,4,7,10-tetraacetic acid europium (III) complex H[(Eu-*S*-SSSS-NB-DOTMA)] H[(Eu-*S*-SSSS-2)] side isomer**

The title compound was prepared according to the method described for Eu-*S*-SSSS-2 corner isomer. HPLC:  $R_T = 19.7$  min. NMR data were consistent with that previously published (referred to as Eu-*S*-RSSS in the reference):<sup>1</sup>  $^1\text{H}$  NMR (400 MHz,  $\text{D}_2\text{O}$ ),  $\delta$  28.6 (1H), 23.01 (1H), 18.75 (1H), 18.22 (1H), 10.84 (2H), 9.79 (2H), 8.39 (1H), 4.7 (1H), 0.19 (1H), -0.57 (3H), -1.56 (1H), -1.82 (3H), -1.83 (1H), -2.2 (3H), -2.92 (1H), -3.02 (3H), -5.75 (1H), -6.56 (1H), -6.72 (1H), -6.92 (1H), -7.08 (1H), -7.26 (1H), -8.38 (1H), -9.66 (1H), -9.77 (1H), -11.79 (1H), -12.04 (1H) ppm.

**(1*R*,4*R*,7*R*,10*R*)- $\alpha$ ,  $\alpha'$ ,  $\alpha''$ ,  $\alpha'''$ -tetramethyl (*S*)-2-(4-nitrobenzyl)-1,4,7,10-tetraazacyclododecane-1,4,7,10-tetraacetate gadolinium (III) complex H[Gd-(*S*-RRRR-2)] corner isomer**

Using a portion of the solution of *S*-RRRR-2 prepared as described above (1 - 2 mL), the title compound was prepared according to the method described for Eu-*S*-RRRR-2 using  $\text{GdCl}_3$  hydrate (0.024 g, 0.064 mmol), yielding a colorless solid (0.003 g, 10%). The isomers were identified based on the order of elution of the Eu-*S*-RRRR-2 and -*S*-RRRR-2 chelates.  $R_T = 17.1$  min. Mass data were consistent with that previously published:<sup>1</sup>  $m/z$  (ESMS ESI-): 749.2 (100%, [M]<sup>-</sup>, with appropriate isotope distribution).

**(1*S*,4*R*,7*R*,10*R*)- $\alpha$ ,  $\alpha'$ ,  $\alpha''$ ,  $\alpha'''$ -tetramethyl (S)-2-(4-nitrobenzyl)-1,4,7,10-tetraazacyclododecane-1,4,7,10-tetraacetate gadolinium (III) complex H[Gd-(*S*-*SRRR*-2)] corner isomer**

The title compound was prepared according to the method described for Gd-*SRRRR*-2 corner isomer, yielding a colorless solid (0.003 g, 10%).  $R_T = 15$  min.

**(1*R*,4*R*,7*R*,10*R*)- $\alpha$ ,  $\alpha'$ ,  $\alpha''$ ,  $\alpha'''$ -tetramethyl (S)-2-(4-nitrobenzyl)-1,4,7,10-tetraazacyclododecane-1,4,7,10-tetraacetate gadolinium (III) complex H[Gd-(*S*-*RRRR*-2)] side isomer**

The title compound was prepared according to the method described for Gd-*SRRRR*-2 corner isomer, yielding a colorless solid (0.001 g, 3%).  $R_T = 18.5$  min.

**(1*S*,4*R*,7*R*,10*R*)- $\alpha$ ,  $\alpha'$ ,  $\alpha''$ ,  $\alpha'''$ -tetramethyl (S)-2-(4-nitrobenzyl)-1,4,7,10-tetraazacyclododecane-1,4,7,10-tetraacetate gadolinium (III) complex H[Gd-(*S*-*SRRR*-2)] side isomer**

The title compound was prepared according to the method described for Gd-*SRRRR*-2 corner isomer, yielding a colorless solid (0.001 g, 3%).  $R_T = 19.5$  min.

**(1*R*,4*R*,7*R*,10*R*)- $\alpha$ ,  $\alpha'$ ,  $\alpha''$ ,  $\alpha'''$ -tetramethyl (S)-2-(4-nitrobenzyl)-1,4,7,10-tetraazacyclododecane-1,4,7,10-tetraacetate yttrium (III) complex H[Y-(*S*-*RRRR*-2)] corner isomer**

Using a portion of the solution of *S*-*RRRR*-2 prepared as described above (1 - 2 mL), the yttrium chelate was prepared according to the same protocol as for Eu-*SRRRR*-2 using

Y(OTf)<sub>3</sub>, (0.036 g, 0.067 mmol) yielding a colorless solid (0.010 g, 37%). The product Y-*S*-*RRRR*-**2** mass was confirmed. The isomers were identified based on the order of elution of the Eu-*S*-*RRRR*-**2** and -*S*-*SRRR*-**2** chelates.  $R_T = 16.4$  min.  $m/z$  (ESMS ESI-): 680.2 (100%, [M<sup>+</sup>], with appropriate isotope distribution).

**(1*S*,4*R*,7*R*,10*R*)- $\alpha$ ,  $\alpha'$ ,  $\alpha''$ ,  $\alpha'''$ -tetramethyl (*S*)-2-(4-nitrobenzyl)-1,4,7,10-tetraazacyclododecane-1,4,7,10- tetraacetate yttrium (III) complex H[Y-(*S*-*SRRR*-**2**)] corner isomer**

The title compound was prepared according to the method described for Y-*S*-*RRRR*-**2** corner isomer, yielding a colorless solid (0.007 g, 26%).  $R_T = 14.9$  min.

**(1*R*,4*R*,7*R*,10*R*)- $\alpha$ ,  $\alpha'$ ,  $\alpha''$ ,  $\alpha'''$ -tetramethyl (*S*)-2-(4-nitrobenzyl)-1,4,7,10-tetraazacyclododecane-1,4,7,10- tetraacetate yttrium (III) complex H[Y-(*S*-*RRRR*-**2**)] side isomer**

The title compound was prepared according to the method described for Y-*S*-*RRRR*-**2** corner isomer, yielding a colorless solid (0.003 g, 11%).  $R_T = 17.3$  min.

**(1*S*,4*R*,7*R*,10*R*)- $\alpha$ ,  $\alpha'$ ,  $\alpha''$ ,  $\alpha'''$ -tetramethyl (*S*)-2-(4-nitrobenzyl)-1,4,7,10-tetraazacyclododecane-1,4,7,10- tetraacetate yttrium (III) complex H[Y-(*S*-*SRRR*-**2**)] side isomer**

The title compound was prepared according to the method described for Y-*S*-*RRRR*-**2** corner isomer, yielding a colorless solid (0.003 g, 11%).  $R_T = 19$  min.

**(1*S*,4*S*,7*S*,10*S*)- $\alpha,\alpha',\alpha'',\alpha'''$ -Tetramethyl [(*S*)-2-(4-nitrobenzyl)]-1,4,7,10-tetraazacyclododecane-1,4,7,10-tetraacetic acid gadolinium (III) complex H[(Gd-*S*-SSSS-NB-DOTMA)] H[(Gd-*S*-SSSS-2)] corner isomer**

The title complex was prepared according to the method described for Eu-*S*-RRRR-2 using *S*-SSSS-7 (0.100 g, 0.153 mmol) gadolinium chloride hexahydrate (0.050 g, 0.128 mmol) yielding a colorless solid (0.013 g, 13%). The regioisomeric chelates were purified from one another according to the gradient used for resolution of Eu-*S*-RRRR-2. The isomers were identified based on the order of elution of the Eu-*S*-SSSS-2 and chelates.  $R_T = 17.6$  min. Mass data were consistent with that previously published:<sup>1</sup>  $m/z$  (ESMS ESI-): 749.2 (100%, [M], with appropriate Gd isotopic distribution).

**(1*S*,4*S*,7*S*,10*S*)- $\alpha,\alpha',\alpha'',\alpha'''$ -Tetramethyl [(*S*)-2-(4-nitrobenzyl)]-1,4,7,10-tetraazacyclododecane-1,4,7,10-tetraacetic acid gadolinium (III) complex H[(Gd-*S*-SSSS-NB-DOTMA)] H[(Gd-*S*-SSSS-2)] side isomer**

The title compound was prepared according to the method described for Gd-*S*-SSSS-2 corner isomer, yielding a colorless solid (0.013 g, 13%).  $R_T = 19.7$  min.

*6.2.2 Variable concentration and pH conditions for the chelation of Yb<sup>3+</sup> with S-RRRR-2*

The following stock solutions of Yb<sup>3+</sup> and of *S*-RRRR-2 were prepared in water or buffer:

Stock	Diluent	Concentration
Ytterbium (III) chloride Hexahydrate	1.0 M acetate buffer, pH 5.0	170.3 mM
Ytterbium (III) chloride Hexahydrate	Water	170.3 mM
<i>S-RRRR-2</i>	Water	56.4 mM

A series of buffer solutions (Table 6.3) were prepared with a concentration of 1.0 M. The pH of the solutions was adjusted at 60 °C.

Buffer	pH
bisulfate (K)	3.0
bisulfate / acetate	3.5
acetate (Na)	4.0
acetate (Na)	4.5
acetate (Na)	5.0
MES (hydrate)	5.5
MES (hydrate)	6.0

**Table 6.3:** where MES = 2-(N-morpholino)ethanesulfonic acid.

Test samples (500  $\mu$ L) combining ligand and  $\text{Yb}^{3+}$  were prepared for incubation; in each case, the concentration of  $\text{Yb}^{3+}$  was twice that of the ligand. For the concentration dependence study, ligand concentrations of 0.5, 1.0, 2.5, 5.0, 10, 25 and 50 mM in pH 5.0 acetate buffer were tested. For the pH dependence study, the concentration of *S-RRRR-2* was 7.1 mM in each of the buffers in Table 5.3. All buffers and stock solutions were



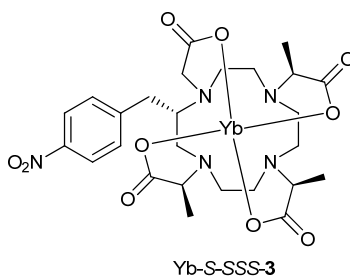
equilibrated at 60 °C prior to dispensing. The test samples were incubated at 70 °C for 64 days.

The chelate solutions were allowed to cool to room temperature and diluted to 50  $\mu\text{M}$  in 1:1 Methanol:Water for LC/MS analysis. These samples were eluted from a Phenomenex Luna C18(2) 250 x 2.0 mm column at 375  $\mu\text{L}/\text{min}$  with 0.05% Formic acid and 0 - 80% Acetonitrile over 35 minutes. The entire eluent flowed directly into the ESMS ESI-MS, which was monitored at 765  $m/z$  in negative ionization mode over the course of the run. The two largest peaks observed in each chromatogram were integrated manually and their relative areas were reported. The samples from the concentration study were combined and resolved by preparative HPLC using the same mobile phase gradient. The fractions were freeze dried and the resulting solids were analyzed by  $^1\text{H}$  NMR to determine which HPLC peak corresponded to which Yb-*S-RRRR-2* regioisomer. NMR and  $m/z$  data were consistent with that previously published:<sup>5</sup> Corner isomer:  $R_T = 24.34$  min;  $^1\text{H}$  NMR (400 MHz,  $\text{D}_2\text{O}$ )  $\delta$  144.10, 137.89, 41.37, 41.26, 37.32, 25.12, 23.47, 21.49, 16.84, 13.93, 10.49, 9.46, 9.43, 7.33, 7.31, 3.61, 3.51, -20.60, -22.75, -23.16, -24.38, -24.53, -26.29, -39.82, -43.30, -49.59, -50.75, -69.69 ppm. Side isomer:  $R_T = 25.68$  min;  $^1\text{H}$  NMR (400 MHz,  $\text{D}_2\text{O}$ )  $\delta$  145.04, 138.63, 35.78, 33.29, 31.61, 27.39, 25.97, 21.22, 21.07, 20.84, 18.01, 17.11, 12.81, 3.61, 3.53, -20.75, -23.96, -25.19, -30.68, -37.05, -42.99, -44.68, -56.52, -73.89 ppm.

## 6.2.3 Epimerization study of Yb-S-SSS-3

**(4*S*,7*S*,10*S*)- $\alpha$ ,  $\alpha'$ ,  $\alpha''$ -trimethyl (S)-2-(4-nitrobenzyl)-1,4,7,10-tetraazacyclododecane-1,4,7,10-tetraacetate ytterbium (III) complex H[(Yb-S-SSS-NB-DO3MA-1A)]**

**H[(Yb-S-SSS-3)] corner and side isomers**

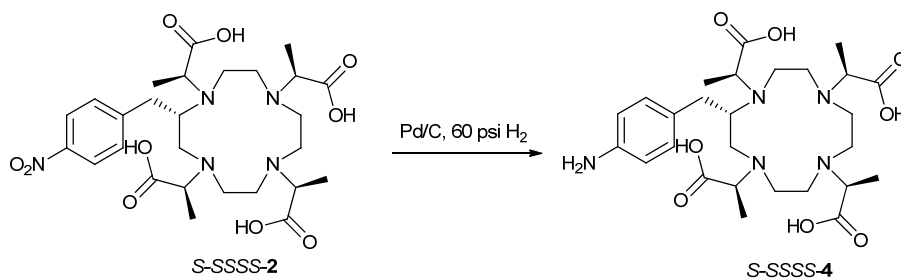


A solution of Yb-S-SSS-3 in D<sub>2</sub>O (0.5 mL, 20 mM) was adjusted to pD ~1 using 35% DCl solution in D<sub>2</sub>O. This sample was sealed in an NMR tube and incubated at ~90 °C using an oil bath over the course of the study. For a given time point, the sample tube was removed from the bath and allowed to cool to room temperature, and oil was removed from the outside of the tube with acetone. <sup>1</sup>H NMR scans of the sample were taken at 1 week intervals; later in the study the intervals were 2 - 3 weeks. All scans were recorded on a Bruker 600 MHz NMR spectrometer with an acquisition time of 0.3 sec, 0 delay time, and a spectral window of 250 ppm. Line broadening of 50 Hz was used in processing. After the last time point was obtained, the solution was removed from the NMR tube and a portion was analyzed to confirm the product as a mixture of isomers. <sup>1</sup>H NMR (600 MHz, D<sub>2</sub>O)  $\delta$  97.46, 96.06, 94.19, 92.06, 90.91, 87.89, 21.50, 18.91, 18.40, 17.23, 16.94, 15.68, 14.85, 14.11, 13.67, 13.26, 11.76, 11.24, 10.96, 8.15, 7.47, 6.82, 6.74, 3.68, 3.41, 3.12, 2.90, 2.79, 1.57, 1.47, 1.29, 1.08, 1.03, 0.08, -0.83, -12.07, -13.08,

-13.72, -15.79, -16.51, -16.87, -17.59, -21.76, -23.65, -26.51, -27.93, -31.37, -38.23, -41.90, -46.04, -46.58, -56.15, -57.80, -65.03, -68.92, -69.58, -69.94 ppm.  $m/z$  (ESMS ESI-): 751 (100% [M]).

#### 6.2.4 Modification of *S*-SSSS-2 to form a bifunctional chelate

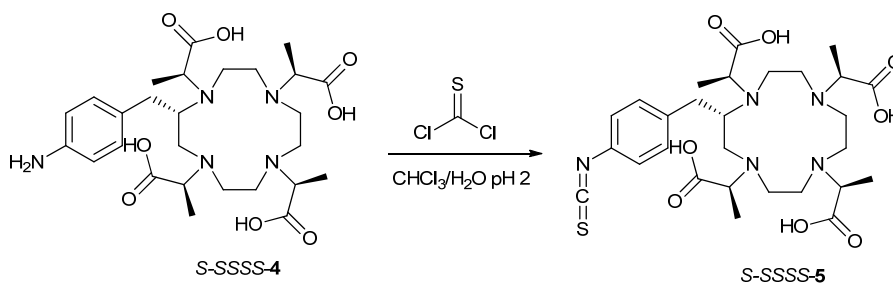
#### (1*S*,4*S*,7*S*,10*S*)- $\alpha$ , $\alpha'$ , $\alpha''$ , $\alpha'''$ -tetramethyl (*S*)-2-(4-aminobenzyl)-1,4,7,10-tetraazacyclododecane-1,4,7,10-tetraacetic acid (*S*-SSSS-4)



The nitrobenzyl ligand *S*-SSSS-2 (0.380 g, 0.65 mmol) was added to water (approximately 50 mL) in a thick-walled 500 mL hydrogenation bottle, affording an orange suspension. 10% weight palladium-on-carbon (76 mg) was added to this suspension. The vessel was attached to a Parr hydrogenator, purged 3 times with hydrogen, and reacted overnight at 25 psi H<sub>2</sub>. The catalyst was removed by gravity filtration yielding a clear orange solution, and solvents were removed by lyophilization, affording a waxy colorless solid (quantitative yield). <sup>1</sup>H NMR (400 MHz, D<sub>2</sub>O)  $\delta$  (ppm) = 7.00 (2H, br s, Ar), 6.71 (2H, br s, Ar), 1.7 - 4.0 (24H, br m, NCH<sub>2</sub>CH<sub>2</sub>N, NCHCH<sub>3</sub>, benzylic, aryl NH<sub>2</sub>), 1.09 - 1.23 (12H, overlapping doublets, CH<sub>3</sub>); <sup>13</sup>C NMR (100 MHz, D<sub>2</sub>O),  $\delta$  (ppm) = 16.7, 18.4, 18.6, 20.0 (CH<sub>3</sub>), 24.9, 25.2, 27.1, 28.4, 29.3, 29.5, 34.0, 57.4, 61.5, 61.6, 68.5, 116.9, 118.0, 121.2, 129.7, 129.9 (Ar), 181.7, 181.8, 182.5, 183.1

(CO<sub>2</sub>); Infrared  $\nu_{\max}$  / cm<sup>-1</sup> (thin-cast film from water); 3363 (NH/OH), 2958, 2846, 1588 (CO<sub>2</sub>), 1365, 1254, 1165, 1125, 1030.  $m/z$  (ESMS ESI+): 608.4 (100%, [M+H, tri(methyl ester)]), 594.4 (20%, [M+H, di(methyl ester)]), 622.4 (30%, [M+H, tetra(methyl ester)]), and 644.4 (<5%, [M+Na, tetra(methyl ester)]). The tetraacid is not believed to ionize appreciably in the mass spectrum. The product was hydrolyzed further (to remove remaining esters), then taken directly to the next synthetic step.

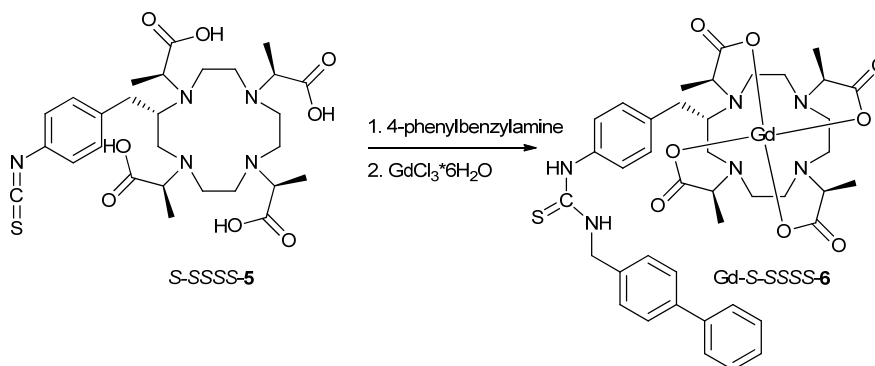
**(1*S*,4*S*,7*S*,10*S*)- $\alpha$ ,  $\alpha'$ ,  $\alpha''$ ,  $\alpha'''$ -tetramethyl (*S*)-2-(4-isothiocyanatobenzyl)-1,4,7,10-tetraazacyclododecane-1,4,7,10-tetraacetic acid (*S*-SSSS-5)**



The aminobenzyl ligand *S*-SSSS-4 was taken up in water (approximately 20 mL) and the pH adjusted to 2 using dilute HCl. In a round-bottom flask, chloroform (30 mL) was added to the aqueous solution of ligand. Thiophosgene (0.270 g, 2.36 mmol) was added to the biphasic mixture while stirring vigorously. The mixture was stirred for 18 h then the layers were transferred to a separatory funnel and allowed to separate. The organic layer was removed and the aqueous layer was washed twice with chloroform and then freeze-dried, yielding a waxy colorless solid (0.286 g, 68%). <sup>1</sup>H NMR (400 MHz, D<sub>2</sub>O)  $\delta$  (ppm) = 7.24 (4H, m, Ar), 3.4 - 4.4 (34H, br m), 1.09 - 1.40 (12H, overlapping doublets, CH<sub>3</sub>); <sup>13</sup>C NMR (100 MHz, D<sub>2</sub>O),  $\delta$  (ppm) = 16.9, 18.0, 19.3, 21.6 (CH<sub>3</sub>), 25-

33 multiple peaks, 57.5, 58.7, 59.9, 61.1, 61.6, 66.4, 114.9, 118.0, 121.2, 124.3, 126.4, 130.5 (Ar), 139.3 (SCN) 161.3, 165.7, 177.0, 178.5 (CO<sub>2</sub>); *m/z* (ESMS ESI<sup>+</sup>): 608.4 (25%, [M+H]), 622.3 (37%, [M+H mono(methyl)ester]), 636.3 (85%, [M+H, di(methyl ester)]), 650.3 (100%, [M+H, tri(methyl ester)]), 664.3 (37%, [M+H, tetra(methyl ester)]). Infrared  $\nu_{\max}$  / cm<sup>-1</sup> (thin-cast film from water); 3393 (NH/OH), 2953, 2103 (SCN), 1717 (carbonyl), 1635, 1457, 1249, 1165, 1124, 1030.

**(1*S*,4*S*,7*S*,10*S*)- $\alpha$ ,  $\alpha'$ ,  $\alpha''$ ,  $\alpha'''$ -tetramethyl ((*S*)-2-(4-(3-([1,1'-biphenyl]-4-ylmethyl)thioureido)benzyl)-1,4,7,10-tetraazacyclododecane-1,4,7,10-tetraacetate gadolinium (III) complex H[(Gd-*S*-*S**S**S*-6)] corner isomer**



The isothiocyanate *S*-*S**S**S*-**5** was dissolved in water and the pH was adjusted to 8 using 1M NaOH and dilute HCl, for a final volume of approximately 35 mL. The solution was stirred at room temperature. A separate solution of 4-phenylbenzylamine (0.121 g, 0.661 mmol) in dioxane (15 mL) was added to the solution of isothiocyanate. After 6 hours, the pH was confirmed to be between 8 and 9. After 18 hours, 5 equivalents of GdCl<sub>3</sub>·6H<sub>2</sub>O (0.878 g, 2.36 mmol) were added to the reaction, which turned cloudy. The pH was held constant at 6 for 6 days. Solvents were then removed *in vacuo*, and the residue was

freeze-dried, affording a yellow-orange residue. The crude residue was dissolved in THF/water/MeCN, filtered, and purified by preparative HPLC according to the gradient in Table 6.4. The HPLC fraction was freeze-dried to constant mass, again affording a yellow-orange residue. The product mass was confirmed prior to HPLC purification:  $R_T = 37.7$  minutes.  $m/z$  (ESMS ESI-): 299.8 (90%, unidentified), 301.8 (100%, unidentified), 944.3 (50%, [(M-H)]<sup>-</sup>, with appropriate Gd isotope distribution), 994.3 (25%, [(M(trimethylester)-H)]<sup>-</sup>, with appropriate Gd isotope distribution).

The sample of Gd-S-SSSS-6 isolated via HPLC purification above was then resolved from its regioisomer using the following gradient (Table 6.5). Purification was repeated until a single peak remained in the HPLC trace, affording a colorless solid (< 1 mg). The regiochemistry was determined by synthesizing the Eu analogues. The mass spectrum was acquired after purification.  $R_T = 27.4$  min.  $m/z$  (ESMS ESI-): 944.3 (100%, [(M-H)]<sup>-</sup> with appropriate isotope distribution).

Time (min)	% H <sub>2</sub> O (0.037% HCl)	% MeCN
0	100	0
5	100	0
40	20	80
40.1	100	0
45	100	0

**Table 6.4:** Step-wise solvent gradient used during the RP-HPLC purification of crude Gd-S-SSSS-6

Time (min)	% H <sub>2</sub> O (0.037% HCl)	% MeCN
0	63	37
3	63	37
23	53.5	46.5
30	53.5	46.5
30.5	20	80
31.1	63	37
35	63	37

**Table 6.5:** Step-wise solvent gradient used to resolve corner and side isomers of Gd-S-SSSS-6

**(1*S*,4*S*,7*S*,10*S*)- $\alpha$ ,  $\alpha'$ ,  $\alpha''$ ,  $\alpha'''$ -tetramethyl ((*S*)-2-(4-(3-([1,1'-biphenyl]-4-ylmethyl)thioureido)benzyl)-1,4,7,10-tetraazacyclododecane-1,4,7,10-tetraacetate gadolinium (III) complex H[(Gd-S-SSSS-6)] side isomer**

The title complex was synthesized following the same protocol as for Gd-S-SSSS-6, corner isomer, affording a colorless solid (< 1 mg). HPLC:  $R_T = 28.6$  min.

**(1*S*,4*S*,7*S*,10*S*)- $\alpha$ ,  $\alpha'$ ,  $\alpha''$ ,  $\alpha'''$ -tetramethyl ((*S*)-2-(4-(3-([1,1'-biphenyl]-4-ylmethyl)thioureido)benzyl)-1,4,7,10-tetraazacyclododecane-1,4,7,10-tetraacetate europium (III) complex H[(Eu-S-SSSS-6)] corner isomer**

The title complex was synthesized using EuCl<sub>3</sub>•6H<sub>2</sub>O (0.200 g, 0.546 mmol) following the same protocol as for Gd-S-SSSS-6, affording a colorless solid (< 1 mg). The title complex was purified according to the gradient in Table 5.5 until a single peak remained. <sup>1</sup>H NMR spectra were recorded at 298.15 K on a Bruker Avance III spectrometer operating at 600.13 MHz. A 1.7 mm microprobe was employed, acquiring 1024 × 1024

points. The  $ax^S$  peak patterns were matched to those of Eu-*S*-SSSS-2 corner isomer, previously identified by COSY. HPLC:  $R_T = 27.0$  min.  $m/z$  (ESMS ESI-): 939.2 ( $[M^-]$ , with appropriate Eu isotope distribution).

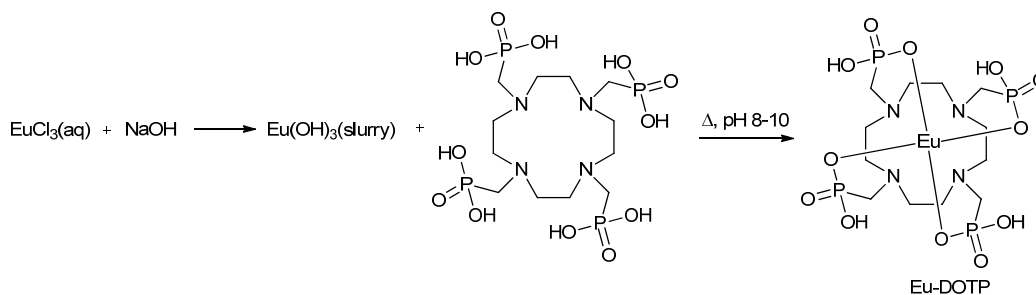
**(1*S*,4*S*,7*S*,10*S*)- $\alpha$ ,  $\alpha'$ ,  $\alpha''$ ,  $\alpha'''$ -tetramethyl ((*S*)-2-(4-(3-([1,1'-biphenyl]-4-ylmethyl)thioureido)benzyl)-1,4,7,10-tetraazacyclododecane-1,4,7,10-tetraacetate europium (III) complex H[(Eu-*S*-SSSS-6)] side isomer**

The title complex was synthesized following the same protocol as for Eu-*S*-SSSS-6 corner isomer, affording a colorless solid (< 1 mg). The  $ax^S$  peak patterns were matched to those of Eu-*S*-SSSS-2 side isomer, previously identified by COSY. HPLC:  $R_T = 28.4$  min.

### 6.3 Variable-temperature NMR analysis

#### 6.3.1 Synthesis

**((1,4,7,10-tetraazacyclododecane-1,4,7,10-tetrayl)tetrakis(methylene))tetraphosphonic acid europium (III) complex (Eu[DOTP]<sup>5-</sup>)**





Europium (III) chloride hexahydrate (0.032 g, 0.089 mmol) was dissolved in water (242  $\mu$ L). To this was added an equal volume of sodium hydroxide solution (1.94 M) while stirring until a white precipitate was observed. This slurry was diluted with water (3.85 mL) and the  $\text{Eu}(\text{OH})_3$  which formed was allowed to settle out overnight. The supernatant was removed, and the slurry was washed three times with water (3.85 mL) each. The combined supernatant was removed.

$\text{H}_8\text{DOTP}$  (48 mg, 0.0875 mmol) was suspended in water (1.9 mL). To this was added sodium hydroxide solution (49  $\mu$ L, 9 M), producing a clear solution. The  $\text{Eu}(\text{OH})_3$  slurry was added in small portions to the DOTP solution under constant stirring over 20 hours. After the DOTP solution had gone clear, any remaining  $\text{Eu}(\text{OH})_3$  was transferred to the DOTP solution using water (50  $\mu$ L). To this was added additional DOTP (2 mg). The pH was measured to be between 7 and 8. The reaction mixture was then heated under a stream of Argon overnight, allowed to cool to room temp., and pH again measured at 7 - 8. The solution was freeze dried, affording the product as a colorless solid. NMR data were consistent with that previously published:<sup>6</sup>  $^1\text{H}$  NMR: (400 MHz,  $\text{D}_2\text{O}$ , 25  $^\circ\text{C}$ )  $\delta$  (ppm) = 29.7, 4.70 (HOD), 3.24 (free ligand,  $\text{PCH}_2\text{N}$ ), 3.00 (free ligand,  $\text{NCH}_2\text{CH}_2\text{N}$ ), -0.90, -5.23, -5.42, -9.66, -15.62.

**((1,4,7,10-tetraazacyclododecane-1,4,7,10-tetrayl)tetrakis(methylene))tetraphosphonic acid ytterbium (III) complex (Yb[DOTP]<sup>5-</sup>)**

The title complex was synthesized following the same protocol as for Eu-DOTP. Ytterbium (III) chloride (0.034 g, 0.088 mmol) was used in place of Europium (III) chloride, affording the product as a colorless solid. NMR data were consistent with that previously published:<sup>7</sup> <sup>1</sup>H NMR: (400 MHz, D<sub>2</sub>O)  $\delta$  (ppm) = 90.2, 18.0, 13.5, 4.71 (HOD), -24.3, -29.8, -61.4.

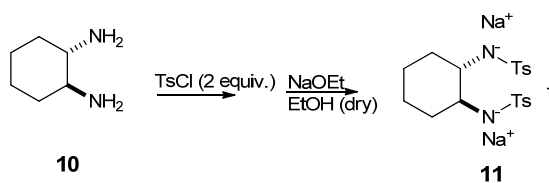
*6.3.2 Variable-temperature NMR studies:*

Samples of each isomer of Eu- and Yb-2 were prepared in NMR tubes. NMR solutions of Yb- and Eu[DOTP]<sup>5-</sup> were prepared and the pD adjusted to ~11 using KOD. The concentrations were not measured but kept uniform for all NMR analyses of the same chelate. The sample tube was adjusted to the target temperature (with a temperature change gradient no steeper than 3 K per minute) in the probe and allowed to equilibrate for 1-20 minutes once the probe temperature and target temperature had become identical. The length of this additional equilibration time did not affect the spectra. Spectra were acquired in 5 degree increments from 278.15 - 313.15 K. Acquisition parameters were adjusted as the temperature was increased to account for the change in magnetic properties with changing temperature: the acquisition time varied from 0.21-0.23 s (0.32 s for Yb[DOTP]); the relaxation delay varied from 0.5-1.4 s; and the number of scans varied from 64 to 256. All spectra were referenced with the HOD peak at 4.7

ppm. Spectral assignments were made on the basis of COSY NMR spectra recorded for each chelate at 278.15 and 313.15 K.

#### 6.4 Synthesis of precursors to a fused-ring macrocycle

##### *N,N'*-((1*R*,2*R*)-cyclohexane-1,2-diyl)bis(4-methylbenzenesulfonamide) disodium salt (11)<sup>8</sup>

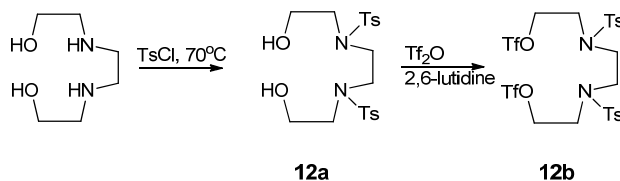


(1*R*,2*R*)-1,2-diaminocyclohexane (0.78 g, 6.84 mmol) was dissolved in acetonitrile (100 mL) and potassium carbonate (1.46 g, 10.6 mmol) was added, producing a suspension which was heated to 70 °C while stirring. *p*-Toluenesulfonyl chloride (2.875 g, 15.1 mmol) was added to this suspension in small increments over a period of 30-60 min. The reaction was heated at 70 °C for 18 h, then allowed to cool to room temperature. The solvents were removed *in vacuo*, affording an off-white residue. The residue was extracted into dichloromethane under basic conditions (potassium carbonate solution). Crystals were formed by slow evaporation at -20 °C, and were filtered and recrystallized from MeOH/H<sub>2</sub>O, affording a colorless solid. NMR was taken at this stage. The di-tosylamide (1.0 g, 2.36 mmol) was dissolved in 21% sodium ethoxide in dry ethanol (1.53 g, 4.72 mmol) and diluted with dry methanol (50 mL). This solution was heated at reflux for 1 h, then allowed to cool to room temperature. Solvents were removed *in vacuo* first by rotary evaporation and then on a Schlenk line. The residue was used

without purification in attempts to cyclize with **15b**, but a successful procedure was not found.  $^1\text{H}$  NMR (400 MHz,  $\text{CDCl}_3$ ):  $\delta$  7.68 (4H, d,  $^3J_{\text{H-H}} = 8$  Hz, Ar), 7.24 (4H, d,  $^3J_{\text{H-H}} = 8$  Hz, Ar), 4.83 (2H, d,  $^3J_{\text{H-H}} = 6$  Hz, NH), 2.67 (2H, m,  $\text{CH}_2\text{NHTs}$ ), 2.36 (6H, s, tolyl), 1.77 (2H, d, cyclohexyl), 1.48 (2H, d, cyclohexyl), 1.03 (4H, m, cyclohexyl) ppm.  $^{13}\text{C}$  NMR ( $\text{CDCl}_3$ ):  $\delta$  (ppm) 143.6 (Ar), 137.1 (Ar), 129.8 (Ar), 127.3 (Ar), 56.6 ( $\text{CH}_2\text{NHTs}$ ), 33.4, 24.3, 21.6.

**(Ethane-1,2-diylbis(azanediyl))bis(ethane-2,1-diyl) bis(4-methylbenzenesulfonate)<sup>8</sup>**

**(12a)**

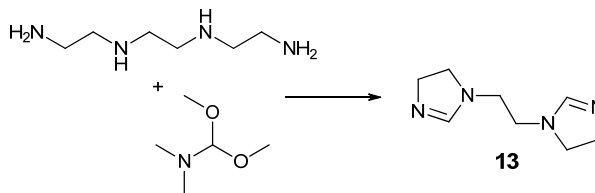


2,2'-(Ethane-1,2-diylbis(azanediyl))diethanol (5.00 g, 33.7 mmol) was dissolved in acetonitrile (200 mL) and heated to 70 °C while stirring. Potassium carbonate (4.89 g, 35.4 mmol) was added, resulting in a white suspension. *p*-Toluenesulfonyl chloride (12.85 g, 67.4 mmol) was added to this suspension in small increments over a period of 30-60 min. The reaction was heated at 70 °C for 18 h, then allowed to cool to room temp. Solvents were removed *in vacuo* and the residue taken up in potassium carbonate solution and extracted into dichloromethane). Crystals were formed by slow evaporation at -20 °C, and were filtered and recrystallized from MeOH/ $\text{H}_2\text{O}$ .  $^1\text{H}$  NMR (400 MHz,  $\text{CDCl}_3$ ):  $\delta$  (ppm) 7.71 (4H, d,  $^3J_{\text{H-H}} = 8$  Hz, aryl), 7.33 (4H, d,  $^3J_{\text{H-H}} = 8$  Hz, aryl), 4.80 (4H, s,  $\text{TsNCH}_2\text{CH}_2\text{NTS}$ ), 3.81 (4H, t,  $^3J_{\text{H-H}} = 5$  Hz,  $\text{CH}_2\text{OH}$ ), 3.25 (4H, t,  $^3J_{\text{H-H}} = 5$  Hz,

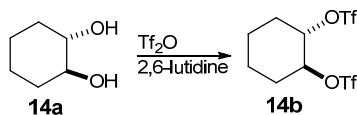
OCH<sub>2</sub>CH<sub>2</sub>NTs), 2.44 (6H, s, tolyl). <sup>13</sup>C NMR (100 MHz, CDCl<sub>3</sub>): δ (ppm) 143.9, 134.9, 129.9, 127.4, 61.0, 53.1, 50.3, 21.5.

**(Ethane-1,2-diylbis(azanediyl))bis(ethane-2,1-diyl) bis(trifluoromethanesulfonate)<sup>9</sup>  
(12b)**

A 2-necked round-bottomed flask with stir bar was purged with argon. To this flask was added 75 mL dry dichloromethane by cannulation. **12a** (0.5 g, 1.1 mmol) was added under argon. 2,6-lutidine (0.255 mL, 2.2 mmol) was next added *via* syringe and the mixture was stirred at -78 °C. Trifluoromethanesulfonic anhydride (0.37 mL, 2.2 mmol) was then added drop-wise *via* syringe, and the reaction mixture was stirred at -78 °C for one hour. The solution was then allowed to warm to room temperature, followed by stirring at room temperature for 3 h. Solvents were removed *in vacuo*, and the residue taken up in ethyl ether. The insoluble portion was removed using a separatory funnel and the ether solution was evaporated *in vacuo*, affording the title compound as a colorless solid (0.864 g, 55%). <sup>1</sup>H NMR (400 MHz, CDCl<sub>3</sub>): δ (ppm) 8.24 (4H, overlapping doublets, <sup>3</sup>J<sub>H-H</sub> = 8 Hz, aryl), 7.57 (4H, overlapping doublets, <sup>3</sup>J<sub>H-H</sub> = 8 Hz, aryl), 4.68 (4H, t, <sup>3</sup>J<sub>H-H</sub> = 5 Hz, CH<sub>2</sub>OTf), 3.51 (4H, t, <sup>3</sup>J<sub>H-H</sub> = 5 Hz, OCH<sub>2</sub>CH<sub>2</sub>NTs), 3.37 (4H, s, TsNCH<sub>2</sub>CH<sub>2</sub>NTS), 2.46 (6H, s, tolyl). <sup>13</sup>C NMR (100 MHz, CDCl<sub>3</sub>): δ (ppm) 154.0, 145.9, 144.6, 134.3, 130.2, 127.4, 124.9, 75.2, 50.3, 49.8, 21.6, 19.6.

**1-[2-(4,5-dihydroimidazol-1-yl)ethyl]-4,5-dihydroimidazole (13)**

Triethylene tetramine (2.0 g, 13.6 mmol) was combined with *N,N*-dimethylformamide dimethyl acetal (3.46 g, 27.2 mmol) in an N<sub>2</sub>-purged, 2-necked round-bottom flask fitted with screw tap. Under N<sub>2</sub>, the mixture was heated to reflux and magnetically stirred for approximately 40 minutes. The product was dried *in vacuo* using a Schlenk line, affording a colorless solid. These solids were recrystallized from dry THF and isolated by filtration under nitrogen to afford the title compound as a colorless solid (1.5 g, 66%). NMR data were consistent with that previously published:<sup>10</sup> <sup>1</sup>H NMR (400 MHz, CDCl<sub>3</sub>) δ 6.7 (2H, s, N=CHN), 3.8 (4H, t, NCH<sub>2</sub>CH<sub>2</sub>N), 3.2 - 3.3 (8H, 4 overlapping signals, C=NCH<sub>2</sub>CH<sub>2</sub>N) ppm; <sup>13</sup>C NMR (100 MHz, CDCl<sub>3</sub>) δ 157.3 (CH), 55.0 (CH<sub>2</sub>), 48.6 (CH<sub>2</sub>), 46.6 (CH<sub>2</sub>) ppm.

***Trans*-[2-(trifluoromethanesulfonyloxy)cyclohexyl] trifluoromethanesulfonate (14b)**

A 2-necked round-bottom flask fitted with screw tap was charged with *trans*-1,2-cyclohexanediol **14a** (0.5 g, 4.3 mmol) and purged with N<sub>2</sub>. Dry dichloromethane and 2,6-lutidine (0.92 g, 8.6 mmol) were added to the reaction flask by cannulation. The

mixture was cooled in a dry-ice/acetone bath, and triflic anhydride (2.43 g, 8.6 mmol) was added dropwise, under N<sub>2</sub>. The reaction was stirred magnetically at approximately -78 °C for one hour, then allowed to warm to room temperature and stirred an additional 3 hours. Solvents were removed *in vacuo*, and the residue taken up in ethyl ether. The insoluble portion was removed using a separatory funnel and the ether solution was evaporated *in vacuo*, affording the title compound as an off-white solid (5.5 g, 76%). NMR data were consistent with that previously published:<sup>11</sup> <sup>1</sup>H NMR (400 MHz, CDCl<sub>3</sub>) δ 4.87 (2H, td, CHOTf), 2.41 (2H, m, cyclohexyl), 1.7 - 1.9 (4H, overlapping signals, cyclohexyl), 1.43 (2H, m, cyclohexyl) ppm; <sup>13</sup>C NMR (100 MHz, CDCl<sub>3</sub>) δ 118.3 (q, CF<sub>3</sub>, <sup>2</sup>J<sub>C-F</sub> = 319 Hz), 86.0, 31.3, 22.1 ppm.

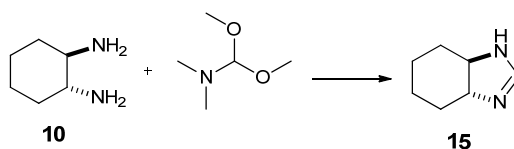
***Trans*-(1,2)-cyclohexane-1,2-diyl dimethanesulfonate (14c)**



Triethylamine (2.61 g, 25.8 mmol) was added to a solution of *trans*-1,2-cyclohexanediol **14a** (43 mL, 0.2 M) in dichloromethane, which was then cooled in an ice water/methanol bath. Methanesulfonyl chloride (2.27 g, 19.8 mmol) was added to this solution over 5 - 10 minutes. The reaction was stirred an additional 10 - 15 minutes then was transferred in one portion to a separatory funnel. The organic layer was washed with cold water, cold 10% HCl, saturated sodium bicarbonate and saturated NaCl solutions. The organic extracts were dried (sodium sulfate), and the solvents were removed *in vacuo* to afford the title compound. <sup>1</sup>H NMR (400 MHz, CDCl<sub>3</sub>) δ 4.58 (2H, m, CHOMs), 3.09 (6H, s,

SO<sub>3</sub>CH<sub>3</sub>), 2.30 (2H, m, cyclohexyl), 1.60 - 1.84 (4H, overlapping signals, cyclohexyl), 1.38 (2H, m, cyclohexyl) ppm; <sup>13</sup>C NMR (100 MHz, CDCl<sub>3</sub>) δ 80.6, 39.0, 31.7, 23.1 ppm.

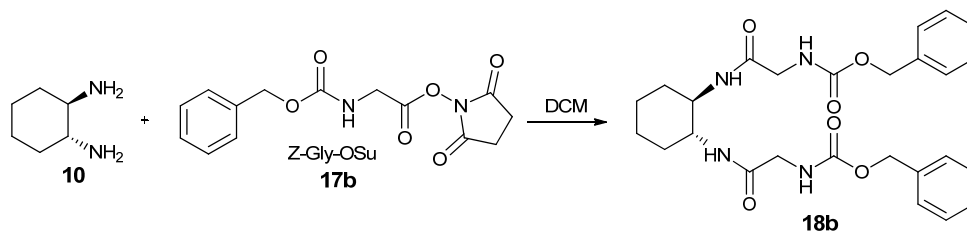
**(*trans*-3,7)-3a,4,5,6,7,7a-hexahydro-1H-benzo[d]imidazole (15)**



**10** (1.902 g, 16.7 mmol) was combined with *N,N*-dimethylformamide dimethyl acetal (2.0 g, 16.8 mmol) in an N<sub>2</sub>-purged, 2-necked round-bottom flask fitted with screw tap. Under N<sub>2</sub>, the mixture was heated to reflux and magnetically stirred for approximately 40 minutes. The product was dried *in vacuo* using a Schlenk line, leaving an oily residue. Recrystallization from dry THF was attempted, but the NMR spectrum indicates a product which is still impure. <sup>1</sup>H NMR (400 MHz, CDCl<sub>3</sub>) δ 7.33 (1H, s, NH), 7.17 (1H, s, imine CH), 2.76 (1H, m, CHN=C), 2.44 (1H, t, CHNH), 1.87 - 1.05 (8H, overlapping signals, cyclohexyl) ppm; <sup>13</sup>C NMR (100 MHz, CDCl<sub>3</sub>) δ 155 (CH), 55.0 (CH), 37 (CH), 35 (4 peaks, CH<sub>2</sub> in conformational exchange), 25 ppm (4 peaks, CH<sub>2</sub> in conformational exchange).

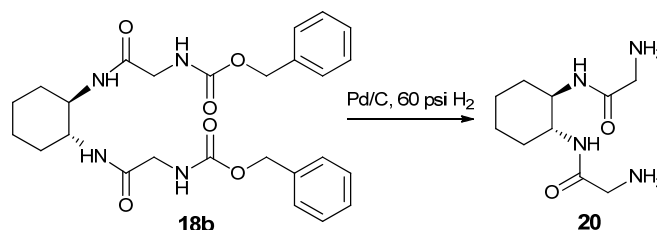


**Benzyl-*N*-[2-[[*(1R,2R)*-2-[(2-benzyloxycarbonylaminoacetyl)amino]cyclohexyl]amino]-2-oxo-ethyl]carbamate (18b)**



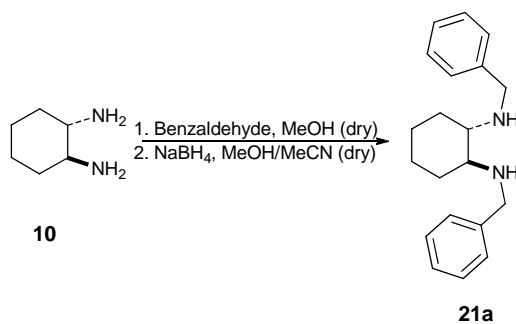
Z-Gly-OSu (0.613 g, 2.0 mmol) and *R,R*-**10** (0.114 g, 1.0 mmol) were dissolved in dichloromethane and stirred at ambient temperature for 18 h. The reaction mixture was transferred to a separatory funnel and extracted twice with an aqueous solution of potassium carbonate (pH 11 - 12) and once with a dilute acetic acid solution (pH 3). The organic extracts were dried (sodium sulfate), and the solvents removed *in vacuo*, yielding a colorless solid (99% yield). <sup>1</sup>H NMR (400 MHz, CDCl<sub>3</sub>) δ (ppm) 7.24 (10H, m, aryl), 6.42 (2H, br d, <sup>3</sup>J<sub>H-H</sub> = 5 Hz, NH), 5.68 (2H, br s, NH), 5.02 (4H, overlapping triplets, <sup>2</sup>J<sub>H-H</sub> = 12 Hz, PhCH<sub>2</sub>COON), 3.70 (4H, qd, <sup>2</sup>J<sub>H-H</sub> = 31 Hz, <sup>3</sup>J<sub>H-H</sub> = 6 Hz, NCOCH<sub>2</sub>N), 3.63 (2H, m, cyclohexyl CHNH), 1.89 (2H, br d, J = 9 Hz, cyclohexyl), 1.68 (2H, br d, J = 6 Hz), 1.2 (4H, m, cyclohexyl).

**2-amino-*N*-[*(1R,2R)*-2-[(2-aminoacetyl)amino]cyclohexyl]acetamide (20)**



Compound **18b** (2.7 g, 0.4 mmol) was added to a 500 mL hydrogenation bottle and dissolved in a minimal volume of methanol or ethanol by gentle heating. The solution was cooled and Palladium-on-carbon (10% w/w) (0.20 g,  $2 \times 10^{-4}$  mmol) added carefully. The reaction vessel was stoppered and clamped into position on a Parr hydrogenator, and purged and refilled with 50 Psi  $H_2$ . The reaction was agitated for 3 days. The reaction mixture was filtered, and solvents were removed from the filtrate *in vacuo*, affording the title compound as a yellow oil (0.96 g, 77%).  $^1H$  NMR (400 MHz,  $CDCl_3$ )  $\delta$  (ppm) 7.31 (2H, br s, amide NH), 3.63 (2H, m, cyclohexyl  $\underline{C}HNH$ ), 3.2 (4H, br s,  $NCOCH_2N$ ), 1.92 (2H, br d,  $J = 9$  Hz, cyclohexyl), 1.70 - 1.68 overlapping (8H, br s, amine and cyclohexyl), 1.2 (4H, m, cyclohexyl).

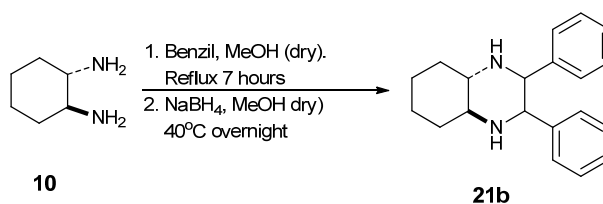
***N,N'*-dibenzyl-*trans*-1,2-diaminocyclohexane (21a)**



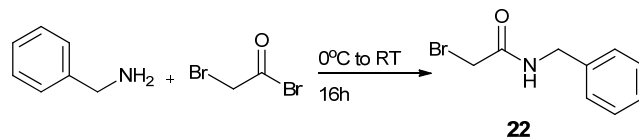
Benzaldehyde (0.2 mL; 2.0 mmol) was added drop-wise to a stirred solution of **10** (0.12 mL, 1.0 mmol) in dry methanol. The reaction was stirred at room temperature for 2 hours. The solvents were removed *in vacuo*, affording a white precipitate. The solid was dissolved in dry methanol/acetonitrile (1:1) and sodium borohydride (1.0 g, 26 mmol) added in tablet form. The solution was stirred at room temperature for 4 hours. Solvents

were removed *in vacuo* to afford the product as a colorless solid. NMR data were consistent with that previously published:<sup>12</sup> <sup>1</sup>H NMR (400 MHz, CDCl<sub>3</sub>) δ (ppm) 7.31 (10H, m, aromatic), 3.85/3.61 (4H, a aa' doublets, benzylic), 2.22 (4H, m, cyclohexyl), 1.76 (2H, m, cyclohexyl), 1.17 (4H, m, cyclohexyl).

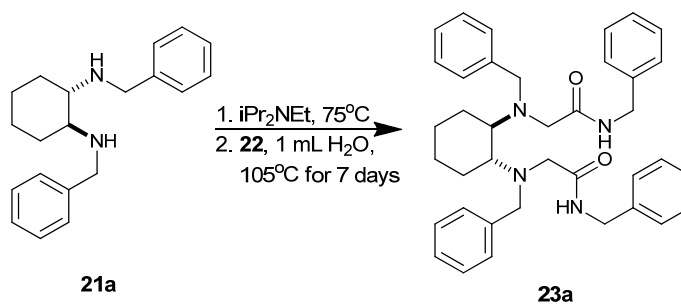
### 2,3-diphenyl-1,2,3,4,4a,5,6,7,8,8a-decahydroquinoxaline (21b)



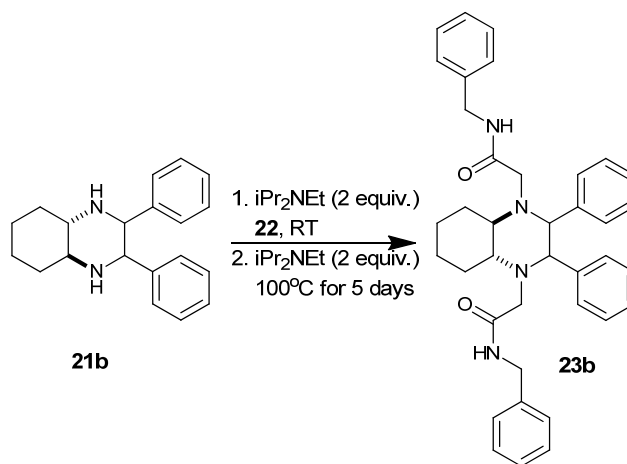
Benzil (0.94 g, 4.4 mmol) was added to a stirred solution of **10** (0.53 mL, 4.4 mmol) in dry methanol. The reaction was heated to reflux and stirred for 7 hours. The reaction was allowed to cool to room temperature, and the solvents were removed *in vacuo*. The residue was heated in a minimum volume of methanol, affording a colorless solid which was isolated by filtration. Following dissolution of this solid in dry methanol, sodium borohydride (0.5 g, 12.7 mmol) was added in tablet form. The solution was heated to 40 °C for 18 h. The reaction was quenched with water and the solvents removed *in vacuo* to afford the product as a yellow solid. NMR data were consistent with that previously published:<sup>13</sup> <sup>1</sup>H NMR (400 MHz, CDCl<sub>3</sub>) δ (ppm) 7.12 (10H, m, aromatic), 3.86 (2H, s, benzylic), 2.64 (2H, m, cyclohexyl), 1.3 - 1.9 (8H, m, cyclohexyl). <sup>13</sup>C δ = 141 (Ar), 128 (Ar), 127 (Ar), 68 (NCH-Ar), 61 (NCH-cyclohexyl), 32 (CH<sub>2</sub>CHN), 25 (CH<sub>2</sub>CH<sub>2</sub>CHN) ppm. *m/z* (ESMS ESI-) 293 ([M-H]<sup>-</sup>)

**N-benzyl-bromoacetamide (22)**

A stirred solution of benzylamine (1.07 g, 10.0 mmol) in dichloromethane was cooled in an ice bath. Potassium carbonate (0.69 g, 5.0 mmol) was added, resulting in a white suspension. Bromoacetyl bromide (2.02 g, 10.0 mmol) was added drop-wise using an addition funnel. After 1 hour, the ice bath was removed, and the reaction was stirred for 18 h at room temperature. The reaction mixture was added to a separatory funnel and washed three times with water, ensuring that the pH was moderately acidic (pH~3 - 5). The organic extracts were dried (sodium sulfate), and the solvents were removed *in vacuo*. The crude product was recrystallized at -20 °C *via* slow diffusion of hexanes into methanolic solution. Crystals were isolated by vacuum filtration, affording the title compound as an off-white solid (yield = 1.15g, 50%). NMR data were consistent with that previously published:<sup>14</sup> <sup>1</sup>H NMR (400 MHz, CDCl<sub>3</sub>) δ (ppm) 7.26 (5H, m, aryl), 6.68 (1H, br s, NH), 4.42 (2H, d, <sup>2</sup>J<sub>H-H</sub> = 6 Hz, benzylic), 3.88 (2H, s, BrCH<sub>2</sub>CON).

**2,2'-(trans-cyclohexane-1,2-diylbis(benzylazanediyl))bis(N-benzylacetamide) (23a)**

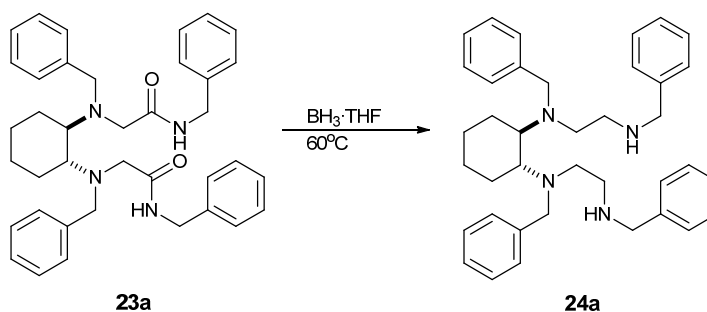
**21a** (0.2 g, 0.69 mmol) added to a solution of *N,N*-diisopropylethylamine (Hünig's base) (0.48 mL, 2.76 mmol) in toluene (125 mL), and the resulting suspension heated to 75 °C. Approximately 1 mL DI water was added to the mixture to dissolve the **21a**. The bromoacetamide **22** (0.64 g, 2.76 mmol) was added to the hot solution as a solid in one portion. The temperature was increased to 105 °C and heating and stirring continued for 7 days. Reaction progress was monitored after three days by mass spectrometry. The reaction was then allowed to cool and the solvents were removed *in vacuo*. The residue taken up in ethyl ether and the resulting cloudy solution washed with saturated sodium sulfite solution. The product was extracted three times from the ether phase. The organic extracts were dried (sodium sulfate), and the solvents were removed *in vacuo*. The colorless solid residue was purified by column chromatography (silica gel, 80:20 ethyl ether/hexanes followed by 75:25 ethyl ether/MeOH), affording the title compound as a colorless solid (0.32 g, 79%).  $R_f = 0.43$  (75:25 ethyl ether/MeOH, SiO<sub>2</sub>).  $m/z$  (ESMS ESI+) 589.3 (100%, [M+H]), 532.3 (45%, possible reduction of cyclohexyl group to yield an ethenyl amine bridge). <sup>1</sup>H NMR (CDCl<sub>3</sub>)  $\delta$  (ppm) 7.45 (2H, br t, NH), 7.30 - 6.97 (20H, m, aryl), 4.46 and 4.24 (4H, a aa' dd, <sup>2</sup>J<sub>H-H</sub> = 15 Hz, <sup>3</sup>J<sub>N-H</sub> = 6 Hz, CONHCH<sub>2</sub>Ph), 3.43 and 3.26 (4H, a aa' d, <sup>2</sup>J<sub>H-H</sub> = 12 Hz, NCH<sub>2</sub>CON), 2.82 and 2.62 (4H, a aa' d, <sup>2</sup>J<sub>H-H</sub> = 16 Hz, NCH<sub>2</sub>Ph), 2.29 (1H, d, <sup>3</sup>J<sub>H-H</sub> = 9 Hz, cyclohexyl CHN), 1.92 (1H, d, <sup>3</sup>J<sub>H-H</sub> = 11 Hz, cyclohexyl CHN), 1.69 (1H, s, cyclohexyl), 1.61 (1H, d, <sup>3</sup>J<sub>H-H</sub> = 9 Hz, cyclohexyl), 1.18 (1H, q, <sup>3</sup>J<sub>H-H</sub> = 6 Hz, cyclohexyl), 0.90 (1H, t, <sup>3</sup>J<sub>H-H</sub> = 10 Hz, cyclohexyl), 0.75 (1H, m, cyclohexyl)

**2,3-(2,3-diphenyl-1,2,3,4,4a,5,6,7,8,8a-decahydroquinoxaline)bis(*N*-benzylacetamide) (23b)**

A 2-necked round-bottom flask with stir bar containing toluene (100 mL) was purged with argon. **21b** (0.112 g, 0.38 mmol) and Hunig's base (0.098 g, 0.76 mmol) were added to the flask at room temperature and allowed to dissolve fully. Bromoacetamide **22** (0.349 g, 1.5 mmol) was then added to the mixture in one portion. The temperature was slowly increased to  $100^\circ\text{C}$ , adding additional Hunig's base (0.095 g, 0.74 mmol) in small portions. The reaction progress was monitored by TLC (9:1 ethyl ether:hexanes on alumina) over 5 days. The reaction was then removed from the heat, allowed to cool, and decanted. The yellow supernatant was concentrated *in vacuo*. The crude residue was purified by column chromatography (basic alumina, 9:1 ethyl ether:hexanes), affording the title compound as a yellow oil.  $R_f = 0.45$  (9:1 ethyl ether:hexanes,  $\text{Al}_2\text{O}_3$ ).  $^1\text{H}$  NMR (400 MHz,  $\text{CDCl}_3$ )  $\delta$  7.38 (4H, ddd, *m*-Ar), 7.36 (4H, d, *o*-Ar), 7.33 (4H, ddd, *m*-Ar), 7.20 (4H, d, *o*-Ar), 7.04 (2H, dd, *p*-Ar), 6.97 (2H, dd, *p*-Ar), 6.84 (2H, br s, NH), 4.55 (1H, dd,  $\text{PhCH}_2\text{NHCO}$ ), 4.51 (2H, d,  $\text{COCH}_2\text{N}$ ), 4.25 (1H, dd,  $\text{PhCH}_2\text{NHCO}$ ), 4.15 (1H,

s, COCH<sub>2</sub>N), 3.58 (1H, s, COCH<sub>2</sub>N), 3.17 (1H, d, NCHPh), 2.85 (1H, d, NCHPh), 2.40 (1H, d, CH<sub>2</sub>CHN), 1.91 (1H, d, CH<sub>2</sub>CHN), 1.73 (2H, m, cyclohexyl), 1.4 - 1.22 (6H, m, cyclohexyl) ppm. *m/z* (ESMS ESI<sup>+</sup>): 587.3 [(M+H)<sup>+</sup>]

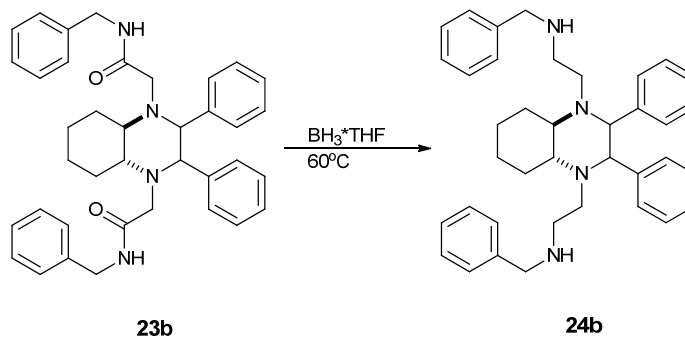
*N*<sup>1</sup>,*N*<sup>1'</sup>-(*trans*-(1,2)-cyclohexane-1,2-diyl)bis(*N*<sup>1</sup>,*N*<sup>2</sup>-dibenzylethane-1,2-diamine) (**24a**)



A 2-necked flask containing diamide **23a** (0.639 g, 1.1 mmol) and a magnetic stir bar was evacuated and purged with argon three times. Dry THF (100 mL) was added to the flask containing **23a**, and the mixture was cooled in an ice bath. Ice-cold BH<sub>3</sub>·THF (30 mL, 1M) was added to the **23a** solution via cannulation. The Suba-seal plugging the flask was replaced with an air condenser under positive pressure of argon. The solution was allowed to warm to room temperature over 30 minutes, stirred for 1 hour, then heated at 40 °C for 3 days. A portion was removed and quenched with MeOH, then analyzed by mass spectrometry. The reduction was found to be incomplete. The reaction was heated at 60 °C for another 5 days, then allowed to come to room temperature. The reaction was cooled in an ice bath, and methanol was added drop-wise to quench any remaining borane. Solvents were removed *in vacuo*. Two additional portions of methanol were added followed by removal *in vacuo* each time. The residue was dissolved in hydrochloric acid (30 mL, 2N) and heated to boiling for 18 h. The solution was allowed

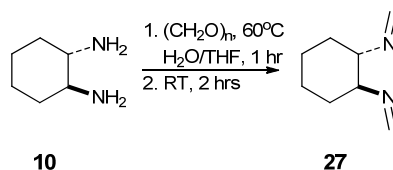
to come to room temperature, then solvents were removed *in vacuo*. The greenish residue was purified by column chromatography (silica gel, 84:14:3 DCM:MeOH:NH<sub>4</sub>OH), affording the title compound as a brownish oil (0.2 g, 32%).  $R_f = 0.66$  (84:14:3 DCM:MeOH:NH<sub>4</sub>OH, SiO<sub>2</sub>).  $m/z$  (ESMS ESI<sup>+</sup>): 561.3 (100%, [M+H]<sup>+</sup>), 428.4 (50%, [M-EtNHCH<sub>2</sub>Ph]<sup>+</sup>).

**2,3-(2,3-diphenyl-1,2,3,4,4a,5,6,7,8,8a-decahydroquinoxaline)-bis(dibenzylethanamine) (24b)**



The title compound was synthesized in crude form from **23b** (0.75 g, 1.28 mmol) following the same protocol as described for **24a**, affording the title compound as a colorless gel. Column chromatography was not performed. <sup>1</sup>H NMR (400 MHz, CDCl<sub>3</sub>)  $\delta$  7.2 (20H, m, aryl), 3.6 - 2.2 (16H, br m, NCH<sub>2</sub>CH<sub>2</sub>N, NCHPh, cyclohexyl CHN, benzylic), 1.5 - 0.8 (8H, br m, cyclohexyl) ppm.

**(1S,2S)-N<sup>1</sup>,N<sup>2</sup>-dimethylenecyclohexane-1,2-diamine (27)**





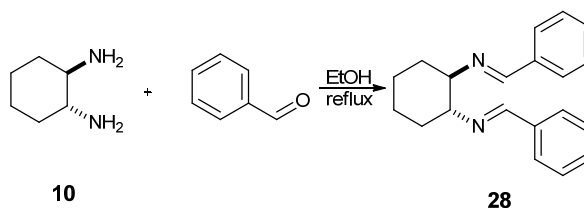
*Trans*-**10** (0.2 g, 1.75 mmol) was dissolved in THF with stirring. To this was added paraformaldehyde in solid form (0.126 g, 4.2 mmol). The temperature was increased to 60 °C. Water was added drop-wise until the paraformaldehyde dissolved. The reaction was heated for 1 hour, allowed to cool to room temp., and stirred an additional 2 hours. The solvents were removed *in vacuo*. The resulting slurry was suction-filtered and the product was freeze dried, affording the title compound as a waxy pink solid (0.2 g; 82% yield). <sup>1</sup>H NMR (400 MHz, CDCl<sub>3</sub>): δ 4.05 and 3.85 (2H each, dd, imine protons), 2.5 (2H, m, NCH-cyclohexyl), 1.9 - 1.7 (4H, m, cyclohexyl), 1.4 - 1.1 (4H, m, cyclohexyl) ppm.

This material was reacted overnight at room temp. with KCN (2 equiv) in THF with a drop of HCl and enough solvent to solubilize the salts. Solvents were removed *in vacuo*, yielding a colorless oily residue. Extraction of the product from DCM was attempted using potassium carbonate solution. The combined organic extracts were dried (sodium sulfate) and solvents were again removed *in vacuo*, yielding a colorless oil. <sup>13</sup>C NMR of the resulting oil shows a peak at 107 ppm, which is somewhat in the right range for nitriles. Addition of a couple of drops of this oil to Cu(II)CO<sub>3</sub> in water showed no change, but upon heating, the solution turned deep blue. Analysis of the oil and of the copper solution by MS did not show any logical product peaks, however.

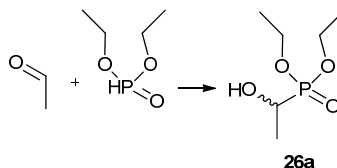
It was also discovered in the literature that an organic base such as 1,8-Diazabicyclo[5.4.0]undec-7-ene (DBU) can be used to catalyze nitro-Mannich reactions. A ~6-7 hour reaction of **27** with nitroethane in THF at room temp. was performed using 20 mol% DBU. The reaction was worked up in the same way as **27** with

KCN. MS of the extracted residue shows no product masses, though the sample may have been too dilute. It may be necessary to do the reaction longer or with heat, or to use a different catalyst (acid or base).

***N*-[*trans*-(1,2)-2-(benzylideneamino)cyclohexyl]-1-phenyl-methanimine (28)**



Diamine **10** (1.0 g, 8.70 mmol), benzaldehyde (1.9 g, 17.50 mmol), and Na<sub>2</sub>SO<sub>4</sub> (anhydrous) (2.5 g, 17.50 mmol) were heated in EtOH (40 mL) at reflux for 2 h. The resulting mixture was filtered hot and the filtrate concentrated *in vacuo*. Crystals were formed after allowing this solution to cool to room temperature. The mother liquor was decanted, affording the title compound as yellow, needle-like crystals. <sup>1</sup>H NMR (400 MHz, CDCl<sub>3</sub>) δ 8.2 (2H, bs, HC=N), 7.6 (4H, m, *o*-aryl), 7.3 (6H, m, *m,p*-aryl) 3.2–3.6 (2H, overlapping signals, HC-N=C) 1.0–2.0 (8H, overlapping signals, cyclohexyl) ppm. (lit. <sup>1</sup>H NMR (200 MHz, CDCl<sub>3</sub>) δ 1.03–2.07 (m, 8H, CH<sub>2</sub>, Cyclohexane), 3.21–3.45 (m, 2H, CH, Cyclohexane), 7.12–7.64 (m, 10H, Ar), 8.15 (s, 2H, -N=CH).<sup>15</sup>

**6.5 Synthesis and kinetic resolution of pendant arms****6.5.1 Synthesis****Diethyl (1-hydroxyethyl)phosphonate (26a)**

Potassium carbonate (5.53 g, 40.0 mmol) was added to a 100 mL 2-necked round bottom flask fitted with screw-tap, and the flask was purged with N<sub>2</sub>. Dry dichloromethane (50 mL) was added, and the flask was cooled in an ice bath. Diethyl phosphite (5.00 g, 36.2 mmol) and acetaldehyde (4.80 g, 109 mmol) were subsequently added to the reaction flask, and the mixture was then stirred for approximately 45 minutes. The reaction was allowed to warm to room temperature and was stirred for 1 additional hour. The soluble portion was transferred to a separatory funnel by decanting and was washed twice with 2N HCl. The organic extracts were dried (sodium sulfate), and the solvents were removed *in vacuo*, affording the title compound as a colorless to slightly yellow liquid (4.81 g, 72.5%). <sup>1</sup>H NMR (CDCl<sub>3</sub>) δ 4.2 (4H, qt, <sup>3</sup>J<sub>H-H</sub> = 7 Hz, <sup>3</sup>J<sub>H-P</sub> = 4 Hz, OCH<sub>2</sub>CH<sub>3</sub>), 4.0 (1H, dq, <sup>3</sup>J<sub>H-H</sub> = 7 Hz, <sup>3</sup>J<sub>H-P</sub> = 4 Hz, PCHOH), 1.4 (3H, dd, <sup>3</sup>J<sub>H-H</sub> = 7 Hz, <sup>4</sup>J<sub>H-P</sub> = 18 Hz, CH<sub>3</sub>CH(OH)P), 1.3 (6H, td, <sup>3</sup>J<sub>H-H</sub> = 7 Hz, <sup>4</sup>J<sub>H-P</sub> = 3 Hz, OCH<sub>2</sub>CH<sub>3</sub>) ppm

**4-chlorophenyl acetate**

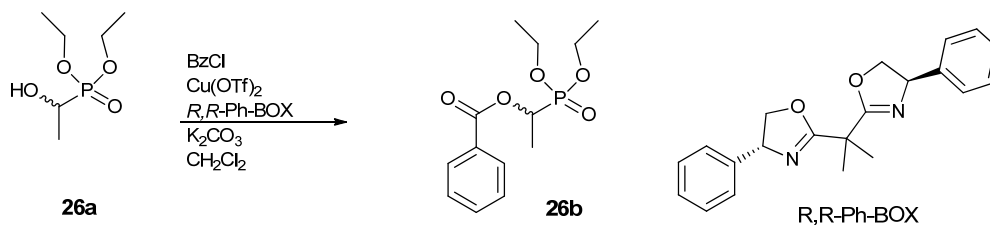
4-chlorophenol (3.86 g, 30 mmol) was dissolved in dichloromethane (250 mL). To this was added 1,8-Diazabicyclo[5.4.0]undec-7-ene (DBU) (5.023 g, 33 mmol), and the solution was cooled in an ice bath and the flask purged with argon. Acetyl chloride (4.4 mL, 60 mmol) was added drop-wise while stirring. The solution was allowed to warm to room temperature and stirred for 18 h. The reaction mixture was added to a separatory funnel containing diethyl ether and an aqueous solution of potassium hydroxide (pH ~10). The product was extracted into the organic phase. The organic extracts were dried (sodium sulfate), and the solvents were removed *in vacuo*. DBU was removed by washing the neat product with water (pH 5.5 from equilibrating with air), affording the title compound as a clear, yellow liquid (4.58 g, 89.4% yield). NMR data were consistent with that previously published:<sup>16,17</sup> <sup>1</sup>H NMR (CDCl<sub>3</sub>) δ 7.36 (2H, dt, <sup>3</sup>J<sub>H-H</sub> = 7 Hz, <sup>4</sup>J<sub>H-H</sub> = 2 Hz, Ar), 7.06 (2H, dt, <sup>3</sup>J<sub>H-H</sub> = 7 Hz, <sup>4</sup>J<sub>H-H</sub> = 2 Hz, Ar), 2.31 (3H, s, *ac*)

*6.5.2 Enantiomeric enrichment using enzymatic resolution*

Enzymatic resolution of phosphonate **26a** and was attempted using *C. Antarctica* lipase B and 4-chlorophenyl acetate according to the reference procedure.<sup>18</sup> However, the acetate of **26a** is difficult to separate from the alcohol. Chromatographic purification of the crude mixture (phosphonyl alcohol, phosphonyl acetate, and acetylating agent/free alcohol) was attempted. No satisfactory method of purification was found. Acetylating agents including acetyl chloride, 4-nitrobenzylacetate, and 4-chlorophenylacetate were tested. The enzyme is also expensive and seemed to acylate the substrate slowly.

## 6.5.3 Kinetic resolution of phosphonyl alcohols with copper catalyst

Enantiomeric resolution experiments with a metal catalyst were performed according to the literature procedure<sup>19</sup> on a previously-synthesized and -purified racemic sample of **26a**. The use of a copper (II) salt with a chiral 4-phenyl-bisoxazolidine ligand promoted selective benzylation of the *R* isomer. This reaction was performed repeatedly using  $K_2CO_3$  as the base and DCM as solvent, either at the scale in the reference (0.5 mmol) or scaled up (5 mmol). Enantioselective benzylation was also performed on **26c** (5 mmol scale).

1-(diethoxyphosphoryl)ethyl benzoate (**26b**)

**Initial (test) reaction:** Cu(II) triflate (0.009 g, 0.025 mmol) and (+)-2,2'-isopropylidene-bis[(4*R*)-4-phenyl-2-oxazoline] (abbreviated  $R,R$ -Ph-BOX) (0.008 g, 0.025 mmol) were weighed directly into a tared 20 mL scintillation vial and taken up in dichloromethane (3 mL). The solution was stirred for 10 minutes and cooled in an ice bath. Potassium carbonate (0.069 g, 0.5 mmol), **26a** (0.091 g, 0.5 mmol), and benzoyl chloride (0.035 g, 0.25 mmol) were added to the reaction mixture. The solution was allowed to warm to room temperature and stirred for 12 hours. Water (3 mL) was added and the biphasic mixture transferred to a separatory funnel. The crude product was extracted three times

with dichloromethane into the organic phase. Solvents were removed *in vacuo*. The benzoate **26b** and the alcohol **26a** were recovered by silica gel chromatography (1:1 hexanes:ethyl acetate followed by 1:1 ethyl acetate:methanol). Typical yield: 0.2 g alcohol (73% yield) + 0.5 g (50%) of the title compound as a colorless solid.  $R_f = 0.43$  (1:1 EtOAc:hexanes, SiO<sub>2</sub>). <sup>1</sup>H NMR (400 MHz, CDCl<sub>3</sub>)  $\delta$  (ppm) 8.1 (2H, d, aryl), 7.5 (1H, dt, aryl), 7.4 (2H, t, aryl), 5.5 (1H, dq, chiral  $\alpha$ -hydroxy H), 4.2 (4H, dq, P-O-CH<sub>2</sub>-CH<sub>3</sub>), 1.6 (3H, dd,  $\alpha$ -hydroxy CH<sub>3</sub>), 1.3 (6H, dt, P-O-CH<sub>2</sub>-CH<sub>3</sub>).

A solution of the alcohol was prepared in an NMR tube (CDCl<sub>3</sub>) and proton spectra were obtained with 0, 0.1, and 0.2 equivalents of a Eu<sup>3+</sup> chiral shift reagent (Europium tris[3-(heptafluoropropylhydroxymethylene)-(+)-camphorate]) (Eu(hfc)<sub>3</sub>).

The reaction was repeated with modification (underlined). Cu(II) triflate (0.090 g, 0.25 mmol) and *R,R*-Ph-BOX (0.084 g 0.25 mmol) were weighed directly into a 250 mL round-bottom flask and taken up in dichloromethane (125 mL). The solution was stirred for 10 minutes and cooled in an ice bath. Potassium carbonate (0.69 g, 5 mmol), **26a** (0.91 g, 5 mmol), and benzoyl chloride (0.49 g, 3.5 mmol) were added to the reaction mixture. The solution was allowed to cool to room temperature and stirred for 18 h. The crude product was extracted three times from the organic phase after mixing thoroughly with water. Solvents were removed *in vacuo*. The benzoate was resolved from the alcohol by silica gel chromatography (1:1 hexanes:ethyl acetate followed by 1:1 ethyl acetate:methanol). A solution of the alcohol was prepared in an NMR tube (CDCl<sub>3</sub>) and enantiomeric excess was determined to be ~60% (4:1 *S*:*R*) using Eu(hfc)<sub>3</sub>.

Kinetic resolution with alternative base/solvent: Cu(II) triflate (0.090 g, 0.25 mmol) and *R,R*-Ph-BOX (0.084 g, 0.25 mmol) were weighed directly into a 100 mL round-bottom flask and taken up in chlorobenzene. The solution was stirred for 10 minutes and cooled in an ice bath. Barium carbonate (0.987 g, 5 mmol), **26a** (0.91 g, 5 mmol), and benzoyl chloride (0.49 g, 3.5 mmol) were added to the reaction mixture. The solution was allowed to come to room temperature and stirred for 18 h. The reaction mixture was transferred to a separatory funnel containing DCM/water (~pH 7), forming an emulsion. The aqueous phase was adjusted to pH ~5.5 with triflic anhydride to try and break the suspension, but this was unsuccessful. The crude product was extracted with successive additions of DCM and solids were removed by suction filtration. Solvents were removed *in vacuo* with heating and a dry ice trap. The benzoate was resolved from the alcohol by silica gel chromatography (1:1 hexanes:ethyl acetate followed by 1:1 ethyl acetate:methanol). Yield: 0.13 g alcohol (48%) + 0.6 g benzoate (60%). A solution of the alcohol was prepared in an NMR tube (CDCl<sub>3</sub>) and enantiomeric excess determination was attempted using Eu(hfc)<sub>3</sub>, but the enantiomeric proton peaks were overlapping significantly, deterring precise quantitation.

Kinetic resolution of *S*-enriched **26a**: The isolated alcohol from both potassium/DCM and barium/chlorobenzene chiral separations were combined and again subjected to enantioselective benzylation (same procedure as for racemic alcohol, 1.65 mmol scale). The benzoate and alcohol were separated by flash chromatography(1:1 hexanes:ethyl acetate followed by 1:1 ethyl acetate:methanol). A solution of the alcohol was prepared in an NMR tube (CDCl<sub>3</sub>) and enantiomeric excess determination was attempted using

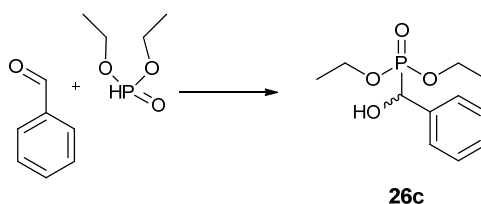
Eu(hfc)<sub>3</sub>, but the enantiomeric proton peaks were overlapping significantly, deterring precise quantitation. It appears that the amount of the *S* isomer has been enriched further, but this could not be confirmed.

Results indicate that this reaction is reproducible and robust with respect to variations to scale, %ee of starting alcohol, and between methyl or phenyl groups at the chiral center. In each case, the extracted products were separated by column chromatography. (Eu(hfc)<sub>3</sub>) was used to determine enantiomeric ratios for each of the two products (benzoate and alcohol). The extraction using BaCO<sub>3</sub> / chlorobenzene was more challenging – a difficult-to-break emulsion formed and chlorobenzene requires a harder vacuum to evaporate off. The enantiomeric excess of (*S*)-alcohol seemed to be higher using BaCO<sub>3</sub> / chlorobenzene, but the yield was lower and the Eu-shifted peaks in the %ee determination NMR spectra were very broad (possibly due to incomplete removal of salts/solvent), making precise quantitation impossible. The enriched alcohol products were combined and reacted a second time using the potassium/DCM conditions, extracted, and resolved by flash chromatography. NMR peaks representing Eu-shifted protons are not baseline resolved from the non-shifted enantiomeric peaks, but the %ee is conservatively estimated at 60% (4:1 *S* isomer). Acquisition at higher field strength or a different sample:shift reagent ratio may improve spectroscopic resolution. Deprotection of **26b**. Under argon, the benzoate (2.4 mmol, 0.7 g) was dissolved in dry methanol. A 1% solution of NaOH in methanol (2.5 equiv) was added dropwise *via* addition funnel. The reaction was stirred for 1 hour, then solvents were removed *in vacuo*. The residue was taken up in ethyl acetate, which was washed twice with water. Solvents were



removed *in vacuo* and the residue was analyzed by  $^1\text{H}$  NMR. The phosphonate alcohol **26a** peaks are present, as are mono-substituted phenyl peaks and a large singlet  $\sim 1.6$  ppm. No shifts from the parent compound are observed at 5.5 or 1.6 ppm. The procedure appeared to convert the compound back to the alcohol, but unidentified impurities were also present ( $\sim 15\%$  of peak area in  $^1\text{H}$  NMR).

### Diethyl (hydroxy(phenyl)methyl)phosphonate (**26c**)

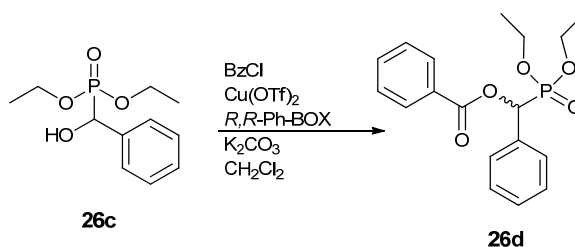


A 100 mL 2-necked RB flask with stir bar was evacuated and purged with argon. To this was added  $\text{K}_2\text{CO}_3$  (2.0 g, 14 mmol) under a positive pressure of argon. Dry THF was added by cannulation and the suspension was cooled in an ice bath. Diethyl phosphite (2.32 g, 18 mmol) was injected via Suba-seal, followed by drop-wise injection of benzaldehyde (2.12 g, 20 mmol). The reaction was stirred in an ice bath for 45 min., allowed to warm to room temp. with stirring over one hour, then heated at  $45\text{ }^\circ\text{C}$  for two hours. Solvents were removed *in vacuo*. The residue was taken up in DCM and added to 2N HCl (20 mL) in a separatory funnel. The product was extracted from the organic phase three times. The combined organic extracts were dried (sodium sulfate), and solvents were removed *in vacuo*, affording an off-white solid. Instead of column purification, this compound was recrystallized from THF at  $-20\text{ }^\circ\text{C}$ , affording the title compound. NMR data were consistent with that previously published:<sup>20</sup>  $^1\text{H}$  NMR (400

MHz, CDCl<sub>3</sub>)  $\delta$  (ppm) 7.5 (2H, dd, ortho(aryl)), 7.3 (3H, dd + dt, m/p(aryl)), 5.0 (1H, d,  $\alpha$ -hydroxy), 4.0 (4H, dq, P-O-CH<sub>2</sub>-CH<sub>3</sub>); 1.3 (6H, dt, P-O-CH<sub>2</sub>-CH<sub>3</sub>). <sup>13</sup>C  $\delta$  (ppm) 136.7 (d,  $\beta$ -hydroxy quaternary C) 127-128.2 (3 peaks, d, aryl C) 68, 70, 71, 63 (dd, <sup>2</sup>J<sub>C-P</sub> = 31, 7 Hz ethoxy), 16 (dd, ethyl).

This reaction was previously attempted without the heating step and using 10 mmol base, and was determined to be incomplete based on <sup>1</sup>H NMR scan of the extracted residue.

### Kinetic resolution of **26c**:



Cu(II) triflate (0.090 g, 0.25 mmol) and R,R-Ph-BOX (0.084 g, 0.25 mmol) were weighed directly into a 250 mL round-bottom flask and dissolved in dichloromethane. The solution was stirred for 10 minutes and cooled in an ice bath. Potassium carbonate (0.69 g, 5 mmol), **26c** (1.22 g, 5 mmol), and benzoyl chloride (0.49 g, 3.5 mmol) were added to the reaction mixture. The solution was let come to room temperature and stirred overnight. The reaction progress was monitored by <sup>1</sup>H NMR and determined to be incomplete – an additional 24 h stirring was done prior to workup. The crude product was extracted 3 times from the organic phase after mixing thoroughly with water. The combined organic extracts were dried (sodium sulfate) and solvents were removed *in vacuo*. The benzoate was resolved from the alcohol by silica gel chromatography (60:40

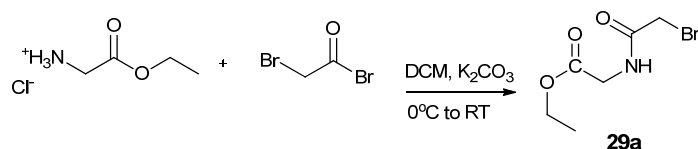
hexanes:ethyl acetate followed by 1:1 ethyl acetate:methanol), affording the title compound.  $R_f = 0.3$  (1;1 EtOAc:hexanes, SiO<sub>2</sub>). NMR data were consistent with that previously published:<sup>19</sup> <sup>1</sup>H NMR data (400 MHz, CDCl<sub>3</sub>)  $\delta$  (ppm) 8.1 (2H, d, benzoate(ortho)); 7.6-7.3 (8H, d/t/m, benzoate and  $\alpha$ -hydroxy phenyl); 6.4 (1H, d,  $\alpha$ -hydroxy); 4.2 (4H, dq, P-O-CH<sub>2</sub>-CH<sub>3</sub>); 1.3 (6H, dt, P-O-CH<sub>2</sub>-CH<sub>3</sub>).

A solution of the alcohol was prepared in an NMR tube (CDCl<sub>3</sub>) and enantiomeric excess determination was attempted using Eu(hfc)<sub>3</sub>, but no shift was observed upon successive additions of this reagent, only broadening of all peaks in the spectrum. Successive additions of shift reagent to an NMR sample were unable to resolve the enantiomeric **26c** species. The most plausible explanation is that steric hindrance prevents the bulky Eu(hfc)<sub>3</sub> from binding to this phosphonate with  $\alpha$ -phenyl chiral center. It is possible, though, that this steric hindrance produces *enantiospecific* benzylation of the alcohol, leading to only one isomer observed in the NMR.

## 6.6 DOTAM derivatives to be used for CEST

### 6.6.1 Synthesis of DOTAM-(Gly)<sub>4</sub> for water exchange measurement in liposomes

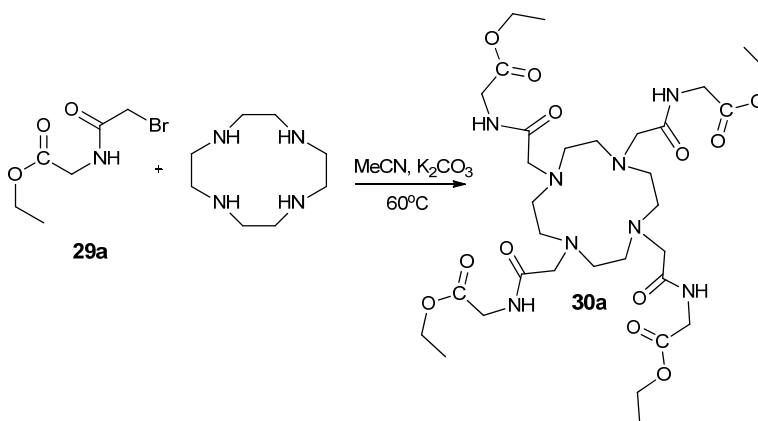
#### Ethyl 2-(2-bromoacetamido)acetate (**29a**)



Glycine ethyl ester hydrochloride (0.698 g, 5 mmol) and potassium carbonate (1.38 g, 10 mmol) were suspended in dichloromethane (50 mL) at 0 °C. Bromoacetyl bromide (1.01

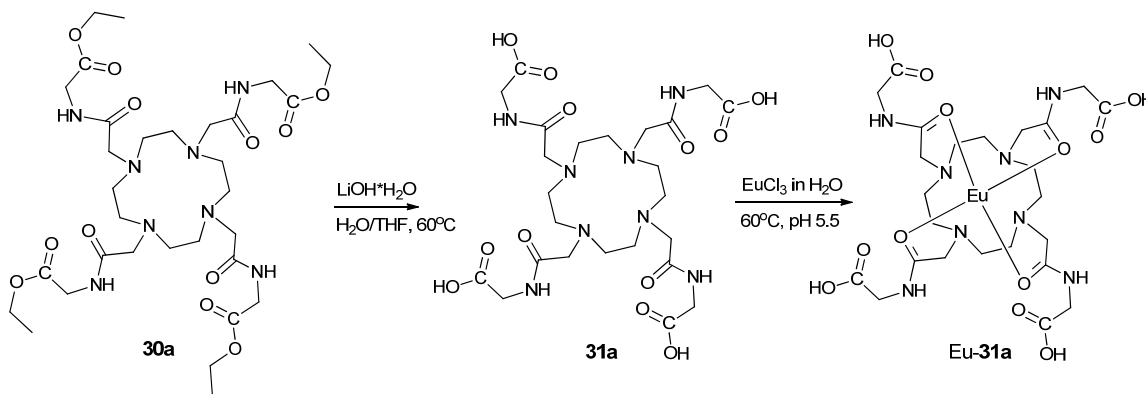
g, 5 mmol) was added drop-wise at the same temperature. The mixture was stirred at 0 °C for 1 h then at room temperature for 18 h. The organic layer was transferred to a separatory funnel and was washed with water (3 × 50 mL), ensuring the pH remained basic. The organic extracts were dried (sodium sulfate), and the solvents were removed *in vacuo* to afford a colorless solid (0.785 g, 70%). NMR data were consistent with that previously published:<sup>21</sup> <sup>1</sup>H NMR (400 MHz, CDCl<sub>3</sub>) δ (ppm) 7.04 (1H, br s, NH), 4.24 (2H, q, OCH<sub>2</sub>), 4.06 (2H, d, CH<sub>2</sub>CO<sub>2</sub>), 3.92 (2H, s, BrCH<sub>2</sub>), 1.30 (3H, t, CH<sub>3</sub>).

### 1,4,7,10-Tetraazacyclododecane-1,4,7,10-tetrakis(ethyl-acetamidoacetate) (**30a**)



A mixture of cyclen (0.15 g, 0.875 mmol), bromoacetamide **29a** (0.785 g, 3.50 mmol), and potassium carbonate (0.483 g, 3.50 mmol) in acetonitrile (250 mL) was heated at 60–70 °C for 18 h. Solvents were removed *in vacuo*. The residue was used without further purification. *m/z* (ESMS ESI<sup>+</sup>): 745.4 ([M+H]<sup>+</sup>). NMR data were consistent with that previously published:<sup>22</sup> <sup>1</sup>H NMR (CDCl<sub>3</sub>) δ (ppm) 7.5 (4H, br t, <sup>3</sup>J<sub>H-H</sub> = 5 Hz, NH), 4.19 (8H, q <sup>3</sup>J<sub>H-H</sub> = 7 Hz, CO<sub>2</sub>CH<sub>2</sub>CH<sub>3</sub>), 3.99 (8H, d, <sup>3</sup>J<sub>H-H</sub> = 5 Hz, CO<sub>2</sub>CH<sub>2</sub>N), 3.10 (8H, s, NCH<sub>2</sub>CON), 2.77 (16H, m, NCH<sub>2</sub>CH<sub>2</sub>N), 1.30 (12H, t, <sup>3</sup>J<sub>H-H</sub> = 7 Hz, CH<sub>3</sub>CH<sub>2</sub>).

**1,4,7,10-Tetraazacyclododecane-1,4,7,10-tetrakis(acetamidoacetate) europium (III) complex H[(Eu-31a)]**

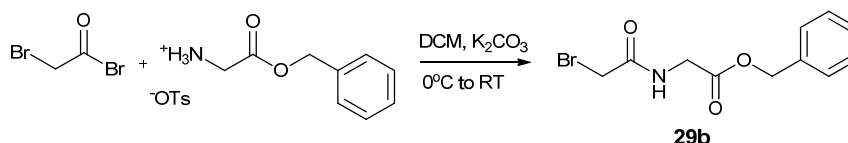


The crude **30a** was suspended in tetrahydrofuran (3 mL) and added to a solution of LiOH (3 mL, 0.29 M) which was heated at 60 °C for 3 days. The pH was monitored and adjusted to ~14 as needed with LiOH. After 3 days, any remaining THF was removed *in vacuo* and the pH was adjusted to 7.2 with HCl. This solution was used to form complexes with  $\text{Eu}^{3+}$  without further purification.

Europium chloride hexahydrate (22.5 mg, 0.875 mmol) was added to the solution of **31a** and the pH found to be between 5 and 6. The sample was heated at 60 °C for an additional 4 days. The sample was removed from heat and freeze dried, then recrystallized from water/methanol at pH 4 - 5. NMR data were consistent with that previously published.<sup>23</sup>  $^1\text{H}$  NMR ( $\text{D}_2\text{O}$ ):  $\delta$  (ppm) 26.4, 7.86, -2.51, -5.49, -8.37, -11.1, -13.4.

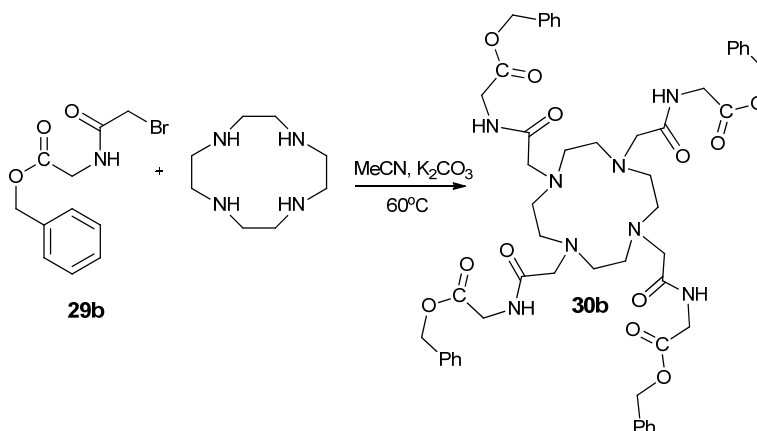
These conditions were used in attempt to scale up (~15 g) the reaction, but the alkylation of cyclen with Ethyl Bromoacetamidoacetate could not be performed reproducibly, and the ethyl esters could not be removed cleanly.

### Benzyl 2-(2-bromoacetamido)acetate (29b)



A suspension of potassium carbonate (27.66 g, 0.2 mol) and glycine benzyl ester *p*-Toluenesulfonate salt (33.6 g, 0.1 mol) was prepared in dichloromethane (1000 mL) and cooled in an ice bath. Under vigorous stirring, bromoacetyl bromide (0.1 mol, 19.8 g) was added drop-wise to the suspension, which was stirred and allowed to warm to room temperature overnight. The mixture was transferred to a separatory funnel and washed 3 times with water (150 mL) while holding the pH of the aqueous phase at 10 or above. The organic extracts were dried (sodium sulfate), and the solvents were removed *in vacuo*. The product was recrystallized successively from DCM, DCM/hexanes, and hexanes, and then washed with hexanes/ethyl ether to yield a colorless solid (9.8 g, 34%). NMR data were consistent with that previously published:<sup>24</sup> <sup>1</sup>H NMR (400 MHz, CDCl<sub>3</sub>): δ 7.39 (5H, m, aryl); 7.02 (1H, br s, NH); 5.23 (2H, s, PhCH<sub>2</sub>O); 4.13 (2H, d, O<sub>2</sub>CCH<sub>2</sub>N); 3.93 (2H, s, BrCH<sub>2</sub>CO).

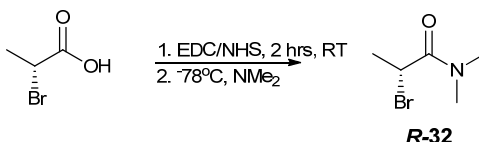
*N,N',N'',N'''*-[1,4,7,10-tetraazacyclododecane-1,4,7,10-tetrayltetrakis(1-oxoethane-2,1-diyl)]tetrakis[glycine] Tetrabenzyl Ester (**30b**)



A solution of cyclen (0.762 g, 4.4 mmol) in acetonitrile (100 mL) was prepared. Potassium carbonate (2.69 g, 19.5 mmol) was added to this, forming a suspension. The temperature was increased to 70 °C. After approximately 30 minutes, bromoacetamide **29b** (5.6 g, 19.5 mmol) was added as a solution in acetonitrile. The reaction was stirred at 70°C for 18 h. The mixture was cooled and filtered through a glass frit, and solvents were removed *in vacuo*. The crude product could not be crystallized from MeOH/H<sub>2</sub>O or from DCM/hexanes. Approximately 0.4 g crude product was purified on silica gel (95:5 chloroform:methanol first to remove impurities, elution with 7:2:1 CHCl<sub>3</sub>:MeOH:NH<sub>4</sub>OH), yielding a yellow oil (0.35 g, 75%).  $R_f = 0.47$  (7:2:1 CHCl<sub>3</sub>:MeOH:NH<sub>4</sub>OH, SiO<sub>2</sub>). NMR data were consistent with that previously published: <sup>1</sup>H NMR: δ (ppm) 7.3 (20H, m, aryl), 5.1 (8H, d, PhCH<sub>2</sub>O), 4.0 (8H, br s, O<sub>2</sub>CH<sub>2</sub>N), 3.65 (8H, d, NCH<sub>2</sub>CON), 3.2 - 3.6 (16H, br s, macrocyclic CH<sub>2</sub>).  $m/z$  (ESMS ESI<sup>+</sup>): 497.2

(100%,  $[M+H]^{2+}$ ), 993.5 (40%,  $[M+H]^+$ ); 917.4, 841.4, 765.4, 689.4 (trans-esterification of benzylic with methyl groups, instrumental artifact).

**R-2-bromo-(N,N-dimethyl)propanamide (R-32)**



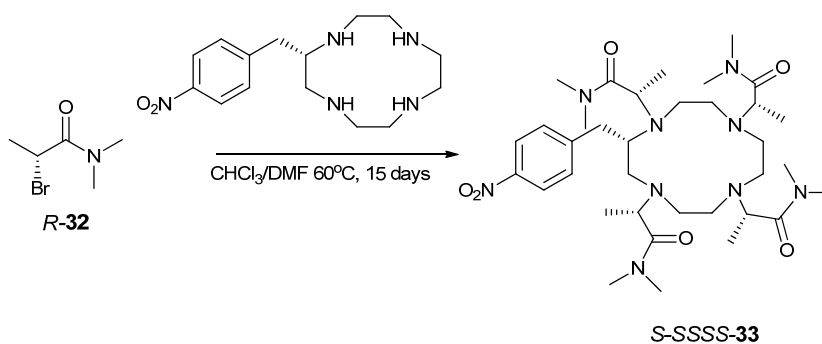
Dichloromethane was added to an Argon-purged, 2-neck flask via cannulation. R-2-bromopropionic acid (1.0 g, 6.6 mmol) was added to the flask *via* Suba-seal while stirring. Under a positive flow of Argon, N-hydroxysuccinimide (NHS, 1.14 g, 9.9 mmol) followed by 1-Ethyl-3-(3-dimethylaminopropyl)carbodiimide (EDC, 1.91 g, 9.9 mmol) were added to the reaction mixture. The solution was stirred for 2 hours. A double-outlet (to inert gas line and from reagent gas cylinder) dry ice trap was connected over the reaction flask. An excess of dimethylamine was added to the reaction mixture drop-wise, under argon, as a condensate from the dry ice trap. The solution was stirred for an additional 2 hours in an ice bath. The reaction mixture was then removed from the argon line, transferred to a separatory funnel, and washed twice with base (potassium carbonate in water, pH 12 - 14) then three times with acid (HCl in water, pH 1 - 5). The organic extracts were dried (sodium sulfate), and the solvents were removed *in vacuo*. The title compound was afforded as a clear/pale yellow oil (0.6 g, 50.5% yield).  $^1\text{H}$  NMR:  $\delta$  (ppm) 4.58 (1H, q,  $^3J_{\text{H-H}} = 7$  Hz,  $\alpha$ -bromo); 2.91 and 3.10 (3H each, s, methylamido); 1.81 (3H, d,  $^3J_{\text{H-H}} = 7$  Hz,  $\text{CH}_3\text{CHBr}$ ).



**S-2-bromo-(N,N-dimethyl)-propanamide (S-32)**

The title complex was synthesized from S-2-bromopropionic acid following the same protocol as described for synthesis of R-32.  $\delta$  (ppm) 4.58 (1H, q,  $^3J_{\text{H-H}} = 7$  Hz,  $\alpha$ -bromo); 2.98 and 3.10 (3H each, s, methylamido); 1.80 (3H, d,  $^3J_{\text{H-H}} = 7$  Hz,  $\text{CH}_3\text{CHBr}$ ).

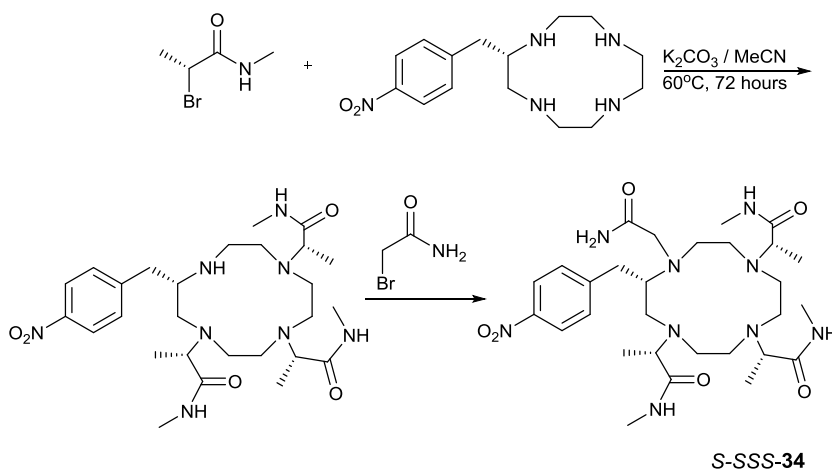
***N*<sup>1</sup>,*N*<sup>1</sup>,*N*<sup>4</sup>,*N*<sup>4</sup>,*N*<sup>7</sup>,*N*<sup>7</sup>,*N*<sup>10</sup>,*N*<sup>10</sup>-octamethyl-(1*S*,4*S*,7*S*,10*S*-  $\alpha$ ,  $\alpha'$ ,  $\alpha''$ ,  $\alpha'''$ -tetramethyl-(*S*)-2-(4-nitrobenzyl)-1,4,7,10-Tetraazacyclododecane-1,4,7,10-tetraacetamide) (33)**



Potassium carbonate (0.2 g, 1.45 mmol) was added to an acid-washed, 2-necked round-bottom flask with magnetic stir bar. The flask was evacuated and purged with argon. An air condenser was attached, evacuated, and purged with argon as well. The following were added to the reaction flask, under a positive pressure of argon, in order: chloroform (50 mL), S-nitrobenzyl cyclen (0.100 g, 0.325 mmol), and R-32 drop-wise (0.261 g, 1.45 mmol). The heat was slowly increased from room temperature to 60 °C over 1-1.5 hours and stirred at that temperature for 4 days. A 1.0 mL aliquot was then removed, washed with water, and extracted with dichloromethane. Solvents were removed *in vacuo*. The brown, tar-like residue was analyzed by mass spectrometry. *m/z* (ESMS ESI<sup>+</sup>): 605.4, 100%, M+H; 506.3, 60%, di-alkylated macrocycle; 407.3, 20%; mono-alkylated). The

solvent from the entirety of the reaction mixture was removed *in vacuo* and the residue re-suspended in acetonitrile and heated at reflux under argon for an additional 4 days, increasing the ionization proportion of the product:  $m/z$  (ESMS ESI<sup>+</sup>): 605.6 (100%, [M+H(trialkylated)]<sup>+</sup>), 506.4 (10%, [di-alkylated macrocycle]), 704.6, (10% ([M+H]<sup>+</sup>). The solvent was then changed to *N,N*-dimethylformamide (DMF), heated for another 7 days, and found to contain the product. Salts were removed by partitioning the reaction mixture between DCM (200 mL) and water (5 mL). The organic extracts were dried (sodium sulfate), and the solvents were removed *in vacuo*. The residue was taken up in water and divided into 2 equal portions. To these were added Gd<sup>3+</sup> and Eu<sup>3+</sup> chloride hydrates (1 equivalent each), adjusted to pH 5 - 6 with HCl/KOH, and stirred at 60°C for 48 hours. The intended chelates were not formed as a result, possibly due to hydrolysis of the amides or impurities carried through the reaction.

***N*<sup>4</sup>,*N*<sup>7</sup>,*N*<sup>10</sup>-trimethyl-(4*S*,7*S*,10*S*-  $\alpha'$ ,  $\alpha''$ ,  $\alpha'''$ -trimethyl-(*S*)-2-(4-nitrobenzyl)-1,4,7,10-Tetraazacyclododecane-1,4,7,10-tetraacetamide) (*S*-SSS-34)**



Samples of *S*- and *R*-2-bromo-*N*-methylpropanamide were provided by M. Woods and were analyzed by  $^1\text{H}$  NMR: *R* isomer:  $\delta$  (ppm) 6.37 - 6.75 (1H, br q, NH); 4.44 (1H, q, BrCHCO); 2.87 (3H, d, NHCH $\underline{\text{H}}_3$ ); 1.90 (3H, d, BrCHCH $\underline{\text{H}}_3$ ). *S* isomer:  $\delta$  (ppm) 6.40 - 6.77 (1H, br q,  $^3J_{\text{H-H}} = 5$  Hz, NH); 4.44 (1H, q,  $^3J_{\text{H-H}} = 7$  Hz, BrCHCO); 2.87 (3H, d,  $^3J_{\text{H-H}} = 5$  Hz, NHCH $\underline{\text{H}}_3$ ); 1.90 (3H, d,  $^3J_{\text{H-H}} = 7$  Hz, BrCHCH $\underline{\text{H}}_3$ ).

*R*-2-bromo-*N*-methylpropanamide (0.119 g, 0.717 mmol) was added to a tared 20 mL scintillation vial and dissolved in approximately 10 mL acetonitrile.  $\text{K}_2\text{CO}_3$  (0.100 g, 0.717 mmol) and nitrobenzyl cyclen (0.050 g, 0.163 mmol) were then added and the combined suspension was heated to 60 °C, checking pH (~10) after 24 hours. The mixture was heated for 72 hours, after which solvents were removed *in vacuo*, yielding a colorless solid (0.55 g, product + salts) and the residue stored at -20 °C. *m/z* (ESMS ESI+): 563.4 ( $[\text{M}+\text{H}]^+$ ).

The trialkylated macrocycle (0.092 g, 0.163 mmol) and 2-bromoacetamide (0.025 g, 0.179 mmol) were dissolved in acetonitrile (2 mL). Potassium carbonate (0.045 g, 0.326 mmol) was added, and the reaction was stirred at 60 °C for two days. The reaction was filtered, and the filter cake was washed with hot acetonitrile. The solvents were removed from the filtrate *in vacuo*, and MS analysis revealed a mixture of products. *m/z* (ESMS ESI+): 563.4 ( $[\text{trialkylated macrocycle}+\text{H}]^+$ ), 620.4 ( $[\text{M}+\text{H}]^+$ ), 648.4 ( $[\text{M}+\text{N-methylpropanamide}]^+$ ); all peaks roughly 1:1:1).

***N*<sup>4</sup>,*N*<sup>7</sup>,*N*<sup>10</sup>-trimethyl-(4*R*,7*R*,10*R*- $\alpha'$ ,  $\alpha''$ ,  $\alpha'''$ -trimethyl-(*S*)-2-(4-nitrobenzyl)-1,4,7,10-Tetraazacyclododecane-1,4,7,10-tetraacetamide) (*S*-RRR-34)**

The title compound was prepared according to the method described for *S*-SSS-34. *m/z* (ESMS ESI+): 563.4 ([trialkylated macrocycle+H]<sup>+</sup>), 620.4 ([M+H]<sup>+</sup>), 648.4 ([M+N-methylpropanamide]<sup>+</sup>); all peaks roughly 1:1:1).

### 6.7 References

- (1) Woods, M.; Botta, M.; Avedano, S.; Wang, J.; Sherry, A. D. *Dalton Transactions* **2005**, 3829.
- (2) Avedano, S.; Botta, M.; Haigh, J.; Longo, D.; Woods, M. *Inorganic Chemistry* **2013**, *52*, 8436.
- (3) Hoffman, R. V.; Tao, J. *Tetrahedron* **1997**, *53*, 7119.
- (4) Wang, Z.-F.; Xu, J.-C. *Tetrahedron* **1998**, *54*, 12597.
- (5) Di Bari, L.; Pescitelli, G.; Sherry, A. D.; Woods, M. *Inorganic Chemistry* **2005**, *44*, 8391.
- (6) Aime, S.; Botta, M.; Crich, S. G.; Terreno, E.; Anelli, P. L.; Uggeri, F. *Chemistry – A European Journal* **1999**, *5*, 1261.
- (7) Geraldes, C. F. G. C.; Sherry, A. D.; Kiefer, G. E. *Journal of Magnetic Resonance (1969)* **1992**, *97*, 290.
- (8) *Macrocyclic Synthesis: A Practical Approach*; Parker, D., Ed.; Oxford University Press: USA, 1996.
- (9) Kang, H.; Facchetti, A.; Jiang, H.; Cariati, E.; Righetto, S.; Ugo, R.; Zuccaccia, C.; Macchioni, A.; Stern, C. L.; Liu, Z.; Ho, S.-T.; Brown, E. C.; Ratner, M. A.; Marks, T. J. *Journal of the American Chemical Society* **2007**, *129*, 3267.
- (10) Athey, P. S.; Kiefer, G. E. *The Journal of Organic Chemistry* **2002**, *67*, 4081.
- (11) Hembre, R. T.; Scott, C. P.; Norton, J. R. *The Journal of Organic Chemistry* **1987**, *52*, 3650.
- (12) Alexakis, A.; Chauvin, A.-S.; Stouvenel, R.; Vrancken, E.; Mutti, S.; Mangeney, P. *Tetrahedron: Asymmetry* **2001**, *12*, 1171.
- (13) Shono, T.; Kise, N.; Shirakawa, E.; Matsumoto, H.; Okazaki, E. *The Journal of Organic Chemistry* **1991**, *56*, 3063.
- (14) Smith, A. M. R.; Rzepa, H. S.; White, A. J. P.; Billen, D.; Hii, K. K. *The Journal of Organic Chemistry* **2010**, *75*, 3085.

- (15) Shaikh, A. L.; Puranik, V. G.; Deshmukh, A. R. A. S. *Tetrahedron* **2005**, *61*, 2441.
- (16) Persson, B. A.; Larsson, A. L. E.; Le Ray, M.; Bäckvall, J.-E. *Journal of the American Chemical Society* **1999**, *121*, 1645.
- (17) Khersonsky, O.; Tawfik, D. S. *Biochemistry* **2005**, *44*, 6371.
- (18) Pàmies, O.; Bäckvall, J.-E. *The Journal of Organic Chemistry* **2003**, *68*, 4815.
- (19) Demizu, Y.; Moriyama, A.; Onomura, O. *Tetrahedron Letters* **2009**, *50*, 5241.
- (20) Malinowska, B.; Majewska, P.; Szatkowski, P.; Kafarski, P.; Lejczak, B. *Biocatalysis & Biotransformation* **2011**, *29*, 271.
- (21) Katakya, R.; Parker, D.; Teasdale, A.; Hutchinson, J. P.; Buschmann, H.-J. *Journal of the Chemical Society, Perkin Transactions 2* **1992**, 1347.
- (22) Zhang, S.; Wu, K.; Biewer, M. C.; Sherry, A. D. *Inorganic Chemistry* **2001**, *40*, 4284.
- (23) Aime, S.; Barge, A.; Delli Castelli, D.; Fedeli, F.; Mortillaro, A.; Nielsen, F. U.; Terreno, E. *Magnetic Resonance in Medicine* **2002**, *47*, 639.
- (24) Vasalatiy, O.; Zhao, P.; Woods, M.; Marconescu, A.; Castillo-Muzquiz, A.; Thorpe, P.; Kiefer, G. E.; Dean Sherry, A. *Bioorganic & Medicinal Chemistry* **2011**, *19*, 1106.

## COMPLETE LIST OF REFERENCES

- (1) Iglehart, J. K. *New England Journal of Medicine* **2006**, 354, 2822.
- (2) Brenner, D. J.; Hall, E. J. *New England Journal of Medicine* **2007**, 357, 2277.
- (3) de González, A. B.; Darby, S. *The Lancet* **2004**, 363, 345.
- (4) Rothkamm, K.; Balroop, S.; Shekhdar, J.; Fernie, P.; Goh, V. *Radiology* **2007**, 242, 244.
- (5) Kwong, R. Y.; Yucel, E. K. *Circulation* **2003**, 108, e104.
- (6) Tatlisumak, T. *Stroke* **2002**, 33, 2144.
- (7) Gupta, R. T.; Kauffman, C. R.; Polascik, T. J.; Taneja, S. S.; Rosenkrantz, A. B. *Oncology-Ny* **2013**, 27, 262.
- (8) Li, X.; Priest, R. A.; Woodward, W. J.; Siddiqui, F.; Beer, T. M.; Garzotto, M. G.; Rooney, W. D.; Springer Jr, C. S. *Journal of Magnetic Resonance* **2012**, 218, 77.
- (9) Li, X.; Priest, R. A.; Woodward, W. J.; Tagge, I. J.; Siddiqui, F.; Huang, W.; Rooney, W. D.; Beer, T. M.; Garzotto, M. G.; Springer, C. S. *Magnetic Resonance in Medicine* **2013**, 69, 171.
- (10) Lauterbur, P. C. *Nature* **1973**, 242, 190.
- (11) Damadian, R. *Science* **1971**, 171, 1151.
- (12) Andrew, E. R.; Bottomley, P. A.; Hinshaw, W. S.; Holland, G. N.; Moore, W. S.; Simaraj, C. *Physics in Medicine and Biology* **1977**, 22, 971.
- (13) Damadian, R.; Goldsmith, M.; Minkoff, L. *Physiol Chem Phys* **1977**, 9, 97.
- (14) Hinshaw, W. S.; Bottomley, P. A.; Holland, G. N. *Nature* **1977**, 270, 722.
- (15) Kumar, A.; Welte, D.; Ernst, R. R. *Journal of Magnetic Resonance (1969)* **1975**, 18, 69.
- (16) Harris, R. K.; Grant, D. M. *Methods in Biomedical Magnetic Resonance Imaging and Spectroscopy*; John Wiley & Sons, Inc, 2000; Vol. 1.
- (17) *Magnetic Resonance in Medicine*; 4 ed.; Rinck, P. A., Ed.; Wiley-Blackwell, 2001.
- (18) Canet, D. In *Advances in Inorganic Chemistry*; Academic Press: 2005; Vol. Volume 57, p 3.
- (19) *2007 MRI Market Summary Report*, IMV, Ltd., 2007.
- (20) Aime, S.; Botta, M.; Terreno, E. In *Advances in Inorganic Chemistry*; Academic Press: 2005; Vol. Volume 57, p 173.
- (21) Huang, W.; Tudorica, L. A.; Li, X.; Thakur, S. B.; Chen, Y.; Morris, E. A.; Tagge, I. J.; Korenblit, M. E.; Rooney, W. D.; Koutcher, J. A.; Springer, C. S. *Radiology* **2011**, 261, 394.
- (22) Eisinger, J.; Shulman, R. G.; Blumberg, W. E. *Nature* **1961**, 192, 963.
- (23) Cohn, M.; Leigh, J. S. *Nature* **1962**, 193, 1037.

- (24) Caravan, P.; Ellison, J. J.; McMurry, T. J.; Lauffer, R. B. *Chemical Reviews* **1999**, *99*, 2293.
- (25) Brucher, E.; Sherry, A.; Merbach, A. E., Tóth, E. v., Eds.; John Wiley & Sons: Chichester, 2001, p 243.
- (26) Cacheris, W. P.; Quay, S. C.; Rocklage, S. M. *Magnetic Resonance Imaging* **1990**, *8*, 467.
- (27) Sherry, A. D.; Caravan, P.; Lenkinski, R. E. *Journal of Magnetic Resonance Imaging* **2009**, *30*, 1240.
- (28) Elizondo, G.; Fretz, C. J.; Stark, D. D.; Rocklage, S. M.; Quay, S. C.; Worah, D.; Tsang, Y. M.; Chen, M. C.; Ferrucci, J. T. *Radiology* **1991**, *178*, 73.
- (29) Frydrychowicz, A.; Lubner, M. G.; Brown, J. J.; Merkle, E. M.; Nagle, S. K.; Rofsky, N. M.; Reeder, S. B. *Journal of Magnetic Resonance Imaging* **2012**, *35*, 492.
- (30) Bousquet, J. C.; Saini, S.; Stark, D. D.; Hahn, P. F.; Nigam, M.; Wittenberg, J.; Ferrucci, J. T. *Radiology* **1988**, *166*, 693.
- (31) Shellock, F. G.; Spinazzi, A. *American Journal of Roentgenology* **2008**, *191*, 1129.
- (32) Lanthanide. <http://www.daviddarling.info/encyclopedia/L/lanthanide.html> (accessed June 21st, 2013).
- (33) Kaltsoyannis, N.; Scott, P. *The elements*; Oxford University Press, Inc.: New York, 1999; Vol. 76.
- (34) Tweedle MF, E. S., Eckelman WC, Gaughan GT, Hagan JJ, Wedeking PW, Yost FJ. *Invest. Radiol.* **1988**, Suppl 1:S236.
- (35) Loncin, M. F.; Desreux, J. F.; Merciny, E. *Inorganic Chemistry* **1986**, *25*, 2646.
- (36) Meyer, D.; Schaefer, M.; Bonnemain, B. *Investigative Radiology* **1988**, *23*.
- (37) Aime, S.; Botta, M.; Ermondi, G. *Inorganic Chemistry* **1992**, *31*, 4291.
- (38) Wang, X.; Jin, T.; Comblin, V.; Lopez-Mut, A.; Merciny, E.; Desreux, J. F. *Inorganic Chemistry* **1992**, *31*, 1095.
- (39) Toth, E.; Brucher, E.; Lazar, I.; Toth, I. *Inorganic Chemistry* **1994**, *33*, 4070.
- (40) Marques, M. P. M.; Geraldès, C. F. G. C.; Sherry, A. D.; Merbach, A. E.; Powell, H.; Pubanz, D.; Aime, S.; Botta, M. *Journal of Alloys and Compounds* **1995**, *225*, 303.
- (41) Viola-Villegas, N.; Doyle, R. P. *Coordination Chemistry Reviews* **2009**, *253*, 1906.
- (42) Boulon, M.-E.; Cucinotta, G.; Luzon, J.; Degl'Innocenti, C.; Perfetti, M.; Bernot, K.; Calvez, G.; Caneschi, A.; Sessoli, R. *Angewandte Chemie International Edition* **2013**, *52*, 350.
- (43) Richman, J. E.; Atkins, T. J. *Journal of the American Chemical Society* **1974**, *96*, 2268.

- (44) Athey, P. S.; Kiefer, G. E. *The Journal of Organic Chemistry* **2002**, *67*, 4081.
- (45) Weisman, G. R.; Reed, D. P. *The Journal of Organic Chemistry* **1996**, *61*, 5186.
- (46) Anet, F. A. L.; Krane, J.; Dale, J.; Daasvatn, K.; Kristiansen, P. O.; Swahn, C.-G. *Acta Chemica Scandinavica* **1973**, *27*, 3395.
- (47) Meyer, M.; Dahaoui-Gindrey, V.; Lecomte, C.; Guilard, R. *Coordination Chemistry Reviews* **1998**, *178–180, Part 2*, 1313.
- (48) Desreux, J. F. *Inorganic Chemistry* **1980**, *19*, 1319.
- (49) Spirlet, M. R.; Rebizant, J.; Desreux, J. F.; Loncin, M. F. *Inorganic Chemistry* **1984**, *23*, 359.
- (50) Aime, S.; Botta, M.; Fasano, M.; Marques, M. P. M.; Geraldes, C. F. G. C.; Pubanz, D.; Merbach, A. E. *Inorganic Chemistry* **1997**, *36*, 2059.
- (51) Hermann, P.; Kotek, J.; Kubicek, V.; Lukes, I. *Dalton Transactions* **2008**, 3027.
- (52) Jacques, V.; Desreux, J. F. *Inorganic Chemistry* **1994**, *33*, 4048.
- (53) Woods, M.; Botta, M.; Avedano, S.; Wang, J.; Sherry, A. D. *Dalton Transactions* **2005**, 3829.
- (54) Ishiguchi, T.; Takahashi, S. *Drugs in R&D* **2010**, *10*, 133.
- (55) Solomon, I. *Physical Review* **1955**, *99*, 559.
- (56) Solomon, I.; Bloembergen, N. *The Journal of Chemical Physics* **1956**, *25*, 261.
- (57) Bloembergen, N. *The Journal of Chemical Physics* **1957**, *27*, 572.
- (58) Morgan, L. O.; Nolle, A. W. *The Journal of Chemical Physics* **1959**, *31*, 365.
- (59) Bloembergen, N.; Morgan, L. O. *Journal of Chemical Physics* **1961**, *34*, 842.
- (60) Bertini, I.; Luchinat, C. *NMR of Paramagnetic Molecules in Biological Systems*; Benjamin/Cummings: Menlo Park, CA, 1986.
- (61) Lauffer, R. B. *Chemical Reviews* **1987**, *87*, 901.
- (62) Chen, J. W.; Belford, R. L.; Clarkson, R. B. *The Journal of Physical Chemistry A* **1998**, *102*, 2117.
- (63) Datta, A.; Raymond, K. N. *Accounts of Chemical Research* **2009**, *42*, 938.
- (64) Aime, S.; Calabi, L.; Cavallotti, C.; Gianolio, E.; Giovenzana, G. B.; Losi, P.; Maiocchi, A.; Palmisano, G.; Sisti, M. *Inorganic Chemistry* **2004**, *43*, 7588.
- (65) Moreau, G.; Helm, L.; Purans, J.; Merbach, A. E. *The Journal of Physical Chemistry A* **2002**, *106*, 3034.
- (66) Laus, S.; Ruloff, R.; Tóth, É.; Merbach, A. E. *Chemistry – A European Journal* **2003**, *9*, 3555.
- (67) Nicolle, G. M.; Yerly, F.; Imbert, D.; Böttger, U.; Bünzli, J.-C.; Merbach, A. E. *Chemistry – A European Journal* **2003**, *9*, 5453.
- (68) Lincoln, S. F.; Merbach, A. E. In *Advances in Inorganic Chemistry*; Sykes, A. G., Ed.; Academic Press: 1995; Vol. Volume 42, p 1.
- (69) Koenig, S. H.; Schillinger, W. E. *Journal of Biological Chemistry* **1969**, *244*, 3283.



- (70) Stephens, E. M.; Grisham, C. M. *Biochemistry* **1979**, *18*, 4876.
- (71) Powell, D. H.; Merbach, A. E.; González, G.; Brücher, E.; Micskei, K.; Ottaviani, M. F.; Köhler, K.; Von Zelewsky, A.; Grinberg, O. Y.; Lebedev, Y. S. *Helvetica Chimica Acta* **1993**, *76*, 2129.
- (72) Aime, S.; Botta, M.; Fasano, M.; Terreno, E. *Chemical Society Reviews* **1998**, *27*, 19.
- (73) Powell, D. H.; Dhubhghaill, O. M. N.; Pubanz, D.; Helm, L.; Lebedev, Y. S.; Schlaepfer, W.; Merbach, A. E. *Journal of the American Chemical Society* **1996**, *118*, 9333.
- (74) Benmelouka, M.; Borel, A.; Moriggi, L.; Helm, L.; Merbach, A. E. *The Journal of Physical Chemistry B* **2007**, *111*, 832.
- (75) Senn, F.; Helm, L.; Borel, A.; Daul, C. A. *Comptes Rendus Chimie* **2012**, *15*, 250.
- (76) Caravan, P.; Farrar, C. T.; Frullano, L.; Uppal, R. *Contrast Media & Molecular Imaging* **2009**, *4*, 89.
- (77) Tóth, E. v.; Helm, L.; Merbach, A. E.; Wiley: New York, 2001, p 45.
- (78) Sherry, A. D.; Wu, Y. *Current Opinion in Chemical Biology* **2013**, *17*, 167.
- (79) Werner, E. J.; Datta, A.; Jocher, C. J.; Raymond, K. N. *Angewandte Chemie International Edition* **2008**, *47*, 8568.
- (80) Terreno, E.; Castelli, D. D.; Viale, A.; Aime, S. *Chemical Reviews* **2010**, *110*, 3019.
- (81) Muller, R. N.; Elst, L. V.; Rinck, P. A.; Vallet, P.; Maton, F.; Fischer, H.; Roch, A.; Haverbeke, Y. V. *Investigative Radiology* **1988**, *23*.
- (82) Bertini, I.; Luchinat, C.; Parigi, G. In *Advances in Inorganic Chemistry*; Academic Press: 2005; Vol. Volume 57, p 105.
- (83) Banci, L.; Bertini, I.; Luchinat, C. *Inorganica Chimica Acta* **1985**, *100*, 173.
- (84) Strandberg, E.; Westlund, P.-O. *Journal of Magnetic Resonance, Series A* **1996**, *122*, 179.
- (85) Horrocks, W. D.; Sudnick, D. R. *Accounts of Chemical Research* **1981**, *14*, 384.
- (86) Beeby, A.; M. Clarkson, I.; S. Dickins, R.; Faulkner, S.; Parker, D.; Royle, L.; S. de Sousa, A.; A. Gareth Williams, J.; Woods, M. *Journal of the Chemical Society, Perkin Transactions 2* **1999**, 493.
- (87) Alpoim, M. C.; Urbano, A. M.; Geraldés, C. F. G. C.; Peters, J. A. *Journal of the Chemical Society, Dalton Transactions* **1992**.
- (88) Koenig, S. H.; Brown Iii, R. D. *Progress in Nuclear Magnetic Resonance Spectroscopy* **1990**, *22*, 487.
- (89) Frey, U.; Merbach, A. E.; Powell, D. H.; Delpuech, J.-J., Ed.; John Wiley & Sons Ltd.: Chichester, 1995, p 263.
- (90) Zech, S. G.; Eldredge, H. B.; Lowe, M. P.; Caravan, P. *Inorganic Chemistry* **2007**, *46*, 3576.

- (91) Rast, S.; Borel, A.; Helm, L.; Belorizky, E.; Fries, P. H.; Merbach, A. E. *Journal of the American Chemical Society* **2001**, *123*, 2637.
- (92) Astashkin, A. V.; Raitsimring, A. M.; Caravan, P. *The Journal of Physical Chemistry A* **2004**, *108*, 1990.
- (93) Moreau, J.; Guillon, E.; Aplincourt, P.; Pierrard, J.-C.; Rimbault, J.; Port, M.; Aplincourt, M. *European Journal of Inorganic Chemistry* **2003**, *2003*, 3007.
- (94) Aime, S.; Botta, M.; Ermondi, G. *Journal of Magnetic Resonance (1969)* **1991**, *92*, 572.
- (95) Rooney, W. D.; Johnson, G.; Li, X.; Cohen, E. R.; Kim, S.-G.; Ugurbil, K.; Springer, C. S. *Magnetic Resonance in Medicine* **2007**, *57*, 308.
- (96) Dirac, P. A. M. *Proceedings of the Royal Society of London. Series A* **1928**, *117*, 610.
- (97) Peters, J. A.; Huskens, J.; Raber, D. J. *Progress in Nuclear Magnetic Resonance Spectroscopy* **1996**, *28*, 283.
- (98) Bleaney, B. *Journal of Magnetic Resonance (1969)* **1972**, *8*, 91.
- (99) Golding, R. M.; Halton, M. P. *Australian Journal of Chemistry* **1972**, *25*, 2577.
- (100) Piguet, C.; Geraldes, C. F. G. C. In *Handbook on the Physics and Chemistry of Rare Earths*; Gschneidner, K. A., Bünzli, J.-C., Pecharsky, V. K., Eds.; Elsevier: 2003; Vol. Volume 33, p 353.
- (101) Bleaney, B.; Dobson, C. M.; Levine, B. A.; Martin, R. B.; Williams, R. J. P.; Xavier, A. V. *Journal of the Chemical Society, Chemical Communications* **1972**, 791b.
- (102) Horrocks, W. D.; Sipe, J. P. *Journal of the American Chemical Society* **1971**, *93*, 6800.
- (103) Reuben, J. *Journal of Magnetic Resonance (1969)* **1982**, *50*, 233.
- (104) Muller, G.; Kean, S. D.; Parker, D.; Riehl, J. P. *The Journal of Physical Chemistry A* **2002**, *106*, 12349.
- (105) Dickins, R. S.; Parker, D.; Bruce, J. I.; Tozer, D. J. *Dalton Transactions* **2003**, 1264.
- (106) Borel, A.; Bean, J. F.; Clarkson, R. B.; Helm, L.; Moriggi, L.; Sherry, A. D.; Woods, M. *Chemistry – A European Journal* **2008**, *14*, 2658.
- (107) Ren, J.; Zhang, S.; Sherry, A. D.; Geraldes, C. F. G. C. *Inorganica Chimica Acta* **2002**, *339*, 273.
- (108) Platas-Iglesias, C. *European Journal of Inorganic Chemistry* **2012**, *2012*, 2023.
- (109) Di Pietro, S.; Piano, S. L.; Di Bari, L. *Coordination Chemistry Reviews* **2011**, *255*, 2810.
- (110) Horrocks, W. D.; Schmidt, G. F.; Sudnick, D. R.; Kittrell, C.; Bernheim, R. A. *Journal of the American Chemical Society* **1977**, *99*, 2378.

- (111) Horrocks, W. D.; Sudnick, D. R. *Journal of the American Chemical Society* **1979**, *101*, 334.
- (112) Beeby, A.; S. Dickins, R.; Faulkner, S.; Parker, D.; A. Gareth Williams, J. *Chemical Communications* **1997**, *0*, 1401.
- (113) Parker, D.; Williams, J. A. G. *Journal of the Chemical Society, Dalton Transactions* **1996**, *0*, 3613.
- (114) Dickins, R. S.; Howard, J. A. K.; Lehmann, C. W.; Moloney, J.; Parker, D.; Peacock, R. D. *Angewandte Chemie International Edition in English* **1997**, *36*, 521.
- (115) A. K. Howard, J.; M. Kenwright, A.; M. Moloney, J.; Parker, D.; Woods, M.; Port, M.; Navet, M.; Rousseau, O. *Chemical Communications* **1998**, 1381.
- (116) Swift, T. J.; Connick, R. E. *Journal of Chemical Physics* **1962**, *37*, 307.
- (117) Swift, T. J.; Connick, R. E. *The Journal of Chemical Physics* **1964**, *41*, 2553.
- (118) McConnell, H. M. *The Journal of Chemical Physics* **1958**, *28*, 430.
- (119) Southwood-Jones, R. V.; Earl, W. L.; Newman, K. E.; Merbach, A. E. *The Journal of Chemical Physics* **1980**, *73*, 5909.
- (120) Micskei, K.; Powell, D. H.; Helm, L.; Brücher, E.; Merbach, A. E. *Magnetic Resonance in Chemistry* **1993**, *31*, 1011.
- (121) Gonzalez, G.; Powell, D. H.; Tissieres, V.; Merbach, A. E. *The Journal of Physical Chemistry* **1994**, *98*, 53.
- (122) Dunand, F. A.; Borel, A.; Merbach, A. E. *Journal of the American Chemical Society* **2002**, *124*, 710.
- (123) Aime, S.; Barbero, L.; Botta, M.; Ermondi, G. *Journal of the Chemical Society, Dalton Transactions* **1992**, *0*, 225.
- (124) Bénazeth, S.; Purans, J.; Chalbot, M.-C.; Nguyen-van-Duong, M. K.; Nicolas, L.; Keller, F.; Gaudemer, A. *Inorganic Chemistry* **1998**, *37*, 3667.
- (125) Rudovský, J.; Cígler, P.; Kotek, J.; Hermann, P.; Vojtíšek, P.; Lukeš, I.; Peters, J. A.; Vander Elst, L.; Muller, R. N. *Chemistry – A European Journal* **2005**, *11*, 2373.
- (126) Werner, E. J.; Avedano, S.; Botta, M.; Hay, B. P.; Moore, E. G.; Aime, S.; Raymond, K. N. *Journal of the American Chemical Society* **2007**, *129*, 1870.
- (127) Rodríguez-Rodríguez, A.; Esteban-Gómez, D.; de Blas, A.; Rodríguez-Blas, T.; Fekete, M.; Botta, M.; Tripier, R.; Platas-Iglesias, C. *Inorganic Chemistry* **2012**, *51*, 2509.
- (128) Laus, S.; Sour, A.; Ruloff, R.; Tóth, É.; Merbach, A. E. *Chemistry – A European Journal* **2005**, *11*, 3064.
- (129) Rudovský, J.; Botta, M.; Hermann, P.; Hardcastle, K. I.; Lukeš, I.; Aime, S. *Bioconjugate Chemistry* **2006**, *17*, 975.

- (130) Aime, S.; Botta, M.; Fasano, M.; Terreno, E. *Accounts of Chemical Research* **1999**, *32*, 941.
- (131) Aime, S.; Barge, A.; Bruce, J. I.; Botta, M.; Howard, J. A. K.; Moloney, J. M.; Parker, D.; de Sousa, A. S.; Woods, M. *Journal of the American Chemical Society* **1999**, *121*, 5762.
- (132) Woods, M.; Aime, S.; Botta, M.; Howard, J. A. K.; Moloney, J. M.; Navet, M.; Parker, D.; Port, M.; Rousseaux, O. *Journal of the American Chemical Society* **2000**, *122*, 9781.
- (133) Pierrard, J.-C.; Rimbault, J.; Aplin-court, M.; Le Greneur, S.; Port, M. *Contrast Media & Molecular Imaging* **2008**, *3*, 243.
- (134) Häussinger, D.; Huang, J.-r.; Grzesiek, S. *Journal of the American Chemical Society* **2009**, *131*, 14761.
- (135) Brittain, H. G.; Desreux, J. F. *Inorganic Chemistry* **1984**, *23*, 4459.
- (136) Comblin, V.; Gilsoul, D.; Hermann, M.; Humblet, V.; Jacques, V.; Mesbahi, M.; Sauvage, C.; Desreux, J. F. *Coordination Chemistry Reviews* **1999**, *185-186*, 451.
- (137) Woods, M.; Kovacs, Z.; Zhang, S.; Sherry, A. D. *Angewandte Chemie International Edition* **2003**, *42*, 5889.
- (138) Bottrill, M.; Kwok, L.; Long, N. J. *Chemical Society Reviews* **2006**, *35*, 557.
- (139) Lauffer, R. B.; Parmelee, D. J.; Dunham, S. U.; Ouellet, H. S.; Dolan, R. P.; Witte, S.; McMurry, T. J.; Walovitch, R. C. *Radiology* **1998**, *207*, 529.
- (140) Muller, R. N.; Radüchel, B.; Laurent, S.; Platzek, J.; Piérart, C.; Mareski, P.; Vander Elst, L. *European Journal of Inorganic Chemistry* **1999**, *1999*, 1949.
- (141) Caravan, P.; Cloutier, N. J.; Greenfield, M. T.; McDermid, S. A.; Dunham, S. U.; Bulte, J. W. M.; Amedio, J. C.; Looby, R. J.; Supkowski, R. M.; Horrocks, W. D.; McMurry, T. J.; Lauffer, R. B. *Journal of the American Chemical Society* **2002**, *124*, 3152.
- (142) Zhou, X.; Caravan, P.; Clarkson, R. B.; Westlund, P.-O. *Journal of Magnetic Resonance* **2004**, *167*, 147.
- (143) Løkling, K.-E.; Fossheim, S. L.; Klaveness, J.; Skurtveit, R. *Journal of Controlled Release* **2004**, *98*, 87.
- (144) Gianolio, E.; Porto, S.; Napolitano, R.; Baroni, S.; Giovenzana, G. B.; Aime, S. *Inorganic Chemistry* **2012**, *51*, 7210.
- (145) Kielar, F.; Tei, L.; Terreno, E.; Botta, M. *Journal of the American Chemical Society* **2010**, *132*, 7836.
- (146) Polášek, M.; Hermann, P.; Peters, J. A.; Geraldès, C. F. G. C.; Lukeš, I. *Bioconjugate Chemistry* **2009**, *20*, 2142.
- (147) Botta, M.; Tei, L. *European Journal of Inorganic Chemistry* **2012**, *2012*, 1945.
- (148) Kobayashi, H.; Brechbiel, M. W. *Advanced Drug Delivery Reviews* **2005**, *57*, 2271.

- (149) Tweedle, M. F.; Eaton, S. M.; Eckelman, W. C.; Gaughan, G. T.; Hagan, J. J.; Wedeking, P. W.; Yost, F. J. *Investigative Radiology* **1988**, *23*.
- (150) Nicolle, G. M.; Helm, L.; Merbach, A. E. *Magnetic Resonance in Chemistry* **2003**, *41*, 794.
- (151) Gianolio, E.; Giovenzana, G. B.; Longo, D.; Longo, I.; Menegotto, I.; Aime, S. *Chemistry – A European Journal* **2007**, *13*, 5785.
- (152) Bornhop, D. J.; Hubbard, D. S.; Houlne, M. P.; Adair, C.; Kiefer, G. E.; Pence, B. C.; Morgan, D. L. *Analytical Chemistry* **1999**, *71*, 2607.
- (153) Sarka, L.; Burai, L.; Brücher, E. *Chemistry – A European Journal* **2000**, *6*, 719.
- (154) White, G. W.; Gibby, W. A.; Tweedle, M. F. *Invest Radiol* **2006**, *41*, 272.
- (155) Aime, S.; Caravan, P. *Journal of Magnetic Resonance Imaging* **2009**, *30*, 1259.
- (156) Avedano, S.; Botta, M.; Haigh, J.; Longo, D.; Woods, M. *Inorganic Chemistry* **2013**, *52*, 8436.
- (157) Miller, K. J.; Saherwala, A. A.; Webber, B. C.; Wu, Y.; Sherry, A. D.; Woods, M. *Inorganic Chemistry* **2010**, *49*, 8662.
- (158) Aime, S.; Barge, A.; Batsanov, A. S.; Botta, M.; Castelli, D. D.; Fedeli, F.; Mortillaro, A.; Parker, D.; Puschmann, H. *Chemical Communications* **2002**, 1120.
- (159) Barge, A.; Botta, M.; Parker, D.; Puschmann, H. *Chemical Communications* **2003**, 1386.
- (160) Merbach, A. E.; Helm, L.; Tóth, E. v. *The Chemistry of Contrast Agents in Medical Magnetic Resonance Imaging*; 2nd ed. ed.; Wiley, 2013.
- (161) Brechbiel, M. W.; Gansow, O. A.; Atcher, R. W.; Schlom, J.; Esteban, J.; Simpson, D.; Colcher, D. *Inorganic Chemistry* **1986**, *25*, 2772.
- (162) Moi, M. K.; Meares, C. F.; DeNardo, S. J. *Journal of the American Chemical Society* **1988**, *110*, 6266.
- (163) Aime, S.; Botta, M.; Fasano, M.; Crich, S. G.; Terreno, E. *Journal of Biological Inorganic Chemistry* **1996**, *1*, 312.
- (164) Elst, L. V.; Maton, F.; Laurent, S.; Seghi, F.; Chapelle, F.; Muller, R. N. *Magnetic Resonance in Medicine* **1997**, *38*, 604.
- (165) Faulkner, S.; Pope, S. J. A. *Journal of the American Chemical Society* **2003**, *125*, 10526.
- (166) Di Bari, L.; Pescitelli, G.; Sherry, A. D.; Woods, M. *Inorganic Chemistry* **2005**, *44*, 8391.
- (167) Ranganathan, R. S.; Raju, N.; Fan, H.; Zhang, X.; Tweedle, M. F.; Desreux, J. F.; Jacques, V. *Inorganic Chemistry* **2002**, *41*, 6856.
- (168) Webber, B. C.; Woods, M. *Inorganic Chemistry* **2012**, *51*, 8576.
- (169) Karplus, M. *Journal of the American Chemical Society* **1963**, *85*, 2870.
- (170) The Nuclear Overhauser Effect. <http://www.chem.wisc.edu/areas/reich/nmr/08-tech-02-noe.htm> (accessed June 17th, 2013).

- (171) Woods, M.; Kovacs, Z.; Kiraly, R.; Brücher, E.; Zhang, S.; Sherry, A. D. *Inorganic Chemistry* **2004**, *43*, 2845.
- (172) Schlesinger, J.; Rajander, J.; Ihalainen, J. A.; Ramesh, D.; Eklund, P.; Fagerholm, V.; Nuutila, P.; Solin, O. *Inorganic Chemistry* **2011**, *50*, 4260.
- (173) Tircso, G.; Webber, B. C.; Kucera, B. E.; Young, V. G.; Woods, M. *Inorganic Chemistry* **2011**, *50*, 7966.
- (174) Delgado, R.; da Silva, J. J. R. F. *Talanta* **1982**, *29*, 815.
- (175) Hancock, R. D.; Motekaitis, R. J.; Mashishi, J.; Cukrowski, I.; Reibenspies, J. H.; Martell, A. E. *Journal of the Chemical Society, Perkin Transactions 2* **1996**, *0*, 1925.
- (176) Cacheris, W. P.; Nickle, S. K.; Sherry, A. D. *Inorganic Chemistry* **1987**, *26*, 958.
- (177) Polášek, M.; Kotek, J.; Hermann, P.; Císařová, I.; Binnemans, K.; Lukeš, I. *Inorganic Chemistry* **2008**, *48*, 466.
- (178) Vitha, T.; Kubicek, V.; Kotek, J.; Hermann, P.; Vander Elst, L.; Muller, R. N.; Lukes, I.; Peters, J. A. *Dalton Transactions* **2009**, 3204.
- (179) Rohovec, J.; Vojtisek, P.; Hermann, P.; Ludvik, J.; Lukes, I. *Journal of the Chemical Society, Dalton Transactions* **2000**, *0*, 141.
- (180) Kotek, J.; Rudovský, J.; Hermann, P.; Lukeš, I. *Inorganic Chemistry* **2006**, *45*, 3097.
- (181) Klimentová, J.; Vojtišek, P. *Journal of Molecular Structure* **2007**, *826*, 82.
- (182) Campello, M. P. C.; Lacerda, S.; Santos, I. C.; Pereira, G. A.; Geraldies, C. F. G. C.; Kotek, J.; Hermann, P.; Vaněk, J.; Lubal, P.; Kubíček, V.; Tóth, É.; Santos, I. *Chemistry – A European Journal* **2010**, *16*, 8446.
- (183) Ren, J.; Sherry, A. D. *Journal of Magnetic Resonance, Series B* **1996**, *111*, 178.
- (184) Payne, K. M.; Woods, M. *unpublished results*.
- (185) Langford, C. H.; Gray, H. B. *Ligand Substitution Processes*; W.A. Benjamin: New York, 1966.
- (186) Koenig, S. H.; Epstein, M. *The Journal of Chemical Physics* **1975**, *63*, 2279.
- (187) Caravan, P.; Astashkin, A. V.; Raitsimring, A. M. *Inorganic Chemistry* **2003**, *42*, 3972.
- (188) Aime, S.; Botta, M.; Garda, Z. n.; Kucera, B. E.; Tircso, G.; Young, V. G.; Woods, M. *Inorganic Chemistry* **2011**, *50*, 7955.
- (189) Lebduskova, P.; Hermann, P.; Helm, L.; Toth, E.; Kotek, J.; Binnemans, K.; Rudovsky, J.; Lukes, I.; Merbach, A. E. *Dalton Transactions* **2007**, *0*, 493.
- (190) Horrocks, W. D.; Arkle, V. K.; Liotta, F. J.; Sudnick, D. R. *Journal of the American Chemical Society* **1983**, *105*, 3455.
- (191) Woods, M. Ph.D. Dissertation, University of Durham, 1998.
- (192) Payne, K. M.; Valente, E. J.; Aime, S.; Botta, M.; Woods, M. *Chemical Communications* **2013**, *49*, 2320.

- (193) Persson, B. A.; Larsson, A. L. E.; Le Ray, M.; Bäckvall, J.-E. *Journal of the American Chemical Society* **1999**, *121*, 1645.
- (194) Demizu, Y.; Moriyama, A.; Onomura, O. *Tetrahedron Letters* **2009**, *50*, 5241.
- (195) Slack, J.; Woods, M., unpublished results.
- (196) Aime, S.; Botta, M.; Frullano, L.; Crich, S. G.; Giovenzana, G. B.; Pagliarin, R.; Palmisano, G.; Sisti, M. *Chemistry – A European Journal* **1999**, *5*, 1253.
- (197) Aime, S.; Botta, M.; Fedeli, F.; Gianolio, E.; Terreno, E.; Anelli, P. *Chemistry – A European Journal* **2001**, *7*, 5261.
- (198) Gianolio, E.; Napolitano, R.; Fedeli, F.; Arena, F.; Aime, S. *Chemical Communications* **2009**, *0*, 6044.
- (199) Kuduk, S. D.; Ng, C.; Feng, D.-M.; Wai, J. M. C.; Chang, R. S. L.; Harrell, C. M.; Murphy, K. L.; Ransom, R. W.; Reiss, D.; Ivarsson, M.; Mason, G.; Boyce, S.; Tang, C.; Prueksaritanont, T.; Freidinger, R. M.; Pettibone, D. J.; Bock, M. G. *Journal of Medicinal Chemistry* **2004**, *47*, 6439.
- (200) Feng, D.-M.; Wai, J. M.; Kuduk, S. D.; Ng, C.; Murphy, K. L.; Ransom, R. W.; Reiss, D.; Chang, R. S. L.; Harrell, C. M.; MacNeil, T.; Tang, C.; Prueksaritanont, T.; Freidinger, R. M.; Pettibone, D. J.; Bock, M. G. *Bioorganic & Medicinal Chemistry Letters* **2005**, *15*, 2385.
- (201) André, J. P.; Tóth, É.; Fischer, H.; Seelig, A.; Mäcke, H. R.; Merbach, A. E. *Chemistry – A European Journal* **1999**, *5*, 2977.
- (202) Nicolle, G.; Tóth, É.; Eisenwiener, K.-P.; Mäcke, H.; Merbach, A. *JBIC* **2002**, *7*, 757.
- (203) Torres, S.; Martins, J. A.; André, J. P.; Geraldes, C. F. G. C.; Merbach, A. E.; Tóth, É. *Chemistry – A European Journal* **2006**, *12*, 940.
- (204) Schühle, D. T.; Schatz, J.; Laurent, S.; VanderElst, L.; Muller, R. N.; Stuart, M. C. A.; Peters, J. A. *Chemistry – A European Journal* **2009**, *15*, 3290.
- (205) Dunand, F. A.; Tóth, É.; Hollister, R.; Merbach, A. E. *JBIC* **2001**, *6*, 247.
- (206) Desreux, J. F.; F., T. M.; Ratsep, P. C.; Wagler, T. R.; Marinelli, E. R. Hepatobiliary tetraazamacrocyclic magnetic resonance contrast agents Bristol Myers Squibb, Princeton, N.J. 1994
- (207) Brechbiel, M. W.; Chong, H.-S. Backbone-substituted bifunctional DOTA ligands, complexes and compositions thereof, and methods of using same. United States Dept. of Health and Human Services, USA WO2004021996 (A3) 2004
- (208) Vanasschen, C.; Bouslimani, N.; Thonon, D.; Desreux, J. F. *Inorganic Chemistry* **2011**, *50*, 8946.
- (209) Camp, C.; Guidal, V.; Biswas, B.; Pécaut, J.; Dubois, L.; Mazzanti, M. *Chemical Science* **2012**, *3*, 2433.
- (210) Scully, C. C. G.; Rai, V.; Poda, G.; Zaretsky, S.; Burns, D. C.; Houliston, R. S.; Lou, T.; Yudin, A. K. *Chemistry – A European Journal* **2012**, *18*, 15612.

- (211) Guo, S.; Wang, G.; Ai, L. *Tetrahedron: Asymmetry* **2013**, *24*, 480.
- (212) Stetter, H.; Mayer, K.-H. *Chemische Berichte* **1961**, *94*, 1410.
- (213) Alexakis, A.; Chauvin, A.-S.; Stouvenel, R.; Vrancken, E.; Mutti, S.; Mangeney, P. *Tetrahedron: Asymmetry* **2001**, *12*, 1171.
- (214) Boschetti, F.; Denat, F.; Espinosa, E.; Guillard, R. *Chemical Communications* **2002**, *0*, 312.
- (215) Flann, C.; Malone, T. C.; Overman, L. E. *Journal of the American Chemical Society* **1987**, *109*, 6097.
- (216) Fabbriizzi, L.; Licchelli, M.; Manotti Lanfredi, A. M.; Vassalli, O.; Ugozzoli, F. *Inorganic Chemistry* **1996**, *35*, 1582.
- (217) Gèrbèlèu, N. V.; Gerbeleu, N. V.; Arion, V. B.; Burgess, J. *Template synthesis of macrocyclic compounds*; Wiley-VCH, 1999.
- (218) Kang, S.-G.; Nam, K.; Kweon, J. K.; Jung, S.-K.; Lee, U. *Bulletin of the Korean Chemical Society* **2006**, *27*, 577.
- (219) Gurumoorthy, P.; Ravichandran, J.; Karthikeyan, N.; Palani, P.; Rahiman, A. K. *Bulletin of the Korean Chemical Society* **2012**, *33*, 2279.
- (220) Hoffman, R. V.; Tao, J. *Tetrahedron* **1997**, *53*, 7119.
- (221) Wang, Z.-F.; Xu, J.-C. *Tetrahedron* **1998**, *54*, 12597.
- (222) Aime, S.; Botta, M.; Crich, S. G.; Terreno, E.; Anelli, P. L.; Uggeri, F. *Chemistry – A European Journal* **1999**, *5*, 1261.
- (223) Geraldes, C. F. G. C.; Sherry, A. D.; Kiefer, G. E. *Journal of Magnetic Resonance (1969)* **1992**, *97*, 290.
- (224) *Macrocyclic Synthesis: A Practical Approach*; Parker, D., Ed.; Oxford University Press: USA, 1996.
- (225) Kang, H.; Facchetti, A.; Jiang, H.; Cariati, E.; Righetto, S.; Ugo, R.; Zuccaccia, C.; Macchioni, A.; Stern, C. L.; Liu, Z.; Ho, S.-T.; Brown, E. C.; Ratner, M. A.; Marks, T. J. *Journal of the American Chemical Society* **2007**, *129*, 3267.
- (226) Hembre, R. T.; Scott, C. P.; Norton, J. R. *The Journal of Organic Chemistry* **1987**, *52*, 3650.
- (227) Shono, T.; Kise, N.; Shirakawa, E.; Matsumoto, H.; Okazaki, E. *The Journal of Organic Chemistry* **1991**, *56*, 3063.
- (228) Smith, A. M. R.; Rzepa, H. S.; White, A. J. P.; Billen, D.; Hii, K. K. *The Journal of Organic Chemistry* **2010**, *75*, 3085.
- (229) Shaikh, A. L.; Puranik, V. G.; Deshmukh, A. R. A. S. *Tetrahedron* **2005**, *61*, 2441.
- (230) Khersonsky, O.; Tawfik, D. S. *Biochemistry* **2005**, *44*, 6371.
- (231) Pàmies, O.; Bäckvall, J.-E. *The Journal of Organic Chemistry* **2003**, *68*, 4815.
- (232) Malinowska, B.; Majewska, P.; Szatkowski, P.; Kafarski, P.; Lejczak, B. *Biocatalysis & Biotransformation* **2011**, *29*, 271.



- (233) Katakya, R.; Parker, D.; Teasdale, A.; Hutchinson, J. P.; Buschmann, H.-J. *Journal of the Chemical Society, Perkin Transactions 2* **1992**, 1347.
- (234) Zhang, S.; Wu, K.; Biewer, M. C.; Sherry, A. D. *Inorganic Chemistry* **2001**, *40*, 4284.
- (235) Aime, S.; Barge, A.; Delli Castelli, D.; Fedeli, F.; Mortillaro, A.; Nielsen, F. U.; Terreno, E. *Magnetic Resonance in Medicine* **2002**, *47*, 639.
- (236) Vasalatiy, O.; Zhao, P.; Woods, M.; Marconescu, A.; Castillo-Muzquiz, A.; Thorpe, P.; Kiefer, G. E.; Dean Sherry, A. *Bioorganic & Medicinal Chemistry* **2011**, *19*, 1106.